

Institute of Experimental Pharmacology and Toxicology
Center for Experimental Medicine
University Medical Center Hamburg-Eppendorf

**Modeling primary carnitine deficiency-mediated dilated
cardiomyopathy in engineered heart tissue format**

Dissertation

Submitted to the Department of Biology

Faculty of Mathematics, Informatics, and Natural Sciences

University of Hamburg

for the degree of

Doctor of Natural Sciences

(Dr. rer. nat.)

by

Malte Florian Loos

from Giessen

Hamburg, 2021

1. Referee: Prof. Dr. Arne Hansen

2. Referee: Prof. Dr. Julia Kehr

Date of disputation: 28.01.2022

Disputation committee:

Prof. Dr. Baris Tursun

Prof. Dr. Julia Kehr

Prof. Dr. Friederike Cuello

This thesis was carried out from January 2018 until November 2021 at the Institute of Experimental Pharmacology and Toxicology (Director: Prof. Dr. Thomas Eschenhagen) under the supervision of Prof. Dr. Arne Hansen.

Table of contents

1	Introduction	1
1.1	Cardiac metabolism.....	1
1.2	Carnitine shuttle	4
1.3	Primary carnitine deficiency.....	7
1.3.1	Animal models of primary and secondary carnitine deficiency.....	9
1.4	Dilated cardiomyopathy.....	10
1.5	Cardiac differentiation and metabolic maturation.....	11
1.6	Genome editing by CRISPR/Cas9.....	14
1.7	Modeling disease with human induced pluripotent stem cells.....	16
2	Aim.....	20
3	Material and methods.....	21
3.1	Cell culture media	21
3.2	HiPSC cell culture conditions	23
3.3	CRISPR/Cas9-mediated gene editing	23
3.3.1	OCTN2 (N32S) missense mutation	23
3.3.2	OCTN2 (-/-) knockout.....	24
3.4	Cell line generation by CRISPR/Cas9	25
3.4.1	Nucleofection	26
3.4.2	Subcloning and off-target analysis.....	27
3.5	Karyotyping	28
3.6	Cardiac differentiation	29
3.7	Engineered heart tissues (EHT)	32
3.7.1	Video-optical contraction analysis	33
3.7.2	Electrical pacing & average peak measurement.....	34
3.7.3	Glucose and lactate measurement.....	34
3.7.4	Fatty acid and carnitine supplementation	35
3.7.5	Transmission electron microscopy	35
3.8	Analysis of acylcarnitines and ceramides	36
3.8.1	Acylcarnitines.....	36
3.8.2	Ceramides.....	36
3.9	Tandem Mass Tag (TMT)-based quantitative proteomic analysis.....	37
3.9.1	EHT harvesting for quantitative mass spectrometry.....	37
3.9.2	Tissue protein extraction and digestion for mass spectrometry	37
3.9.3	Sample labeling for mass spectrometry.....	38
3.9.4	Mass spectrometry analysis	38
3.9.5	Pathway enrichment analysis of significant proteins.....	39
3.10	TRIzol extraction	39

Table of contents — II

3.11	Gene expression analysis & mitochondrial DNA quantification	40
3.12	Southern blot	41
3.13	Single-nucleus RNA sequencing	42
3.14	Statistical analysis	42
4	Results	43
4.1	CRISPR/Cas9	43
4.1.1	TIDER analysis and clone picking for OCTN2 (N32S) generation	43
4.1.2	Gel electrophoresis for knockout validation of the <i>SLC22A5</i> gene	45
4.1.3	Southern blot analysis	47
4.1.4	Karyotype analysis	49
4.2	Cardiac differentiation	50
4.3	Characterization of the contractile phenotype in EHT format	51
4.3.1	EHT development under baseline conditions	51
4.3.2	EHT force development in fatty acid medium	56
4.4	Glucose consumption and lactate production	57
4.5	EHT carnitine supplementation – contractile analysis	58
4.6	EHT carnitine supplementation – glucose and lactate measurements	64
4.7	Acylcarnitine and ceramide EHT content	66
4.8	Transmission electron microscopy	68
4.9	Quantitative proteomic analysis	70
4.10	Quantitative reverse transcription PCR	76
4.11	Single-nucleus RNA sequencing	78
5	Discussion	87
5.1	Biotechnological challenges towards a reliable disease model	87
5.1.1	Principal aspects of disease modeling: Clinically relevant point mutation versus complete knockout	89
5.2	Faithful reproduction of the PCD DCM phenotype in the hiPSC-CM model	89
5.2.1	Impact of carnitine supplementation on force development and contractile kinetics	90
5.3	Fibrosis phenotype in OCTN2-defective EHTs	91
5.4	Metabolic remodeling	92
5.4.1	Lipid metabolism and tissue content of acylcarnitine	92
5.4.2	Consequences of acyl-CoA accumulation: Ceramides, TAG, ferroptosis	95
5.4.3	Glucose and pyruvate metabolism	97
5.4.4	New aspects of PCD: O-linked β -N-acetylglucosamine pathway	99
5.5	Single-nucleus RNA sequencing	100
5.5.1	Cardiomyocyte cluster definition and deviation in OCTN2-defective cell lines	100
5.5.2	Fibroblast cluster and endocardium-like cluster	102

Table of contents — III

5.5.3	Lipid metabolism and leukocytes.....	103
5.6	Conclusion & outlook.....	104
6	Summary.....	105
7	Zusammenfassung.....	107
8	References.....	109
9	Supplement.....	135
9.1	Supplementary figures and tables.....	135
9.2	List of abbreviations.....	150
9.3	Devices, materials and substances.....	158
9.3.1	Devices.....	158
9.3.2	Software.....	158
9.3.3	Materials and equipment.....	159
9.3.4	Cell culture medium and serum.....	159
9.3.5	Reagents.....	160
9.3.6	Kits and enzymes.....	161
9.3.7	Composition of reagents, buffers, and solutions.....	161
9.3.8	Antibodies.....	162
9.3.9	Primer, ssODN and gRNA sequences.....	163
9.4	Financial support.....	165
9.5	Publications.....	165
10	Declaration of contributions.....	166
11	Acknowledgements.....	167
12	Thesis English language declaration.....	169
13	Declaration of academic honesty - Eidesstattliche Erklärung.....	170

1 Introduction

1.1 Cardiac metabolism

The adult human heart circulates 7200 liters of blood per day by performing 100,000 heart contractions and consuming 35 liters of oxygen (Taegtmeyer et al. 2016). To maintain the performance of the heart, it requires ATP supply for myofibrillar shortening, myofilament relaxation via SERCA2-mediated calcium reuptake into the sarcoplasmic reticulum (SR) and maintenance of ion homeostasis. However, the cardiomyocyte capacity to store ATP is low, demonstrated by a complete myocardial ATP turnover every 10 seconds under resting conditions (Stanley et al. 2005). Accordingly, the heart constantly produces ATP with a rate of 6 kg per day. An essential prerequisite for this is the cardiomyocyte's ability to use various substrates for ATP production (e.g. fatty acids, glucose, lactate) in a complex network of metabolic pathways (Figure 1).

During embryogenesis, cardiomyocytes primarily rely on glucose and lactate as substrates for ATP production, while fatty acids play an inferior role. Accordingly, 50% of the cardiac ATP demand is derived from anaerobic glycolysis during the early phase of development (Lopaschuk et al. 1991). Through the transition from the fetal to a neonatal state, the heart is confronted with increasing oxygen levels and pressure due to a sudden inclusion of pulmonary circulation (Rudolph et al. 1975; Hew and Keller 2003). To accomplish the requirements of an increased cardiac workload and haemodynamic load, the heart responds by hyperplasia (cell division) and developmental hypertrophy in the early postnatal period (Li et al. 1996). Within this progression, the heart undergoes a substrate shift from glucose to fatty acids as a primary energy substrate. Furthermore, this developmental change is accompanied by an increased mitochondrial abundance and size (Pohjoismäki et al. 2010).

Approximately 5-10% of the adult cardiac ATP demand is generated from cytosolic glycolysis and 90-95% from mitochondrial oxidative phosphorylation under normoxic conditions. Fatty acids represent with 90% the primary substrate of oxidative phosphorylation, whereas the residual part of ATP is derived from pyruvate oxidation (Stanley et al. 2005). The contribution of lactate, ketones and amino acids is low but can increase during fasting or pathological conditions (Kolwicz et al. 2013). The ability to modulate substrate preference depending on oxygen supply, hormonal milieu and substrate availability is an indispensable property of the healthy adult heart and justifies the cardiomyocyte description as an omnivore (Taegtmeyer et al. 2004). This flexibility enables metabolic adaptation during ischemia and heart failure, where the contribution of glucose to ATP generation via aerobic and anaerobic glycolysis increases (Tran and Wang 2019). However, sustained anaerobic glycolysis uncoupled from oxidation of pyruvate is uneconomic and may be more detrimental than beneficial since elevated pyruvate

to lactate conversion results in acidification and disruption of ionic homeostasis (Jaswal et al. 2011).

The glycolytic shift under stress conditions is mainly related to an economic use of oxygen: Glucose requires 10% less oxygen for glucose oxidation than the equivalent ATP amount produced from fatty acids. In contrast, fatty acids are required to generate large amounts of ATP as one molecule of fatty acid can produce over 3-fold more ATP than one molecule of glucose (31 ATP per molecule glucose, 105 ATP per molecule palmitate; Karwi et al. 2018). Importantly, also maladaptive changes in fatty acid metabolism contribute to cardiac dysfunction. Accordingly, excessive fatty acid beta-oxidation as seen in diabetes, starvation or fasting results in increased mitochondrial reactive oxygen species (ROS) production, oxidative stress and impaired cardiac function (Lopaschuk et al. 2010; Kaludercic and Di Lisa 2020).

Fatty acids originate from three different endogenous and exogenous sources. First, fatty acids are synthesized from acetyl coenzyme A (acetyl-CoA) by endogenous *de novo* synthesis (Cooper et al. 2015). Moreover, long-chain fatty acids (LCFA) can be released by adipose tissue and are bound to albumin after entry into the circulation (Longo et al. 2006). This is followed by the active transport of non-esterified LCFA across the plasma membrane into the cytosol (cardiomyocyte) by cell type-specific membrane-bound transporters. In cardiomyocytes, the fatty acid translocase (FAT/CD36), fatty acid transport proteins (FATP1-6) and caveolins are relevant for intracellular uptake of LCFA (Chabowski et al. 2008). In addition, fatty acids derive from intracellular hydrolysis of triglycerides (TAG), phospholipids, or acylated proteins (Cooper et al. 2015). In turn, these lipid species can be obtained from endogenous lipoproteins such as chylomicrons or to a minor extent from very-low-density lipoprotein (VLDL) and low-density lipoprotein (LDL) (Lopaschuk et al. 2010).

The cardiac metabolism of fatty acids, glucose, ketones and amino acid yields acetyl-CoA that is shunted into the tricarboxylic acid (TCA) cycle to produce the pyridine nucleotides FADH₂ and NADH. These reducing equivalents enable an exergonic electron flow in the inner mitochondrial membrane, the initial step of oxidative phosphorylation, by delivering electrons to the coupled transfer of the respiratory chain. The proton gradient and resulting chemical potential is the driving force for ATP synthase to produce ATP from ADP by phosphorylation (Balaban 2009).

Preferential use of specific energy substrates by cardiomyocytes is primarily regulated by availability (i.e. plasma concentration), the transport of substrate into the cytosol and the catalytic activities of rate-limiting metabolic enzymes. This activity is regulated by the abundance of the respective enzymes, substrates, products and co-factors (Stanley et al. 2005; Taegtmeyer et al. 2016; Geraets et al. 2019).

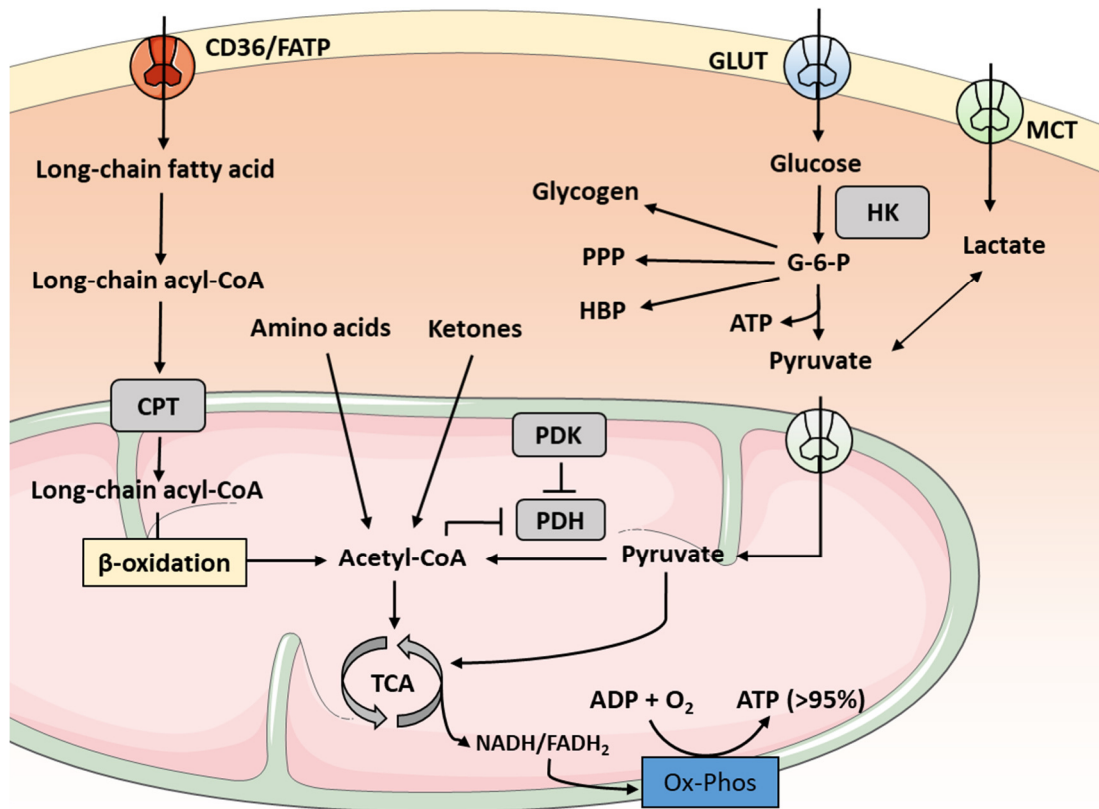


Figure 1: Overview of the cardiac metabolic network. The energy-yielding substrates (glucose, fatty acids, amino acids and ketones) converge on acetyl-CoA production via individual catabolic pathways and subsequently enter the tricarboxylic acid (TCA) cycle. Oxidative phosphorylation represents the final step of ATP production and supplies 95% of cardiac ATP demand. In healthy adult individuals, acetyl-CoA is primarily derived from fatty acid and to a lower extent from pyruvate oxidation. The contribution of amino acids and ketones to metabolism can increase under fasting conditions or starvation. CD36: Cluster of differentiation 36; FATP: Fatty acid transport protein; GLUT: Glucose transporter; MCT: Monocarboxylate transporter; HK: Hexokinase; G6P: Glucose-6-phosphate; PPP: Pentose phosphate pathway; HBP: Hexosamine biosynthetic pathway; CPT: Carnitine palmitoyltransferase; TCA: Tricarboxylic acid cycle; PDH: Pyruvate dehydrogenase; PDK: Pyruvate dehydrogenase kinase; NADH: Nicotinamide adenine dinucleotide phosphate; FADH₂: Flavin adenine dinucleotide; Ox-Phos: Oxidative phosphorylation; ATP: Adenosine triphosphate; ADP: Adenosine diphosphate.

Alternatively, post-translational modifications, such as acetylation and phosphorylation, control the activity of key metabolic enzymes. For instance, the flux of glucose and fatty acids is regulated by a competitive mechanism between the two pathways, known as the Randle cycle (Randle et al. 1963). In this context, the phosphorylation of pyruvate dehydrogenase (PDH) by different pyruvate dehydrogenase kinases (PDK) suppresses glucose oxidation via decreasing pyruvate to acetyl-CoA conversion in response to an increase in fatty acid oxidation (fasting

condition; Zhang et al. 2014). Conversely, elevated glucose oxidation leads to a decrease in fatty acid oxidation (fed condition).

Additional posttranslational modifications, like O-linked attachment of N-acetylglucosamine (GlcNAc) moieties, as end-products of the hexosamine biosynthetic pathway (HBP), have been proposed to control metabolic processes as glycosylation controls the activity of lipoproteins and glycolytic proteins (Chaiyawat et al. 2015; Bacigalupa et al. 2018; Pirillo et al. 2021). Similarly, acetyl-CoA serves as a source for acetylation of various proteins that can critically control mitochondrial function and beta-oxidation. Acetylation is mediated by acetyltransferases attaching acetyl groups to lysine residues or mitochondrial proteins (Xiong and Guan 2012). This underlines that not only the flux through the respective metabolic pathways but also the accumulation of intermediary metabolites have significant impact on cardiac substrate use and ATP production (Karamanlidis et al. 2013; Zuurbier et al. 2020). Substantial alteration of the described physiological cardiac metabolic mechanism is termed metabolic remodeling and can be an important driver of cardiac dysfunction, different forms of cardiomyopathy and heart failure (Doenst et al. 2013; Bertero and Maack 2018; Tran and Wang 2019).

1.2 Carnitine shuttle

L-carnitine (β -hydroxy- γ -trimethylammonium butyrate) is a naturally occurring hydrophilic amine with an essential role in human metabolism and fatty acid beta-oxidation. Under physiological conditions carnitine consists of a carboxyl-, a trimethylamine- and a hydroxyl-group, which allows the formation of ester bonds with acidic molecules. Therefore, carnitine is mainly present as the esterified form (acylcarnitine) or as free carnitine.

Approximately 25% of the human required carnitine amount derives from *de novo* synthesis from the amino acids lysine and methionine with an approximate turnover of 1-2 $\mu\text{mol}/\text{kg}$ body weight/day (Vaz and Wanders 2002; Rebouche 2004; Stanley 2004). This biosynthesis requires several converting enzymes that are distributed across different tissues. For instance, γ -butyrobetaine hydroxylase (BBOX1), the final and rate-limiting enzyme of carnitine biosynthesis, is exclusively expressed in kidney, liver and to a lower amount in the brain (Rebouche and Engel 1980). Hence, the skeletal and the heart muscle are not able to synthesize carnitine. For non-vegetarian individuals consuming a normal mixed diet, the residual 75% of carnitine is obtained from predominantly dairy products, red meat and fish. Consequently, diet supplies approximately 2-10 μmol carnitine/kg body weight/day (Stanley 2004).

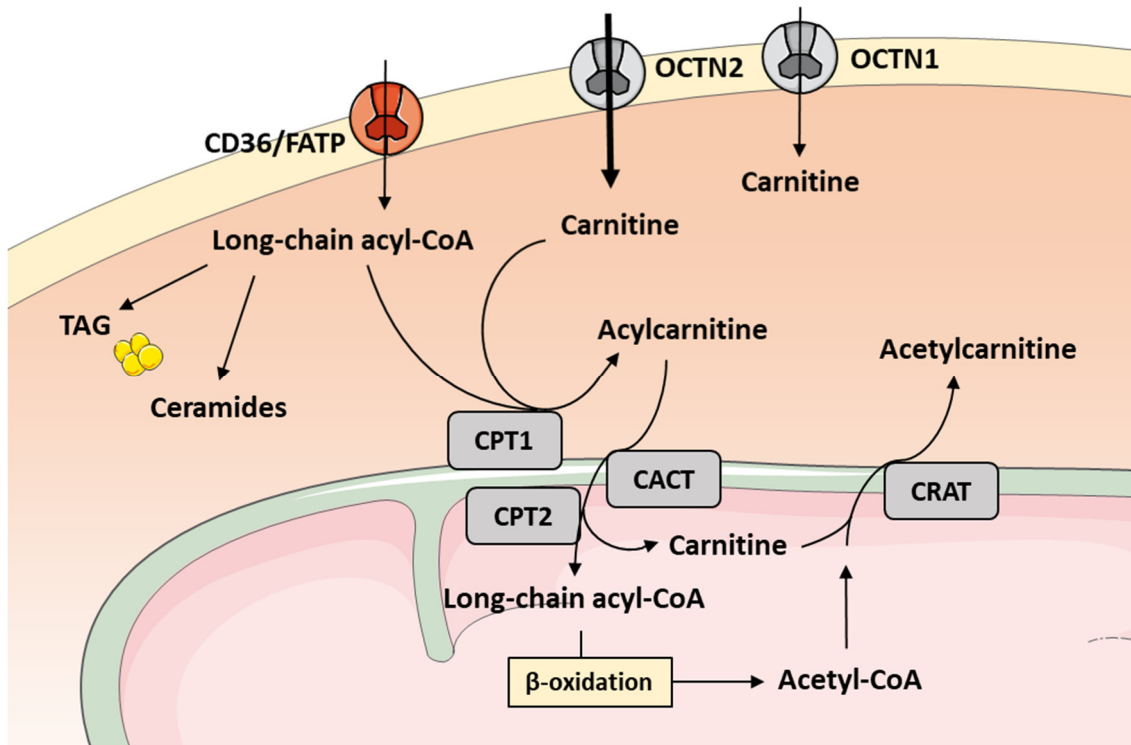


Figure 2: Schematic representation of the carnitine shuttle system. Long-chain fatty acids enter the cell from the circulation via fatty acid transporter and are directly activated by thioesterification to form long-chain acyl-CoA. CPT1 conjugates acyl residues with carnitine allowing their entry into the mitochondria where CPT2 reconverts acylcarnitine to acyl-CoA. Subsequent beta-oxidation of acyl-CoA produces acetyl-CoA that is used to form acetylcarnitine which is shuttled back into the cytosol via CRAT. Carnitine is actively transported into the cytosol via the high-affinity transporter OCTN2 but can also be transported by the low-affinity transporter OCTN1. Acylcarnitine formation prevents acyl-CoA accumulation which results in ceramide and TAG formation. CD36: Cluster of differentiation 36; FATP: Fatty acid transport protein; OCTN: Organic cation transporter; CPT: Carnitine palmitoyltransferase; TCA: tricarboxylic acid cycle; TAG: triglycerides; CRAT: Carnitine acetyltransferase; CACT: Carnitine-acylcarnitine translocase.

Due to its water solubility, carnitine and ester-derivatives are excreted by glomerular filtration in the kidney (Rebouche 2004). However, 95% of excreted carnitine is reabsorbed in the proximal tube under physiological carnitine plasma concentrations (25-50 $\mu\text{mol/l}$). When carnitine plasma concentrations exceed approximately 50 $\mu\text{mol/l}$, a high percentage is not reabsorbed and excreted via the urine. Therefore, carnitine homeostasis in mammals reflects the balance between endogenous *de novo* synthesis, exogenous supply, and excretion by the kidney. Of note, *de novo* synthesis and efficient carnitine conservation by renal tubular reabsorption also ensure physiological carnitine levels observed in strict vegetarians (Rebouche 2004).

Plasma carnitine represents less than 1% of the entire carnitine pool in the human body. The vast majority of carnitine is accumulated in the skeletal and heart muscle (>98%), the liver (1%) and the kidney (0.2%, Evans and Fornasini 2003). The hydrophilic property of carnitine requires an active transport against a concentration gradient to cross the cellular plasma membrane. This transport is primarily catalyzed by the family of organic cation transporters (OCTN). Among these transporters, OCTN2, encoded by the *SLC22A5* gene, has the highest affinity for carnitine ($K_m = 3\text{--}5\ \mu\text{M}$) and is strongly expressed in the myocardium, skeletal muscle, fibroblasts, renal tubules, placental tissue and intestine (Wagner et al. 2000). OCTN2 operates in a sodium-dependent manner and maintains intracellular carnitine concentrations 20–50-fold higher than the extracellular space (Tamai et al. 1998; Wu et al. 1998). Furthermore, the amino acid transporter OCTN1 (*SLC22A4*) and $\text{ATB}^{0,+}$ (*SLC6A14*) are able to transport carnitine. These systems have a lower affinity ($K_m = 800\ \mu\text{M}$) but a higher concentrative capacity for carnitine (Wagner et al. 2000; Nakanishi et al. 2001; Lamhonwah and Tein 2006; Rotoli et al. 2020).

LCFAs cannot pass the mitochondrial membrane for beta-oxidation without prior cytoplasmic carnitine modification (Longo et al. 2006, 2016). This process is sustained by a group of four mitochondrial membrane-bound catalytic enzymes (CPT1, CPT2, CACT, CRAT) that represent the carnitine shuttle system (Figure 2). Directly after the entry into the cytosol, a group of acyl-CoA synthetases (ACSL) activates fatty acids to fatty acyl-CoA via thioesterification using Coenzyme A (CoA). This process takes place at the outer mitochondrial membrane and is ATP-dependent (Watkins et al. 2007). However, the mitochondrial inner membrane is not permeable for acyl-CoAs. Consequently, a following step is the generation of a high-energy ester bond between carnitine and the LCFA to form acylcarnitine, catalyzed by carnitine palmitoyltransferase 1 (CPT1). CPT1 is located at the outer mitochondrial membrane and is the rate-limiting enzyme of the carnitine shuttle. Therefore, CPT1 activity controls the rate of LCFA oxidation (Longo et al. 2006). Carnitine-acylcarnitine translocase (CACT) transports acylcarnitine across the mitochondrial membrane into the mitochondria, where carnitine palmitoyltransferase 2 (CPT2) reconverts acylcarnitine to acyl-CoA that subsequently enters the beta-oxidation. Importantly, carnitine is transported back into the cytosol via the conversion of acetylcarnitine by carnitine acetyltransferase (CRAT), where it can be reused for entry into the carnitine shuttle. CPT1 and CPT2 mainly use long-chain acyl-CoA, for instance linoleoyl-CoA, palmitoyl-CoA and oleoyl-CoA as substrates for the formation of ester bonds with carnitine. In contrast, the transport of short-chain (C4–C6) and mid-chain (C6–C12) fatty acids is primarily carnitine independent, as they can pass the mitochondrial inner membrane in a non-esterified form (Schönfeld and Wojtczak 2016). Apart from mitochondrial fatty acid transfer, carnitine conjugation has a crucial role to reduce the number of coenzyme A (CoA) molecules attached to acyl residues. Excessive accumulation of

cytoplasmic acyl-CoA results in the formation of ceramides, TAG and cholesteryl-ester that were reported to induce inflammation and apoptosis in different organs (Cooper et al. 2015).

1.3 Primary carnitine deficiency

Primary carnitine deficiency (PCD) is an autosomal recessive disorder of the carnitine cycle resulting in insufficient cellular uptake and low intracellular carnitine content (Longo et al. 2016). PCD is caused by pathogenic variants in the *SLC22A5* gene, resulting in dysfunction of the encoded transporter OCTN2. Despite inhibited cellular uptake, PCD patients have low plasma carnitine concentrations (0-5 $\mu\text{mol/l}$, physiological: 25-50 $\mu\text{mol/l}$). This is related to impaired carnitine reabsorption in the proximal tubules system of the kidney via OCTN2. In consequence, a low carnitine plasma concentration is coupled with high urinary loss of carnitine. Low cytoplasmic carnitine concentrations result in impaired fatty acid beta-oxidation, insufficient ATP generation under high workload conditions and cytosolic lipid accumulation. This leads to increased reliance on glucose as an energy substrate, inhibited gluconeogenesis (due to inhibition of pyruvate carboxylase) and diminished ketogenesis (due to a lack of acetyl-CoA derived from beta-oxidation).

Organs for which this metabolic permutation is particularly relevant and therefore susceptible for PCD, are the liver, the skeletal muscle and the heart. Typical clinical symptoms are hypoglycemia and hypoketonemia under fasting conditions, liver dysfunction, muscular weakness and dilated cardiomyopathy (Magoulas and El-Hattab 2012; Wang et al. 2014b). Furthermore, the hepatic lack of ketone production has been reported to cause impaired brain function with loss of consciousness in PCD patients (Longo et al. 2006). Symptomatic patients are usually diagnosed in the first four to five years of their childhood and receive a lifetime treatment with high dose carnitine (100–200 mg/kg/day, Wang et al. 2014b). Several cases have been reported where a withdrawal of the carnitine treatment against medical advice led to sudden cardiac death (Longo et al. 2006). Moreover, numerous untreated PCD patients reach adulthood and remain asymptomatic but still have an increased risk for sudden cardiac death (Spiekerkoetter et al. 2003; Rasmussen et al. 2020). This raised the question about the relevance of including PCD in expanded newborn screening, which consists of a primary screen for low carnitine serum concentrations and subsequent confirmation by genetic testing (Magoulas and El-Hattab 2012). Currently, newborn screening for PCD is routinely performed in the US (Therrell et al. 2014) and in 8 European countries (Loeber et al. 2021).

Numerous homozygous or compound heterozygous mutations in the *SLC22A5* gene have been identified to cause PCD but no specific genotype-phenotype correlation could be observed (Lamhonwah et al. 2002). Even siblings with the same variant show a difference in age of onset and disease progression, suggesting that environmental conditions modulate the

clinical manifestations of carnitine deficiency (Kilic et al. 2011). Still, non-sense and frameshift mutations are generally associated with symptomatic carriers, while missense mutations seem to be more often associated with asymptomatic individuals (Rose et al. 2012). Pathogenic variants were found in all *SCL22A5* exonic coding regions. However, described mutations are often located in the first exon of the *SLC22A5* gene, as reported in a study systemically investigating frequencies of PCD mutations in 143 subjects. In particular, the mutations c.136C>T (p.P46S) and c.424G>T (p.A142S) showed a high prevalence in this study (Li et al. 2010a). OCTN2 is composed of 557 amino acids and consists of 12 predicted transmembrane spanning domains. Exon 1 includes the first transmembrane domain, the N-terminus, and the main part of the first extracellular loop of the transporter. *In vitro* subcellular localization analysis of OCTN2 mutants revealed that this region is indispensable for transporter- trafficking from the endoplasmic reticulum (ER) to the cell membrane (Urban et al. 2006; Maekawa et al. 2007). Therefore, mutations in this region may cause protein structural changes affecting the maturation of OCTN2 to the plasma membrane. In contrast, other mutants such as c.95A>G (p.N32S) localize normally to the plasma membrane but only retain 1-5% of normal transport activity (Steuerwald et al. 2017). This suggests that this mutation disturbs the protein's function most likely via impairment of substrate recognition.

PCD is a rare disease. The reported prevalence ranges from 1:20,000 – 1:70,000 in the United States (Magoulas and El-Hattab 2012) to 1:120,000 in Australia (Wilcken et al. 2003). Recent Chinese studies examined the prevalence of PCD by systemically using tandem mass spectrometry followed by genetic testing in expanded newborn screenings and revealed prevalences of 1:8000 - 1:17,000 (Lin et al. 2021; Yang et al. 2021). The Faroe Island, an isolated archipelago in the North Atlantic, is reported to have by far the highest prevalence of PCD patients worldwide (Rasmussen et al. 2014b) with 1:300 cases. The overall approximate allelic frequency of *SLC22A5* pathogenic variants in the population is 0.5-1%. Moreover, *SLC22A5* was recently reported as the most frequent gene associated with autosomal recessive mitochondrial disorders in a large worldwide genome (gnomAD) dataset (Tan et al. 2020). Although a PCD disease phenotype is typically associated with homozygous mutations, heterozygous carriers have been reported to show 2-3-fold lower plasma carnitine concentrations than controls (Scaglia et al. 1998). However, it is controversial if OCTN2 heterozygosity has pathological relevance or aggravates the impact of more common causes for heart failure, such as hypertension or atherosclerosis (Tang et al. 1999; Takahashi et al. 2007b; Wang et al. 2014b).

1.3.1 Animal models of primary and secondary carnitine deficiency

Juvenile visceral steatosis (JVS) mice have a functional defect in the *SLC22A5* gene and are an animal model of carnitine deficiency (Tomomura et al. 1992). These mutants originate from a C3H-H-2 strain and were unintentionally discovered in 1985 at Kanazawa University, Japan (Koizumi et al. 1988). Subsequent DNA sequencing analysis revealed a missense mutation at codon 352 (p.L352R) located within a transmembrane domain of the OCTN2 transporter. JVS mice demonstrate a high rate of carnitine excretion and tissue lipid accumulation already within the first week and appearance of hyperammonaemia, hypoglycemia, and growth retardation three weeks after birth. Moreover, these mice show hepatic microvesicular steatosis and changes in the mRNA expression of urea cycle enzymes (Horiuchi et al. 1993).

Without any treatment, homozygous mutants die within the first 3-4 months of age. JVS mice develop cardiac hypertrophy 10 days after birth, demonstrated by a higher ventricular weight-to-body weight ratio and cardiac cell volume (Horiuchi et al. 1993; Asai et al. 2006). Echocardiography revealed lower left ventricular fractional shortening and lower systolic blood pressure without changes in heart rate in JVS mice (Asai et al. 2006). Furthermore, JVS mice exhibit an increase in the hypertrophy marker atrial natriuretic peptide (*ANP*) and a high expression of the PDH inhibitor pyruvate dehydrogenase kinase 4 (*PDK4*) in the hypertrophic ventricle (Yoshimine et al. 1997; Horiuchi et al. 1999). The hypertrophic phenotype is accompanied by cardiac steatosis associated with myocardial accumulation of diacylglycerols (DAG) and TAG but no differences in tissue ceramide content (Saburi et al. 2003). Moreover, Asai and colleagues reported a lower myocardial ATP content in JVS mice (Asai et al. 2006). Of note, Masson's trichrome staining revealed no differences in fibrosis in the cardiac ventricles of these mice. Another study reported that different diets could modulate the hypertrophic phenotype of JVS mice. Jalil et al. could show that lowering the dietary lipid supply attenuated the expression of the cardiac hypertrophy marker *ANP* and smooth muscle α -actin (*ACTA2*) in the ventricle of JVS mice (Jalil et al. 2006). This example indicates that nutrient availability may be critical in mediating the onset and the progression of PCD.

Further carnitine deficient animal models were established by administering the carnitine analog *N*-trimethyl-hydrazine-3-propionate (THP), a competitive OCTN2 and BBOX1 inhibitor. Rats that were treated with this inhibitor for three weeks revealed increased renal carnitine excretion and hepatic steatosis. In contrast to the liver phenotype, heart and skeletal muscle showed no severe alteration in this pharmacologically induced carnitine deficiency model (Spaniol et al. 2001). However, these PCD models reveal a compensatory upregulation of proteins involved in the carnitine shuttle system, such as CPT1 (Degrace et al. 2004; Liepinsh et al. 2009; Li et al. 2017).

1.4 Dilated cardiomyopathy

Dilated cardiomyopathy (DCM) is a frequent type of cardiomyopathy with an estimated prevalence of 1:200 and a mortality of 1:17,000 in the global population (Schultheiss et al. 2019; Mazzarotto et al. 2020). It is characterized by left- or biventricular dilation, contractile dysfunction and arrhythmia in the absence of hypertension or coronary artery disease (Schultheiss et al. 2019). This pathology results in a decrease of stroke volume and progresses to heart failure. Heart failure in turn, is defined as an inability of the heart to supply oxygenated blood to peripheral organs and is the most prevalent cardiovascular hospitalization cause for individuals over 60 years of age (Braunwald 2013). Moreover, DCM is the most common indication for heart transplantation (Maron et al. 2006). DCM develops during any age and gender. However, the incidence of idiopathic cardiomyopathy is approximately 3-fold higher in adult men than in women (Fairweather et al. 2013) and is the highest in children younger than 12 months (Towbin et al. 2006).

A number of different causes for DCM have been identified. Although no comprehensive clinical study has systematically investigated genomic backgrounds of DCM patients, DCM is often associated with an inherited basis and a comprehensive genetic heterogeneity. These inherited cardiomyopathies represent 40% of all cardiomyopathies and over 100 genes have been discovered over the last decades and are the basis for genetic testing in DCM (Mazzarotto et al. 2020). The discovery of these genes is mainly related to emerging advances in genetic high throughput sequencing of patient cohorts. The most prevalent genes described are associated with cytoskeletal, sarcomere and nuclear envelope proteins such as *TTN*, *LMNA*, *MYH7*, *BAG3* and *TNNT2* (Schultheiss et al. 2019). Moreover, 5% of all cardiomyopathies are caused by autosomal inborn errors of metabolic-associated genes resulting in a deficiency of the respective enzymes and accumulation of toxic metabolites (Lloyd et al. 2017). Among these, a majority represents glycogen storage disorder caused by mutations in the *GAA* gene (Pompe disease) or the *PRKAG2* gene (Lloyd et al. 2017). Furthermore, mutations in mitochondrially encoded genes can cause mitochondrial dysfunction and DCM (Arbustini et al. 1998).

In addition to genetic causes, cardiomyopathy can also develop due to acquired conditions such as myocarditis, chemotherapy, pathogen infection, toxin exposure, alcohol abuse, and endocrine disturbance (Weintraub et al. 2017). Of note, inherited cardiomyopathies often exhibit incomplete penetrance and inconsistent expressivity even within patients carrying the same pathogenic variant (Hershberger 2010). This demonstrates that the interplay between genetic, acquired, and environmental causes may critically impact DCM progression and the occurrence of sporadic DCM. However, the relationship between environmental factors and pathogenic variants remains to be elucidated in a large multicentre study.

1.5 Cardiac differentiation and metabolic maturation

In 2006 Shinya Yamanaka and colleagues developed a method to reprogram embryonic and adult mouse fibroblasts into induced pluripotent stem cells (iPSC) by inducing the expression of four transcription factors (SOX2, c-MYC, OCT4 and KLF4) via retrovirus transduction (Takahashi and Yamanaka 2006). One year later the authors applied this protocol to human skin fibroblasts to generate human iPSC (hiPSC). Substantial advantages of hiPSCs are the ability to generate these cells from any healthy volunteer or patient, the unlimited expansion capacity and the potential to differentiate these cells into cell types of all three germ layers (Takahashi et al. 2007a).

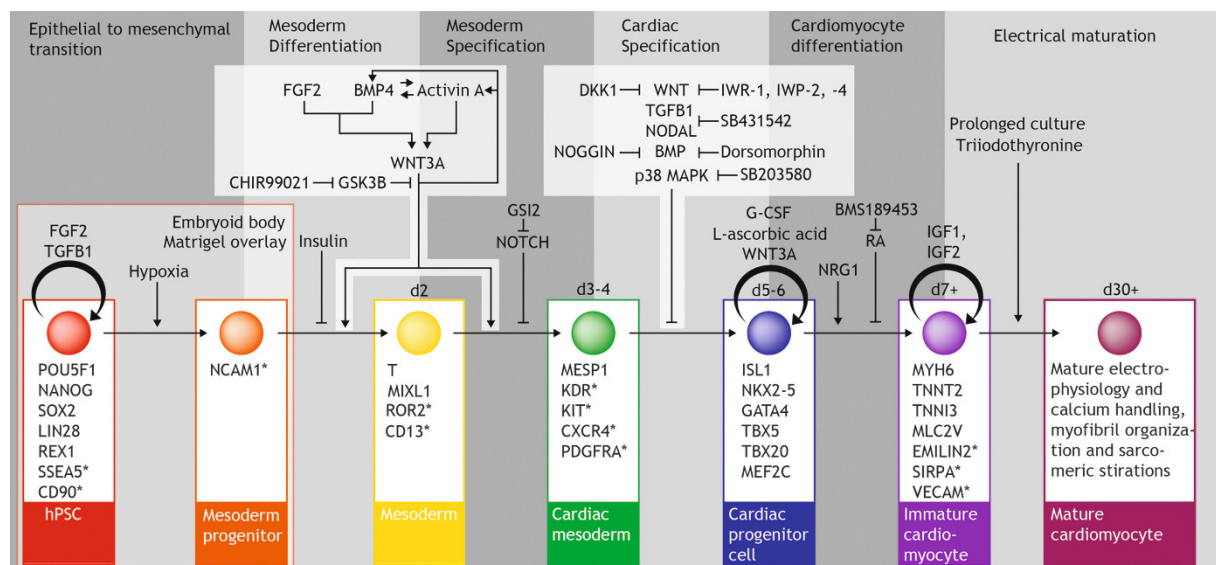


Figure 3: Signaling pathways activated during different stages of hiPSC-CM differentiation. HiPSC-CM differentiation is based on the induction of mesodermal differentiation and specification by Wnt/TGFβ signaling activation. Subsequent cardiomyocyte differentiation is mediated by Wnt inhibition (Burrige et al. 2012).

During the last decade various protocols have been established to differentiate cardiomyocytes from hiPSC. These protocols are designed to replicate critical steps of embryonic cardiomyogenesis via modulation of relevant signaling pathways under chemically defined conditions. In principle, all protocols are based on the induction of mesodermal progenitors by activation of Wnt/TGFβ signaling and subsequent cardiac specification by Wnt signaling inhibition in the second phase (Figure 3). While first efforts were limited by a low differentiation efficiency and insufficient cardiomyocyte purity, continuous improvement over several years provided more reproducible and cost-effective procedures (Mummery et al. 2002; Burrige et al. 2007; Zhang et al. 2012). Cardiomyocyte differentiation protocols can be divided into monolayer- and aggregation-based protocols. Monolayer-based protocols initiate the differentiation of hiPSC which are seeded on a culture substrate (Lian et al. 2013; Burrige et

al. 2014). In contrast, aggregation-based protocols take advantage of the self-assembling properties of hiPSC cultured in suspension and induce the formation of three-dimensional cell aggregates named embryoid bodies (EBs) (Burridge et al. 2007; Breckwoldt et al. 2017). This culture system allows for more scalable hiPSC differentiation (Lecina et al. 2010).

Despite stringent efforts in optimizing differentiation protocols, several drawbacks with hiPSC-cardiomyocyte (hiPSC-CM) platforms remain to be addressed. For instance, prolonged periods of culture time can provoke the accumulation of karyotypic aberrations and copy number variants. Moreover, somatic mutations can arise during the reprogramming process, why hiPSC need to be carefully screened for genetic alteration prior to cardiomyocyte differentiation (Lund et al. 2012). In addition, the hiPSC differentiation efficiency has been demonstrated to be inconsistent across different cell lines (Burridge et al. 2007; Laco et al. 2018). Especially disease-specific cell lines are often not suitable for standard protocols and might require a laborious adaption of the differentiation protocol.

Another critical aspect is the considerable heterogeneity in subpopulations of hiPSC-CMs as differentiated cardiomyocytes often comprise not only ventricular but also atrial and nodal cardiomyocytes (Moretti et al. 2010; Churko et al. 2018). Furthermore, single-nuclear sequencing technologies revealed several subpopulations among the chamber-specific cardiomyocytes in the human adult heart, and it is unclear to what extent this is replicated in hiPSC-CM populations (Litviňuková et al. 2020). Moreover, cardiac differentiation protocols also produce additional mesodermal cell types as by-products, such as fibroblasts, endothelial cells and smooth muscle cells (Ye et al. 2013; Churko et al. 2018).

In addition, hiPSC-CM are immature and represent a fetal/neonatal state of development (Figure 4). Accordingly, they show differences to human adult cardiomyocytes regarding morphology and physiological and pharmacological response. Specifically, hiPSC-CM display smaller and unorganized sarcomeres, a lower contractile force, a higher abundance of the adult myosin heavy chain isoform 7 (MYH7) and different ion channel expression (Yang et al. 2014). Morphological hiPSC-CM immaturity is characterized by a lower cell size, reduced membrane capacitance as well as a smaller length-to-width ratio (anisotropy). Adult cardiomyocytes present an improved calcium handling which is facilitated by the increased volume and calcium storage of the sarcoplasmic reticulum (Satin et al. 2008; Hwang et al. 2015). In addition, more mature cardiomyocytes develop t-tubules and show a decreased ability to proliferate.

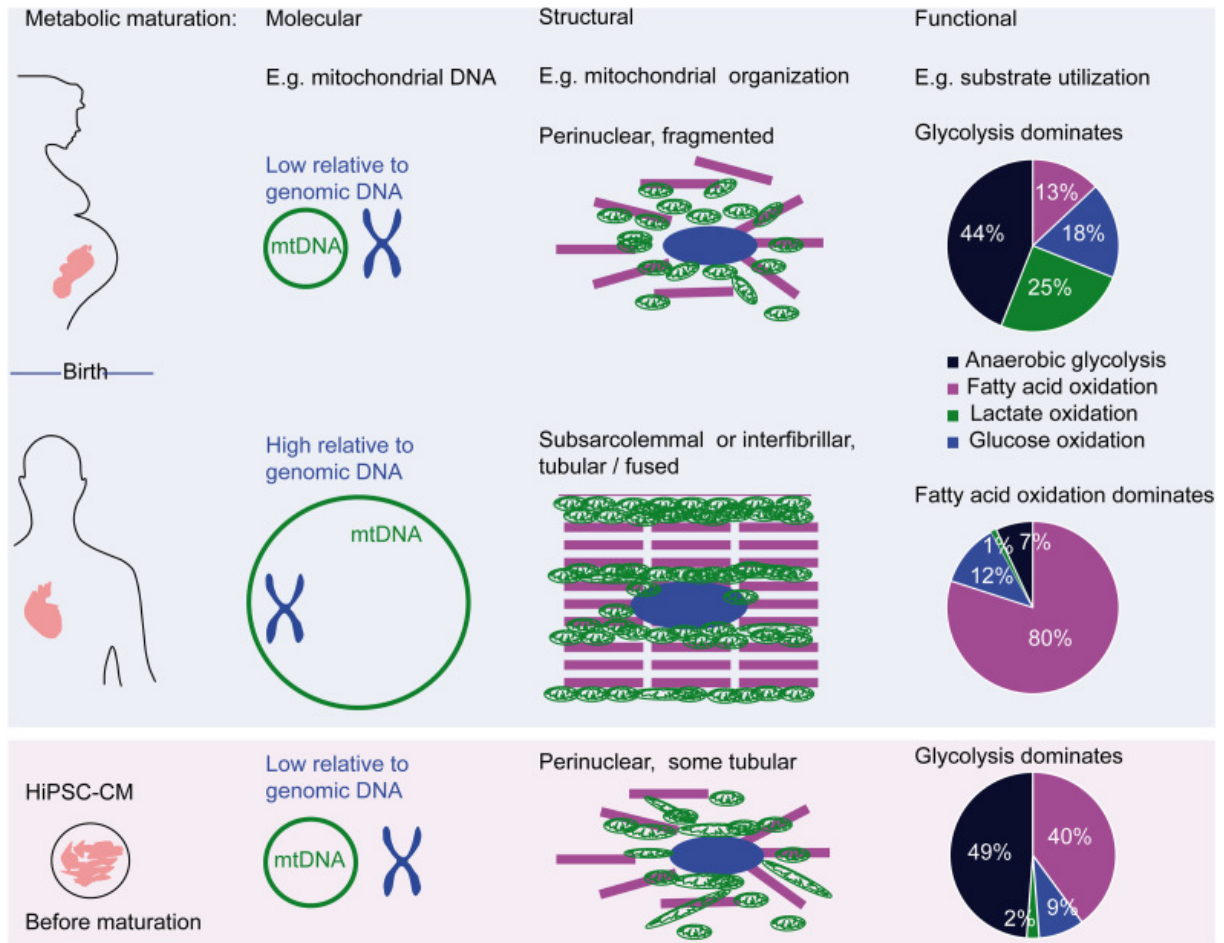


Figure 4: Schematic comparison of metabolic hallmarks between fetal cardiomyocytes, adult cardiomyocytes, and hiPSC-CM. Fetal cardiomyocyte metabolism relies on anaerobic glycolysis accompanied by lower mtDNA abundance and perinuclear mitochondrial organization. MtDNA content increases during metabolic maturation and adult cardiomyocytes exhibit an interfibrillar mitochondrial organization with reliance on fatty acids as a major substrate for ATP production. HiPSC-CM represent an intermediate state between fetal and adult cardiomyocytes and can faithfully recapitulate basic metabolic disease mechanisms (Ulmer and Eschenhagen 2020).

Differences between fetal-like and adult cardiomyocytes also appear on a metabolic level. Immature cardiomyocytes rely on glycolysis as an energy substrate and have small mitochondria located in the perinuclear region. In contrast, ATP production of adult cardiomyocytes primarily relies on oxidative phosphorylation in large intermyofibrillar mitochondria (Garbern and Lee 2021). The metabolic maturation of adult cardiomyocytes is accompanied by a higher oxygen demand, increased fatty acid utilization and a higher expression of CPT1b, the cardiac isoform of the rate-limiting enzyme of the carnitine shuttle system (Longo et al. 2016; Funakoshi et al. 2021). Another reliable marker for mitochondrial maturation is the ratio of mitochondrial DNA (mtDNA) normalized to genomic DNA (gDNA). This ratio is a surrogate for mitochondrial frequency, and it is higher in adult cardiomyocytes

than in fetal and hiPSC cardiomyocytes (Pohjoismäki et al. 2010; Ulmer et al. 2018). Furthermore, a lower mtDNA copy number in the adult myocardium is associated with a higher risk for sudden cardiac death (Zhang et al. 2017).

Different conditions have promoted structural and metabolic maturation of hiPSC-CM. For instance, long-term culture was used as an initial approach to mature hiPSC-CM. Here cardiomyocytes showed a higher degree of sarcomeric organization and increased cell size and anisotropy after 120 days of culture (Lundy et al. 2013). Moreover, electrical and mechanical stimulation emerged as a robust method to mature neonatal rat and human cardiomyocytes *in vitro*. These efforts comprise "fixed-rate" pacing with stimulation close to physiological frequencies (Godier-Furnémont et al. 2015) but also progressive increase of pacing frequencies over several weeks (Nunes et al. 2013; Zhao et al. 2019). Promotion of more adult-like cardiomyocyte properties could also be achieved by defining new media compositions. Lowering glucose and increasing galactose, lactate, and fatty acid concentrations facilitated metabolic and functional maturation of cardiomyocytes (Correia et al. 2017; Horikoshi et al. 2019; Feyen et al. 2020).

Overall, while several procedures have demonstrated some degree of hiPSC-CM maturation, no specific cardiac differentiation and maturation protocol has achieved the generation of subtype-specific cardiomyocytes with adult phenotype until today.

1.6 Genome editing by CRISPR/Cas9

Genome editing describes the targeted manipulation of genomic DNA. During the last decade the field of biology made enormous progress in the genome editing of human cells. Initial approaches that attempted to modify nucleic acids based on the introduction of a double-strand break were zinc finger nucleases (ZNFs) and transcription activator–like effector nucleases (TALEN) (Kim et al. 1996; Boch et al. 2009). Although extensively explored, these systems exhibited insufficient targeting efficiency and required laborious cloning procedures to tether modular DNA-binding proteins with a catalytic endonuclease.

The discovery of a clustered regularly interspaced short palindromic repeats (CRISPR) - associated (CAS) nuclease family in various bacterial strains served as a breakthrough for precise gene editing in biomedical research (Haurwitz et al. 2010; Deltcheva et al. 2011). These nucleases are divided into two subclasses and facilitate an adaptive immune response in prokaryotic organisms. After infection with a virus or a bacteriophage, the bacterial system incorporates fragments of the foreign DNA into the endogenous genome, defined as non-repetitive spacer regions. These regions are flanked by repetitive arrays simultaneously forming the CRISPR region. Spacer-RNA-sequences transcribed from this region are further processed to CRISPR-RNA (crRNA) and build a duplex with the independently expressed

trans-activating crRNA (tracrRNA). The subsequent binding of this duplex to the Cas9-endonuclease results in the formation of a ribonucleoprotein (RNP) complex which is guided towards the foreign loci to cleave pathogenic DNA elements (Jinek et al. 2012).

Adapting this principle allowed genome editing in eukaryotic cells by delivering synthetic CRISPR components into the cell. One important advance constitutes the development of a programmable chimeric single guide RNA (gRNA), suitable for *in vitro* application (Jinek et al. 2012; Cho et al. 2013). This stabilized crRNA-tracrRNA duplex guides Cas9 to a 20 base pair long specific target site which is complementary to the crRNA sequence. The subsequent Cas9 DNA-cleavage requires the presence of a protospacer adjacent motif (PAM) sequence located downstream of the target sequence. The commonly used SpCas9 variant, derived from *streptococcus pyogenes*, recognizes the PAM nucleotide sequence 5'-NGG and induces a DNA double-strand break 3 base pairs upstream of this region (Garneau et al. 2010).

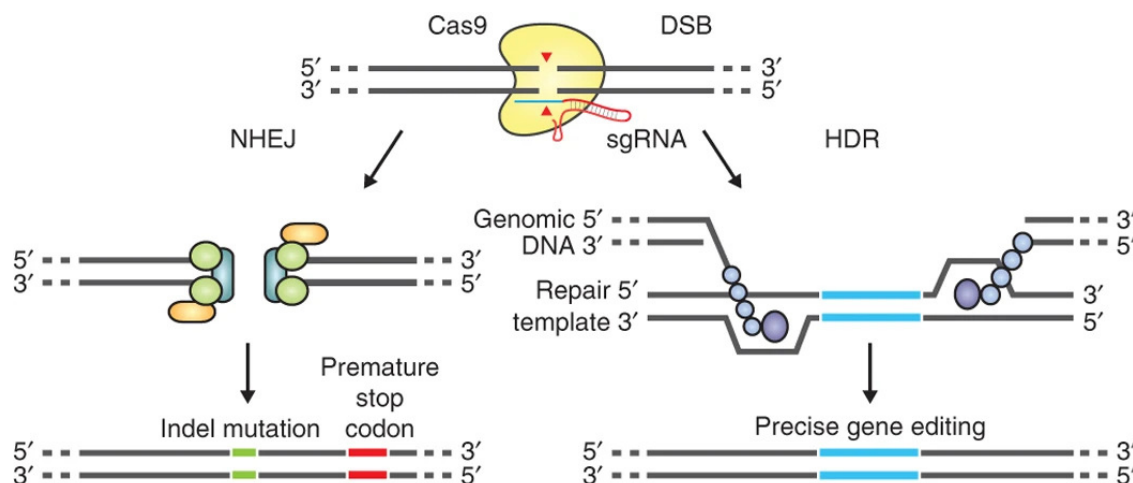


Figure 5: DNA repair pathways after CRISPR-induced DSBs. Cas9-induced DSBs primarily activate one of two DNA repair mechanisms. The more frequent NHEJ pathway re-ligates the two DNA strands resulting in indel mutations and frameshifts. HDR requires a DNA template for homologous recombination and is commonly used for precise introduction of customized DNA fragments (Ran et al. 2013).

CRISPR-based genome editing makes use of the different repair pathways initiated after a DNA break in the eukaryotic genome (Figure 5). The most frequent DNA repair mechanism in eukaryotes is the error-prone non-homologous end-joining (NHEJ) pathway. This mechanism facilitates direct re-ligation of the damaged DNA molecules and results in the introduction of small base pair insertions or deletions (indel) at the DNA target site (Weterings and Chen 2008). The NHEJ repair mechanism is autonomous from a DNA template usage and is therefore independent of cell- cycle and replication (Mao et al. 2008). In contrast, the

homology-directed repair (HDR) pathway uses template DNA for homologous recombination during the S and G2 phases of the cell cycle (Lin et al. 2014). NHEJ is commonly used to induce protein knockouts by introducing mutations that result in frameshifts and premature stop codons. In contrast, the HDR pathway enables the site-specific introductions of point mutations by the co-delivery of CRISPR components with a customized DNA repair template homologous to the target site (Ran et al. 2013; Lin et al. 2014).

The CRISPR/Cas9 technology has been established as an indispensable and accessible gene editing tool for daily laboratory usage and provided the basis for various translational applications. For instance, CRISPR/Cas9 targeting approaches could successfully prevent dystrophin protein degradation by exon skipping and restore cardiac function in animal and hiPSC-models of the severe degenerative disease Duchenne muscular dystrophy (Li et al. 2015; Amoasii et al. 2018). Thus, considering the spectrum of applications, CRISPR/Cas9 is a promising technique for improving biomedical research and revolutionizing treatment strategies for hereditary diseases.

Despite its promises as a gene editing tool, the CRISPR/Cas9 technology faces some considerable drawbacks. For instance, nonspecific Cas9 guidance may also introduce changes at predicted or even unpredictable off-target regions due to a high degree of homology to the target site. Even more concerning is that repair of CRISPR-induced double-strand breaks may lead to complex rearrangement events, large deletions or insertions at the target region (Kosicki et al. 2018). These unintended changes have been consistently identified (Parikh et al. 2015; Shin et al. 2017; Adikusuma et al. 2018) and underline the necessity of accurate genotype characterization, as these lesions can have unpredictable outcomes on gene and protein function.

1.7 Modeling disease with human induced pluripotent stem cells

Despite improvements in therapy, the clinical management for most DCMs is not successful in preventing the progression to heart failure. Consequently, DCMs have a poor prognosis and remain an important cause for heart failure besides hypertension and coronary artery diseases (Weintraub et al. 2017; McNally and Mestroni 2017; Schultheiss et al. 2019). Animal models are relevant to study the pathophysiological mechanism of cardiomyopathies and the development of novel therapies (Houser et al. 2012). However, these approaches remain limited due to the restricted comparability of animal and human cardiac physiology, aggravated by substantial differences in cardiac ventricular contractile and relaxation kinetics.

In comparison to humans, rodent hearts have very high heart rates, which is related to an adaptation of the cardiac function to the smaller body weight (Milani-Nejad and Janssen 2014). The cardiac mouse action potential exhibits a shorter action potential duration (APD) with a

rapid repolarisation phase accompanied by essential differences in ion channel expression (Bruyneel et al. 2018). Furthermore, there are considerable differences in the myofilament protein composition demonstrated by higher myosin heavy chain 6 (MYH6) levels in the mouse ventricle compared to the human ventricle (Alpert et al. 2002; Krenz et al. 2003). Moreover, the mouse heart has a high basal rate of glycolytic ATP production (Belke et al. 1999). Given the high reliance on lipid metabolism of the human adult heart, animal models might therefore especially fail to entirely recapitulate metabolic perturbations and increased glycolysis of human cardiac pathologies. Differences between animals and humans can be even more obvious under pathological conditions and several cardiomyopathy animal models failed to reproduce the human phenotype of certain cardiomyopathy mutations (Lund et al. 2012; Eschenhagen and Carrier 2019). This implies the critical need to develop novel predictive *in vitro* cardiomyopathy models.

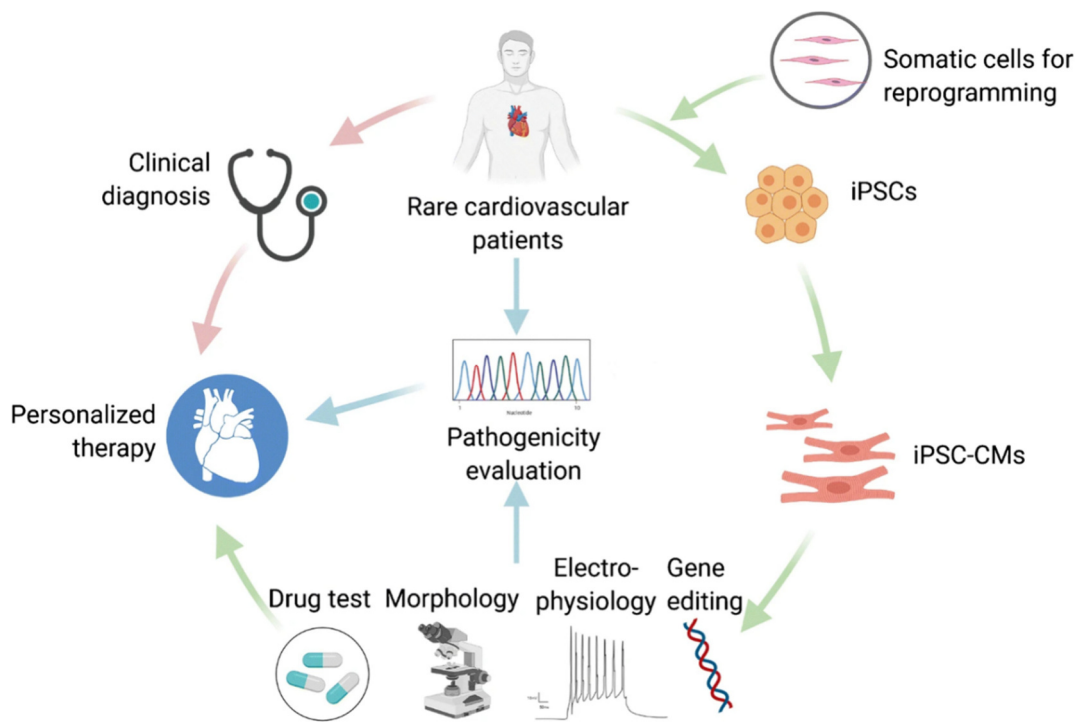


Figure 6: Schematic representation of human iPSCs as models for studying cardiac inherited diseases. A substantial advantage of the iPSC technique is the ability to evaluate functional and molecular readouts of patient derived cardiomyocyte *in vitro*, to unmask pathogenic mechanism and guide novel personalized therapies (Pan et al. 2021). iPSC: Induced pluripotent stem cell.

The advent of the hiPSC technology, along with developments in CRISPR-based genome editing, offered unique prospects to investigate disease mechanisms of inherited cardiomyopathies with human *in vitro* models. Improvement in differentiation protocols of specific cell types like cardiomyocytes opened the possibility of using hiPSCs for various

applications such as cell therapy, drug discovery, cardiotoxicity screening and disease modeling (De Korte et al. 2020).

In addition, the correction or introduction of mutations by CRISPR/Cas9 allow the direct comparison between a disease-specific cell line carrying a pathogenic mutation and an isogenic control. These approaches therefore have several advantages compared to patient-derived primary cells that lack suitable controls and are limited in their availability, survival during *ex vivo* culture and expansion ability (De Korte et al. 2020). Moreover, biopsies obtained from these patients rather reflect the pathological consequences in the disease end-stage while in principle the hiPSC model should demonstrate an early phenotype without many secondary alterations.

While the combination of patient-derived hiPSC models and efficient genomic engineering are strong arguments in favor of the hiPSC disease model, two important drawbacks need to be discussed. HiPSC-based models exhibit not only a line-to-line but also a large batch-to-batch variability implying the need to reproduce functional findings in several differentiation batches (Huo et al. 2017; Kilpinen et al. 2017; Mannhardt et al. 2020).

In addition, existing hiPSC models are able to model disease-relevant perturbations on a cell- and tissue-level, but not on an organ- or organism-level. Still, relevant alterations of cardiovascular pathologies might also be driven by metabolites originating from different organs (e.g. liver or gut) or the impact of the autonomic nervous system. This suggests that current systems are unable to model organ interaction in an organism and might require the addition of non-cardiac cell types to the culture system.

Since the introduction of cardiac differentiation protocols, certain hiPSC-CM models could recapitulate the patient-specific phenotype of monogenic cardiac disease. One example is a model of Barth syndrome, an X-linked disorder that is caused by mutations in the Tafazzin (*TAZ*) gene. The authors reported that the destabilization of cardiolipin results in impaired mitochondrial function, excessive ROS production and cardiac dysfunction. ROS-scavenging could reverse sarcomeric disassembly and improve contractile properties in this model, suggesting this treatment as a potential therapy for Barth syndrome patients (Wang et al. 2014a). Other approaches using hiPSC-CM could improve the mechanistic understanding of cardiomyopathies with ataxia syndrome (DCMA) and Pompe disease, a disorder caused by lysosomal glycogen accumulation (Raval et al. 2015; Sato et al. 2017; Rohani et al. 2020).

Metabolic relevant perturbations like lipid accumulation, mtDNA depletion or mitochondrial fragmentation could also be demonstrated in hiPSC-CM models of Friedreich Ataxia (Hick et al. 2013), arrhythmogenic right ventricular dysplasia (Kim et al. 2013) and Danon's disease (Hashem et al. 2017) respectively. Models of cardiomyopathies related to LCFA disorders exist

but are limited to a small number of studies, additionally underscoring the relevance of novel human models for metabolic cardiomyopathies (Knottnerus et al. 2020; Verkerk et al. 2021)

A systemic review summarising cardiomyopathy models using hiPSC-CM revealed that DCM models in particular reproduce a decline in force development and sarcomeric disassembly as a consistent disease phenotype (Eschenhagen and Carrier 2019). However, the authors also highlighted that only a minority of these studies used isogenic controls. Moreover, the analysis of several functional cardiomyopathy-specific disease parameters such as multinucleation, impaired calcium handling and increased cell size were only consistently reported for *in vitro* models of cardiac hypertrophy but not DCM. The inconsistent characterization of DCM models is related to the limited number of existing DCM *in vitro* models on the one hand but might also be affected by the broad genetic and pathogenic heterogeneity of DCM on the other hand. Moreover, it is important to mention that most of these models are based on 2D monolayer cultivation. However, these systems lack important cardiac physiological properties like a three-dimensional organotypic functionality, cardiomyocyte interaction with extracellular matrix (ECM) and an auxotonic contraction. This is of particular relevance since properties like ECM topography, stiffness, porosity, and proteomic signature contribute to the pathology and the progression of DCM (Kapelko 2001; Louzao-Martinez et al. 2016; Camman et al. 2022). Moreover, a monolayer cannot mimic the impact of cell-to-cell communication as seen in various cardiac disease phenotypes (Tirziu et al. 2010).

Culturing cardiomyocytes in 3D-systems emerged as a successful strategy to overcome these drawbacks. The first successful attempt to develop an engineered heart tissue (EHT) was conducted by embedding chicken cardiomyocytes in a collagen matrix located between two Velcro-coated glass tubes (Eschenhagen et al. 1997). Further improvement of this method included the addition of Matrigel during casting to generate tissue constructs from neonatal rat cardiomyocytes (Zimmermann et al. 2000) and the development of a miniaturized EHT in a 24-well format cultured on a fibrin-based matrix (Hansen et al. 2010). In 2018, Ulmer and colleagues demonstrated that cultivation of hiPSC-CMs in this format substantially contributes to metabolic maturation of hiPSC-CMs in comparison to 2D cultured cardiomyocytes (Ulmer et al. 2018). The authors found a higher mitochondrial protein and DNA abundance accompanied by increased glucose and fatty acid oxidative metabolism. The higher degree of cardiomyocyte maturation in EHT format provides the basis to utilize this system for a more accurate *in vitro* characterization of a pathophysiological mechanism underlying metabolic cardiomyopathies.

2 Aim

Primary carnitine deficiency (PCD) is an autosomal recessive monogenic disorder caused by mutations in the gene encoding for carnitine transporter OCTN2, resulting in dilated cardiomyopathy (DCM). The mechanisms are not fully understood, particularly due to the lack of human *in vitro* models. To unravel novel aspects of PCD DCM disease mechanisms and to establish a platform for the development of new therapies, predictive *in vitro* models are needed. Hence, the aim of this work was the development of a three-dimensional engineered heart tissue (EHT) model for PCD DCM with hiPSC-derived cardiomyocytes and the exploration of disease features/mechanisms.

This work was divided into three main objectives and will be presented in the following chapters:

1. Derivation of two hiPSC lines from an established control hiPSC line (OCTN2 (+/+)), carrying either a full OCTN2-knockout (OCTN2 (-/-)) or a homozygous point mutation (OCTN2 (N32S)) by using the CRISPR/Cas9 technology.
2. Cardiomyocyte differentiation of isogenic control and genetic engineered hiPSC, EHT generation and replication of the PCD disease phenotype in functional (contractility), molecular, morphological, and genome-wide assays.
3. Discovery of potential novel molecular and cellular PCD mechanisms in quantitative proteomic analysis and single-nuclear RNA sequencing assay.

3 Material and methods

A detailed summary of materials, reagents, chemicals and devices used in this work can be found in the supplement (chapter 9.3).

3.1 Cell culture media

The composition of cell culture media is depicted in Table 1.

Table 1: Composition of cell culture media

Medium	Components
Conditioned medium (CDM)	DMEM/F12 without glutamine 1% (v/v) Non-essential amino acids 1% (v/v) L-glutamine 0.5% (v/v) Penicillin/streptomycin 3.5 µL/500 mL 2-Mercaptoethanol 20% (v/v) Knockout serum replacement 10 ng/mL Basic fibroblast growth factor (bFGF) After incubation on mitotically inactivated mouse embryonic fibroblasts (strain CF-1) for 24 hours, CDM medium was collected and sterile filtered (0.1 µm filter). Fresh bFGF (30 ng/mL) was supplemented directly before use.
FTDA	DMEM/F-12 without glutamine 2 mM L-glutamine 0.1% (v/v) Lipid mix 5 mg/L Transferrin 5 µg/L Selenium 0.1% (v/v) Human serum albumin 5 µg/mL Insulin 2.5 ng/mL Activin-A 30 ng/mL bFGF 50 nM Dorsomorphin 0.5 ng/mL TGFβ1
Mesoderm induction medium	RPMI 1640 4 mg/mL Polyvinyl alcohol 10 mM HEPES 0.05% (v/v) Human serum albumin 250 µM Phosphoascorbate 5 mg/l Transferrin 5 µg/l Selenium 0.1% (v/v) Lipid mix 10 µM Y-27632 3 ng/mL Activin-A 10 ng/mL BMP4 5 ng/mL bFGF

EB formation medium	FTDA 4 mg/mL Polyvinyl alcohol 10 μ M Y-27632
Cardiac differentiation medium I	RPMI 1640 10 mM HEPES 0.5% (v/v) Penicillin/streptomycin 0.05% (v/v) Human serum albumin 250 μ M Phosphoascorbate 5 mg/L Transferrin 5 μ g/L Selenium 0.1% (v/v) Lipid mix 1 μ M Y-27632 1 μ M XAV-939
Cardiac differentiation medium II	RPMI 1640 2% (v/v) B27 plus insulin 10 mM HEPES 0.5% (v/v) Penicillin/streptomycin 500 μ M 1-Thioglycerol 1 μ M Y-27632 1 μ M XAV-939
Cardiac differentiation medium III	RPMI 1640, 2% (v/v) B27 plus insulin 10 mM HEPES 0.5% (v/v) Penicillin/streptomycin 500 μ M 1-Thioglycerol 1 μ M Y-27632
EHT casting medium	DMEM 1% (v/v) Penicillin/streptomycin 2 mM L-glutamine 10% (v/v) Horse serum (heat inactivated)
EHT culture medium	DMEM 1% (v/v) Penicillin/streptomycin 10% (v/v) Horse serum 10 μ g/mL Insulin 33 μ g/mL Aprotinin 0.2 mM Transexamic acid
Fatty acid medium	DMEM (without glucose) 1% (v/v) Penicillin/streptomycin 10 μ g/mL Insulin 33 μ g/mL Aprotinin 0.2 mM Transexamic acid 50 ng/mL Hydrocortisone 0.5 ng/mL T ₃ 0.2 mM L-glutamine 50 μ M L-carnitine hydrochloride 1 mg/mL Linoleic acid-oleic acid-albumin

3.2 hiPSC cell culture conditions

An established in-house hiPSC control cell line derived from a healthy individual served as the starting point for the genetic engineering approach and as the isogenic control for the engineered hiPSC lines. This hiPSC line was generated by reprogramming dermal fibroblast from a skin biopsy using the CytoTune (Life Technologies) 2.0 Sendai Reprogramming Kit under feeder-free conditions. The reprogramming procedure was performed by Dr. Aya Domke-Shibamiya and Dr. Sandra Laufer (IEPT, UKE, Hamburg, Germany).

All basic stem cell culture work was performed as recently described (Shibamiya et al. 2020). In brief, hiPSC culture was based on the expansion of a master cell bank (MCB) at passage 25-35 on Geltrex-coated cell culture flasks in FTDA-medium under hypoxic conditions (5% O₂). Standard passaging was performed twice a week (3-4 day passaging interval) with Accutase solution (Sigma-Aldrich). Plating density was 4.5-7×10⁴ hiPSC/cm². Maximal expansion was for 40 passages after thawing. HiPSCs were tested on a regular basis for mycoplasma contamination based on PCR amplification by June Übeler (IEPT, UKE, Hamburg, Germany). Furthermore, the surface marker SSEA3 served as a pluripotency marker and was analyzed by flow cytometry. To this end, hiPSCs were stained with a fluorescent-labeled SSEA3 and isotype control antibody and analyzed by flow cytometry. A representative SSEA3 analysis is depicted in the supplement (Figure S2). HiPSC culture and expansion was kindly supported by Birgit Klampe and Thomas Schulze (IEPT, UKE, Hamburg, Germany).

3.3 CRISPR/Cas9-mediated gene editing

3.3.1 OCTN2 (N32S) missense mutation

The CRISPR/Cas9 technology was used to engineer the *SLC22A5* c.95A>G (N32S) mutation into the genome of the established control hiPSC line. This control hiPSC line served as the isogenic control and is therefore referred to as hiPSC OCTN2 (+/+). To verify the wildtype sequence, the *SLC22A5* gene locus was Sanger sequenced. To engineer the N32S mutation into the *SLC22A5* wildtype locus, the online *in silico* tool IDT Custom Alt-R CRISPR-Cas9 gRNA software and CRISPOR (Concordet and Haeussler 2018) were used to identify potential gRNA binding sites at the gene locus. The N32S mutation was chosen for this approach since it is one of the most prevalent PCD mutations and a well-described founder mutation in the Faroe Islands (Rasmussen et al. 2014b; Steuerwald et al. 2017). The OCTN2 NCBI Reference (NG_008982.2; Gene ID: 6584; Homo sapiens solute carrier family 22 member 5 (*SLC22A5*) RefSeqGene on chromosome 5) was provided as a target sequence. GRNA were chosen based on the lowest cut-to-mutation distance under consideration of a high on-target potential and low off-target risk. A single-stranded oligodeoxynucleotide (ssODN) served as an exogenous donor template, containing the patient-specific mutation c.95A>G, p.N32S.

Additionally, a silent mutation was introduced in the PAM sequence to prevent Cas9 re-cutting after successful genomic integration of the template by HDR. A schematic overview of the HDR strategy is depicted in Figure 7.

Guo et al. (2018) reported a higher chance of HDR genetic engineering efficiency by cultivating the nucleofected hiPSCs at 32 °C for 48-72 hours after nucleofection. Accordingly, for this approach nucleofected hiPSCs were cultivated at both 37 °C and 32 °C for the first 72 hours after nucleofection.

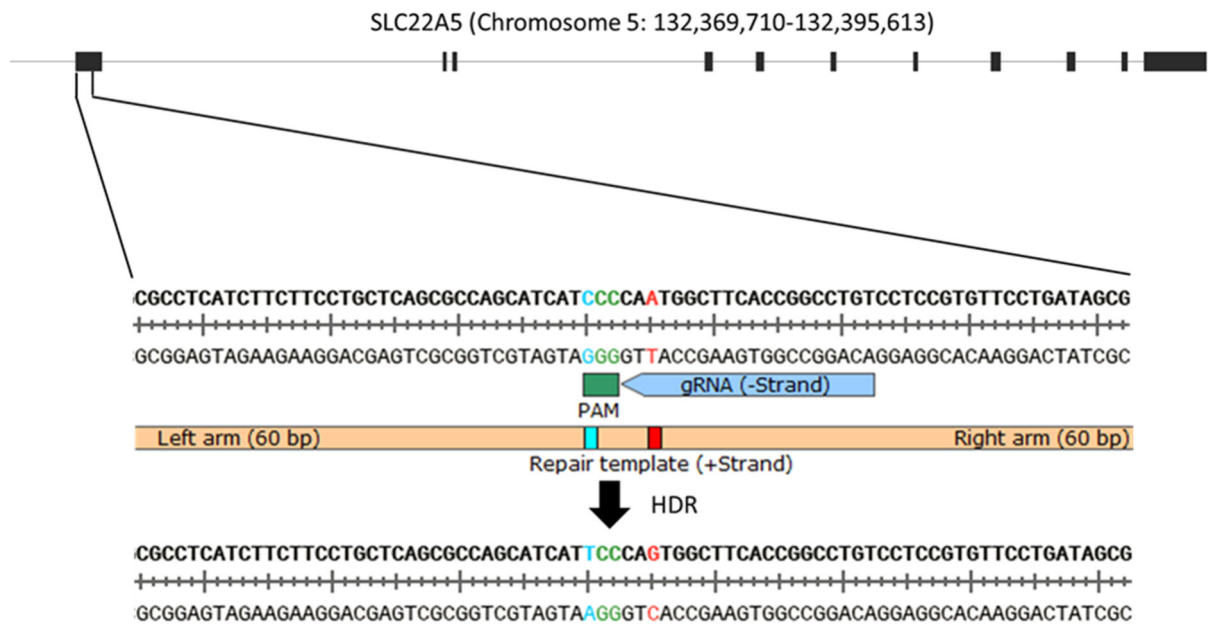


Figure 7: Schematic overview of the CRISPR/Cas9 strategy for OCTN2 (N32S) generation. A ssODN containing the desired point mutation was co-transfected with CRISPR components to introduce the mutation c.95A>G, p.N32S in exon1 of the SLC22A5 gene. Depicted are the gRNA target site and the predictive DNA sequence after successful integration of the repair template.

3.3.2 OCTN2 (-/-) knockout

A combinatorial CRISPR strategy was used to engineer a knockout of the *SLC22A5* gene in the isogenic control hiPSC OCTN2 (+/+). Two gRNA were designed to introduce a deletion of 17.3 kb spanning from the promoter region to exon 5 (NCBI Reference Sequence: NG_008982.2; 5075-22390.). For validation of successful homozygous cleavage, primer pairs were designed to amplify products inside of the deletion region and the gRNA target sites. Moreover, primers flanking the two cutting sites were designed in addition. Successful end ligation of the two double-strand breaks was confirmed by PCR amplification with these primer pairs and subsequent Sanger sequencing. A schematic overview of the knockout strategy and

the corresponding primer binding sites are displayed in Figure 8. To distinguish between unedited clones, heterozygous and homozygous editing, the resulting amplicons for each primer pair were separated using 1% (w/v) agarose gel electrophoresis, followed by Midori green staining.

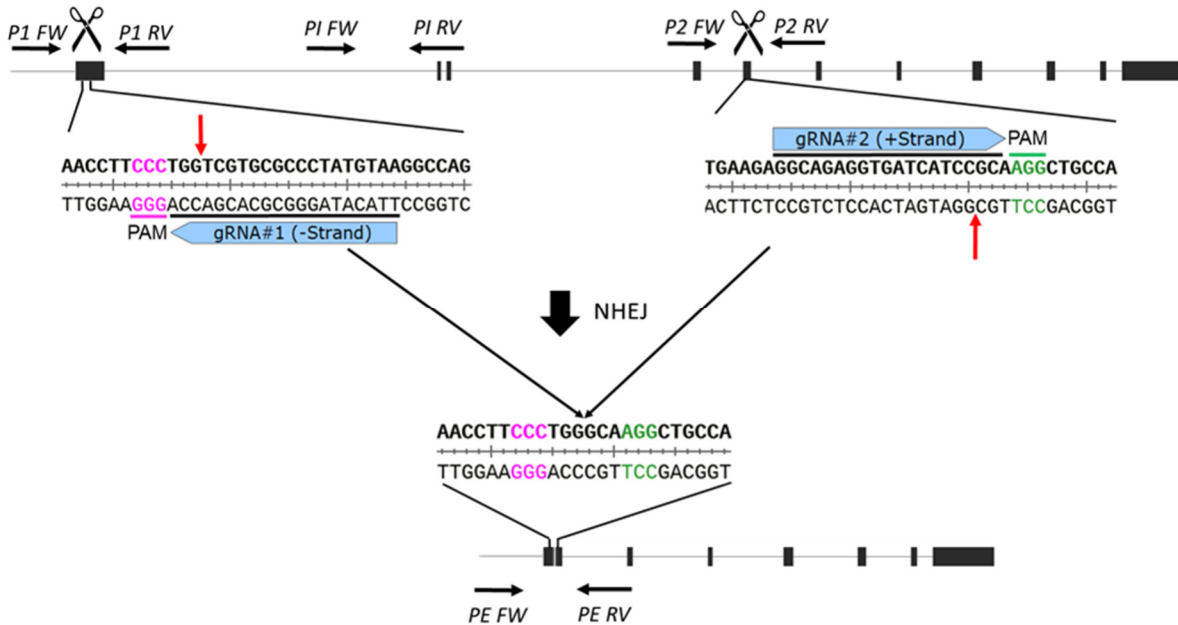


Figure 8 Schematic overview of the CRISPR/Cas9 strategy for OCTN2 (-/-) generation. Two gRNA were co-transfected to induce simultaneous cutting and a large deletion in the *SLC22A5* gene. Depicted are the gRNA target sites and the predictive DNA sequence after successful editing. Red arrows indicate the predicted Cas9 cutting sites. Black arrows indicate the primer binding sites for PCR validation. P1: Primer target region gRNA1; P2: Primer target region gRNA2; PI: Primer internal; PE: Primer external; Pink: PAM1; Green: PAM2.

3.4 Cell line generation by CRISPR/Cas9

In order to validate the genetic engineering result at the OCTN2 target region, genomic DNA was isolated from OCTN2 (+/+) hiPSCs using the DNeasy Blood & Tissue Kit (Qiagen) according to the manufacturer's instructions. The OCTN2 target region was amplified by touchdown PCR (Table 2 and Table 3) using the MyTaq DNA Polymerase (Meridian Bioscience). Amplicons were submitted for Sanger sequencing at MWG/Eurofins according to the manufacturer's submission guidelines.

Primers were designed based on the genetic sequence provided by the NCBI database (NCBI Reference Sequence: NG_008982.2; Gene ID: 6584; Homo sapiens solute carrier family 22 member 5 (*SLC22A5*) RefSeqGene on chromosome 5).

Table 2: PCR mastermix

Component	Volume per reaction (1x)
5x MyTaq Reaction Buffer	10 μ L
MyTaq DNA Polymerase	0.25 μ L
Primer mix (20 μ M)	5 μ L
DNA template	100 ng
Aqua dest.	Ad to 50 μ L

Table 3: MyTaq DNA Polymerase cycler program

Temperature	Time	Cycles
95 °C	7 min	1x
95 °C	30 sec	10x
Tm – 4 °C	30 sec	
72 °C	1min / kb product	
95 °C	30 sec	28x
65 °C	30 sec	
72 °C	1 min / kb product	
72 °C	7 min	1x
4 °C	∞	

3.4.1 Nucleofection

The Amaxa™ P3 Primary Cell 4D-Nucleofector X Kit L (Lonza) was used for delivery of the CRISPR/Cas9 ribonucleoprotein (RNP) complex into hiPSCs. A control hiPSC aliquot from an established working cell bank with a low passage number (25 - 30) was thawed and cultured for at least 2 passages on a 6-well plate to reach a confluency of 60-70% at the day of the experiment. HiPSCs were incubated with FTDA and the apoptosis inhibitor Y-27632 two hours prior to nucleofection.

The fluorescence-labeled tracrRNA-ATTO 550 (IDT) was used to monitor the electroporation efficiency by fluorescence microscopy. The tracrRNA oligos and the CRISPR-Cas9 crRNA (IDT) oligos were resuspended in RNase free IDTE Buffer (IDT) to a final stock concentration of 100 μ M. For gRNA duplex formation, 5 μ L of crRNA (100 μ M) were annealed with 5 μ L tracrRNA (100 μ M), incubated for 5 min at 95 °C and cooled down to room temperature. For formation of the RNP-complex, 5 μ L of the gRNA duplex were mixed with 5 μ L Cas9 protein (61 μ M, IDT) and incubated for 1.5 hours at room temperature under light protection. Additionally, 5 μ L of the second gRNA duplex were added to the suspension in the knockout approach.

To prepare the nucleofector solution, 82 μL P3 reagent and 18 μL supplement reagent (Lonza) were mixed per reaction according to the instruction of the AmaxaTM P3 Primary Cell 4D-Nucleofector X Kit L (Lonza).

Before nucleofection, hiPSCs were washed twice with PBS buffer and incubated with 1 mL Accutase solution (Sigma) per well at 37 °C to dissociate the hiPSCs into single cells. The dissociation was stopped by adding 1 mL FTDA medium per 6-well. The hiPSCs were resuspended in the media by gentle pipetting and centrifuged for 2 min at 200xg. Cells were gently titrated and counted by CASY cell counter and analyzer (Schärfe System). 8×10^5 hiPSCs were used in 100 μL nucleofector solution per electroporation reaction.

Single-stranded DNA oligonucleotide (ssODN) repair template oligos were resuspended in IDTE Buffer (IDT) to a stock concentration of 100 μM . 1 μL of ssODN repair template (100 μM) and 4 μL of RNP-complex were mixed with the hiPSC solution by gently pipetting, incubated for 5 min at room temperature and transferred to the nucleofection cuvette. Additionally, 1 μL Alt-R Cas9 Enhancer (100 μM , IDT) was added to the solution to promote transfection efficiency. The nucleofection cuvette was placed in the 4D-Nucleofector (Lonza) and hiPSCs were nucleofected by using the program CA137. After nucleofection, the cuvette was incubated for 5 min under normal cell culture conditions. Subsequently, hiPSCs were seeded in CDM medium supplemented with Y-27632 and bFGF on a Matrigel-coated 24-well plate.

HiPSCs were cultured for 72 hours at 37 °C or for the 'cold shock' approach at 32 °C respectively. Non-transfected hiPSCs were seeded with a density of 6×10^5 per well to control for hiPSC handling during the procedure and as a reference for electroporation efficiency. The following day, hiPSCs were carefully fed with additional 1 mL CDM medium without medium aspiration and a full medium change was performed 48 hours after the nucleofection. Red fluorescence was monitored by fluorescence microscopy (Thermo Fischer Scientific) 24, 48 and 72 hours after nucleofection to validate successful electroporation (not shown).

3.4.2 Subcloning and off-target analysis

72 hours after nucleofection, cells were dissociated with Accutase and seeded with CDM medium with Y-27632 (10 μM) and bFGF (30 ng/mL) at low seeding densities of 100, 250, 750, 1000 hiPSCs per well (10 cm^2) in a Matrigel-coated 6-well plate. In addition, the remaining nucleofected hiPSCs were seeded at a higher density of 5×10^5 cells per well (10 cm^2) in a Matrigel-coated 6-well plate. After one passage, these hiPSCs were submitted to Sanger sequencing analysis. The bioinformatic webtool TIDER (Brinkman et al. 2018) was used to estimate gene editing efficiency from the Sanger sequencing results. In case TIDER prediction estimated very low gene editing efficiency, low-density hiPSC seedings were discontinued. Low-density hiPSC seedings were expanded for 9 to 10 days under daily

CDM medium change until clonal hiPSC colonies reached an appropriate size to pick. HiPSC cultures were incubated with CDM medium with Y-27632 for 2 hours and sterile 100 μ L-pipette tips were used to carefully scrape individual colonies from the 6-well plate and transfer the clones to Matrigel-coated 48-well plates into individual wells. 30 to 50 clones were picked per transfection approach and subcultivated for 3-4 more days before they reached confluency and were splitted with a ratio of 1:2 into two 48-well copy plates. Colonies were again expanded with daily medium change until they reached confluency. One of the copy plates was used for cryo-preservation, while the second plate was used for DNA isolation. Cryopreservation was performed in 90% FCS medium and 10% DMSO.

After overnight incubation at -80 °C in isopropanol container, frozen aliquots were transferred to -150 °C freezer for long-term storage. The fully automated QIAcube HT System (Qiagen) and QIAamp 96 DNA QIAcube HT kit (Qiagen) were used for DNA isolation according to the manufacturer's instructions. Subsequently, isolated DNA of the OCTN2 (N32S)-approach was used for PCR amplification of the *SLC22A5* target region and following submission to MWG/Eurofins for Sanger sequencing according to the supplier's submission guideline. DNA of the OCTN2 (-/-) knockout approach was used for PCR amplification and subsequent 1% (w/v) agarose electrophoresis to validate putative introduced deletions. Cryotubes corresponding to successfully edited hiPSC clones were thawed and expanded for master cell bank (MCB) and working cell bank (WCB) generation with stepwise adaption from CDM- to FTDA medium.

To control for unintended DNA modifications by off-target cleavage activity of the Cas9 protein, regions in the human genome with high sequence similarities to the target site were identified (highest 10 off-target scores predicted by online *in silico* tool IDT, Custom Alt R CRISPR-Cas9 gRNA software and CRISPOR software). PCR primers to amplify the off-target region were designed according to chapter 3.4. PCR products were analyzed by 1% (w/v) agarose electrophoresis and submitted for Sanger sequencing at Eurofins/MWG. Design of primer sequences and annealing of obtained Sanger sequences traces was conducted according to the genomic locations provided by NCBI. Sanger sequencing results and off-target primer sequences can be found in the supplement (Figure S1 + Table S10).

3.5 Karyotyping

To control for genomic integrity and exclude CRISPR-induced aneuploidy, karyotype analysis was performed using the nCounter Human Karyotype Panel (Nanostring technologies). To this end, hiPSCs were thawed from an MCB cryo-aliquot, cultured under normal culture conditions in FTDA medium and passaged for two passages on Geltrex-coated 6-well plates until hiPSCs reached a confluency of 80-90%. Genomic DNA was isolated using the DNeasy Blood &

Tissue Kit (Qiagen). Pre-analytical processing of the sample was performed according to the manufacturer's instructions. In brief, 250 µg DNA were fragmented by enzymatic digestion and denatured into single-stranded DNA. Digestion of the genomic DNA was verified by agarose gel electrophoresis. The fragmented DNA was hybridized with probes overnight at 65 °C for 16 hours. The following day hybridized DNA in the nCounter Cartridge (Nanostring) was transferred into the nCounter Digital Analyzer (Nanostring) and the program was run for 6 hours. Individually ordered fluorescent reporter probes were used to generate a chromosome-specific fluorescence intensity. The nCounter CNV Collector Tool software (Nanostring) was used for the analysis. The nCounter Karyotyping procedure was kindly performed by Elisabeth Krämer (IEPT, UKE, Hamburg, Germany) and raw data were kindly analyzed by Giulia Mearini (IEPT, UKE, Hamburg, Germany).

3.6 Cardiac differentiation

HiPSC were differentiated into cardiomyocytes (hiPSC-CM) with an embryoid body (EB)- and growth factor-based three-stage protocol which was recently described (Breckwoldt et al. 2017). A simplified overview of the cardiac differentiation protocol is illustrated in Figure 9.

In brief, hiPSC were expanded on Geltrex-coated T80-flasks to a confluency of 90-100% and detached with EDTA. Formation of EBs was induced by transferring cells into 500 mL spinner flasks with a density of 30-35x10⁶ hiPSCs per 100 mL of EB formation medium. HiPSC suspension was cultivated overnight at 40 rpm glass ball impeller rotation speed. Mesoderm induction was induced by estimating the EB volume, washing and transferring the EBs into mesoderm induction medium with a volume of 200-300 µL EB per pluronic-coated T175-flask. Mesoderm induction was conducted for three days under hypoxic conditions with 50% media exchange daily. After washing the EBs again, cardiac differentiation was induced by transferring EBs into cardiac differentiation medium 1 with a volume of 250-300 µL EBs per pluronic-coated T175-flask with 50% media exchange daily for three days under normoxic conditions (21% O₂). Then media was completely removed and exchanged for cardiac differentiation medium 2. After a daily 50% medium change for four days, culturing medium was exchanged with cardiac differentiation medium 3. Typically, EBs developed visible spontaneous beating activity at day 11 to 14 of this protocol and were matured for 7 more days. After washing EBs in HBBS-solution buffer, dissociation of beating cardiomyocytes was conducted by transferring EBs into collagenase II solution (200 units/mL; Worthington) containing myosin II ATPase inhibitor N-benzyl-p-toluene sulphonamide (BTS) for 2-3 hours until dispersing single cells could be observed.

Dissociated hiPSC-CM were frozen in freezing media containing 90% FBS and 10% DMSO using an isopropanol freezing container (Mr. Frosty) overnight at -80 °C and then transferred to -150 °C for long-term storage or resuspended in EHT casting medium for subsequent EHT generation. HiPSC-CM were transferred into -150 °C freezer for long-term storage. The efficiency of the differentiation process was determined by staining hiPSC-CM with a fluorescent-labeled cardiac troponin T (cTNT)- antibody (Miltenyi Biotech) and determining the percentage of cTNT-positive cells by flow cytometer FACSCanto II (BD). Adjustment of gates and flow cytometry conditions were changed according to the isotype control of the antibody and performed with FACSDiva software (BD). A representative cTNT flow cytometry analysis is illustrated in Figure 10. Differentiation runs with at least 75% cTNT-positive cells were used for further functional experiments in this work.

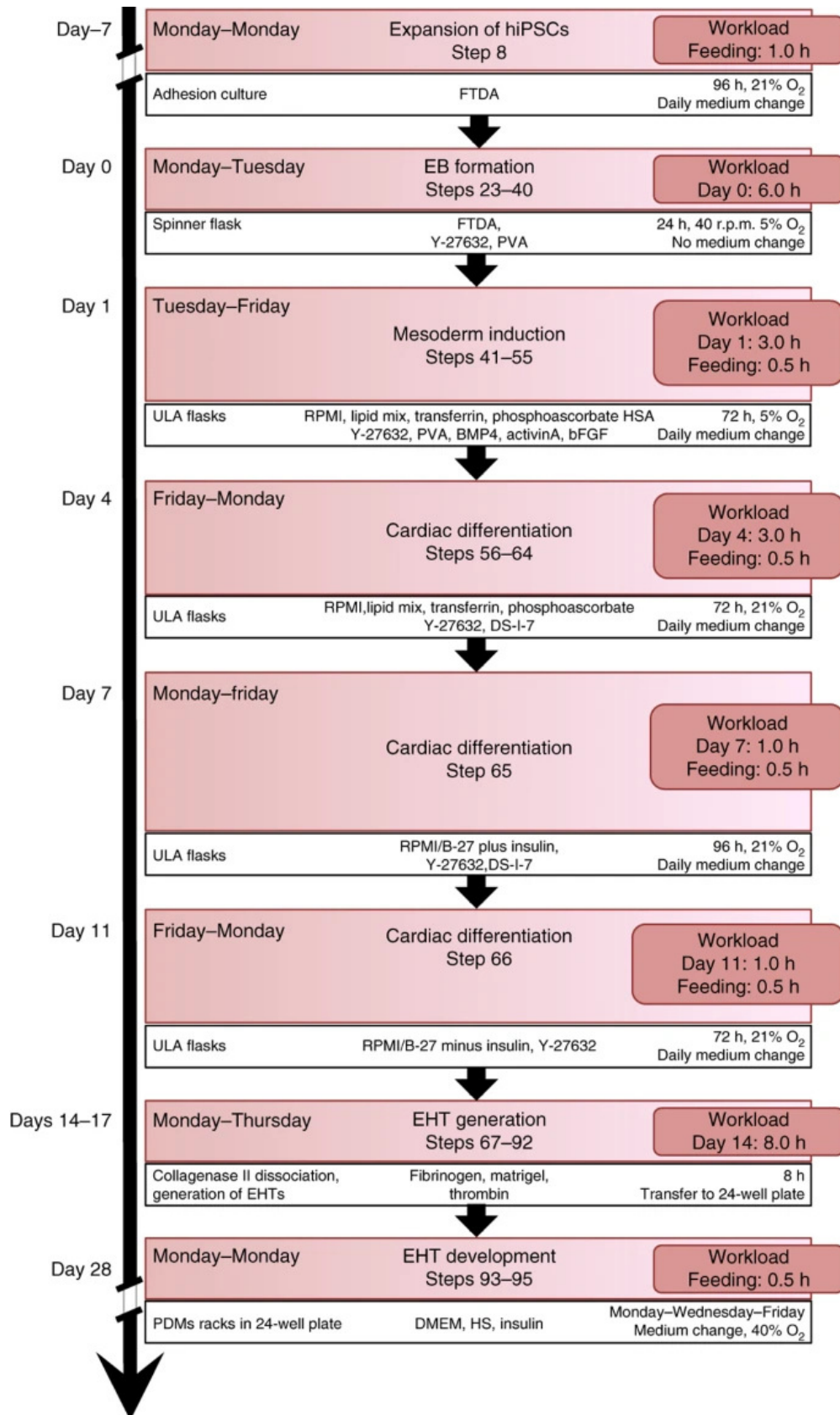


Figure 9: Schematic overview of the EB- and growth factor-based cardiomyocyte differentiation protocol. Displayed are the individual steps of the protocol, including time point, medium composition culture format, and culture conditions (Breckwoldt et al. 2017).

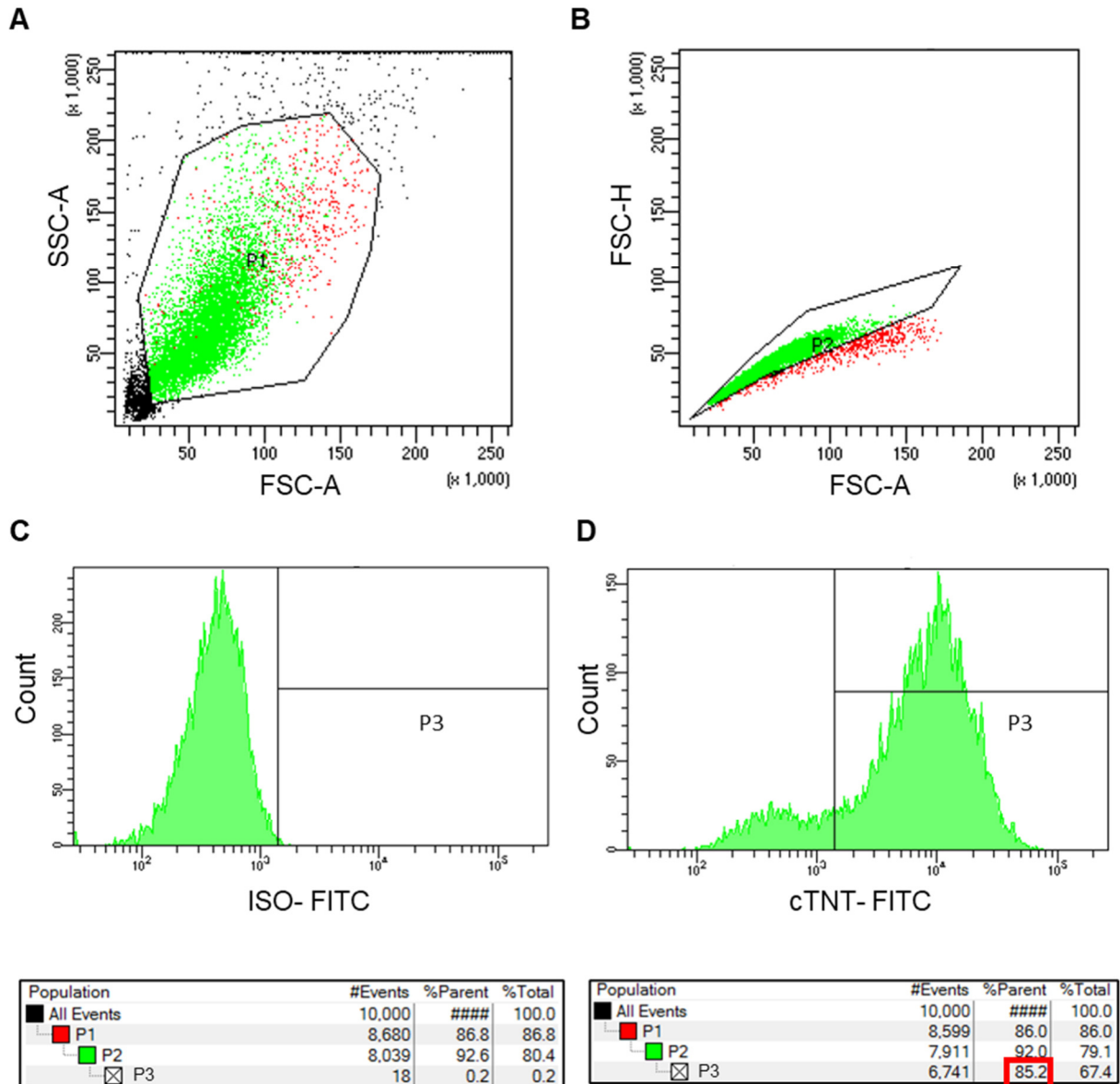


Figure 10: Flow cytometric analysis of hiPSC-CM. First, forward scatter (FSC) and sideward scatter (SSC) were used to exclude cell debris based on size and granularity (P1; A). To only include single cells in the analysis, doublets were gated out subsequently (P2, B). The proportion of cTnT-positive cells was determined by adjusting gate P3 according to FITC staining of the isotype control (P3, C). The red box indicates the percentage of cTnT-positive cardiomyocytes.

3.7 Engineered heart tissues (EHT)

Engineered heart tissues (EHT) consisting of hiPSC-CM were generated according to the protocol published by Mannhardt et al. (2016). In brief, dissociated hiPSC-CM were kept on wet ice after the dissociation process (chapter 3.6), centrifuged and resuspended in EHT

casting medium containing DMEM, horse serum and glutamine (Table 1). Prior to the casting process, polytetrafluorethylene (PTFE) spacers (EHT Technologies) were placed in a warm 2% (w/v) PBS/agarose solution in a 24-well plate. Agarose solidification at room temperature led to the formation of agarose molds. PTFE spacers were removed from the 24 well plates and flexible polydimethylsiloxane (PDMS) posts (EHT Technologies) were placed on the 24-well plates so that pairs of elastic PDMS posts reached into one casting mold. 100 μL of the mastermix (Table 4) containing 2x DMEM, Y-27632, fibrinogen and 1.0×10^6 hiPSC-CMs were resuspended in EHT casting medium, rapidly mixed with 3 μL thrombin and pipetted into one agarose casting mold between the flexible PDMS posts. After finishing all casting molds, the preparation was placed in the incubator for 1.5 hours at 37 °C until a fibrin gel formed in the agarose molds around the PDMS posts. 200-300 μL of pre-warmed EHT culture medium was added dropwise into each well to ameliorate detachment of the fibrin gel from the agarose mold. After additional 15-30 minutes of incubation, racks with fibrin gels attached to the PDMS posts were transferred into a new 24-well plate, filled with pre-warmed EHT culture medium and incubated at 40% O₂, 37 °C, 7% CO₂, and 98% humidity. EHTs were cultured for 28-42 days with medium changes 3 times per week. After 5-7 days of culture, EHTs started to develop spontaneous macroscopic contractions.

Table 4: Mastermix EHT casting

Component	Volume per EHT
hiPSC-CM	1.0×10^6
EHT casting medium	97.68 μL
2x DMEM	6.125 μL
0.1% Y-27632	0.11 μL
Fibrinogen	2.78 μL

3.7.1 Video-optical contraction analysis

The 24 well EHT culture plate was placed inside the test system for automated video-optical analysis. EHT contraction parameters, e.g. force, frequency and contraction kinetics, were consistently monitored over time with a video-optical analysis system 2 hours after each medium change. The system consists of an incubator unit with controlled conditions for temperature, humidity and gas composition (37 °C, 7% CO₂, 72% N₂, and 21% O₂). The upper boundary of the incubator unit consists of a glass roof above on which a camera is positioned and connected to an XYZ axis system. A customized software allows defining XYZ coordinates to record movie files from each EHT/24 well plate which depicts the shorting of the EHT during contraction. Based on automated recognition of both ends of the EHT contour, analysis of EHT shortening during contraction and the geometry and elastic propensity of the PDMS post force is calculated and recorded over time.

A schematic visualization of this test system is depicted in Figure 11. Several contractility parameter parameters (e.g. force, frequency, relaxation time, contraction time and irregularity/RR-scatter) are derived from the original force traces and are calculated in an automated manner.

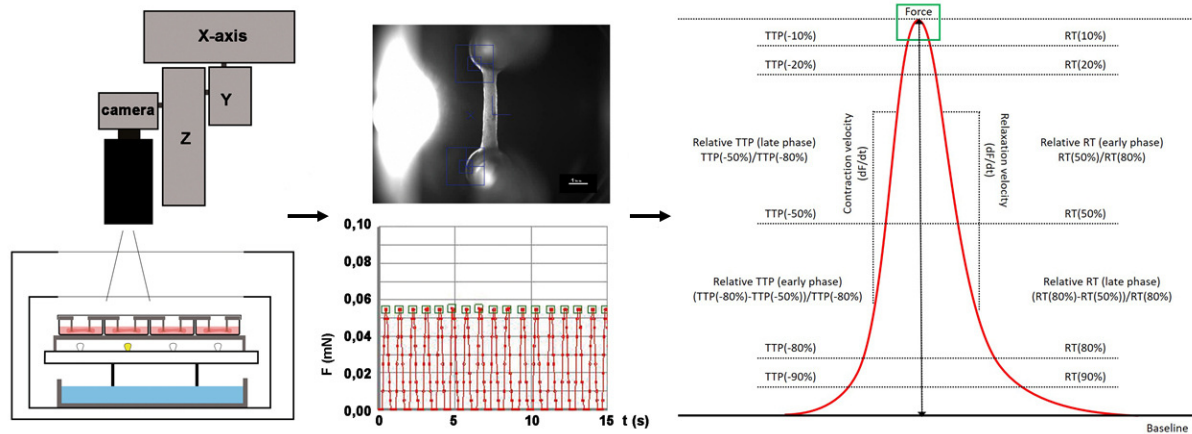


Figure 11: Automated video-optical contraction analysis of EHTs (adapted from Schaaf et al. 2011). Schematic view of the camera system placed over the incubator system with a glass rooftop. EHTs are cultured in a 24-well format and can individually be measured by the camera connected to an X-, Y-, Z- axis system. The software calculates force traces from in the movie file based on the EHT shortening and PDMS post geometry and elastic propensity.

3.7.2 Electrical pacing & average peak measurement

EHTs were electrically stimulated as previously described by Hirt et al. (2014). PDMS racks with EHTs were mounted onto custom-made graphite pacing units and stimulated by using Grass S88X Dual Output Square stimulator (Natus Neurology Incorporated). The pacing frequency was adjusted to a value of 1.5- to 2-fold of the spontaneous beating frequency of the EHT batch with an output voltage of 2 V in biphasic pulses of 4 ms. EHTs that were not able to follow the pacing frequency, were excluded from the analysis. Average contraction peaks were calculated by the software by taking the average traces of 10-15 peaks.

3.7.3 Glucose and lactate measurement

To analyze the glucose consumption and lactate production of EHTs, glucose and lactate concentrations were measured in EHT cell culture media by blood gas analysis. Samples were collected at baseline and after 24 hours of incubation in EHT medium at day 21 of culture and stored at -20 °C. The blood gas analysis instrument ABL90 FLEX Analysator (Radiometer) was used to determine the metabolite concentrations by injecting the supernatant (0.5 mL) into the instrument with a 1 mL syringe. Glucose and lactate concentrations were also normalized to force and frequency data measured by contraction analysis at the day of medium change.

3.7.4 Fatty acid and carnitine supplementation

3.7.4.1 EHT cultivation in fatty acid medium

EHTs of all genotypes were cultured in serum-containing EHT culture medium until force values reached their plateau phase approximately at day 21-28 after generation. Then, EHTs were transferred to a serum- and glucose-free DMEM medium containing linoleic acid- and oleic acid-albumin (Sigma). The serum-free fatty acid medium composition was adapted to a publication by Hirt et al. (2012) and can be found in Table 1. Contraction analysis was done daily after 2 hours of medium incubation over a period of 4 days.

3.7.4.2 EHT carnitine supplementation

A carnitine supplementation experiment was conducted by adding a finale concentration of 2 mM L-carnitine hydrochloride (Sigma) to the EHT medium over the entire time of tissue cultivation. Contraction analysis was done according to chapter 3.7.1 and experiments were terminated between day 33 and 42 of culture time.

3.7.5 Transmission electron microscopy

EHTs were transferred into a 24-well plate containing Tyrode's solution (Table 5) with 1.8 mM Ca^{2+} and 30 mM butanedione monoxime (BDM) for 3-4 hours until EHTs completely stopped contraction. For fixation, EHTs were shifted into 4% paraformaldehyde (PFA) (Thermo Scientific) in 0.1 M phosphate buffer containing 1% glutaraldehyde (Science Services) overnight at 4 °C. Fixed EHTs were transferred to UKE electron microscopy core facility and the microscopy procedure was kindly performed by Dr. Michaela Schweizer (Electron Microscopy Unit, Center for Molecular Neurobiology, UKE, Hamburg, Germany).

Table 5: Tyrode's solution

Component	Final concentration
NaCl	120 mM
KCl	5.4 mM
$\text{MgCl}_2 \times 6 \cdot \text{H}_2\text{O}$	1 mM
NaH_2PO_4	0.4 mM
NaHCO_3	22.6 mM
Glucose	5 mM
Na_2EDTA	0.05 mM
HEPES (pH 7.4, in PBS)	25 mM
Aqua ad injectabilia	

3.8 Analysis of acylcarnitines and ceramides

Engineered heart tissue cells were homogenized in Milli-Q water (approximately 10^6 cells per 100 μ l) using the Precellys 24 Homogenisator (Peqlab). The protein content of the homogenate was routinely determined using bicinchoninic acid. Levels of acylcarnitines and ceramides in the cell homogenates were determined by Liquid Chromatography coupled to Electrospray Ionization Tandem Mass Spectrometry (LC-ESI-MS/MS).

3.8.1 Acylcarnitines

Acylcarnitines were derivatized to butyl esters and using a procedure previously described (Giesbertz et al. 2015) with several modifications:

To 100 μ L of cell homogenate 750 μ L of extraction solution (methanol (containing 0.005% 3,5-di-*tert*-4-butylhydroxytoluol)/Milli-Q water/chloroform 4:1:1 (v/v/v)) and 20 μ L of an internal standard mixture, containing deuterated acylcarnitines (Lyophilized Internal Standard MassChrom Amino Acids and Acylcarnitines from Dried Blood, Chromsystems, reconstituted in 2.5 ml, then 1:5 diluted), were added. After thorough mixing and centrifugation (16,100 RCF, 10 min, 4 °C), the supernatant was transferred to a new tube. The residue was re-extracted with 750 μ L of extraction solution. The supernatants were pooled and dried under a stream of nitrogen. The evaporated extracts were treated with 200 μ L of freshly prepared derivatization solution (*n*-butanol/acetyl chloride 95:5 (v/v)). After incubation for 20 min at 60 °C in a ThermoMixer (Eppendorf) at 800 rpm, the samples were again dried under nitrogen. After addition of 100 μ L of methanol/water 3:1 (v/v) and centrifugation (16,100 RCF, 10 min, 4 °C), 80 μ L of supernatant were transferred to autoinjector vials.

LC-ESI-MS/MS analysis was performed as previously described (Aravamudhan et al. 2021). The LC chromatogram peaks of butyl esters of endogenous acylcarnitines and internal standards were integrated using the MultiQuant 3.0.2 software (SCIEX). Endogenous acylcarnitine species were quantified by normalizing their peak areas to the peak area of the internal standards. These normalized peak areas were normalized to the protein content of the sample.

3.8.2 Ceramides

To 50 μ L of cell homogenate 50 μ L of Milli-Q water, 750 μ L of methanol/chloroform 2:1 (v/v) and internal standard (127 pmol ceramide 12:0, Avanti Polar Lipids) were added. Lipid extraction and LC-ESI-MS/MS analysis were performed as previously described (Schwamb et al. 2012). The LC chromatogram peaks of endogenous ceramide species and the internal standard ceramide 12:0 were integrated using the MultiQuant 3.0.2 software (SCIEX). Endogenous ceramide species was quantified by normalizing their peak areas to the peak area

of the internal standard ceramide 12:0. These normalized peak areas were normalized to the protein content of the sample.

The mass spectrometry procedure was kindly performed by our collaborator Dr. Susanne Brodesser (CECAD Lipidomics/Metabolomics Facility, CECAD Research Center, University of Cologne, Cologne, Germany). Data analysis, visualization and interpretation were conducted by me.

3.9 Tandem Mass Tag (TMT)-based quantitative proteomic analysis

3.9.1 EHT harvesting for quantitative mass spectrometry

EHTs from hiPSC-CMs were cultured in EHT medium for 28 days prior to proteome analysis. For single cell dissociation, EHTs were washed twice in warm PBS buffer and incubated with collagenase II solution (collagenase II (200 units per mL), HBSS minus $\text{Ca}^{2+}/\text{Mg}^{2+}$, HEPES (10 mM), Y-27632 (10 μM), and BTS (30 μM)) in a falcon tube for 3 hours. When detachment of single cells from the fibrin matrix was microscopically visible, dissociated hiPSC-CMs were gently titrated with a 1000 μL -pipette (Eppendorf) until the last cluster of cells was disaggregated. Dissociated hiPSC-CMs were spun down for 5 min at 200xg and supernatant was removed. The pellet was frozen in liquid nitrogen and stored at $-80\text{ }^{\circ}\text{C}$ prior to subjection to quantitative proteome analysis. The following mass spectrometry procedure was kindly performed by our collaborator Dr. Xiaoke Yin (King's British Heart Foundation Centre of Research Excellence (Group leader: Prof. Dr. Manuel Mayr), King's College London, United Kingdom). Data analysis, visualization and interpretation were conducted by me.

3.9.2 Tissue protein extraction and digestion for mass spectrometry

Cell pellets were lysed in 50 mM Tris, 0.1% SDS, pH=8.8, with protease inhibitors. After centrifugation at $4\text{ }^{\circ}\text{C}$ at 16,000xg for 10 min, supernatant was transferred to new 1.5 mL tubes and protein concentration was measured using BCA protein assay kit (Thermo Fisher Scientific). For each sample, 23 μg of proteins were denatured by the addition of 9 M urea, 3 M thiourea (final conc. 6 M urea, 2 M thiourea) and reduced by the addition of 100 mM DTT (final conc. 10 mM) followed by incubation at $37\text{ }^{\circ}\text{C}$ for 1 hour, 240 rpm. The samples were then alkylated by the addition of 500 mM iodoacetamide (final conc. 50 mM) followed by incubation in the dark for 1h at room temperature. Pre-chilled ($-20\text{ }^{\circ}\text{C}$) acetone (1:9 volume ratio) was used to precipitate the samples overnight at $-20\text{ }^{\circ}\text{C}$. Samples were centrifuged at 16,000xg for 30 min at $4\text{ }^{\circ}\text{C}$ and the supernatant subsequently discarded. Protein pellets were dried using a vacuum centrifuge (Thermo Fisher Scientific, Savant SPD131DDA), re-suspended in 0.1M TEAB buffer, pH 8.2 (Sigma T7408), and 0.6 μg trypsin was added. The digestion was performed overnight at $37\text{ }^{\circ}\text{C}$, 240 rpm and stopped by adding 10% TFA (final

conc. 1%). C18 cleanup was performed using Agilent Bravo AssayMAP and the eluted peptides were dried using a vacuum centrifuge.

3.9.3 Sample labeling for mass spectrometry

The samples were resuspended in 0.1 M TEAB and a pooled sample were made by taking same amount of proteins from each individual sample. Samples were labeled with Tandem Mass Tag (TMT) 11-plex reagent (Thermo Fisher Scientific) following the manufacturer's instructions. The pooled sample labeled with TMT-126 was used as internal standard. The samples labeled with different tags of the 11-plex TMT were combined, dried and resuspended in 300 μ l of 0.1% TEA. Samples were further fractionated using high pH RP HPLC (Agilent 300Extend-C18 3.5 μ m 4.6x150mm P/N 763973-902) and 16 fractions were collected for each TMT mixture. All fractions were dried and resuspended in LC solution (2% acetonitrile (ACN), 0.05% TFA).

3.9.4 Mass spectrometry analysis

Samples were injected and separated by a nanoflow HPLC (Ultimate 3000 RSLCnano, Thermo Fisher Scientific) on an EASY-Spray column (C18, 75 μ m x 50 cm, 2 μ m) using 2 hour LC gradient: 0-10 min, 4%-10%B; 10-75 min, 10%-30%B; 75-80 min, 30%-40%B; 80-85 min, 40%-99%B; 85-90 min, 99%B; 90-120 min, 4%B; A=0.1% FA in H₂O and B= 0.1% FA, 80% ACN in H₂O. The flow rate was 250 nL/min and column temperature was set at 45°C. The separated peptides were directly injected to an Orbitrap Fusion Lumos MS (Thermo Fisher Scientific) and analyzed using a synchronous precursor selection (SPS)-based MS₃ method for TMT-labelled sample. Full MS spectra were collected on the Orbitrap with resolution 120,000 and scan range 375-1500 m/z. The most abundant ions were fragmented using CID and MS₂ spectra were collected on a linear ion trap, with dynamic exclusion enabled. The 5 most abundant ions from every MS₂ spectrum were selected and fragmented at the same time using HCD with collision energy 65% and MS₃ spectra were collected on the Orbitrap with resolution 60,000 and a scan range of 110-500 m/z to measure the TMT reporter ions. The cycle time was set at 3 seconds.

Raw data were analyzed using Proteome Discoverer 2.4. The 16 fractions of each TMT mixtures were loaded as fractions and analyzed together. Each TMT tag was assigned to the correct sample and group. Data were searched against human UniProt/SwissProt database (version 2020_01, 20365 protein entries). Trypsin was used as enzyme and maximum 2 missed cleavage was allowed. The precursor mass tolerance was set at 10 ppm and fragment mass tolerance was set at 0.8 Da. Carbamidomethylation on cysteine and TMT 6plex on N-terminal and lysine were used as static modifications. Oxidation on methionine was used as

dynamic modification. Reporter ions S/N were used for quantification. The quantification values were normalized to total peptide amount and scaled on controls (pooled sample labeled with TMT-126). The scaled abundance was exported for further analysis.

The dataset was first imputed to replace missing relative quantities to zeros when these were consistent among any of the examined phenotypes. In specific, when the percent of missing values in one examined phenotype exceeded 90% and the percentage of missing value for the other phenotypes was below 10% then the missing values of the examined phenotype were imputed to zeros. The relative quantities of the proteins were then scaled using log₂ transformation. Next, the dataset was filtered to keep only proteins with less than 30% missing values, without considering the previously imputed missing values as missing. The remaining missing values were imputed using KNN-Impute method with k equal to 3. The limma package has been used to compare between different phenotypes using the Ebayes algorithm and correcting for selected covariates. The initial p-values were adjusted for multiple testing using Benjamini-Hochberg method and a threshold of 0.05 was used for the adjusted p-values to infer statistically significant changes.

3.9.5 Pathway enrichment analysis of significant proteins

The bioinformatic webtool Webgestalt (Liao et al. 2019) was used for pathway enrichment analysis of KEGG terms. KEGG pathways of significantly enriched proteins (fold change ≥ 1.4 as suggested by proteomics core facility) were inferred by Benjamini-Hochberg testing with a p-value threshold of 0.05 and a maximum number of 150 proteins per category. To visualize the samples based on their proteomic profiles, principal component analysis (PCA) was conducted, and samples were projected in a 2D space based on their 2 most significant principal components. Samples were colored based on their phenotype. Volcano plots for the visualization of differentially expressed proteins were generated in GraphPad PRISM.

3.10 TRIzol extraction

Extraction of total RNA, genomic/mitochondrial DNA and protein was done using TRIzol[®]-reagent (Life Technologies) according to the manufacturer's protocol. In brief, 300 μ L TRIzol[®]-reagent per EHT was added and homogenized using a 1mL RNase-free syringe (B.Braun) and hypodermic-needles of 0.9 mm and 0.4 mm diameter (Sterican). Chloroform (Roth) was added, and the homogenate was separated into an aqueous layer containing RNA and an organic layer containing DNA and proteins. Total RNA was isolated by isopropanol precipitation and eluted in 30 μ L nuclease-free Aqua dest., frozen in liquid nitrogen and stored at -80°C. Genomic/mitochondrial DNA was isolated by ethanol precipitation and was solved in 100 μ L Aqua dest. overnight at -4 °C and frozen at -20 °C. Nucleic acid concentrations and purity were

determined by NanoDrop Spectrophotometer (Thermo Scientific). Protein was precipitated from the phenol-ethanol supernatant by isopropanol precipitation and washed with guanidinium chloride prior to solubilization in 100 μ L 1% SDS.

3.11 Gene expression analysis & mitochondrial DNA quantification

Quantitative real-time PCR (qPCR) was performed for gene expression analysis. Complementary DNA (cDNA) was generated by reverse transcription of total RNA preparations using the high-capacity cDNA reverse transcription kit (Applied Biosystems). Mastermix and reaction set-up was used according to the manufacturer's instructions (Table 6 + Table 7). All experiments were performed using technical triplicates. The $\Delta\Delta$ Ct method was used for calculation of relative transcript levels. Primer sequences are listed in the supplement Table S11. Gene expression of target genes was normalized to the reference transcripts of the housekeeping gene glucuronidase-beta (*GUSB*).

QPCR experiments were conducted with the AbiPrism 7900HT Fast Real-Time PCR System (Applied Biosystems) using HOT FIREPol EvaGreen qPCR Mix Plus (Solis BioDyne; Table 8 and Table 9).

Table 6: Mastermix for RNA reverse transcription

Component	Volume per reaction (1x)
10x RT buffer	2.5 μ L
25x dNTP	1 μ L
10x RT random primer	2.5 μ L
RNA	500 ng
Aqua dest.	Ad 25 μ L

Table 7: RNA reverse transcription cycler program

Temperature	Time
25 °C	10 min
37 °C	120 min
85 °C	5 min
4 °C	∞

Quantification of mitochondrial DNA (mtDNA) was performed according to a qPCR protocol recently described by Ulmer et al. (2018). In brief, genomic- and mtDNA were isolated by TRIzol extraction (Chapter 3.10). Mt-DNA concentrations of each sample were adjusted to 16.5 ng/ μ L prior to the experiment by the addition of Aqua dest. Mt-DNA content was quantified by normalizing gene expression values of the mitochondrially encoded NADH dehydrogenase 1

(mt-ND1) and 2 (mt-ND2) to the nuclear-encoded globular actin (β -actin). Primer sequences were used as described (Burkart et al. 2016; Ulmer et al. 2018) and are listed in the supplement (Table S11).

Table 8: Mastermix qPCR & mtDNA quantification

Component	Volume per reaction (1x)
EvaGreen Master mix	2 μ L
Primermix (20 μ M)	0.5 μ L
cDNA / mtDNA	2 μ L
Aqua dest.	5.5 μ L

Table 9: qPCR cyclers program

Temperature	Time	Cycles
50 °C	2 min	1x
95 °C	10 min	
95 °C	15 sec	40x
60 °C	60 sec	
95 °C	15 sec	28x
60 °C	15 sec	
95 °C	15 sec	

3.12 Southern blot

Southern blot was performed to control for CRISPR/Cas9 induced on-target DNA rearrangements resulting from the co-transfection of two gRNA in OCTN2 (-/-) genetic engineering experiments. Southern blot probe design and the procedure were performed according to Skryabin et al (2020). HiPSC were thawed from an MCB aliquot and expanded to T25 flask format with 100% confluency. HiPSCs were washed with 5 mL PBS per flask and lysed in 1 mL standard lysis buffer containing 100 mM Tris-HCl (pH 8.5), 5 mM EDTA, 0.2% SDS, 200 mM NaCl, 100 g/mL Proteinase K (Roche) incubated overnight at 37 °C. DNA was extracted by TRIzol phenol/chloroform extraction (chapter 3.10) and dissolved in 100% ethanol. Southern blot probe design and procedure was kindly performed by Dr. Dr. Boris Skryabin (Transgenic animal and genetic engineering (TRAM), WWU, Münster, Germany). Data interpretation and visualization were performed by me.

3.13 Single-nucleus RNA sequencing

In order to investigate genotype-specific RNA expression at a single cell level, single-nucleus RNA sequencing (snRNA-seq) was performed according to Litviňuková et al. (2020). Prior to the single nuclear isolation and preparation procedure, hiPSC-CM EHTs were generated from frozen cardiomyocytes and cultured for 14 days in EHT culture medium. EHTs were washed with PBS, detached from the PDMS posts, frozen in liquid nitrogen, stored at -150 °C and transferred to the snRNA sequencing facility (Cardiovascular and Metabolic Sciences (Group leader: Prof. Dr. Norbert Hübner), Max Delbrück Center for Molecular Medicine in the Helmholtz Association (MDC), Berlin, Germany).

The procedure and pre-analytical data processing were kindly performed by Sabine Schmidt and Dr. Giannino Patone (MDC, Berlin, Germany). Data analysis, interpretation and visualization were performed by me. The Loupe Cell Browser from 10x Genomics was used to filter single nuclei for counts ($500 < n_counts < 15,000$), genes ($300 < n_genes < 5,000$) and mitochondrial genes ($percent_mito < 1\%$). The same software was used to filter, analyze, and review annotated clusters, based on the implemented t-SNE algorithm.

3.14 Statistical analysis

GraphPad Prism software 8.4.3 was used to perform statistical analysis. All data was depicted as mean \pm SEM either as scatterplots or bar graphs. Where possible, data sets were tested for normal distribution and the appropriate statistical test was chosen accordingly. Either the unpaired or nested Student's t-test, a nested-, a classical one-way ANOVA or a two-way ANOVA (plus Bonferroni's post-test) was used to determine whether the difference between groups was statistically significant. A p-value lower than 0.05 was considered to be statistically significant.

4 Results

4.1 CRISPR/Cas9

An established control hiPSC line (OCTN2 (+/+)) was used as the isogenic control line and a basis for engineering the OCTN2-defective hiPSC lines. To this end, the OCTN2 (+/+) hiPSC line was CRISPR/Cas9 edited to generate a hiPSC line carrying a homozygous missense mutation leading to an amino acid change at position 32 (OCTN2 (N32S)). In parallel, a second approach was performed to generate a full OCTN2 knockout by transfecting two gRNA resulting in a large genomic deletion (OCTN2 (-/-)). Prior to the *in silico* gRNA design, Sanger sequencing was performed on the *SLC22A5* gene locus to confirm the OCTN2 wildtype sequence and the absence of polymorphisms in the target region that could restrict gRNA binding (Figure 13 A). Of note, a heterozygous silent mutation was detected 182 base pairs downstream (c.277C>T) of the mutation of interest (Figure 13 A). *In silico* design of the CRISPR/Cas9 ribonucleoprotein genetic engineering approach was performed with webtool CRISPOR (Concordet and Haeussler 2018) and the Custom Alt-R CRISPR-Cas9 guide RNA design tool (IDT).

Despite increasing progress in CRISPR-mediated gene editing in hiPSC, the introduction of exogenous donor templates remains challenging due to a low efficiency of the HDR pathway in hiPSC (Chen et al. 2011; Mali et al. 2013; Miyaoka et al. 2016). In order to improve the HDR efficiency, the standard cultivation temperature of 37 °C for 48 hours after the nucleofection process was performed in parallel with an experimental condition at 32 °C (cold shock) according to a publication by Gou et al. (2018).

4.1.1 TIDER analysis and clone picking for OCTN2 (N32S) generation

The webtool TIDER served as a platform to investigate the frequency of indels and template-directed HDR events in the nucleofected cell pool by CRISPR/Cas9. This application allows a validation of the on-target region of the nucleofected cell pool prior to the time-consuming clone picking procedure and was exclusively used for OCTN2 (N32S) generation. TIDER evaluation of the standard and 'cold shock' approach revealed an overall Cas9 activity of 62.7% and 76.7%, for 37 °C and 32 °C respectively, and similar distribution of indel sizes (Figure 12 A - B). A one-base pair insertion was detected as the most frequent indel event with 28% per sequence for both approaches. The HDR efficiency was calculated at 19.4% and 32.2% for the 37 °C and the 32 °C approach.

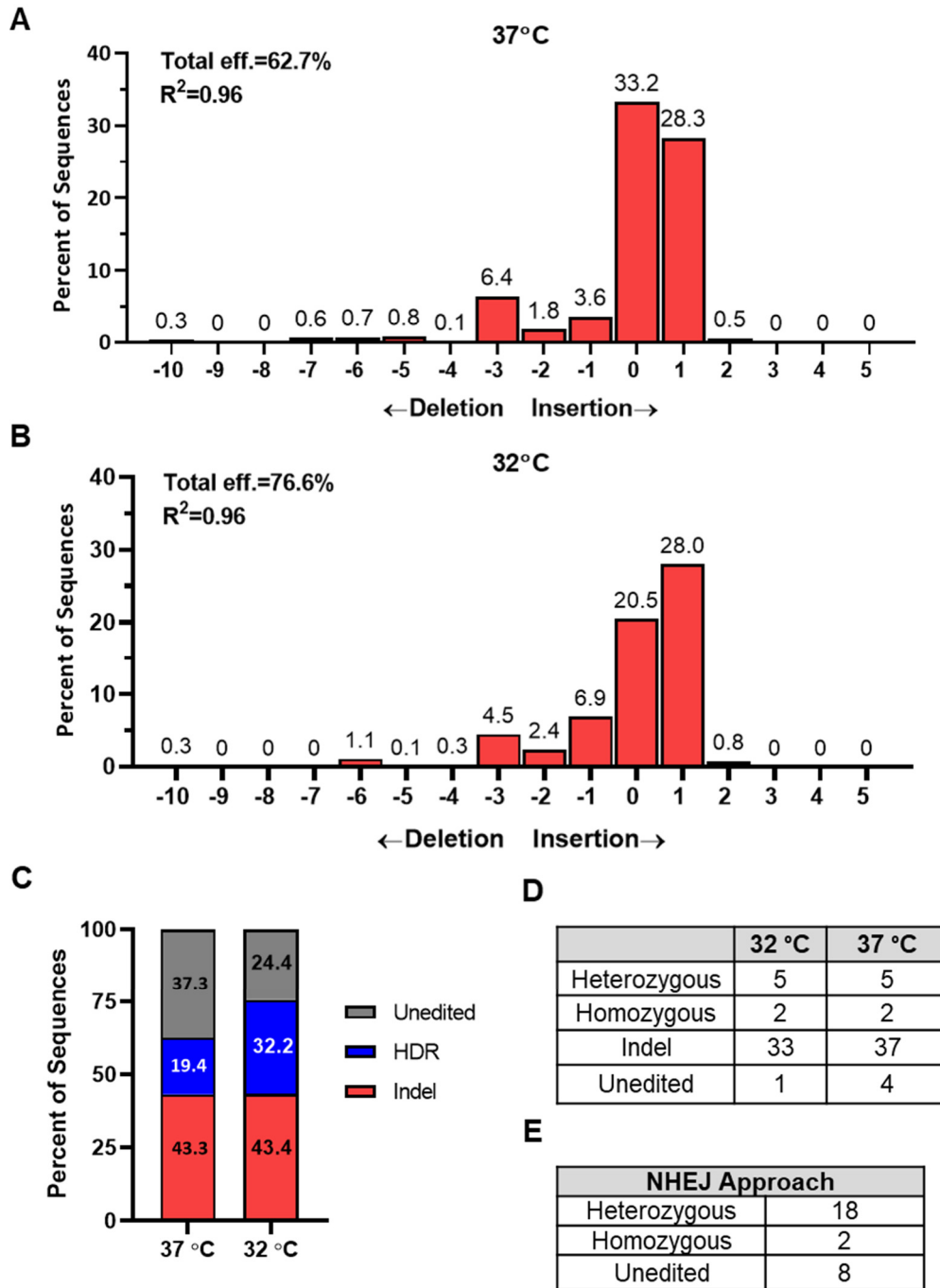


Figure 12: CRISPR TIDER and single clone analysis. A-B: Effect of temperature conditions after transfection on indel-frequencies of the indicated size for the HDR approach. Data originate from cell pool Sanger sequencing of 37 °C and 32 °C approach. R² values represent the goodness-of-fit scores for the TIDER prediction. 'Total eff' indicates the sum of indel- and HDR-frequencies. C: Effect of temperature conditions after transfection on indel, HDR and unedited sequence percentages in stacked bar chart format. D: Number of heterozygous, homozygous, indel containing and unedited clones after clonal expansion of HDR approach. E: Number of heterozygous, homozygous and unedited clones after clonal expansion of NHEJ approach.

According to this prediction of successfully editing, the nucleofected hiPSC were plated at a low density (10-300 hiPSC/cm²), maintained under cell culture conditions, and clonal colonies were picked between day 8 and 10. Copy plates were established for cryopreservation of hiPSC and Sanger sequencing.

This revealed 5 heterozygous and 2 homozygous HDR events for both temperature conditions and 33 versus 37 clones containing indel events. One homozygous clone from the 37 °C approach was used for further cardiac differentiation and functional analysis.

A representative Sanger sequencing trace is depicted in Figure 13 A and shows the OCTN2 wildtype sequence for the control hiPSC line (upper lane) and the heterozygous silent point mutation downstream of the target region (c.277C>T). The middle lane shows the homozygous introduction of the OCTN2 (N32S) c.95A>G point mutation in exon 1 of the *SLC22A5* gene. Due to the large deletion, Sanger sequencing trace of OCTN2 (-/-) could not be aligned within this region.

It has recently been reported that DNA breaks induced by a single-guide RNA/Cas9 can result in kilobase large deletions. These deleted fragments are not detectable by a short-range PCR amplification when occurring monoallelic (Adikusuma et al. 2018; Kosicki et al. 2018). Consequently, a hemizygous clone would mistakenly appear as homozygous in subsequent Sanger sequencing. Nevertheless, the sequenced region in our homozygous OCTN2 (N32S) displayed the presence of the heterozygous silent mutation 182 bp upstream of the target region (c.277C>T). This mutation was already detected in the wildtype sequence and served as evidence for the absence of large fragment deletions in the OCTN2 (N32S) cell line.

4.1.2 Gel electrophoresis for knockout validation of the *SLC22A5* gene

PCR from genomic DNA and subsequent gel electrophoresis were performed to validate a successful knockout in OCTN2 (-/-) hiPSC. A strategy for primer design is schematically depicted in Figure 13 C. Gel electrophoresis showed amplification of products derived from internal primers and primers flanking both CRISPR cutting sites separately in the OCTN2 (+/+) hiPSC line. Amplification with external primers flanking the two cutting sites revealed an expected product size for the OCTN2 (-/-) hiPSC line. Moreover, additional Sanger sequencing of the PCR product amplified by the external primer showed precise end-ligation of the two DNA strands at the predicted gRNA cutting sites (Figure 13 E). The successful knockout was confirmed by quantitative reverse transcription PCR (qPCR) of the *SLC22A5* gene encoding for the OCTN2 transporter (Figure 13 C). Overall, the OCTN2 (-/-) NHEJ approach revealed 2 homozygous and 18 heterozygous OCTN2 (-/-) hiPSC clones.

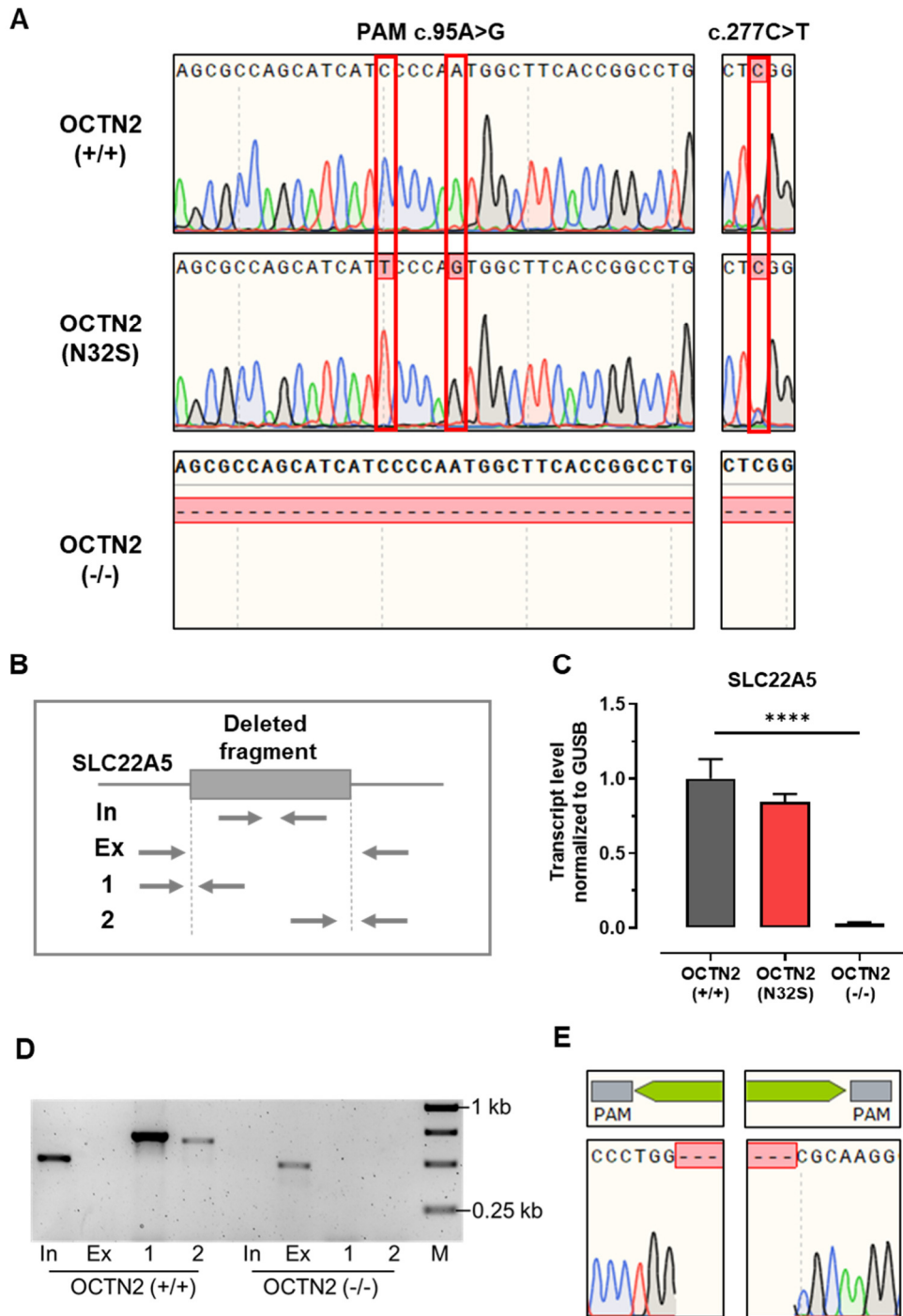


Figure 13: Genotype characterization of CRISPR/Cas9-edited hiPSCs. A: Sanger sequencing traces of OCTN2 (+/+) and derived single cell clones for OCTN2 (N32S) and OCTN2 (-/-) genotypes. The red boxes indicate the silent PAM and c.95A>G mutation and the heterozygous silent c277C>T mutation in the OCTN2 (N32S) clone. B: Schematic overview of primer localization in relation to the deleted fragment in the *SLC22A5* gene. C: qPCR analysis of *SLC22A5* transcripts for all genotypes. D: Gel electrophoresis of PCR products of OCTN2 (+/+) and OCTN2 (-/-) hiPSC clones; M = 1 kb DNA standard marker. E: Sanger sequencing trace of OCTN2 (-/-) PCR product amplified with external primers. Depicted are the binding sites of both gRNA.

4.1.3 Southern blot analysis

The OCTN2 (-/-) approach aimed to introduce a knockout by deleting a large DNA fragment in the *SLC22A5* locus. Since CRISPR-mediated gene editing can cause unwanted DNA rearrangements, like the reintegration of inverted repeats originating from double-stranded DNA fragments (Skryabin et al. 2020), Southern blot was performed to validate the integrity of the edited locus.

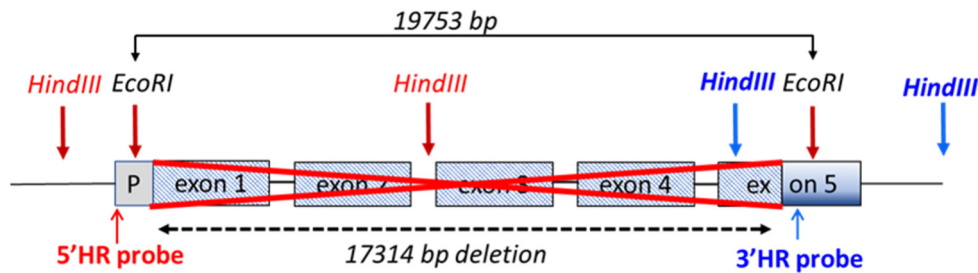


Figure 14: Schematic presentation of Southern blot probe hybridization. HindIII and EcoRI were used for enzymatic digestion prior to probe hybridization.

Figure 14 displays the predicted cutting sites for the two restriction endonucleases HindIII and EcoRI of the *SLC22A5* gene area which is targeted by the OCTN2 (-/-) NHEJ CRISPR/Cas9 approach. Table 10 shows the predicted fragment size for both restriction endonuclease digestion and detection with a 5'HR and 3'HR probe. The unedited OCTN2 (+/+), the heterozygously edited OCTN2 (+/-), and homozygously edited OCTN2 (-/-) hiPSC clones were analyzed in this experiment. Figure 15 shows the Southern blot results. HindIII digestion and hybridization with the 5' probe revealed the expected DNA fragment sizes of 3.2-kb for OCTN2 (-/-) and an 8.2-kb DNA fragment for OCTN2 (+/+), while the heterozygous clone OCTN2 (+/-) showed both fragments.

Table 10 : Fragment size prediction of 5' HR and 3'HR probe after HindIII or EcoRI restriction enzyme digest

	5'HR probe		3'HR probe	
	OCTN2 (+/+)	OCTN2 (-/-)	OCTN2 (+/+)	OCTN2 (-/-)
HindIII	8292 bp	3264 bp	2434 bp	3264 bp
EcoRI	19753 bp	2439 bp	19753 bp	2439 bp

4.1.4 Karyotype analysis

After CRISPR/Cas9 experiments and verification of successful genetic engineering by PCR, Sanger sequencing, and Southern blot, master and working cell banks were established and cryopreserved from the three hiPSC lines used for this study (OCTN2 (+/+), OCTN2 (N32S), OCTN2 (-/-)). As karyotypic abnormalities can accumulate during extended cell culture and genome editing of hiPSCs, the karyotype of these hiPSC lines was investigated by the Nanostring nCounter human karyotype assay. Figure 16 depicts the two copy numbers for all autosomes and X chromosomes in all hiPSC lines. The absence of the gonosomal Y chromosome confirms that this line derives from a female volunteer. Further quality control analysis of this isogenic OCTN2 hiPSC set included mycoplasma PCR screening (not shown) and FACS analysis of SSEA3 pluripotency marker (Supplement, Figure S2).

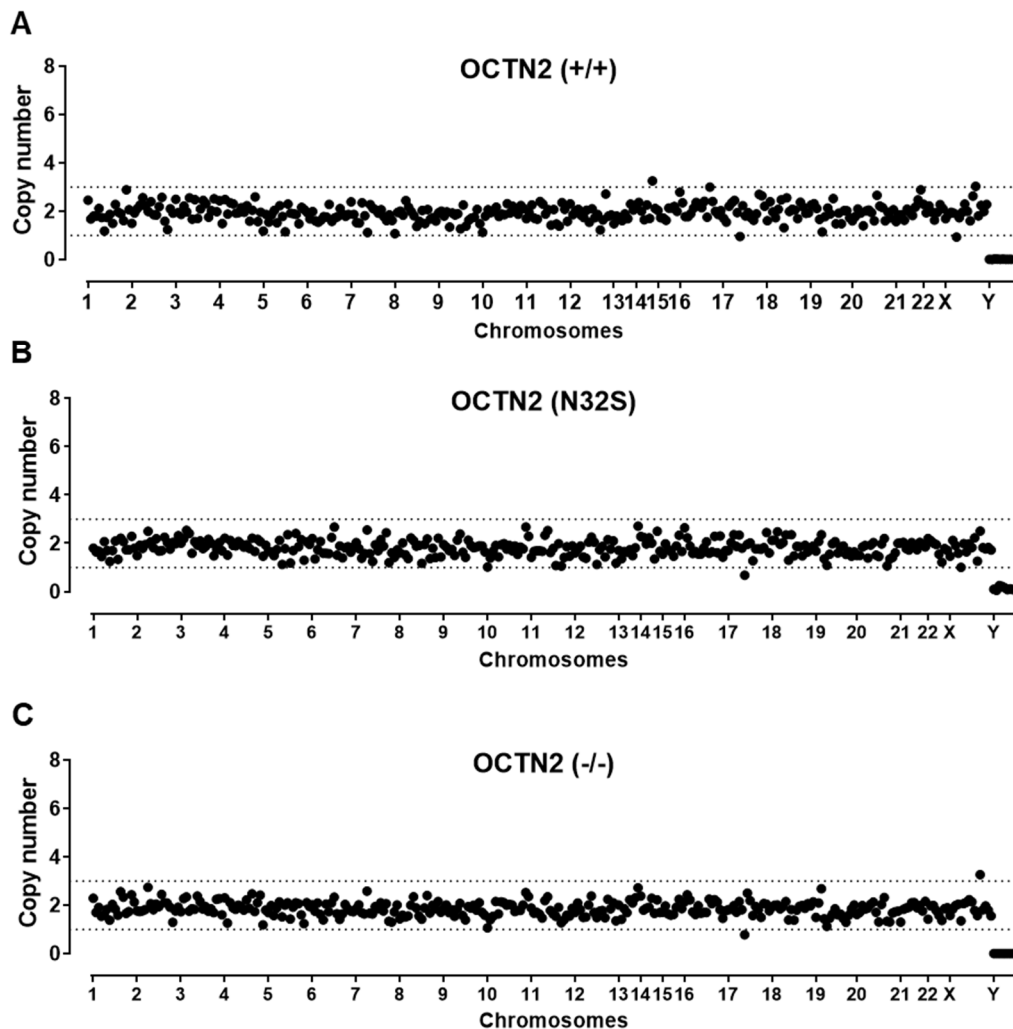


Figure 16: Nanostring karyotype analysis. NanoString nCounter human karyotype analysis revealed regular female karyotypes after CRISPR/Cas9 genome editing and hiPSC expansion. Used was genomic DNA derived from hiPSC master cell bank samples from A: OCTN2 (+/+), B: OCTN2 (N32S) and C: OCTN2 (-/-).

4.2 Cardiac differentiation

HiPSCs were thawed from cryopreserved working cell banks, expanded in 6-well plates and T75 cell culture flasks and embryoid bodies (EB) were formed from dissociated hiPSCs in spinner flasks. With respect to these two initial steps of the differentiation protocol, neither hiPSC expansion nor embryoid body (EB) formation was influenced by the OCTN2 genotype. As a next step, cardiomyocytes (hiPSC-CM) were differentiated in T175-flasks with a three-stage growth factor-based cardiac differentiation protocol. Spontaneous beating of differentiating EBs was observed between day 10 and 12. As visualized in Figure 17, all genotypes developed stable EBs during this stage of differentiation. However, EBs from OCTN2-defective genotypes often appeared morphologically more heterogeneous and had a higher tendency to aggregate. At day 17, beating EBs were dissociated, and hiPSC-CM were counted in Neubauer chambers. 1.0×10^6 hiPSC-CM per differentiation were used for troponin T FACS analysis. The remaining hiPSC-CM were either cryo-preserved or processed directly for functional analysis.

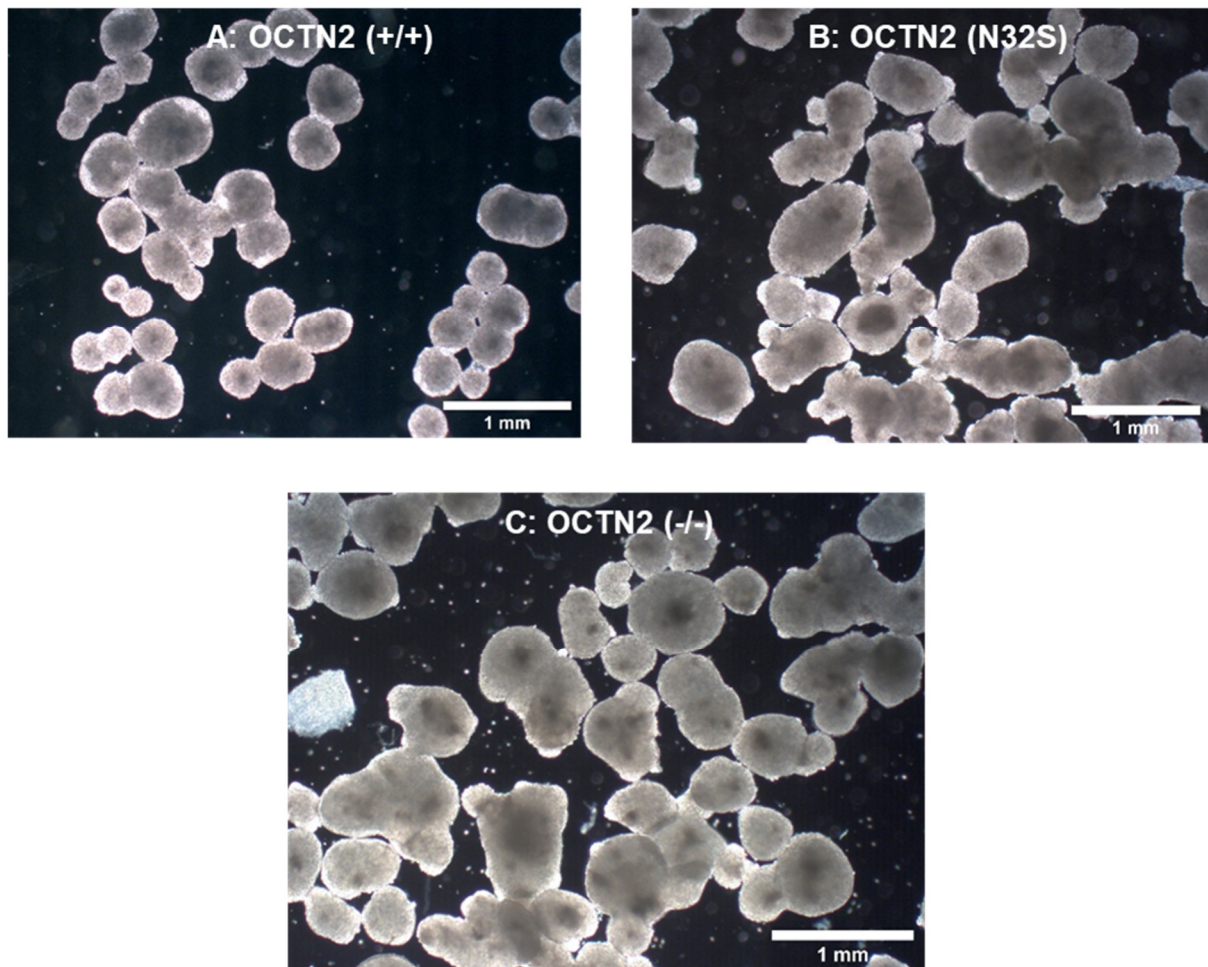


Figure 17: EBs on day 19 of cardiac differentiation. All cell lines formed stable EBs which started to beat between day 10 and 12 of the differentiation procedure. EBs of OCTN2-defective genotypes often revealed a more heterogeneous morphology.

Figure 18 A shows the results for cardiac differentiation of the three OCTN2 hiPSC lines. No significant difference could be observed in the percentage of cardiac troponin T (cTnT) positive cells (OCTN2 (+/+) $87.5 \pm 2.5\%$, $n=10$ differentiations; OCTN2 (N32S): $84.1 \pm 5.0\%$, $n=10$ differentiations; OCTN2 (-/-): $86.2 \pm 8.2\%$, $n=9$ differentiations). Cardiac differentiation efficiency was calculated by dividing the number of output-hiPSC-CM by the number of input-hiPSC cells. This calculation revealed a differentiation efficiency of $79.0 \pm 10.0\%$ for OCTN2 (+/+) and was significantly higher than OCTN2 (N32S) and OCTN2 (-/-), which displayed efficiencies of $23.5 \pm 10.5\%$ and $19.4 \pm 2.8\%$, respectively (Figure 18 B).

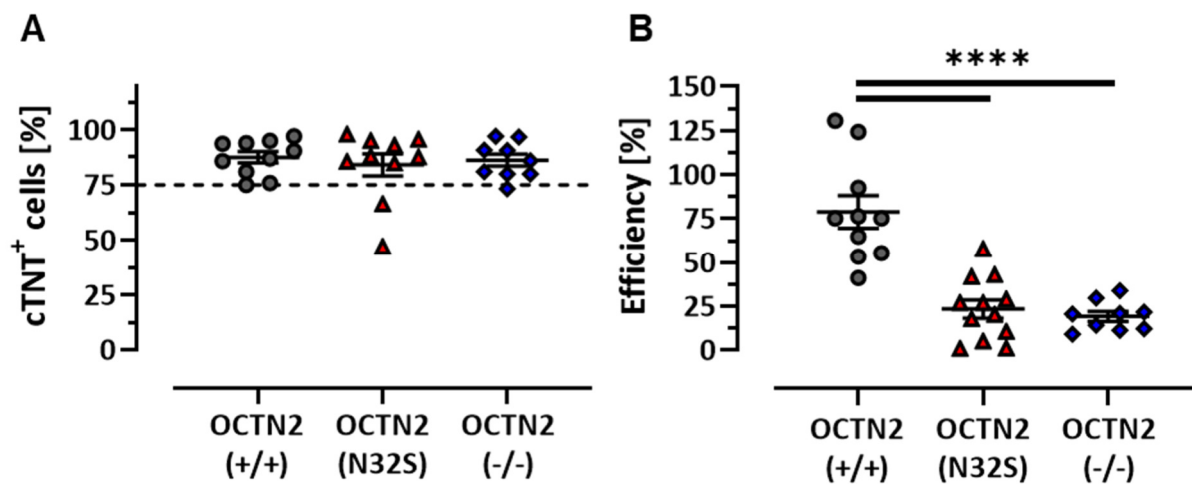


Figure 18: Characterization of cardiomyocyte differentiations. A: FACS analysis of cardiac troponin T positive cells in the differentiated cell population. Dashed line (75%) indicates threshold value for EHT generation. B: Differentiation efficiency calculated as the ratio of number of differentiated cells divided by the number of input hiPSCs. OCTN2 (+/+): $n=10$, OCTN2 (N32S): $n=10$, OCTN2 (-/-): $n=9$ differentiation batches, data are expressed as mean \pm SEM, one-way ANOVA plus Bonferroni's post-test for multiple comparisons, **** $p < 0.0001$.

4.3 Characterization of the contractile phenotype in EHT format

4.3.1 EHT development under baseline conditions

EHTs were generated from hiPSC-CM of the three OCTN2 genotypes and were maintained under established cell culture conditions. Video-optical recording of EHT contraction was performed for the entire time frame of development starting on day 7. Automated analysis of EHT recording revealed quantitative analysis of contractile parameters like force, beating frequency, contraction and relaxation time, resting length and beating regularity (RR-Scatter).

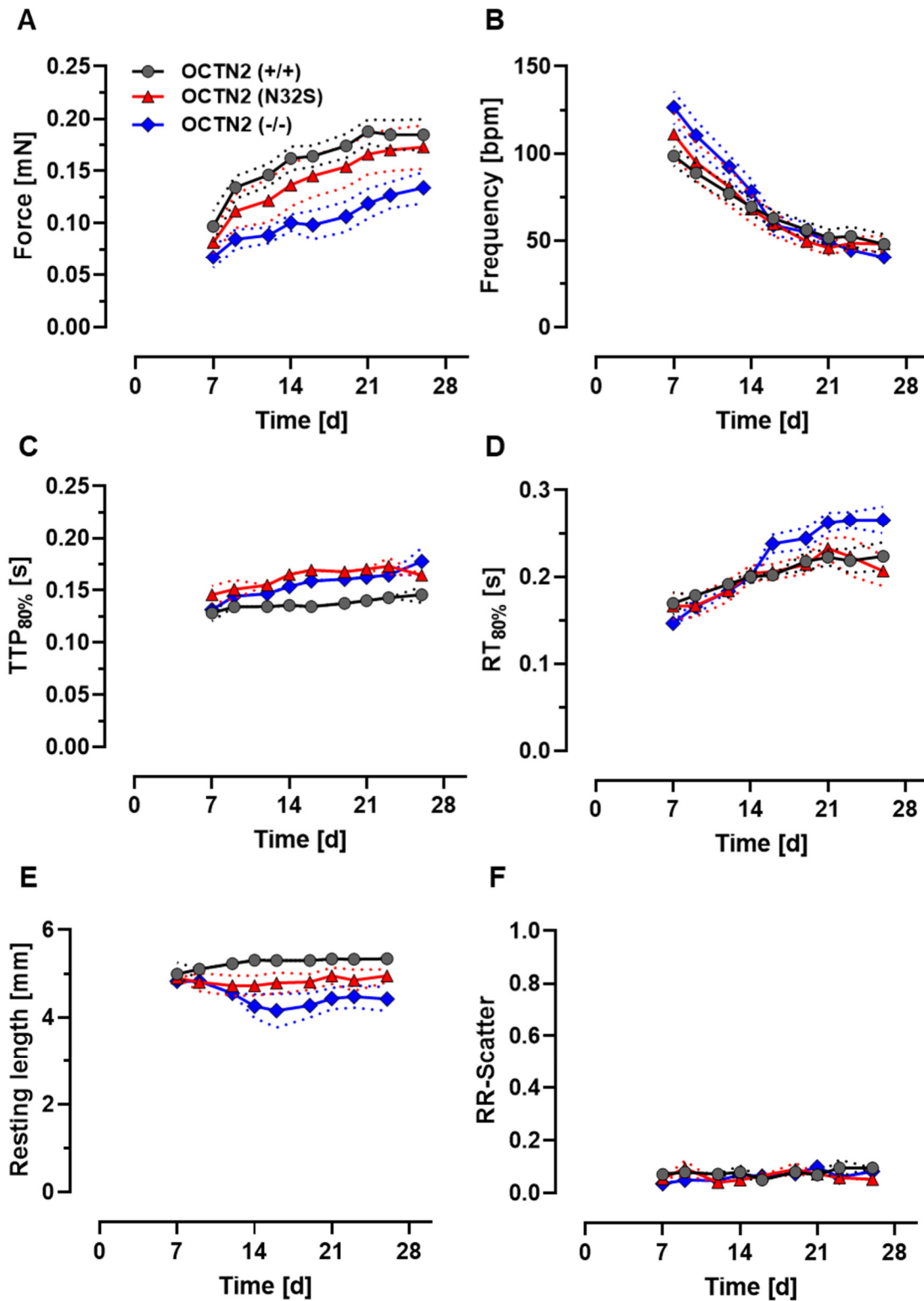


Figure 19: EHT development over time. A-F: Effect of OCTN2 genotype on force, frequency, contraction time (TTP_{80%}), relaxation time (RT_{80%}), resting length and RR-Scatter (parameter of irregularity) of spontaneous beating EHTs between day 7 and day 26. OCTN2 (+/+): n=152 EHTs from 9 batches, OCTN2 (N32S): n=108 EHTs from 7 batches, OCTN2 (-/-): n=91 EHTs from 5 batches, data are expressed as mean \pm SEM of mean from EHTs of each individual batch.

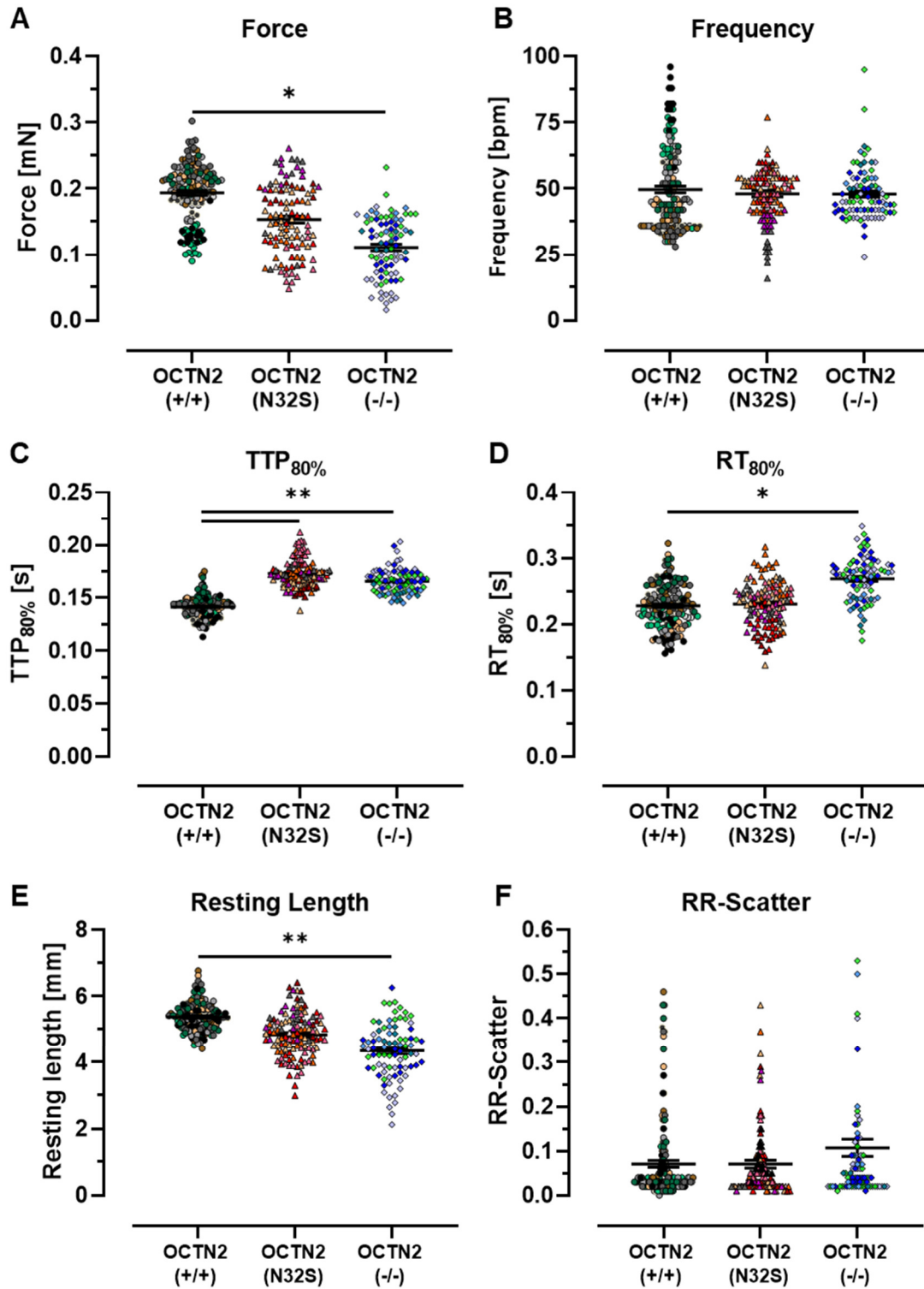


Figure 20: A-F: Effect of OCTN2 genotype on contractile parameters of spontaneous beating EHTs on day 21. OCTN2 (+/+): n=153 EHTs from 9 batches, OCTN2 (N32S): n=108 EHTs from 7 batches, OCTN2 (-/-): n=91 EHTs from 5 batches. Nested one-way ANOVA plus Bonferroni's post-test for multiple comparisons, * $p < 0.05$, ** $p < 0.01$, *** $p < 0.001$, **** $p < 0.0001$. One data point represents one independent EHT. One color represents one independent differentiation batch. Data are expressed as mean \pm SEM.

Additionally, the parameter resting length, demonstrating the maximal length of the EHT during relaxation and progressive shortening of EHTs, was analyzed. 9, 7 and 5 independent differentiation batches were used to generate EHTs for OCTN2 (+/+), OCTN2 (N32S) and OCTN2 (-/-), respectively. Spontaneous contractions of individual hiPSC-CM were observed microscopically around day 3. EHTs showed remodeling of the extracellular matrix and developed coherent beating activity within the first 5 days after EHT generation. The EHT development of different parameters is depicted in Figure 19. EHTs from all OCTN2 genotypes displayed a change in contractile parameters over time until day 21 and reached a plateau thereafter. OCTN2 (-/-) showed a lower force, a higher contraction time and shorter resting length for the entire recording time. In contrast, OCTN2 (N32S) only displayed a similar trend with respect to all mentioned parameters, but only the contraction time was significantly higher. Beating frequency was higher for OCTN2 (N32S) and OCTN2 (-/-) during the initial phase of development, but not thereafter.

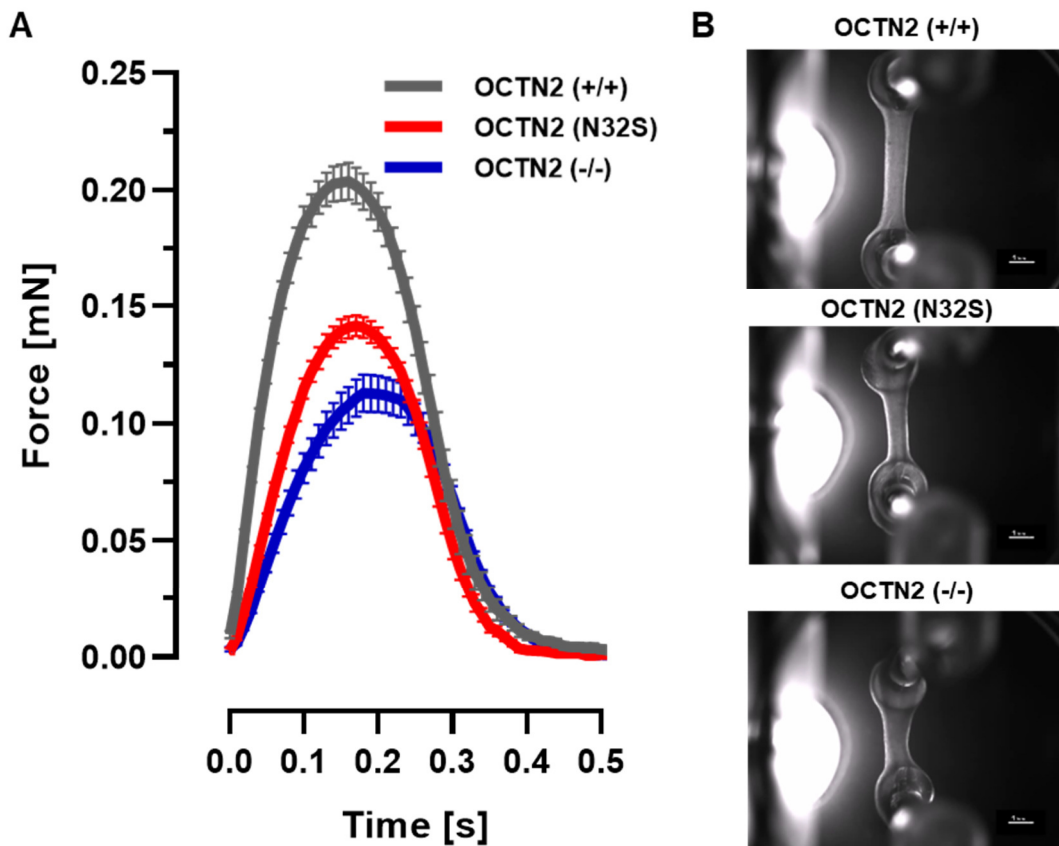


Figure 21: EHT contraction analysis. A: Representative average EHT contraction peaks of OCTN2 (+/+), OCTN2 (N32S) and OCTN2 (-/-). EHTs were electrically paced at 1.5 Hz in standard EHT medium, n=9-14 EHTs from one batch. B: Representative video-optical EHT images, scale bar = 1 mm.

Relaxation time was longer only for OCTN2 (-/-) for the last 2 weeks of development. No difference could be detected for the RR scatter as a surrogate for arrhythmic beating.

To compare contractile parameters of the OCTN2 genotypes, values of day 21 were chosen as a representative parameter (Figure 20 A - F). This analysis revealed lower force and a reduced resting length for OCTN2 (-/-) compared to OCTN2 (+/+) (OCTN2 (+/+): 0.194 ± 0.004 mN, $n=153$ EHTs; OCTN2 (N32S): 0.16 ± 0.01 mN, $n=108$ EHTs; OCTN2 (-/-): 0.11 ± 0.01 mN, $n=91$ EHTs). A similar trend for both parameters was observed for OCTN2 (N32S). However, this did not reach statistical significance. Furthermore, both OCTN2-defective genotypes exhibited a higher contraction time, while only OCTN2 (-/-) additionally showed a higher relaxation time. Figure 21 depicts a representative average contraction peak and video-optical EHT images from each genotype.

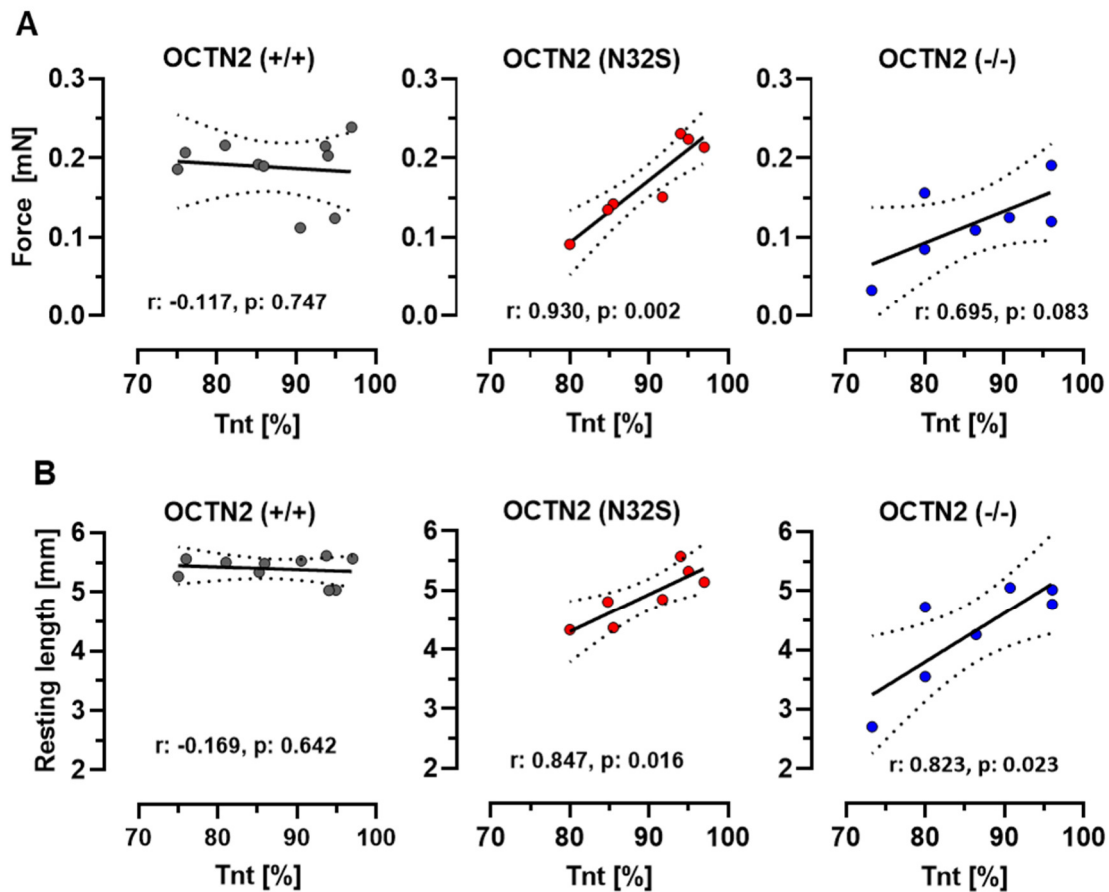


Figure 22: Pearson correlation of A: Force and B: Resting length of EHTs with percentage of cTNT-positive input cells for EHT generation. OCTN2 (+/+): $n=10$; OCTN2 (N32S): $n=7$ and OCTN2 (-/-): $n=7$ differentiation batches. Each replicate represents the mean value of 7 to 20 EHTs for the specific differentiation batch.

Importantly, unlike the isogenic control, force and resting length of both OCTN2-defective genotypes showed a positive correlation with the cardiomyocyte purity of the input cell population as defined in chapter 4.2 (Figure 22). This result implicates an important role of non-cardiomyocytes in OCTN2-defective cell lines which may impact on the contractile EHT phenotype.

4.3.2 EHT force development in fatty acid medium

The most important role of carnitine is the transfer of LCFAs across the mitochondrial membrane for subsequent beta-oxidation and ATP generation (Longo et al. 2006). To demonstrate a LCFA metabolism deficit, force development was analyzed in a medium containing only linoleic and oleic acid as energy substrates. When EHTs cultivated under control conditions reached the force plateau, the standard culture medium was changed to fatty acid medium and EHTs were cultured for four days. OCTN2 (+/+) EHTs revealed stable force development. In contrast, OCTN2-defective EHTs showed a decline in force that became significant after 96 hours of culture (Figure 23). This result indicates impaired LCFA metabolism of OCTN2-defective EHTs.

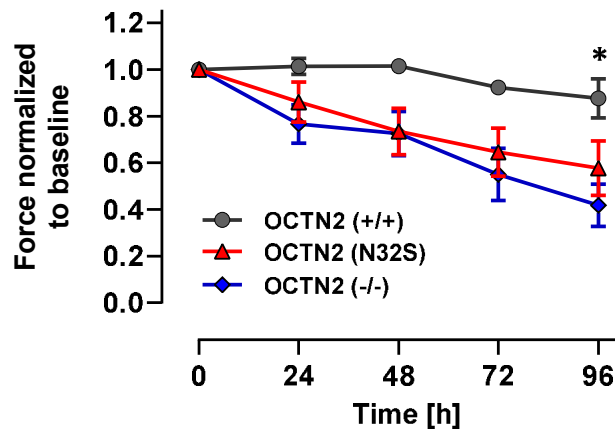


Figure 23: EHT force development in fatty acid medium. Serum-free cell culture medium was supplemented with 50 μ M carnitine, linoleic acid- and oleic acid-albumin. Data are normalized to baseline force. OCTN2 (+/+): n=11 EHTs from 2 batches, OCTN2 (N32S): n=11 EHTs from 2 batches, OCTN2 (-/-): n=12 EHTs from 2 batches. Two-way ANOVA vs OCTN2 (+/+) plus Bonferroni's post-test for multiple comparisons, * $p < 0.05$. Data are expressed as mean \pm SEM.

4.4 Glucose consumption and lactate production

PCD patients exhibit a high reliance on glucose as a primary substrate for energy production (Longo et al. 2006). In order to analyze glucose consumption and lactate production, EHTs from the three OCTN2 genotypes were cultured in standard EHT culture medium, and glucose and lactate cell culture medium concentrations were measured before and after 24 hours of incubation. The delta in concentration was calculated for glucose consumption and lactate production (Figure 24 A - B). In addition, the ratio of these parameters served as a surrogate for anaerobic glucose metabolism (Figure 24 D).

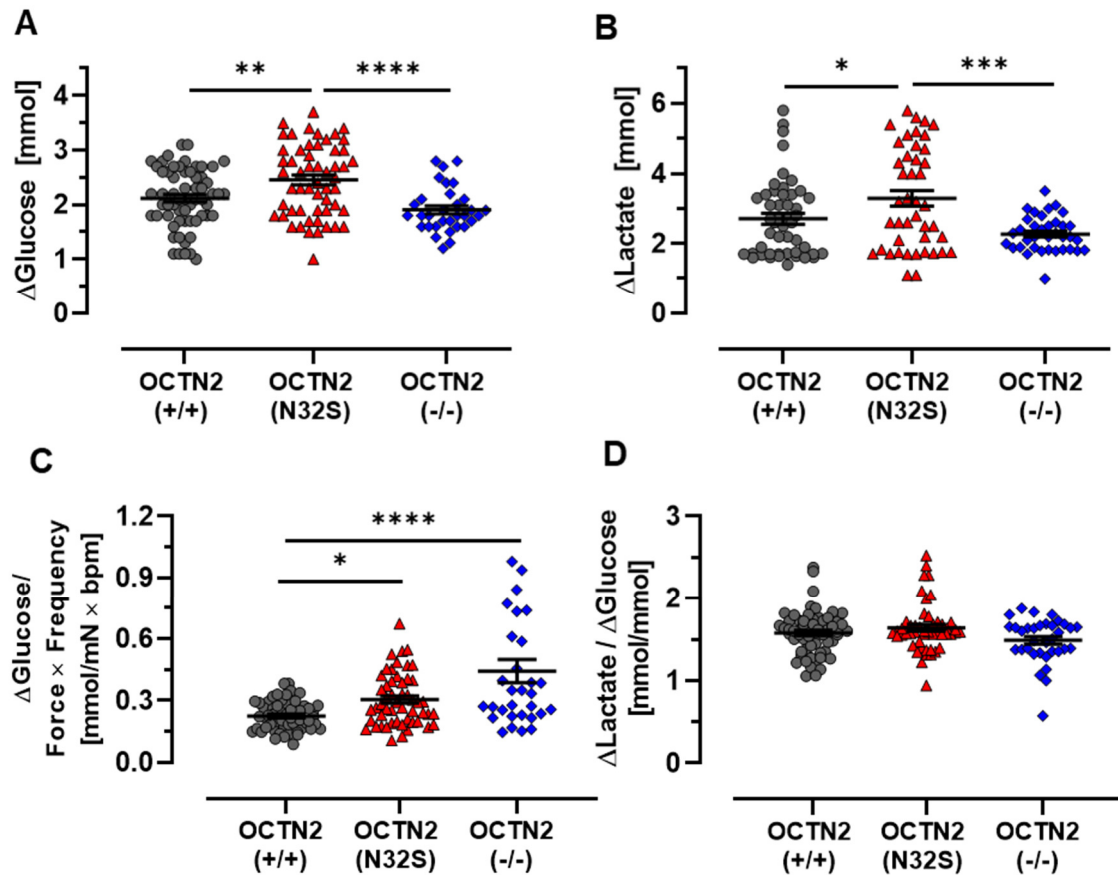


Figure 24. Glucose and lactate measurements. Difference in A: Glucose and B: Lactate concentration of EHT culture media (1.5 mL; Δ Glucose = Glucose concentration at baseline minus glucose concentration after 24 h of incubation, Δ Lactate = Lactate concentration at baseline minus lactate concentration after 24 h of incubation). C: Δ Glucose divided by product of individual spontaneous beating frequency \times force. D: Δ Lactate of EHT culture media divided by Δ Glucose. OCTN2 (+/+): n=59 EHTs from 5 batches, OCTN2 (N32S): n=51 EHTs from 4 batches, OCTN2 (-/-): n=28 EHTs from 4 batches. One-way ANOVA plus Bonferroni's post-test for multiple comparisons, * $p < 0.05$, ** $p < 0.01$, *** $p < 0.001$, **** $p < 0.0001$. One data point represents one independent EHT. Data are expressed as mean \pm SEM.

Delta glucose was higher for OCTN2 (N32S) compared to OCTN2 (+/+), but not OCTN2 (-/-). Similar to glucose measurements, delta lactate values were only higher for OCTN2 (N32S) compared to OCTN2 (+/+).

Data for mean force development and mean frequency for the specific EHTs, as analyzed by automated video-optical recording on the day of EHT medium change, were calculated as a surrogate for EHT workload (Figure 24 C). The ratio of delta glucose/EHT workload revealed a higher glucose consumption per workload for OCTN2 (N32S) and OCTN2 (-/-) compared to OCTN2 (+/+) (OCTN2 (+/+): 0.23 ± 0.01 mM/bpm \times mN; OCTN2 (N32S): 0.3 ± 0.1 mM; OCTN2 (-/-): 0.4 ± 0.1 mM). The delta lactate/delta glucose ratio showed no difference, indicating that glucose consumption and lactate production are linked in this PCD model (Figure 24 D).

4.5 EHT carnitine supplementation – contractile analysis

Since carnitine can also enter the cell via low-affinity transporter, high dose carnitine supplementation therapy is the treatment of choice in PCD patients (Longo et al. 2016). To evaluate the effect of carnitine media supplementation on the phenotype of OCTN2-defective EHTs, EHT media was supplemented with carnitine (2 mM) for the entire time frame of development, and video-optical recording of EHT contractility and automated analysis of contraction parameter were performed. The effect of carnitine supplementation was analyzed per OCTN2 genotype for the entire recording time between day 7 and 42. In addition, the contractile parameters for the last day of recording were analyzed separately as an endpoint analysis.

EHT force values for all three OCTN2 genotypes were higher when supplemented with carnitine for the entire course of development (Figure 25 A - C). However, this positive inotropic effect only reached statistical significance at later time points of cultivation. This was also demonstrated by analysing the last day of EHT contractility recording (Figure 25 D; mean effect of carnitine supplementation on force: OCTN2 (+/+): $+13.0 \pm 4.5\%$; OCTN2 (N32S): $+16.0 \pm 5.0\%$; OCTN2 (-/-): $+13.0 \pm 2.8\%$). Concurrently, carnitine supplementation led to an increase in relaxation time for all genotypes. Of note, the effect was considerably high for OCTN2 (-/-) under spontaneous beating ($+214.7 \pm 0.8\%$, Figure 28 D) but not under electrically paced conditions ($+17.0\%$, Figure 30). Furthermore, carnitine supplementation had no significant effect on the spontaneous beating frequency, and a minor effect on contracting time and resting length in all genotypes.

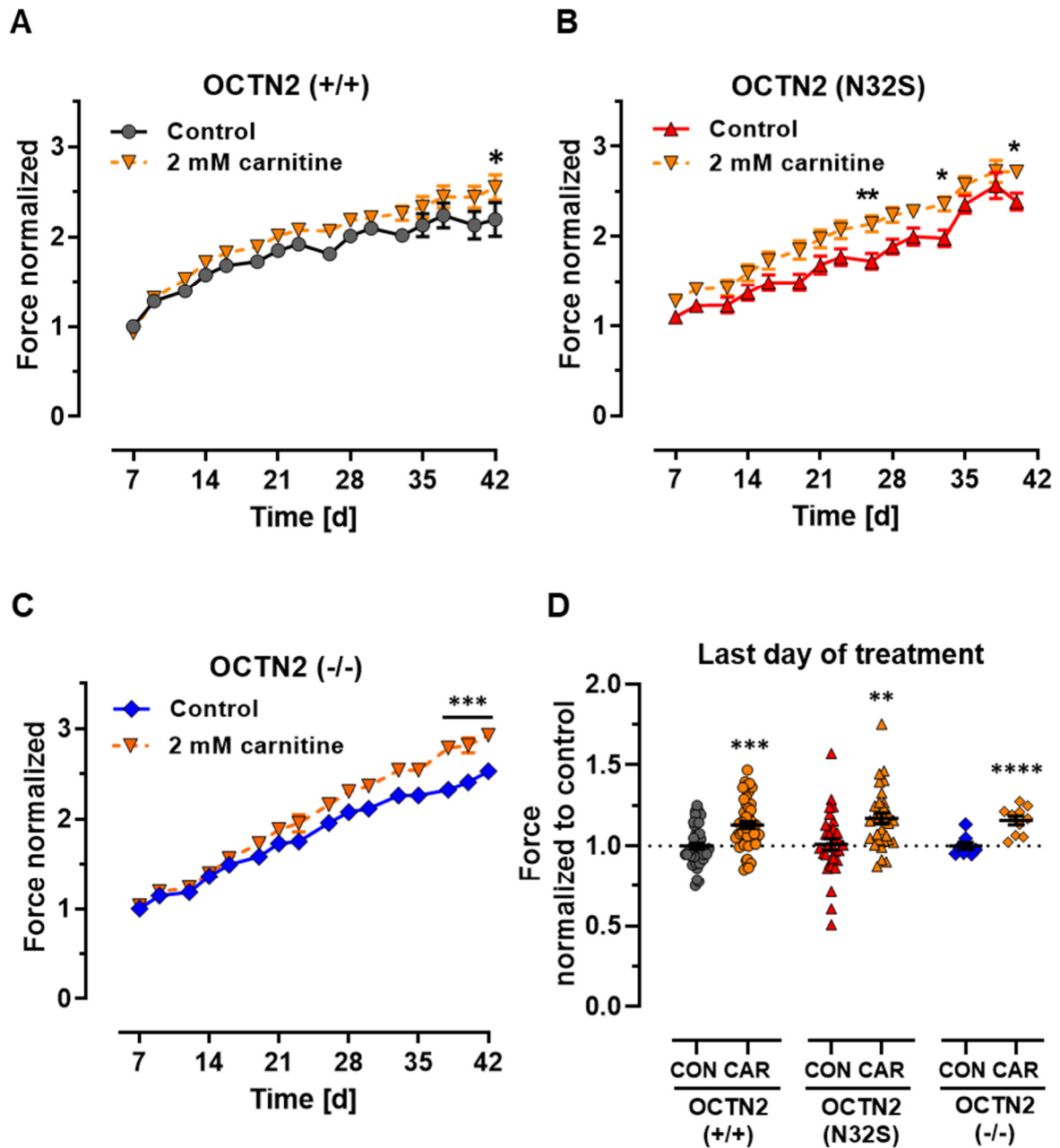


Figure 25: Effect of carnitine supplementation on force of spontaneous beating EHTs. A-C: EHT development between day 7 and day 42. Values were normalized to day 7 of untreated control. Two-way ANOVA plus Bonferroni's post-test for multiple comparisons, * $p < 0.05$, ** $p < 0.01$, *** $p < 0.001$. D: Analysis of force of spontaneous beating EHTs on the last day of carnitine supplementation (Day 33-42). Values were normalized to last day of treatment of untreated control. Student's t-test vs CON, ** $p < 0.01$, *** $p < 0.001$, **** $p < 0.0001$. OCTN2 (+/+) control: $n = 54$ EHTs from 4 batches. OCTN2 (+/+) + carnitine (2 mM): $n = 49$ EHTs from 4 batches. OCTN2 (N32S) control: $n = 36$ EHTs from 3 batches, OCTN2 (N32S) + carnitine (2 mM): $n = 33$ EHTs from 3 batches, OCTN2 (-/-) control: $n = 9$ EHTs from 1 batch, OCTN2 (-/-) + carnitine (2 mM): $n = 9$ EHTs from 1 batch. Data are expressed as mean \pm SEM.

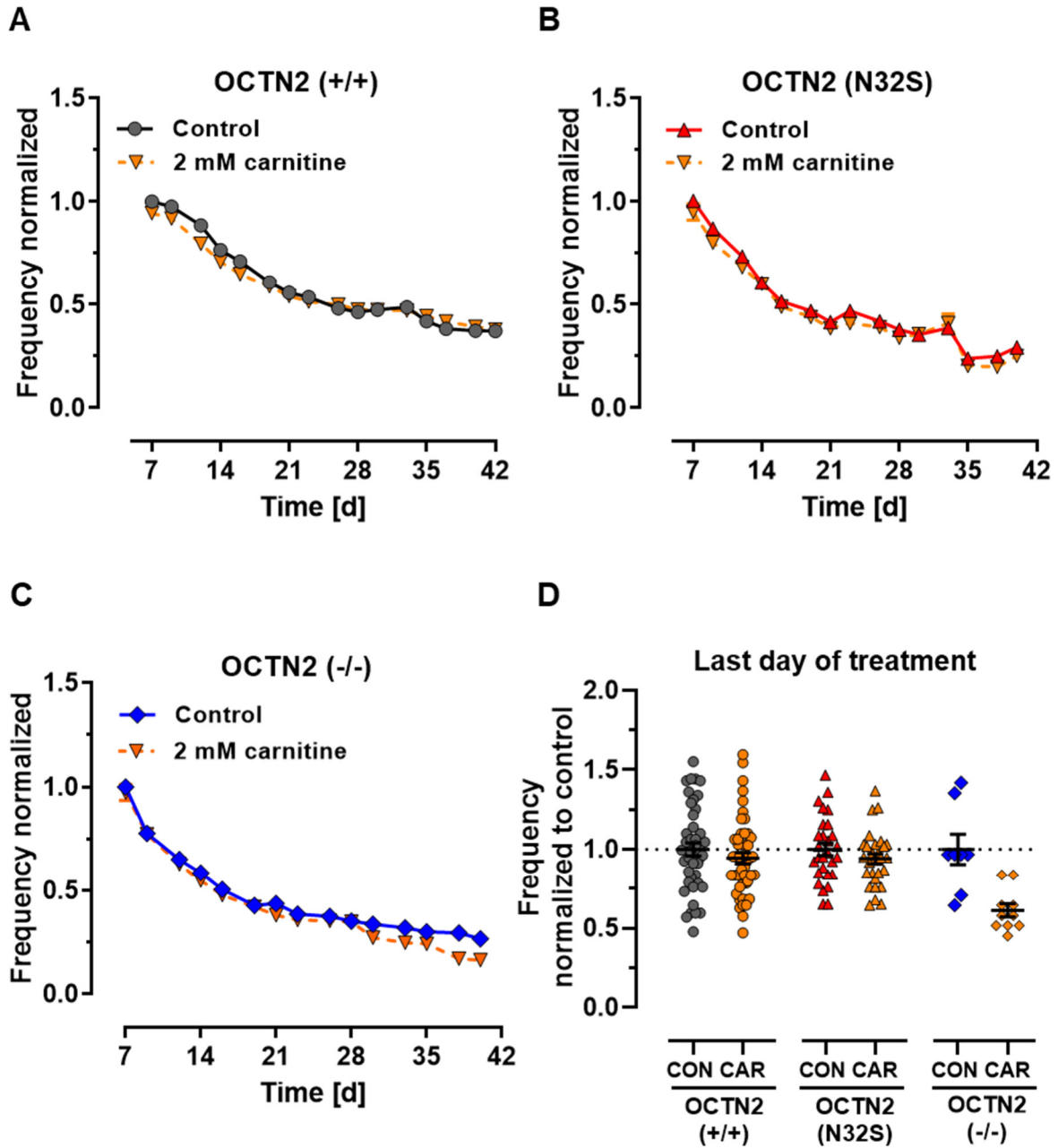


Figure 26: Effect of carnitine supplementation on frequency of spontaneous beating EHTs. A-C: EHT development between day 7 and day 42. Values were normalized to day 7 of untreated control. Two-way ANOVA plus Bonferroni's post-test for multiple comparisons. D: Analysis of frequency of spontaneous beating EHTs on the last day of carnitine supplementation (Day 33-42). Values were normalized to last day of supplementation of untreated control. Student's t-test vs CON. OCTN2 (+/+) control: n=54 EHTs from 4 batches. OCTN2 (+/+) + carnitine (2 mM): n=49 EHTs from 4 batches. OCTN2 (N32S) control: n=36 EHTs from 3 batches, OCTN2 (N32S) + carnitine (2 mM): n=33 EHTs from 3 batches, OCTN2 (-/-) control: n=9 EHTs from 1 batch, OCTN2 (-/-) + carnitine (2 mM): n=9 EHTs from 1 batch. Data are expressed as mean±SEM.

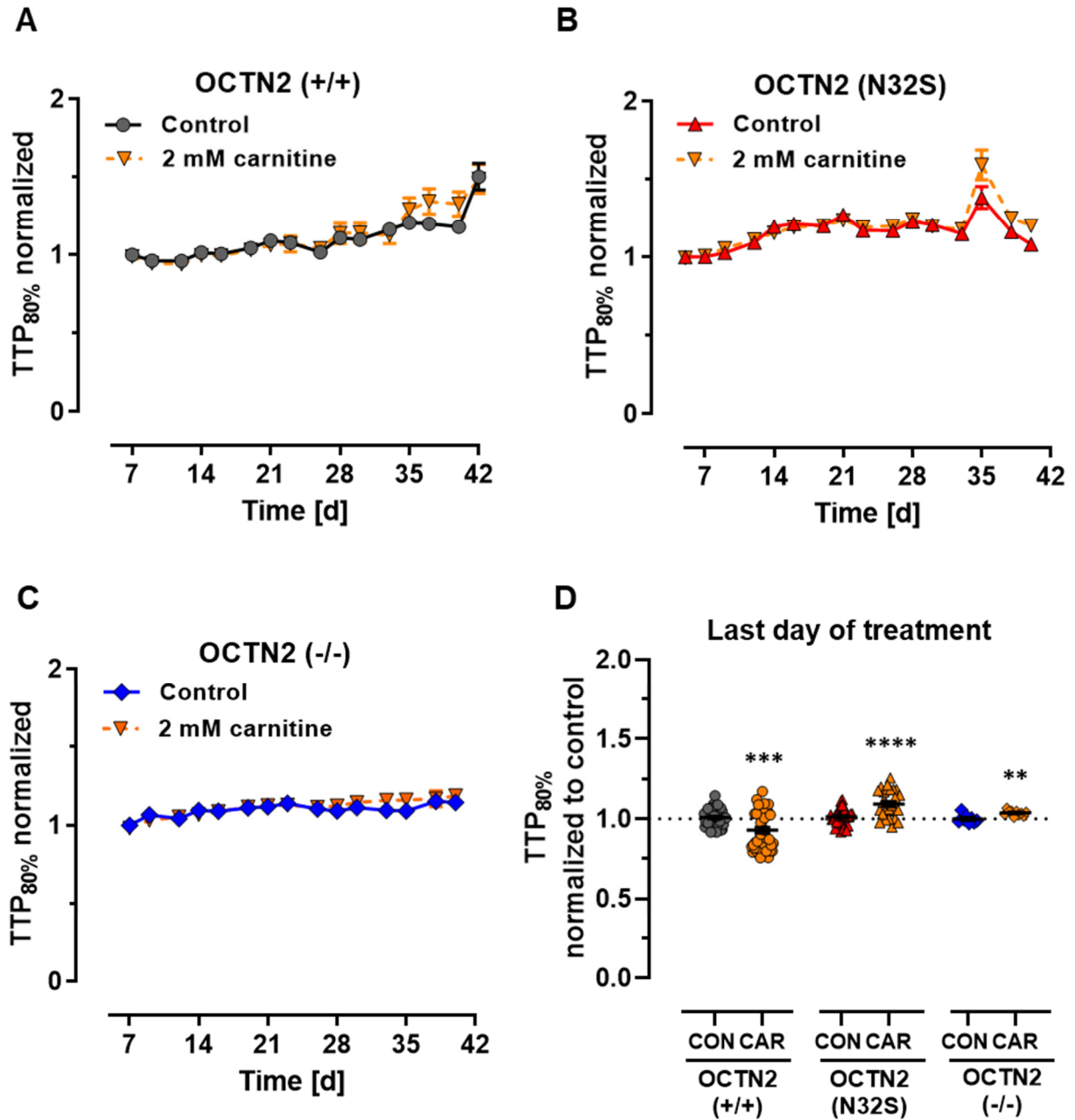


Figure 27: Effect of carnitine supplementation on contraction time (TTP80) of spontaneous beating EHTs. A-C: EHT development between day 7 and day 42. Values were normalized to day 7 of untreated control. Two-way ANOVA plus Bonferroni's post-test for multiple comparisons. D: Analysis of contraction time of spontaneous beating EHTs on the last day of carnitine supplementation (Day 33-42). Values were normalized to last day of supplementation of untreated control. Student's t-test vs CON, ** $p < 0.01$, *** $p < 0.001$, **** $p < 0.0001$. OCTN2 (+/+) control: $n = 54$ EHTs from 4 batches. OCTN2 (+/+) + carnitine (2 mM): $n = 49$ EHTs from 4 batches. OCTN2 (N32S) control: $n = 36$ EHTs from 3 batches, OCTN2 (N32S) + carnitine (2 mM): $n = 33$ EHTs from 3 batches, OCTN2 (-/-) control: $n = 9$ EHTs from 1 batch, OCTN2 (-/-) + carnitine (2 mM): $n = 9$ EHTs from 1 batch. Data are expressed as mean \pm SEM.

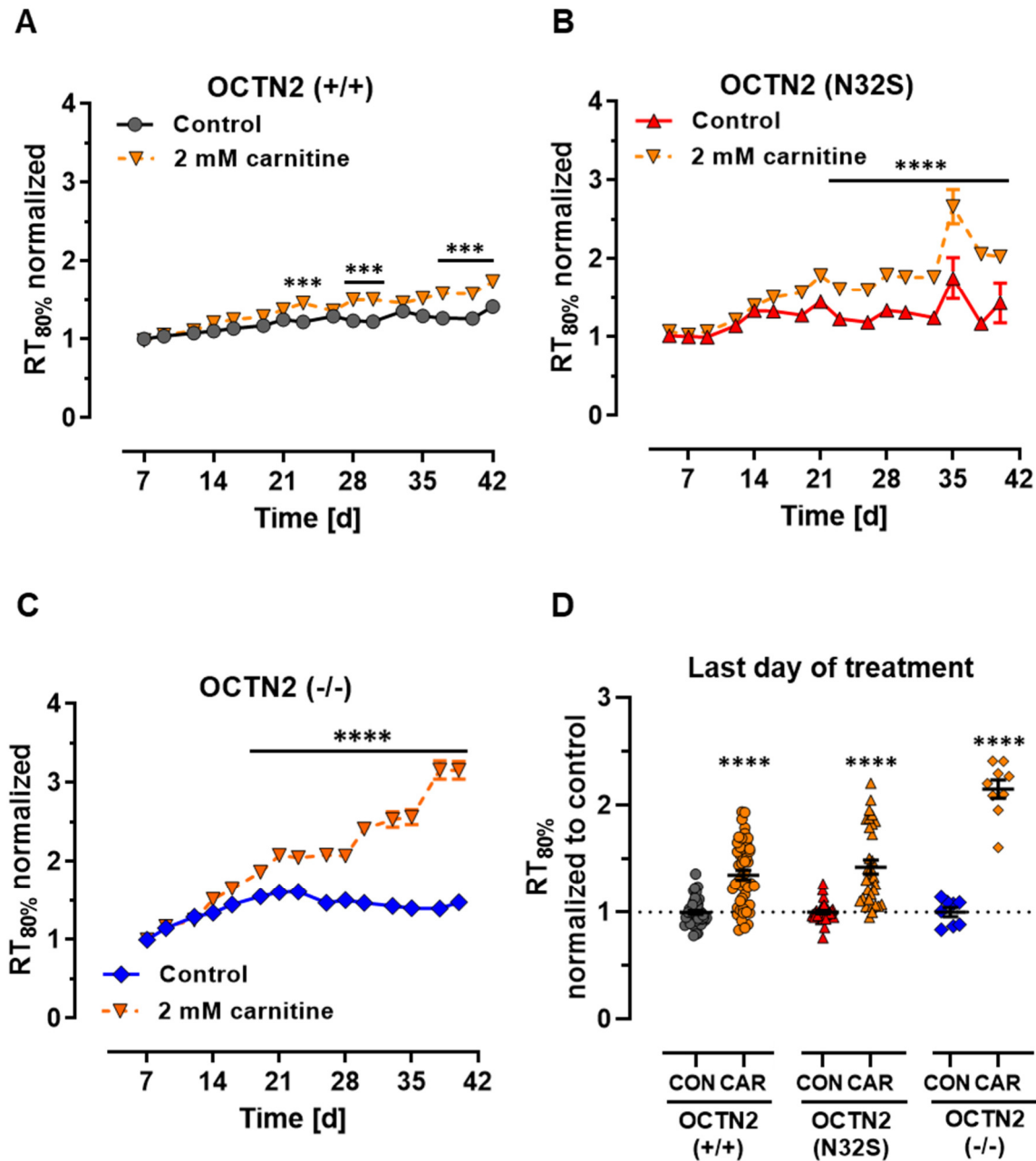


Figure 28: Effect of carnitine supplementation on relaxation time (RT₈₀) of spontaneous beating EHTs. A-C: EHT development between day 7 and day 42. Values were normalized to day 7 of untreated control. Two-way ANOVA plus Bonferroni's post-test for multiple comparisons, *** $p < 0.001$, **** $p < 0.0001$. D: Analysis of relaxation time of spontaneous beating EHTs on the last day of carnitine supplementation (Day 33-42). Values were normalized to last day of treatment of untreated control. Student's t-test vs CON, ** $p < 0.01$, *** $p < 0.001$, **** $p < 0.0001$. OCTN2 (+/+) control: $n = 54$ EHTs from 4 batches. OCTN2 (+/+) + carnitine (2 mM): $n = 49$ EHTs from 4 batches. OCTN2 (N32S) control: $n = 36$ EHTs from 3 batches, OCTN2 (N32S) + carnitine (2 mM): $n = 33$ EHTs from 3 batches, OCTN2 (-/-) control: $n = 9$ EHTs from 1 batch, OCTN2 (-/-) + carnitine (2 mM): $n = 9$ EHTs from 1 batch. Data are expressed as mean \pm SEM.

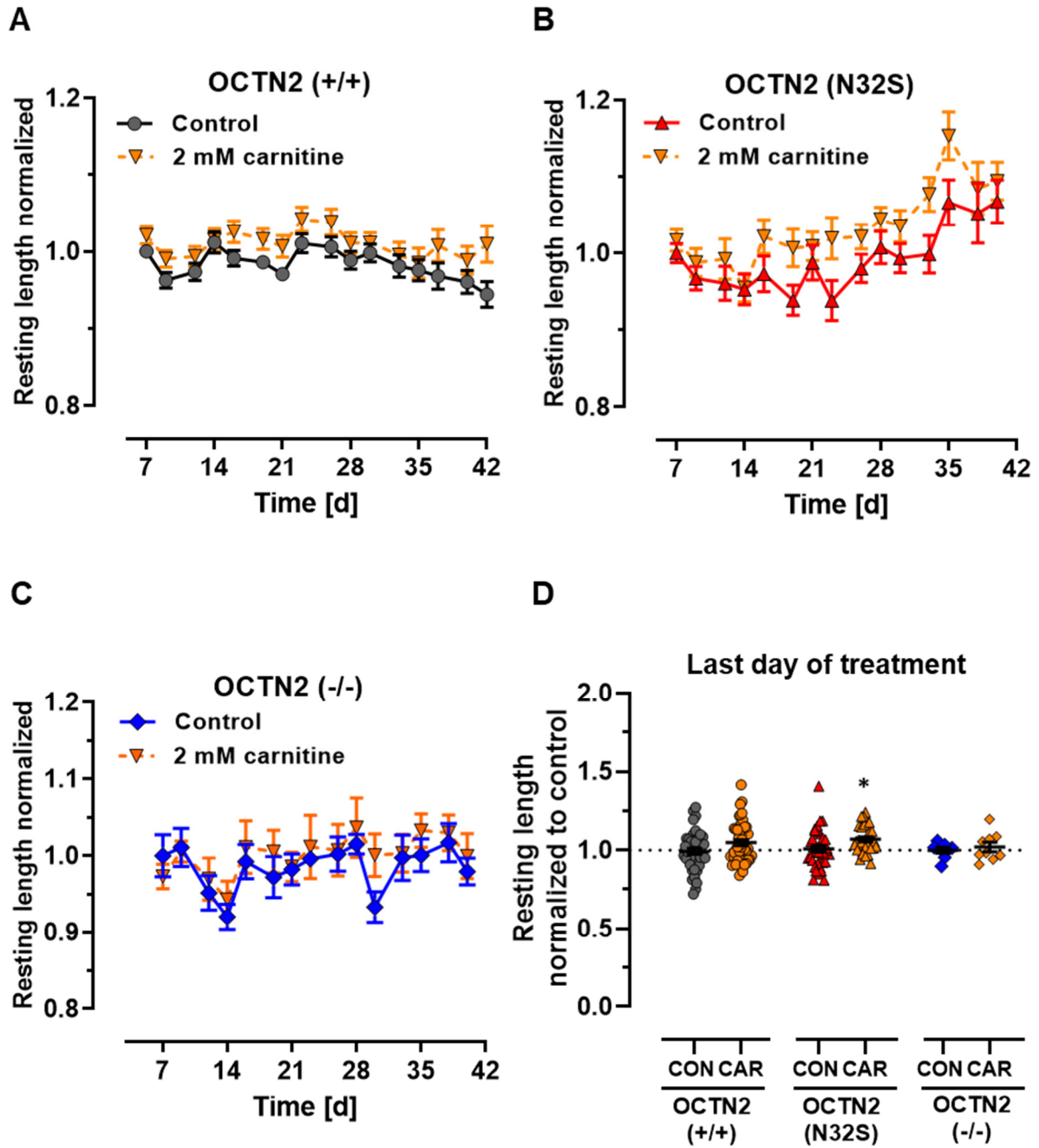


Figure 29: Effect of carnitine supplementation on resting length of spontaneous beating EHTs. A-C: EHT development between day 7 and day 42. Values were normalized to day 7 of untreated control. Two-way ANOVA plus Bonferroni's post-test for multiple comparisons. D: Analysis of resting length of spontaneous beating EHTs on the last day of carnitine supplementation (Day 33-42). Values were normalized to last day of supplementation of untreated control. Student's t-test vs CON, * $p < 0.05$. OCTN2 (+/+) control: $n = 54$ EHTs from 4 batches. OCTN2 (+/+) + carnitine (2 mM): $n = 49$ EHTs from 4 batches. OCTN2 (N32S) control: $n = 36$ EHTs from 3 batches, OCTN2 (N32S) + carnitine (2 mM): $n = 33$ EHTs from 3 batches, OCTN2 (-/-) control: $n = 9$ EHTs from 1 batch, OCTN2 (-/-) + carnitine (2 mM): $n = 9$ EHTs from 1 batch. Data are expressed as mean \pm SEM.

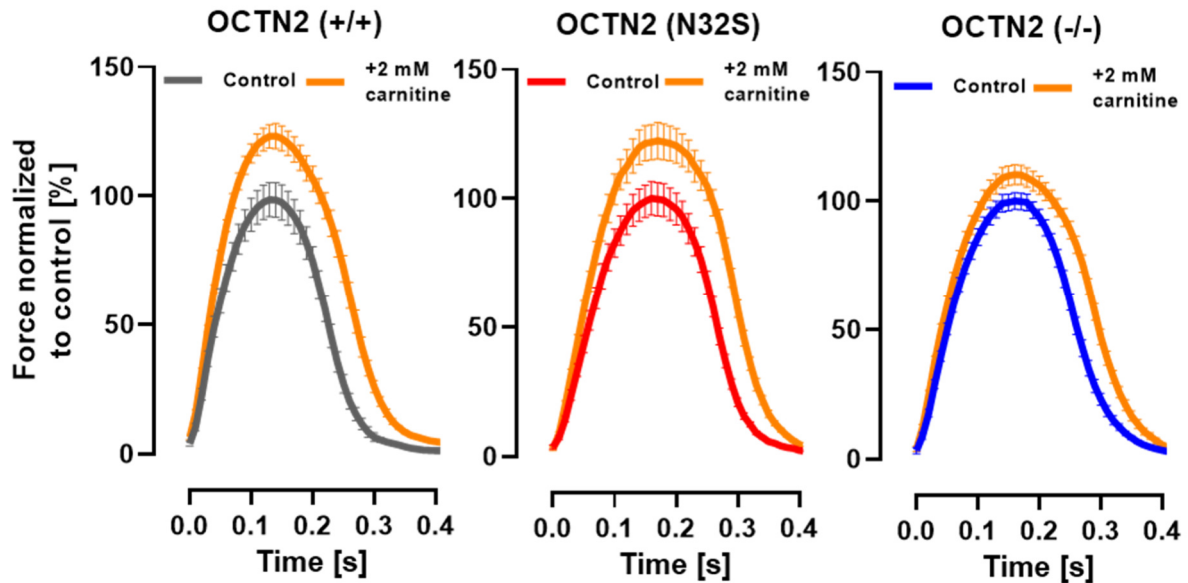


Figure 30: Contraction kinetics of EHTs supplemented with carnitine. Depicted are representative average EHT contraction peaks of OCTN2 (+/+), OCTN2 (N32S), OCTN2 (-/-). EHTs were electrically paced at 1.5 Hz in standard EHT medium \pm carnitine (2 mM). Values were normalized to untreated control. n=9-16 EHTs per condition from 1 batch.

4.6 EHT carnitine supplementation – glucose and lactate measurements

In parallel to contractility measurements, the effect of carnitine supplementation was analyzed on delta glucose and delta lactate concentration between basal and 24 hours. For all three OCTN2 genotypes carnitine supplementation led to a decrease in glucose consumption and lactate production (mean effect of carnitine supplementation on delta glucose: OCTN2 (+/+): $-33.94 \pm 8.50\%$; OCTN2 (N32S): $-38.64 \pm 8.61\%$; OCTN2 (-/-): $-40.35 \pm 11.40\%$; mean effect of carnitine supplementation on delta lactate: OCTN2 (+/+): $-32.15 \pm 4.84\%$; OCTN2 (N32S): $-42.41 \pm 5.51\%$; OCTN2 (-/-): $-45.43 \pm 6.64\%$). Moreover, carnitine treatment led to a decrease in glucose consumption per cardiac workload for the OCTN2-defective cell lines (Figure 31 D).

In summary, carnitine supplementation had, notwithstanding a small positive inotropic and negative lusitropic effect, only minor effects on the contraction properties of EHTs. Carnitine supplementation decreased glucose consumption per workload in OCTN2-defective lines and decreased total glucose consumption and lactate production in all OCTN2 genotypes. The data are compatible with the expectation that carnitine supplementation induced a switch from the relatively inefficient anaerobic glycolysis to the more effective oxidative metabolism of glucose and/or fatty acids and that this effect was stronger in the OCTN2-defective EHTs.

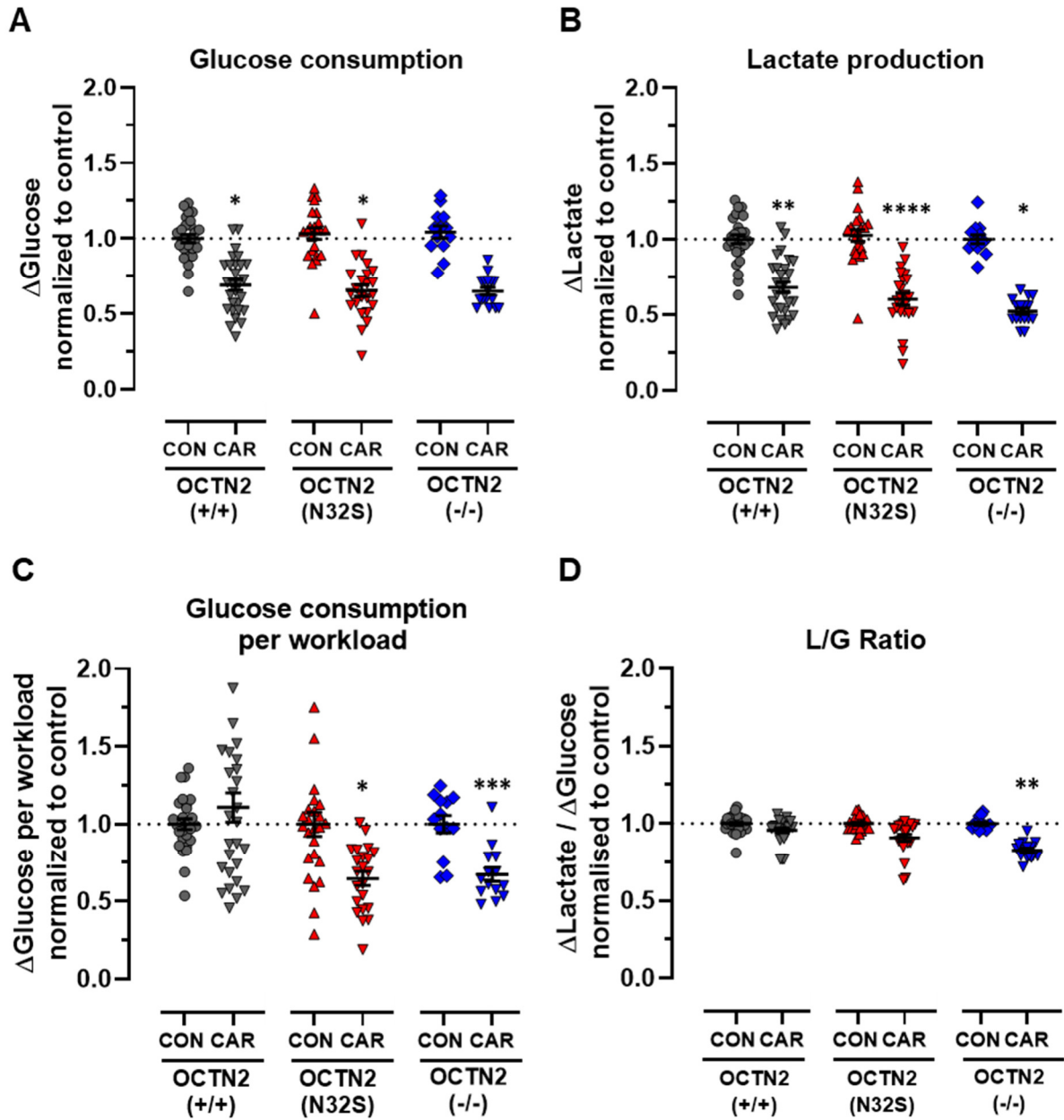


Figure 31: Effect of carnitine supplementation on glucose consumption and lactate production. A: Δ Glucose (Δ Glucose= Glucose concentration at baseline minus glucose concentration after 24 hours of incubation); B: Δ Lactate (Δ Lactate= Lactate concentration after 24 hours of incubation minus lactate concentration at baseline); C: Δ Glucose per workload (workload = force \times frequency) and D: L/G ratio (Δ Lactate/ Δ Glucose) of spontaneous beating EHTs on day 21. Nested t-test vs CON, ** $p < 0.01$, *** $p < 0.001$, **** $p < 0.0001$. OCTN2 (+/+) control: n=27 EHTs from 3 batches. OCTN2 (+/+) + carnitine (2 mM): n=28 EHTs from 3 batches. OCTN2 (N32S) control: n=23 EHTs from 3 batches. OCTN2 (N32S) + carnitine (2 mM): n=23 EHTs from 3 batches, OCTN2 (-/-) control: n=13 EHTs from 3 batches, OCTN2 (-/-) + carnitine (2 mM): n=16 EHTs from 3 batches. Data are expressed as mean \pm SEM.

4.7 Acylcarnitine and ceramide EHT content

The conjugation of carnitine to acyl residues to form acylcarnitine represents a rate-limiting step for the transport of fatty acids into the mitochondria. Accordingly, diminished carnitine conjugation results in cytosolic accumulation of toxic acyl-CoA, a precursor for ceramide synthesis (Longo et al. 2006). In order to investigate the acylcarnitine and ceramide tissue content, liquid chromatography–mass spectrometry (LC-MS) was performed. This revealed a spectrum of acylcarnitine species ranging from 14 to 22-, and ceramides ranging from 14 to 26 carbon atoms in size. OCTN2 (+/+) was compared with the OCTN2 (N32S) genotype. In comparison to acylcarnitines with 16 to 18 carbon atoms in length, shorter or longer acylcarnitines showed a considerably lower abundance and were therefore excluded from the analysis.

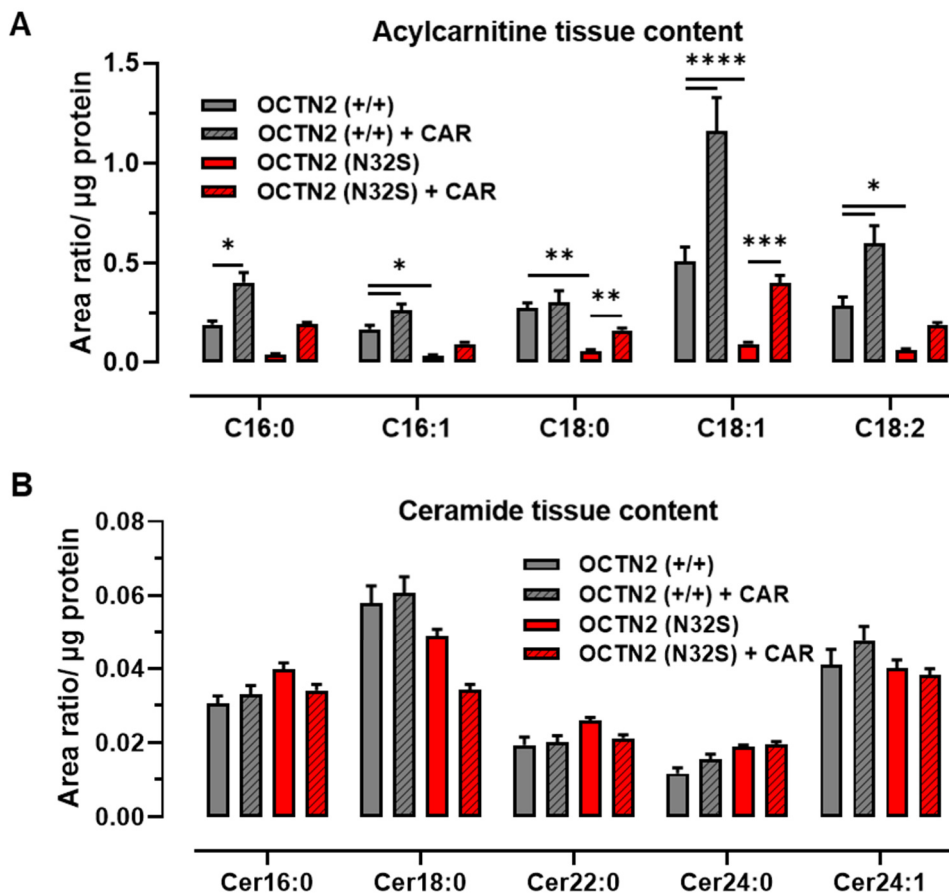


Figure 32: LC-MS- analysis of acylcarnitines and ceramides. Effect of carnitine supplementation on A: Acylcarnitine and B: ceramide content of OCTN2 (+/+) and OCTN2 (N32S) EHTs after 33 days of culture and supplementation. Two-way ANOVA plus Bonferroni's post-test for multiple comparisons, * $p < 0.05$, ** $p < 0.01$, *** $p < 0.001$, **** $p < 0.0001$. Data are expressed as mean \pm SEM. $n = 4$ EHT pools (containing 3 EHTs each) per genotype and carnitine supplementation from 1 batch.

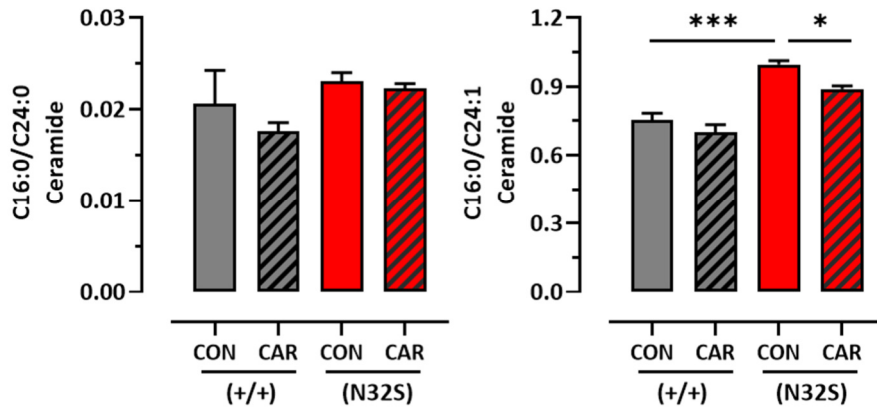


Figure 33: Effect of carnitine supplementation on ceramide ratios. Calculated were ceramide ratios that were proposed as a cardiovascular risk factor. Two-way ANOVA plus Bonferroni's post-test for multiple comparisons, * $p < 0.05$, ** $p < 0.01$, *** $p < 0.001$, **** $p < 0.0001$. Data are expressed as mean \pm SEM. $n = 4$ EHT pools (containing 3 EHTs) per genotype and carnitine supplementation from 1 batch.

The analysis of the five most abundant acylcarnitine and ceramide species is representatively shown in Figure 32 A - B. The abundances of C16:1, C18:0, C18:1 and C18:2 acylcarnitines were 5.1-, 4.9-, 5.6- and 4.8-fold lower in OCTN2 (N32S) compared to OCTN2 (+/+). The same trend could be observed for C16:0 acylcarnitine, but this failed statistical significance. Carnitine supplementation led to a higher abundance of C18:0 and C18:1 acylcarnitines for OCTN2 (N32S) and C16:0, C18:1 and C18:2 acylcarnitines for OCTN2 (+/+). A similar trend of higher acylcarnitine abundance in the presence of carnitine could be observed for C16:0, C16:1, and C18:2 in OCTN2 (N32S) and C16:1 and C18:0 acylcarnitines in OCTN2 (+/+) although the results were not statistically significant (Figure 32 A).

Analysis of EHT ceramide content (Cer16:0, Cer18:0, Cer22:0, Cer24:0, Cer24:1) revealed no difference between the genotypes or effect of carnitine supplementation (Figure 32 B). Calculation of Cer16:0/Cer24:0 and Cer16:0/Cer24:1 ceramide ratio as a proposed cardiovascular risk factor (Laaksonen et al. 2016) revealed a higher Cer16:0/Cer24:1 value for OCTN2 (N32S) vs OCTN2 (+/+) at baseline (+24.2%) and a reduction for OCTN2 (N32S) under carnitine supplementation (-11.1%, Figure 33).

Taken together, LC-MS analysis revealed a remarkable lower abundance of several acylcarnitine residues in OCTN2 (N32S) EHTs, reproducing an important hallmark of the clinical PCD phenotype. The analysis of ceramide tissue content revealed no differences in ceramide content but a higher ratio of specific ceramide, calculated in analogy to studies on cardiovascular risk prediction (Cer16:0/Cer24:1) for OCTN2 (N32S) EHTs.

4.8 Transmission electron microscopy

Ultrastructural analysis was performed by transmission electron microscopy (TEM) with one EHT per genotype and treatment. TEM showed a typical association of myofilaments and elongated mitochondria in OCTN2 (+/+). In contrast, OCTN2 (N32S) EHTs displayed a low frequency of mitochondria with structural defects and a high frequency of large lipid droplets in close association with mitochondria and sarcomeres (Figure 34 C), a finding that corresponds with a higher mitochondrial DNA content (see 4.10). OCTN2 (-/-) also exhibited mitochondria with degraded structure and increased membrane density but no pronounced aggregation of lipid droplets (Figure 34 E). In the presence of carnitine supplementation, the frequency of mitochondria appeared higher in all genotypes (Figure 34 B, D, F). Moreover, carnitine-supplemented OCTN2 (N32S) and OCTN2 (-/-) EHTs showed a considerably lower frequency of detectable lipid droplets (Figure 34 D + F). Mitochondria of these EHTs were located close to sarcomeres, larger in size and appeared more mature compared to the un-supplemented condition. However, the significance of these findings is limited by the small number of replicates (n=1) per genotype and condition.

Taken together, lipid droplet accumulation in OCTN2 (N32S) indicates a maladaptive alteration of fatty acid metabolism. Ultrastructural morphology of carnitine-supplemented EHTs revealed lower lipid droplet formation and higher mitochondrial abundance, corresponding well with the clinical therapeutic effect of carnitine supplementation.

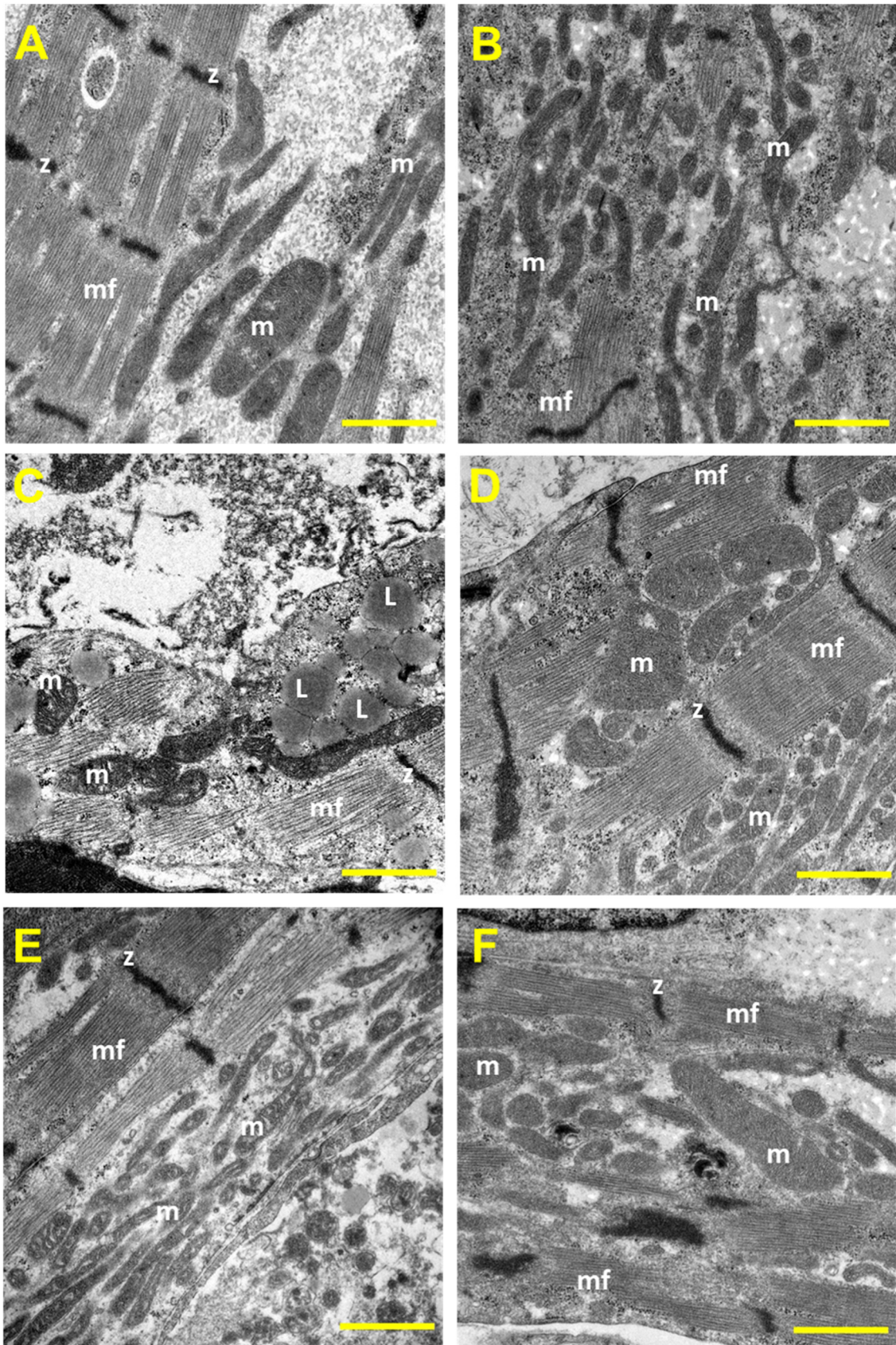


Figure 34: Transmission electron microscopy of EHTs. A + B: OCTN2 (+/+), C + D: OCTN2 (N32S), E + F: OCTN2 (-/-). A, C and E untreated, B, D and F treatment with carnitine (2 mM). mf: myofilaments, z: z-line, m: mitochondria, L: lipid droplet. Scale bar = 1 μm.

4.9 Quantitative proteomic analysis

The primary PCD disease mechanisms are incompletely understood. To identify novel molecular mechanism that contribute to PCD-mediated DCM and to gain insights into the role of carnitine metabolism in hiPSC-CM, EHTs were analyzed via quantitative proteomic analysis.

10 EHTs of each genotype (OCTN2 (+/+), OCTN2 (N32S), OCTN2 (-/-)) were subjected to tandem mass tag (TMT)- based proteomic analysis. In total, 3,425 proteins were detected, of which 1,772 proteins differed significantly between OCTN2 (+/+) and OCTN2 (N32S) and 2050 differed significantly between OCTN2 (+/+) and OCTN2 (-/-) respectively ($p < 0.05$). Principal component analysis revealed separate clustering of OCTN2 (+/+) from OCTN2 (N32S) and OCTN2 (-/-) (Figure 35 A). Volcano plot depiction of this analysis (OCTN2 (N32S) vs OCTN2 (+/+)) additionally highlights a higher abundance of fibrosis-related and extracellular matrix proteins like caldesmon1 (CALD1), collagen type I alpha 1 chain (COL1A1), transgelin 2 (TAGLN2), fibronectin 1 (FN1) and vitronectin (VTN) in OCTN2 (N32S) EHTs (Figure 35 B). Moreover, ceramide transfer protein (CERT) was among the 10 most significant proteins with higher abundance in OCTN2 (N32S). In contrast, the fatty acid transporters cluster of differentiation 36 (CD36) and fatty acid-binding protein 5 (FABP5), as well as GATA binding protein 4 (GATA4), a transcriptional key regulator of cardiomyogenesis, were among the top 10 lower abundant proteins in OCTN2 (N32S).

With respect to the abundance of cardiac-specific proteins, OCTN2-defective EHTs revealed lower protein levels of the ventricle specific myosin regulatory light chain 2 (MYL2) and MYL3 but also a lower abundance of atrial specific myosins MYL4, MYL7 and myosin heavy chain 6 (MYH6). Additionally, OCTN2 (N32S), but not OCTN2 (-/-), exhibited lower levels of CKMT2, the sarcomeric mitochondrial isoform of creatine kinase that provides high energy phosphates to ATPases. In contrast, both disease genotypes showed a higher abundance of sarcoplasmic/endoplasmic reticulum calcium ATPase 2 (ATP2A2) and MYH7, a myosin isoform associated with slow-twitch contraction kinetics and an adult cardiac phenotype (Figure 36 A). Moreover, OCTN2 (N32S) exhibited a lower abundance of laminin subunit alpha-2 (LAMA2), delta-sarcoglycan (SGCD), alpha-sarcoglycan (SGCA) and dystroglycan (DAG1), proteins involved in the dystrophin-associated surface glycoprotein complex.

Additional clustering analysis of proteins related to metabolic key processes like glycolysis, carnitine shuttle, TCA cycle and beta-oxidation revealed a concordant expression pattern for both, OCTN2 (N32S) and OCTN2 (-/-) vs OCTN2 (+/+) (Figure 37 A - E). Here, disease genotypes exhibited a higher abundance of proteins associated with the carnitine shuttle system. Moreover, proteins with higher abundance in OCTN2-defective EHTs revealed an enrichment of proteins associated with the KEGG pathway *oxidative phosphorylation*, demonstrated by a higher number of proteins related to the cytochrome-oxidase, NADH

dehydrogenase and mitochondrial ATP-synthase system (Figure 37 C). As the principal component analysis and the clustering analysis displayed similar proteomic changes for OCTN2 (N32S) and OCTN2 (-/-), the following enrichment analysis was performed comparing only significantly different proteins between OCTN2 (+/+) and OCTN2 (N32S).

Pathway analysis of proteins with higher abundance in OCTN2 (N32S) revealed enrichment of proteins related to KEGG pathways N-glycan and O-glycan biosynthesis, two posttranslational modifications which derive from uridine diphosphate N-acetylglucosamine (UDP-GlcNAc), the end product of the anabolic glucose hexosamine biosynthetic pathway (Figure 38 A). In addition, the KEGG-pathways *cholesterol metabolism*, *ECM-receptor interaction*, *complement and coagulation cascade*, *fatty acid metabolism* and *PPAR signaling* pathway were enriched in OCTN2 (N32S). Notably, OCTN2 (N32S) also showed an enrichment of proteins related to *ferroptosis*, a pathway characterized as a non-apoptotic iron-dependent cell death due to redox imbalance (Dixon et al. 2012).

Pathway enrichment of lower abundant proteins in OCTN2 (N32S) revealed enrichment of KEGG pathways related to pyruvate and propanoate metabolism, glycolysis, pentose phosphate pathway glyoxylate and dicarboxylate metabolism and different pathways associated with amino acid metabolism (Figure 38 B). A detailed summary of specific proteins enriched in the respective pathways is depicted in the supplement (Table S1 + Table S2).

In summary, the proteomic profile of OCTN2-defective EHTs differed notably from OCTN2 (+/+) and revealed a higher abundance of proteins related to several lipid metabolic pathways, fibrosis, glucose anabolism and a reorganization of the glycolytic proteome. Of note, these alterations appeared to be relevant for both OCTN2-defective genotypes. The metabolic remodeling pattern is most likely the consequence of a reduced acylcarnitine content in OCTN2-defective EHTs as described in chapter 4.7. Of note, the compensatory upregulation of proteins involved in the carnitine shuttle was already described in an animal model of PCD (Degrace et al. 2004; Liepinsh et al. 2009; Li et al. 2017). The lower abundance of proteins involved in pyruvate metabolism and glycolysis indicates an impairment of glucose utilization via pyruvate oxidation. In addition, the hexosamine biosynthetic pathway and ferroptosis, two pathways described as a response to maladaptive alteration of glucose and lipid metabolism, were identified as novel molecular pathways activated in PCD. Importantly, the higher abundance of extracellular matrix-proteins and fibroblasts markers implies a contribution of fibroblasts in OCTN2-defective EHTs. The high abundance of these proteins matches the relevance of non-cardiomyocytes in this model, as indicated in the contractile analysis and alluded to in chapter 4.3.1.

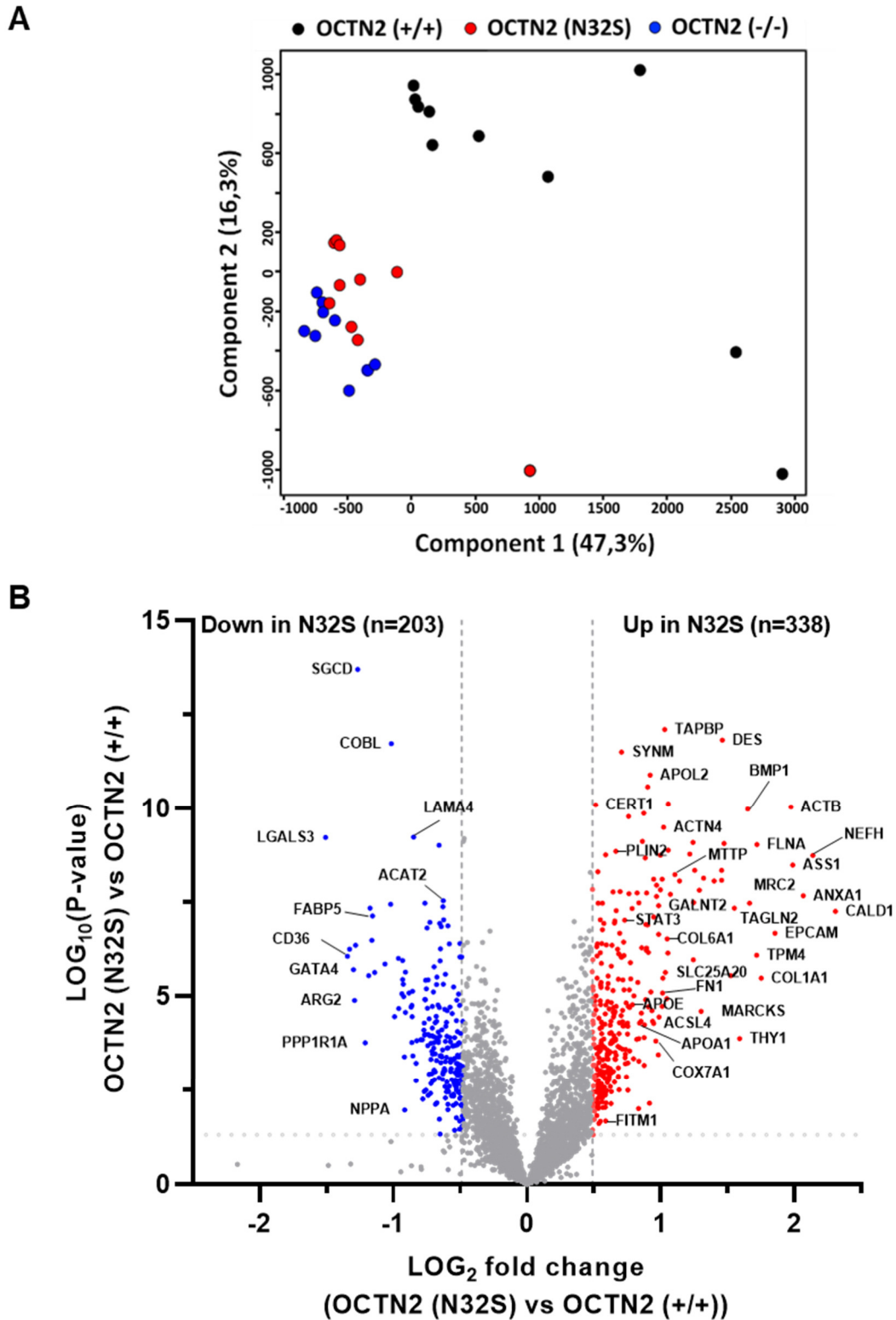


Figure 35: TMT-based quantitative proteomic analysis of EHTs. A: Principal component analysis (PCA) of OCTN2 (+/+) (black, n=10) OCTN2 (N32S) (red, n=10) and OCTN2 (-/-) (blue, n=10) EHTs based on their proteomic profiles. Each dot represents one EHT. B: Volcano plot of log₂ fold changes of OCTN2 (N32S) vs OCTN2 (+/+) and log₁₀ of the p values with color-coded significance levels (p>0.05) and fold change >1.4.

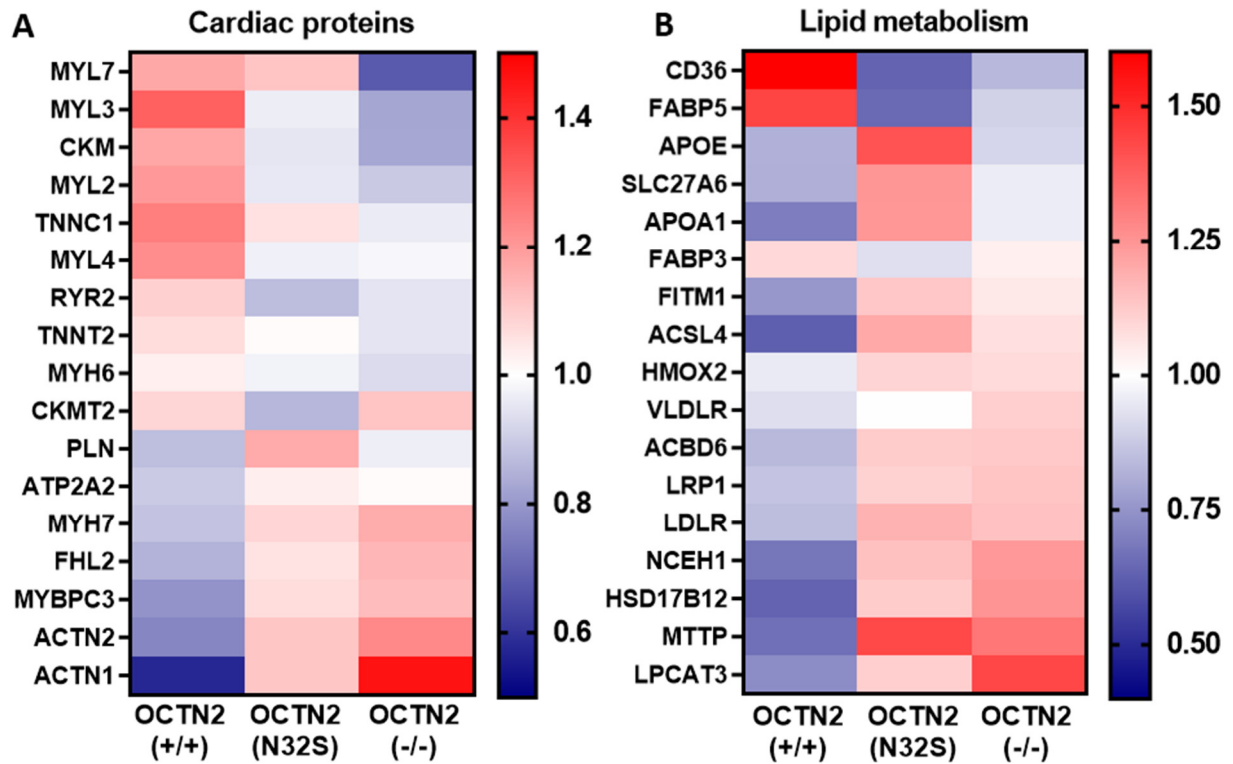


Figure 36: Clustering analysis of proteins related to myocardium and lipid metabolism. Heatmaps display relative abundance of proteins associated with the myocardium, fatty acid transport and cholesterol metabolism. OCTN2 (+/+): mean n=10 EHTs from 1 batch; OCTN2 (N32S): n=10 EHTs from 1 batch; OCTN2 (-/-): n=10 EHTs from 1 batch. Protein levels are depicted as a color code ranging from blue (low abundance) to red (high abundance).

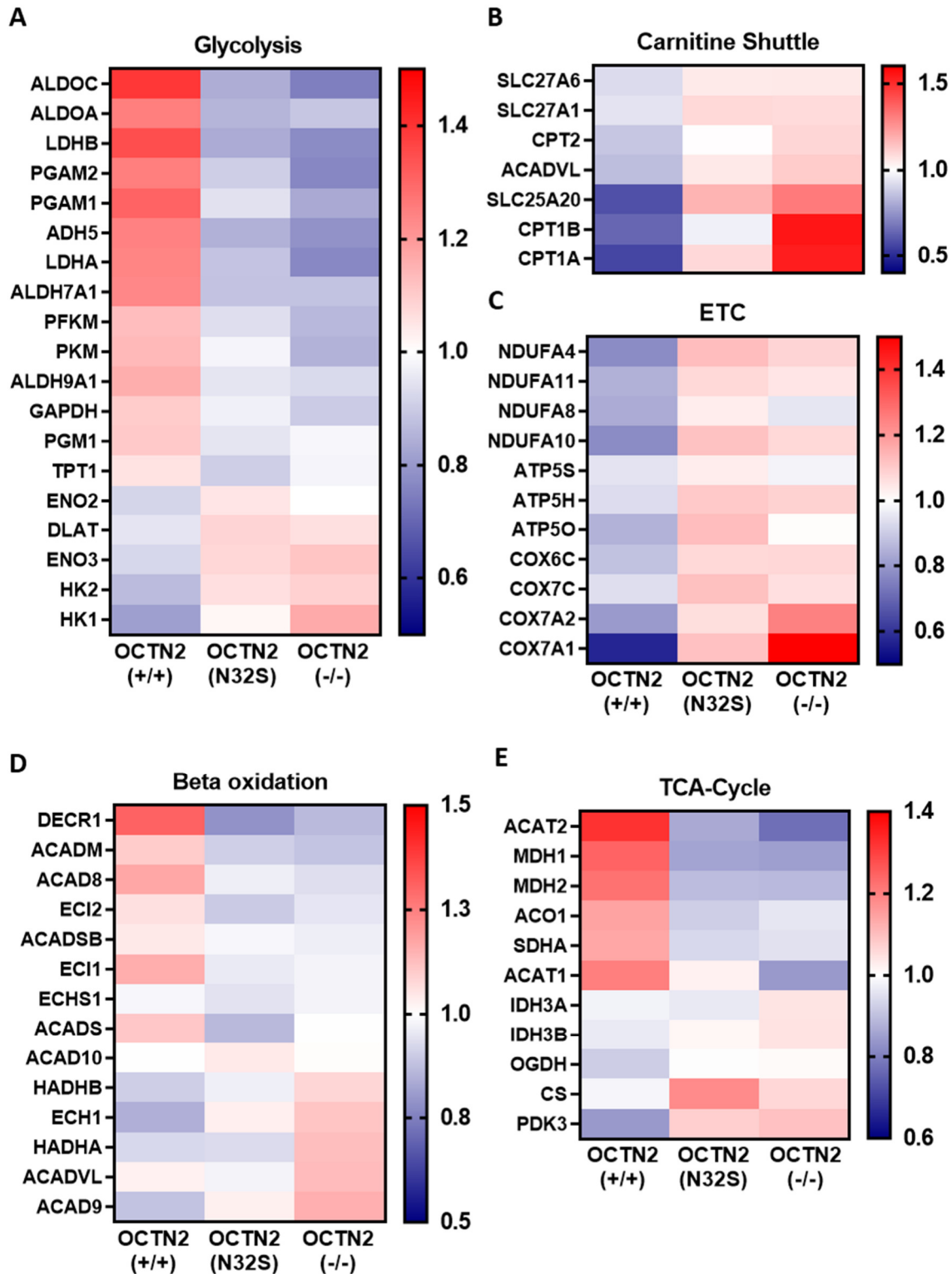


Figure 37: Clustering analysis of proteins related to metabolic pathways. Heatmaps display the relative abundance of proteins involved in glycolysis, carnitine shuttle, electron transport chain (ETC), beta-oxidation and TCA cycle. OCTN2 (+/+): mean of 10 EHTs from 1 batch; OCTN2 (N32S): mean of 10 EHTs from 1 batch; OCTN2 (-/-): mean of 10 EHTs from 1 batch. Protein levels are depicted as a color code ranging from blue (low abundance) to red (high abundance).

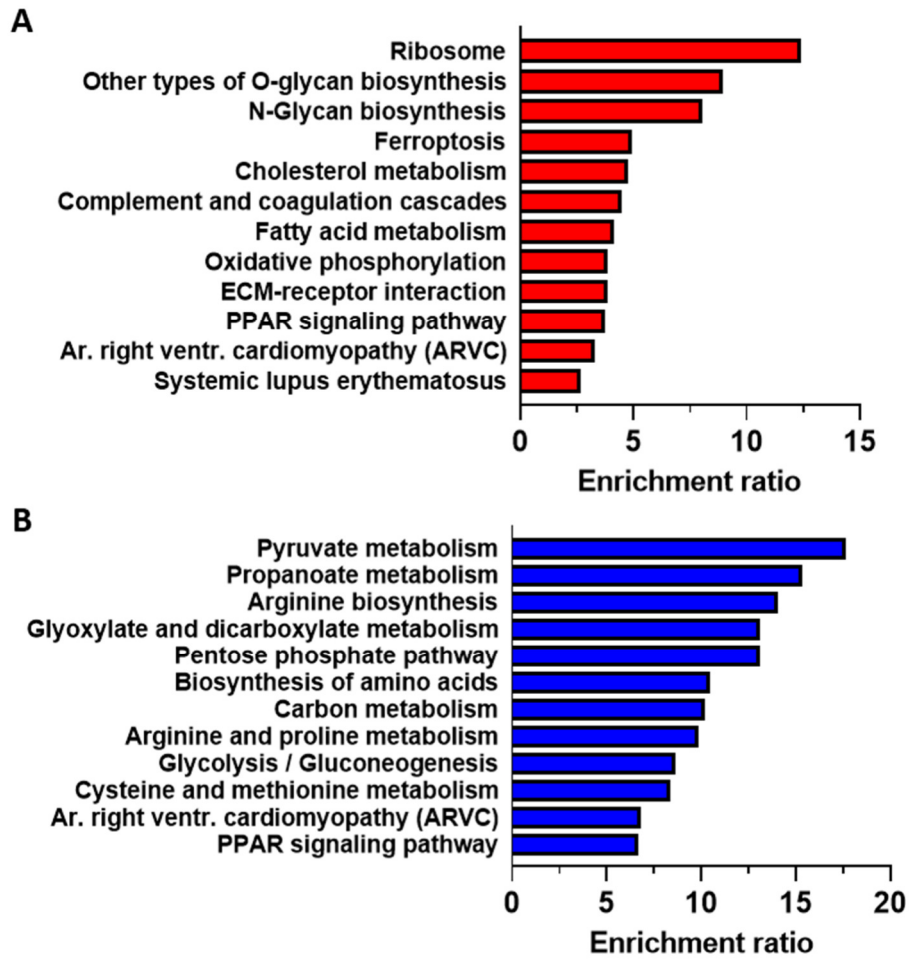


Figure 38: Enrichment analysis of proteins identified by proteomic analysis. Depicted are KEGG pathways of significantly enriched proteins that were significantly A: higher or B: lower abundant in OCTN2 (N32S) vs OCTN2 (+/+), $p < 0.05$, fold change > 1.4 .

4.10 Quantitative reverse transcription PCR

Complementary to the analysis of protein abundances, the effect of the OCTN2 genotype on certain marker genes involved in fatty acid metabolism, glycolysis and fibrosis were analyzed by quantitative reverse transcription PCR (qPCR). Furthermore, mitochondrial DNA (mtDNA) was quantified as a surrogate marker for mitochondrial abundance and metabolic maturation.

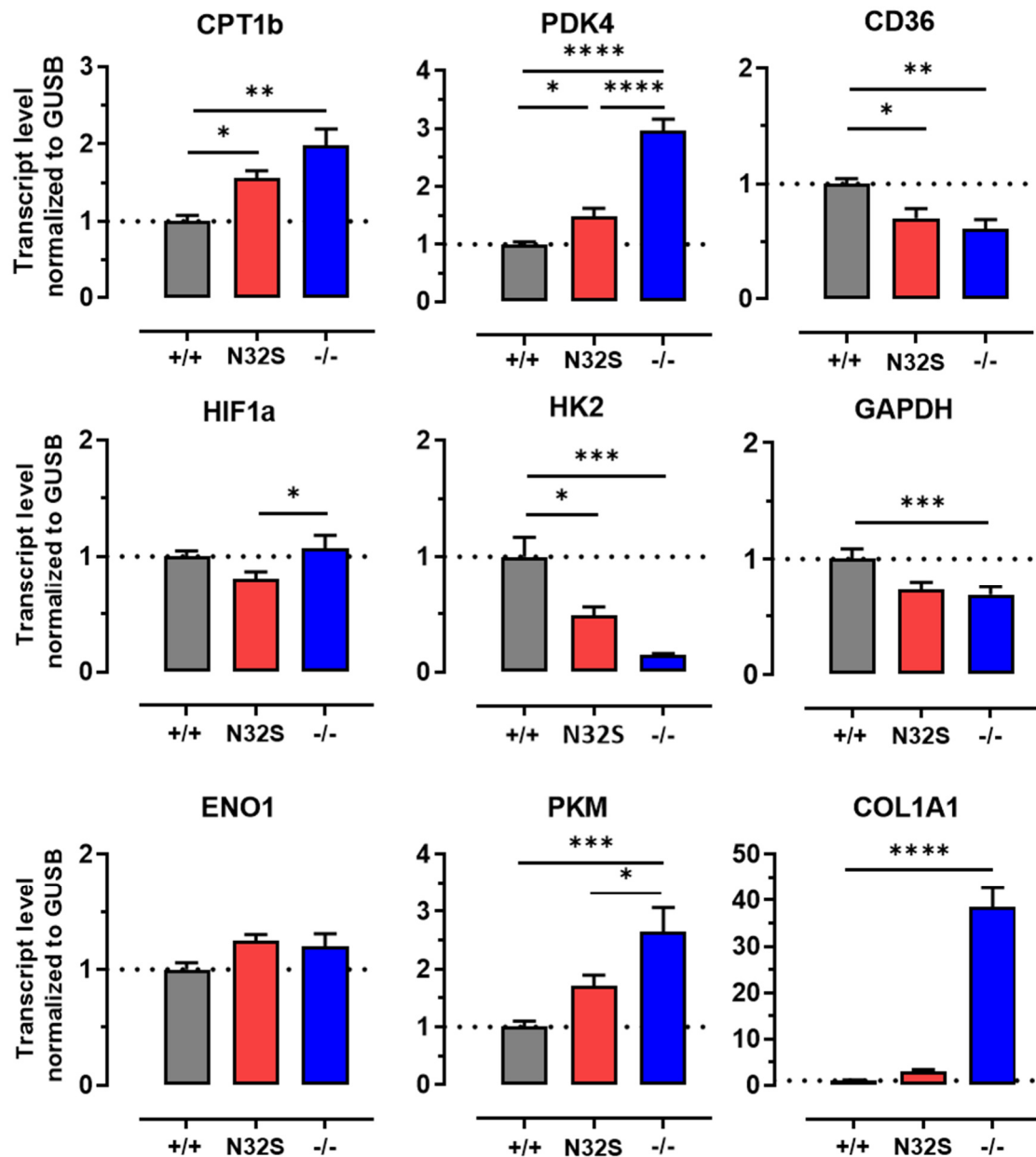


Figure 39: Quantitative PCR analysis of gene expression of disease-related genes. Gene expression was normalized to *GUSB* over OCTN2 (+/+) control. OCTN2 (+/+): n=8 EHTs from 2 batches, OCTN2 (N32S): n=8 EHTs from 2 batches; OCTN2 (-/-): n=6 EHTs from 2 batches. One-way ANOVA plus Bonferroni's post-test for multiple comparisons, * $p < 0.05$, ** $p < 0.01$, *** $p < 0.001$, **** $p < 0.0001$. Data are expressed as mean \pm SEM.

OCTN2 (N32S) and (-/-) EHTs showed higher expression of the fatty acid oxidation associated genes pyruvate dehydrogenase kinase 4 (*PDK4*) and *CPT1b*. Of note, PDK4 inhibits PDH and has thereby an important role in decreasing pyruvate oxidation (Park et al. 2018). The fatty acid transporter *CD36* revealed lower expression in the disease genotypes. Expression analysis of these three targets matched well with proteomics profile (Chapter 4.9).

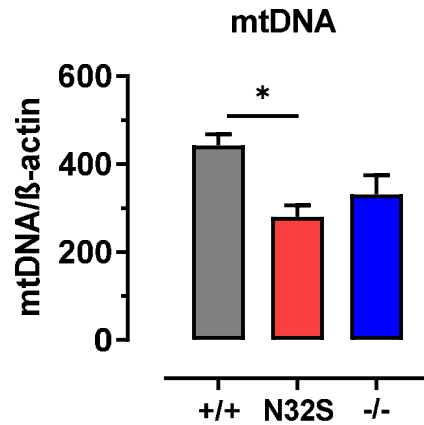


Figure 40: Effect of OCTN2 genotype on mitochondrial DNA analyzed by quantitative PCR. MtDNA was normalized to nuclear-encoded globular actin (β -actin). OCTN2 (+/+): n=5 EHTs from 1 batch, OCTN2 (N32S): n=7 EHTs from 1 batch, OCTN2 (-/-): n=7 EHTs from 1 batch. One-way ANOVA plus Bonferroni's post-test for multiple comparisons, * $p < 0.05$. Data are expressed as mean \pm SEM.

Genes encoding for key enzymes involved in glycolysis, *HK2* and *GAPDH* displayed lower-expression, while *PKM* revealed a higher expression in OCTN2 (N32S) and OCTN2 (-/-). In contrast, the gene expression of hypoxia-inducible factor 1 alpha (*HIF1a*) and enolase 1 (*ENO1*) revealed no significant difference between the isogenic control and OCTN2-defective genotypes. Among these genes, only *GAPDH* was similarly regulated in the expression and proteomic analysis.

OCTN2 (-/-) showed a considerably higher expression of *COL1A1* transcript corresponding to the higher abundance on protein level. However, a similar strong regulation could not be detected for OCTN2 (N32S). Moreover, quantification of mitochondrial DNA revealed a lower level for OCTN2 (N32S). For OCTN2 (-/-), this difference did not reach statistical significance.

Elevated *PDK4* levels in OCTN2 (N32S) were normalized to OCTN2 (+/+) baseline levels by carnitine supplementation (Figure 41). Similarly, carnitine supplementation induced a tendency to normalize the increased *COL1A1* expression in OCTN2 (N32S) EHTs, but this trend did not reach statistical significance (Figure 41).

In summary, OCTN2-defective EHTs revealed mRNA expression of genes related to fatty acid metabolism compatible with the proteomic analysis (*PDK4*, *CPT1*, *CD36*). Genes involved in glucose metabolism showed no or different regulation, indicating that regulatory changes related to glucose and carbohydrate metabolism might rather appear on protein- than mRNA-level in this model.

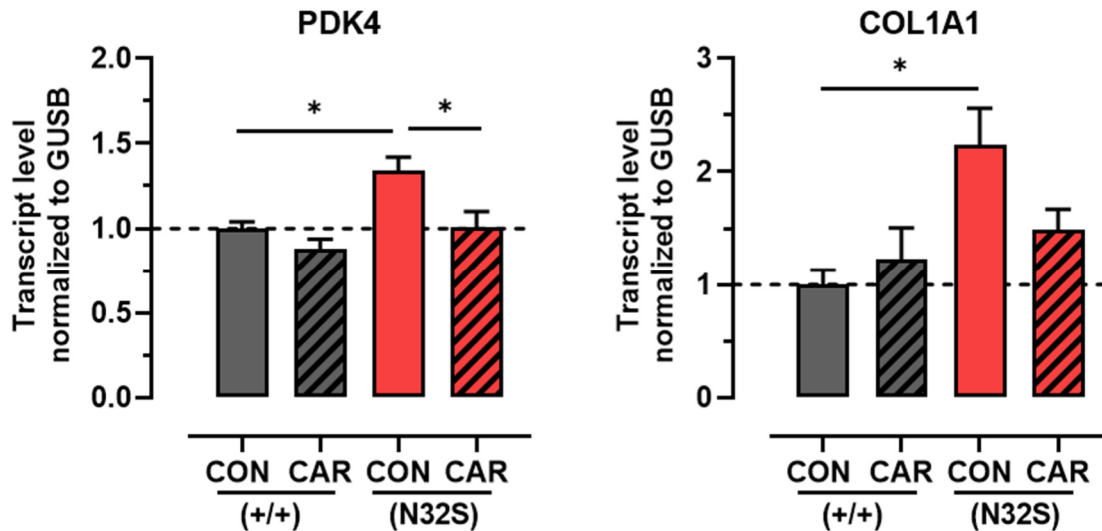


Figure 41: Effect of carnitine supplementation on *PDK4* and *COL1A1* mRNA expression. OCTN2 (+/+) and OCTN2 (N32S) EHTs were treated over the entire culture time harvested on day 42. Gene expression was normalized to *GUSB* over OCTN2 (+/+) control. n=7 EHTs per genotype and carnitine treatment from 1 batch. Two-way ANOVA plus Bonferroni's post-test for multiple comparisons, *p<0.05. Data are expressed as mean±SEM.

4.11 Single-nucleus RNA sequencing

Single-nucleus RNA sequencing (snRNA-seq) sequencing allows to characterize heterogenic cellular subpopulations at high resolution and enables advanced understanding of disease mechanisms. Moreover, this analysis was performed to better understand the high abundance of fibroblast marker and extracellular proteins identified via proteomic analysis.

EHTs from all genotypes were subjected snRNA-seq. OCTN2 (+/+), (N32S) and (-/-) samples were sequenced with a sequencing depth of 39.324, 28.770 and 26.374 read pairs per nucleus. SnRNA-seq data of all three genotypes were pooled to a total number of 13307 nuclei ((OCTN2 (+/+) = 3674, OCTN2 (N32S) = 4525, OCTN2 (-/-) = 5108 cells).

Unsupervised k-means clustering revealed 14 distinct cell clusters (Figure 43). This algorithm aims to partition cells into individual clusters with distinct labels that estimate true biological groups based on their mean expression profile (Amezquita et al. 2020). Subsequent

application of cell type-specific expression markers led to a subdivision into 5 major cell types: A cardiomyocyte cluster comprising 10 cardiomyocyte subclusters, a fibroblast, endocardium-like, endothelial and leukocyte cluster with one subcluster each. An overview of cell-specific marker defining the cell cluster across all OCTN2 genotypes is visualized in Figure 42 as relative gene expression. The cardiomyocyte cluster displayed a high expression of *MYH6*, ryanodine receptor 2 (*RYR2*) and troponin T2 (*TNNT2*). The fibroblasts cluster was characterized by a high expression of fibroblast activation protein alpha (*FAP*), tenascin-C (*TNC*), platelet-derived growth factor receptor beta (*PDGFRB*) and periostin (*POSTN*). The endothelial cell cluster showed a low expression of the established marker cadherin 5 (*CDH5*) and a high expression of polycystic kidney and hepatic disease 1-like protein (*PKHD1L1*), an extracellular matrix protein recently described in endothelial cells of the human lung (Schupp et al. 2021). A small leukocytes cluster was identified, showing a high expression of the established pan-leukocyte marker protein tyrosine phosphatase receptor type C (*PTPRC*). One additional cluster displayed no clear cell type-specific expression pattern of established cell-specific markers, but a high expression of serine proteinase inhibitor 1 (*SERPINE1*), hyaluronan and proteoglycan link protein 1 (*HAPLN1*), transforming growth factor beta 1 (*TGFBI*) and bone morphogenetic protein 6 (*BMP6*). As these genes were described in the regenerating endocardium of zebrafish (Münch et al. 2017; Fang et al. 2020) but also in the human fetal endocardium (Miao et al. 2020), this cluster was annotated as “endocardium-like” cluster.

Next, the genotypes were separated to delineate which clusters were strongly represented in the specific OCTN2 genotypes (Figure 43 A). Pie chart depiction shows the relative composition of the 5 major clusters per OCTN2 genotype (Figure 43 B). In OCTN2 (+/+), the cardiomyocyte cluster represented 93%, fibroblast, endothelial and endocardium-like clusters were similar in percentage and represented 7%. The leukocyte cluster was below 0.1% in OCTN2 (+/+). In contrast, the cardiomyocytes proportion decreased in OCTN2 (N32S) (85%), while the endocardium-like cluster (9%) and leukocyte cluster (0.4%) were higher in percentage. In OCTN2 (-/-), the cardiomyocyte cluster even decreased in fraction (69%) and fibroblast - (19%), endothelial- (6%) and leukocyte cluster (1.5%) showed the highest number of nuclei across all genotypes.

The cardiomyocyte subclusters also differed between the OCTN2 genotypes as visualized in Figure 43 A. Overall, a strong shift in cardiomyocyte subclusters was notable in both OCTN2-defective EHTs, from right to left. Specifically, the cardiomyocyte subclusters CM1, CM3, CM4 and CM10 appeared to be enriched in OCTN2 (N32S) and OCTN2 (-/-). In contrast, the cardiomyocyte subclusters CM5, CM6 and CM8 were predominantly enriched in OCTN2 (+/+).

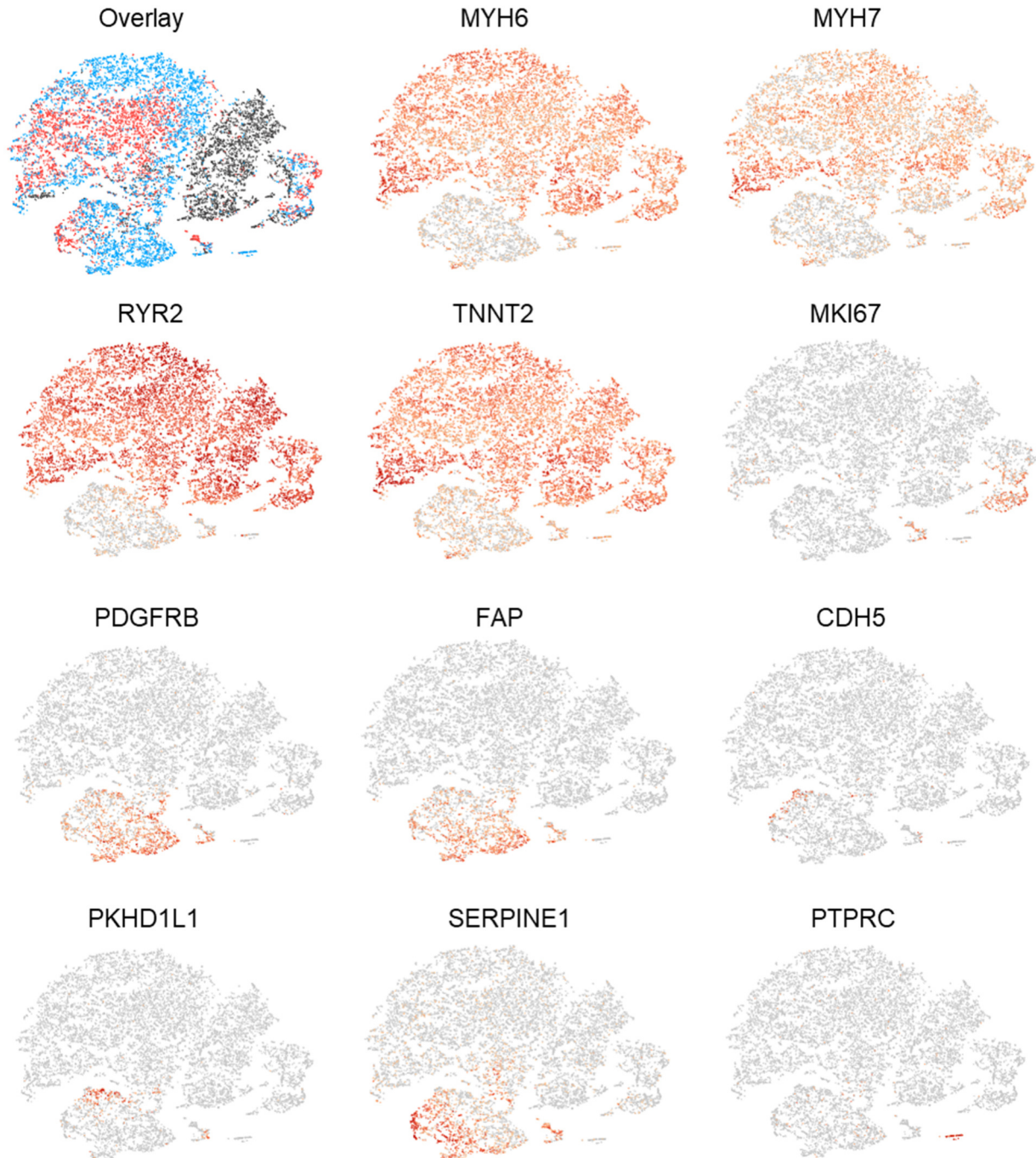


Figure 42: Grouped snRNA-seq analysis of OCTN2 genotypes . T-SNE plots showing an overlay of OCTN2 (+/+) (black, 3674 cells), OCTN2 (N32S) (red, 4525 cells) OCTN2 (-/-) (blue, 5108 cells), and the relative expression of cell cluster-specific genes across all clusters, n=1 EHT pool (4 EHTs) per genotype. Analysis of cell-specific marker genes led to a subdivision into 5 major cell types: Cardiomyocytes (*MYH6*, *MYH7*, *RYR2*, *TNNT2*), fibroblasts (*PDGFRB*, *FAP*), endothelial cells (*CDH5*, *PKHD1L1*), endocardium-like cells (*SERPINE1*) and leukocytes (*PTPRC*). The cell cycle marker *MKI67* characterizes proliferative cardiomyocytes. Expression levels are depicted as a color code ranging from light red (low expression) to dark red (high expression) as mean of log₂ fold of expression. Grey: no expression.

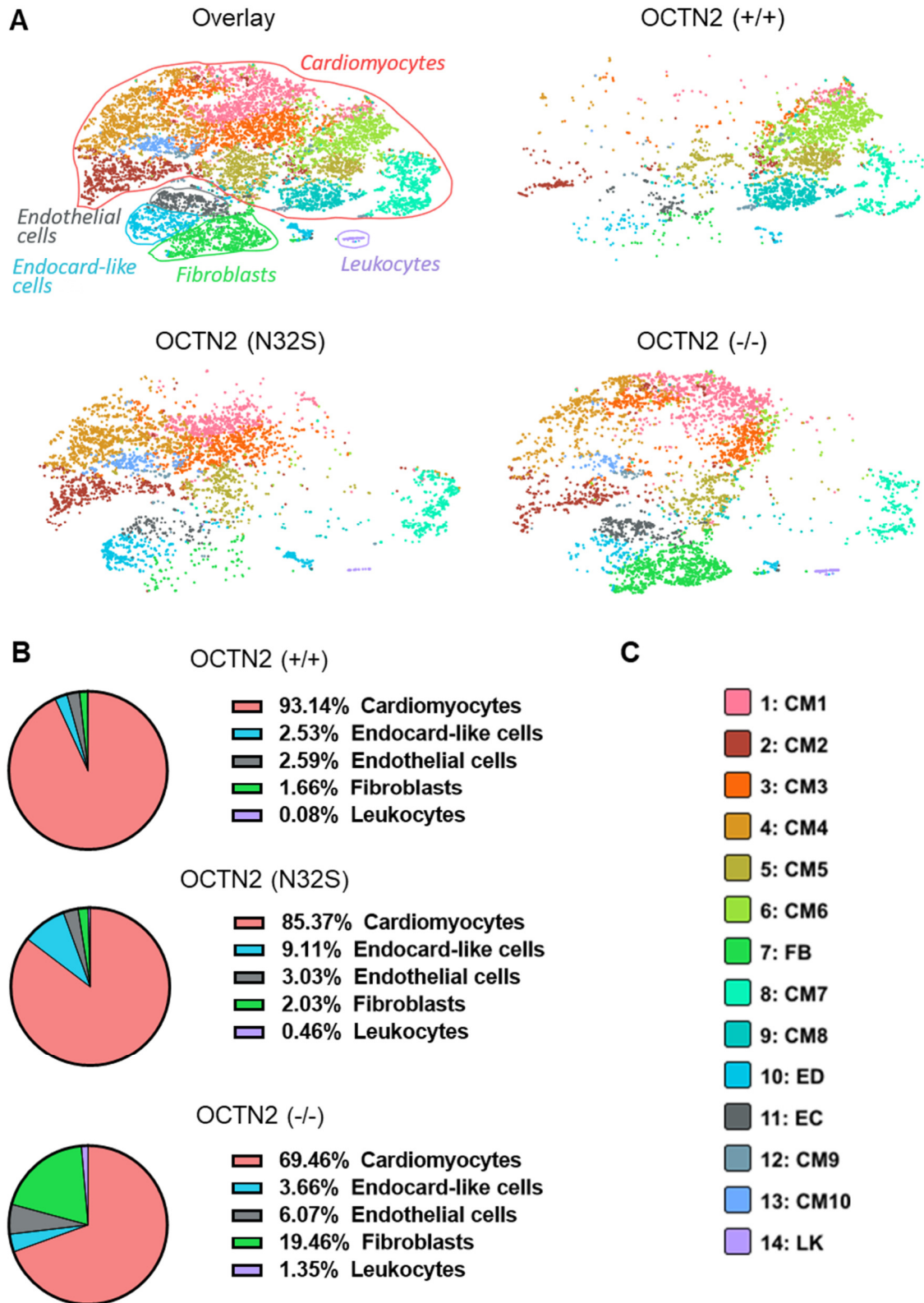


Figure 43: Cellular heterogeneity in OCTN2 genotypes in EHTs. A: Representative t-SNE plot after single-nucleus RNA sequencing of each individual genotype, n=1 EHT pool (4 EHTs) per genotype. 14 distinct cell clusters were identified: 10 cardiomyocyte (CM), 1 endocardium-like (ED), 1 endothelial cell (EC), 1 fibroblast (FB), and 1 leukocyte (LK) cluster. B: Percentage of cell types per genotype. C: Color-code of identified subclusters.

The cardiomyocyte clusters CM2, CM7 and CM9 showed an equal representation among the three OCTN2 genotypes.

To better characterize specific subclusters, pathway enrichment analysis was performed with the 100 most strongly expressed genes per subcluster. An overview showing KEGG and gene ontology terms of genes enriched in specific cell clusters is provided in Figure 44 A-E.

Cardiomyocyte subcluster CM1, enriched in OCTN2 (N32S) and OCTN2 (-/-), revealed an enrichment of genes involved in *n-glycan biosynthesis*, *cortisol synthesis* and *insulin secretion*. Cluster CM6, which was enriched in OCTN2 (+/+) and almost absent in OCTN2-defective lines, showed an enrichment of genes involved in *pyruvate metabolic process* and *nucleotide phosphorylation*. The absence of this cluster in OCTN2-defective EHTs matches with the lower abundance of proteins involved in pyruvate metabolism, as revealed by the proteomic analysis (see chapter 4.9)

The cluster CM2 revealed a high expression of several genes involved in oxidative phosphorylation (*COX6B*, *COX7C*, *ATP5F1B*) but also genes encoding for sarcomeric proteins (*TNNC1*, *MYH7*) and was therefore representing cells with an elevated metabolic activity and a high degree of cardiac maturation (Supplement, Table S3). In contrast, the cluster CM8 displayed a high expression of t-box transcription factor 5 (TBX5, Figure 45), a transcriptional activator involved in cardiac development, which is highly expressed in the human atrium (Steimle and Moskowitz 2017). The high expression of this gene indicates an immature and fetal-like cardiomyocyte state of this cluster. The cardiomyocyte cluster CM7 was identified as a proliferating cell cluster due to high expression of proliferation marker *MKI76*. The fibroblast and endocardium-like clusters showed an enrichment of genes related to extracellular matrix while the leucocyte cluster displayed gene enrichment related to phagocytosis respectively. A detailed overview of upregulated genes per subcluster can be found in the supplement (Table S3 - Table S7).

Figure 44 F depicts a heatmap of fibroblast marker expression in the fibroblast subclusters for the OCTN2 genotypes. Here, a higher expression of cellular communication network factor 2 (*CCN2*) and periostin (*POSTN*) but a lower expression of transcription factor 21 (*TCF21*) could be demonstrated for OCTN2 (N32S) and OCTN2 (-/-), indicating a more proliferative fibroblast phenotype in these genotypes.

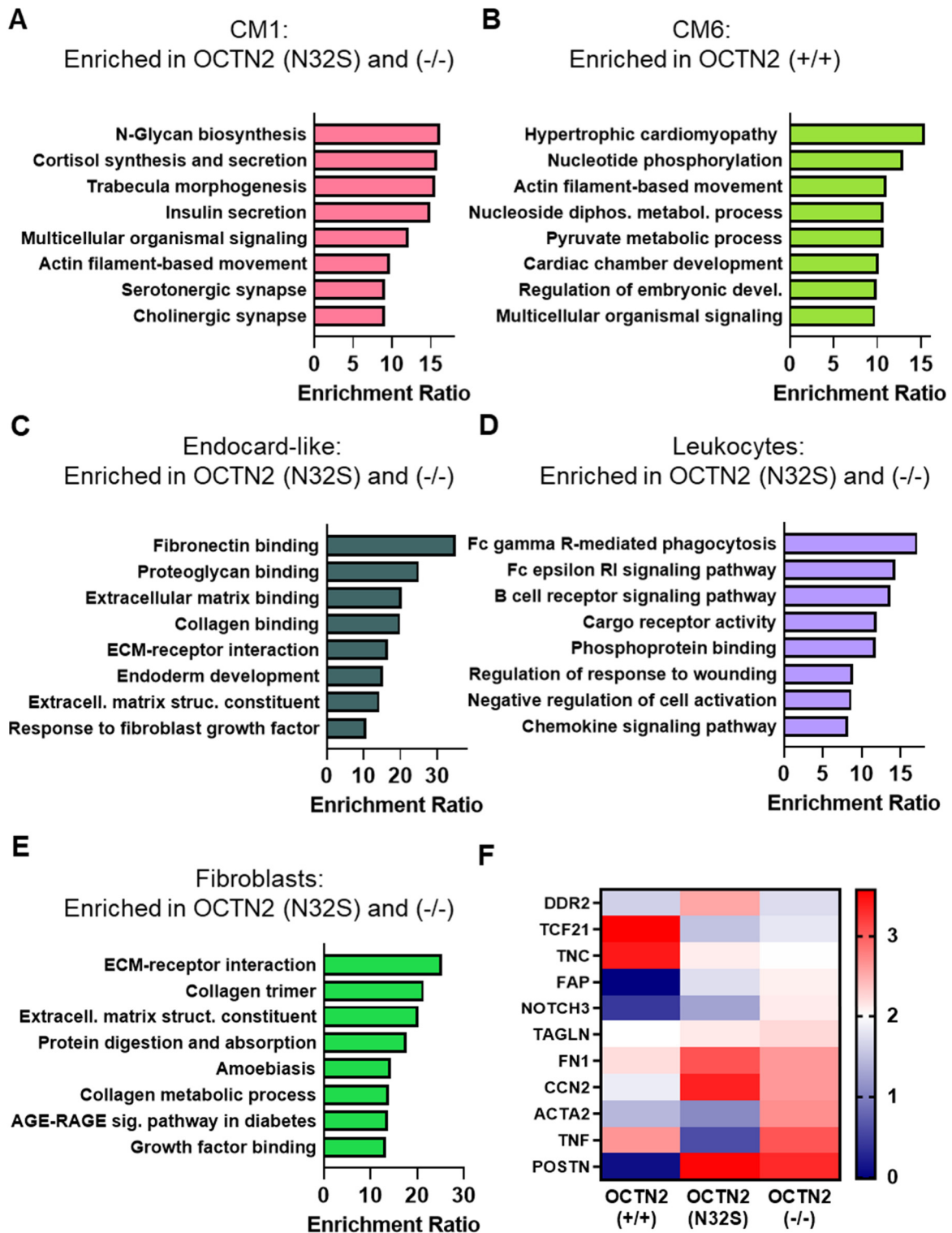


Figure 44: Characterization of subclusters identified by snRNA-seq analysis. A-E: Enrichment analysis of 100 most strongly expressed genes per subclusters as defined in Figure 43. F: Heatmap of fibroblast specific markers in fibroblast cell clusters of respective genotypes. Expression levels are depicted as a color code ranging from blue (low expression) to red (high expression) as log₂ fold of gene expression.

Moreover, the metabolic pathways identified by quantitative proteomics (Chapter 4.9) were investigated in the specific subclusters (Figure 45 + Figure 46). Here, the non-cardiomyocyte clusters showed the highest expression of glutamine-fructose-6-phosphate transaminase 1 (*GFPT1*), the rate-limiting enzyme of the hexosamine biosynthetic pathway (Tran and Wang 2019) and acyl-CoA synthetase long-chain family member 4 (*ACSL4*), one of the central enzymes of pro-ferroptotic lipid metabolism (Doll et al. 2017). In contrast, acetyl-CoA carboxylase beta (*ACACB*), an enzyme known as a negative regulator of fatty acid oxidation (Cheng et al. 2007; Kaushik et al. 2009), was exclusively expressed in cardiomyocyte subclusters, with the highest expression in CM1. Estrogen receptor alpha (*ESR1*), described as a metabolic regulator and activated in female infarct and hydrogen peroxide treated animal models (Klinge 2001; Puzianowska-Kuznicka 2012; Zafirovic et al. 2017), showed a high expression in the cardiomyocyte subcluster CM1, CM3 and CM4, which were enriched in the disease genotypes.

A similar expression pattern was observed for forkhead box protein O1 (*FOXO1*), a central target of insulin signaling and oxidative stress (Gopal et al. 2017, 2021), which showed higher abundance in disease-associated clusters. Remarkably, neutral cholesteryl ester hydrolase 1 (*NCEH1*) was exclusively expressed in leukocytes and to a minor extent in CM1. This enzyme mediates the hydrolysis of intracellular cholesterol ester, representing a central step in the reverse cholesterol transport in macrophage foam cells (Igarashi et al. 2010). This finding relates to the alteration of proteins involved in cholesterol metabolism in OCTN2-defective EHTs as identified by the proteomic analysis.

Taken together, the snRNA-seq analysis revealed a different composition of cellular cardiomyocyte subclusters for the OCTN2 genotypes and a subcluster-specific enrichment of metabolic regulator and marker genes. In particular one subcluster (CM1) revealed a high expression of genes related to altered fatty acid metabolism and oxidative stress (*ACACB*, *ERS1*, *FOXO1*). This cluster was enriched in OCTN2-defective EHTs and corresponds to the role of carnitine as a modulator of lipid metabolism and potent antioxidant. Moreover, the presence of an activated fibroblast cluster matches with the high abundance of extracellular matrix-proteins in OCTN2-defective EHTs revealed by quantitative proteomic analysis (chapter 4.9). Moreover, this cellular subcluster most likely contributed to reduced resting length and low force of OCTN2-defective EHTs as demonstrated in the contraction analysis.

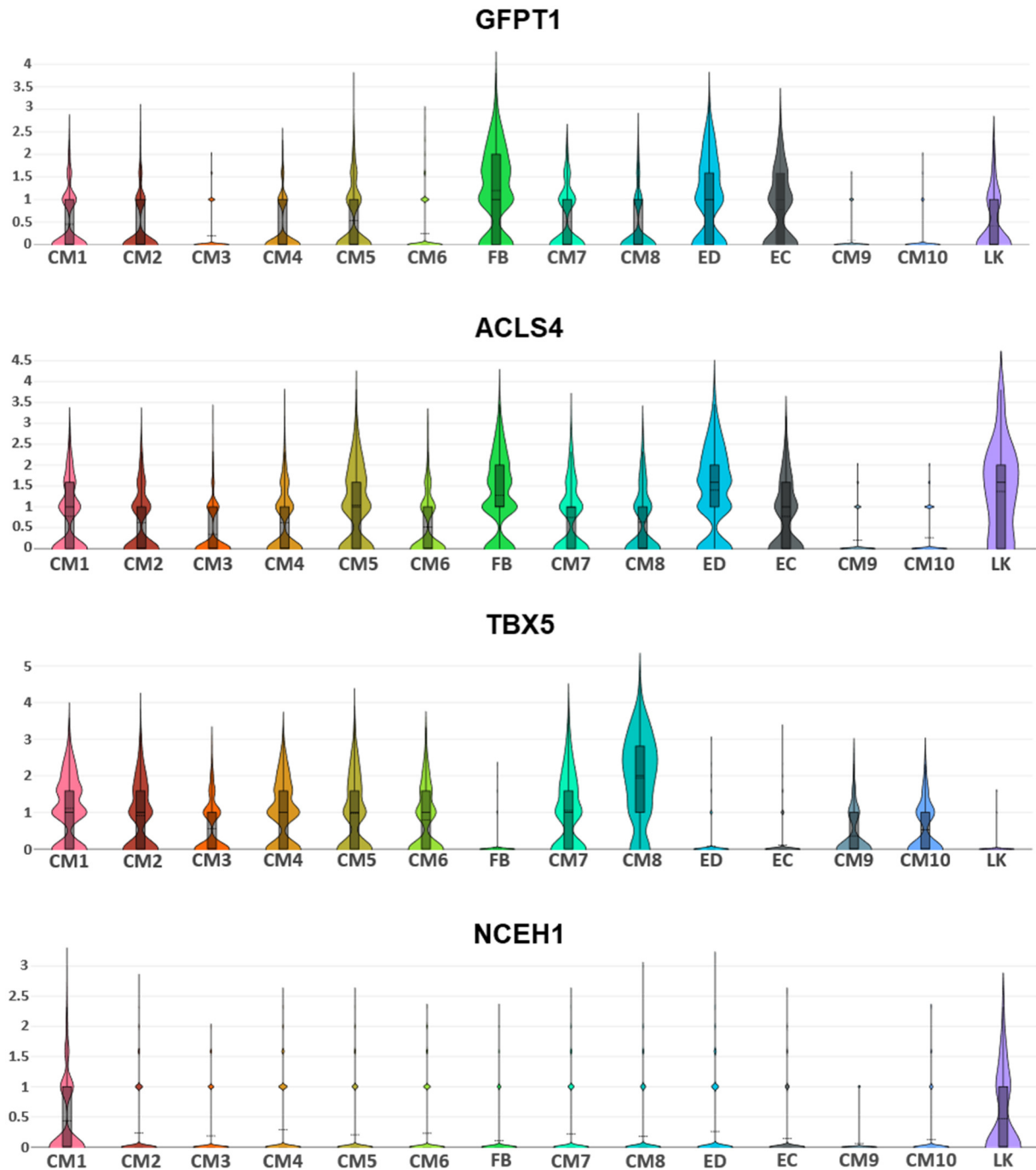


Figure 45: Violin plots of different regulator genes across cellular subclusters identified by snRNA-seq. Data are expressed as log₂ fold of gene expression. *GFPT1*, the rate-limiting enzyme of the hexosamine biosynthetic pathway, and *ACSL4*, a central enzyme of pro-ferroptotic lipid metabolism revealed a high expression in non-cardiomyocytes. *TBX5* represents a transcriptional activator involved in cardiac development, which is highly expressed in the human atrium. *NCEH1*, was exclusively expressed in leukocytes and to a minor extend in CM1. CM: Cardiomyocytes; FB: Fibroblasts; ED: Endocardium-like cells; EC: Endothelial cells; LK: Leukocytes.

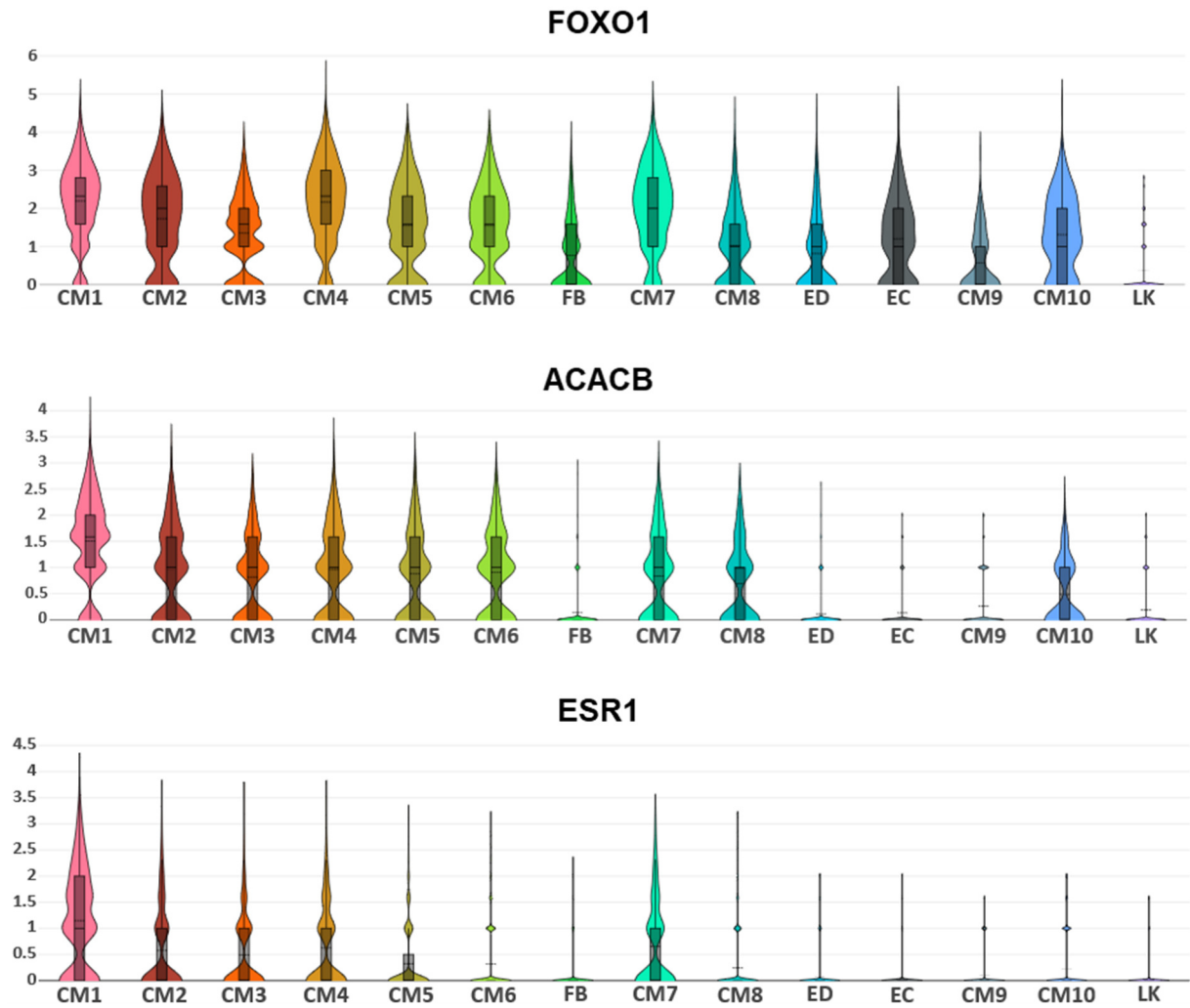


Figure 46: Violin plots of *FOXO1*, *ACACB* and *ERS1* expression across cellular subclusters identified by snRNA-seq. Data are expressed as log2 fold of gene expression. *FOXO1*, *ACACB*, and *ERS1*, genes that were described in the context of elevated oxidative stress, showed a high expression in CM1, a cardiomyocyte cluster enriched in OCTN2-defective EHTs. CM: Cardiomyocytes; FB: Fibroblasts; ED: Endocardium-like cells; EC: Endothelial cells; LK: Leukocytes.

5 Discussion

The goal of this doctoral thesis was to further our understanding of primary carnitine deficiency (PCD) by modeling its cardiomyopathy disease phenotype *in vitro*. To this end, a complex model was established by employing a set of advanced biotechnology methods, including CRISPR/Cas9 genome editing, hiPSC expansion and differentiation, cardiac tissue engineering and functional *in vitro* analysis. The main results are as follows and will be discussed in this section:

1. Successful genetic engineering of two experimental hiPSC lines, the homozygous OCTN2 (N32S) hiPSC line and an OCTN2 (-/-) knockout hiPSC line, hiPSC quality control, differentiation of hiPSC-CM and functional analysis in EHT model.
2. Replication of the PCD DCM phenotype in the OCTN2 (N32S) and knockout hiPSC-CM by low acylcarnitine tissue content and force development sensitive to carnitine supplementation, fibrosis development, complex metabolic remodeling, and ultrastructural alteration.
3. Validation of the disease phenotype of OCTN2 (N32S) loss-of-function hiPSC line by high-level concordance with the OCTN2 (-/-) knockout hiPSC line in various assays.
4. Novel discovery of O-linked β -N-acetylglucosamine and ferroptosis pathway alterations as an aspect of the OCTN2 (N32S) DCM disease phenotype.
5. Alteration of cardiac and non-cardiac subcluster composition of OCTN2-defective genotypes in snRNA-seq analysis.

5.1 Biotechnological challenges towards a reliable disease model

The combination of hiPSC-CRISPR/Cas9 and hiPSC-based tissue engineering technology offers an unprecedented opportunity to discover disease mechanisms and gene function. Nevertheless, the combination of these technologies is also accompanied by a high risk for variability and artifacts. To address this challenge, a set of stringent quality control procedures were implemented in the workflow of this study. Specifically, CRISPR-induced DNA rearrangements and off-target effects, allelic and karyotypic integrity, as well as pluripotency were validated after gene editing and subsequent MCB generation. Despite this stringent multi-step quality assessment, high variability of the hiPSC-CM characterization was evident for many readouts, specifically for the analysis of contractile parameters like force and resting length. High variability is a well-known limitation of hiPSC-based approaches. Kilpinen et al. demonstrated that the donor origin, culture conditions and other factors have a crucial impact on the variability of several hiPSC phenotypes such as genome-wide assays, differentiation capacity and cellular morphology (Kilpinen et al. 2017). Consequently, a more reliable

phenotype prediction requires the generation of isogenic hiPSC controls, which were generated in this study and served as a reference for phenotype description. Moreover, it was shown that hiPSC-CM exhibit high batch-to-batch variability regarding ion-channel expression and contractile parameter readout in engineered heart tissue format (Huo et al. 2017; Mannhardt et al. 2020). Therefore, contractile readouts originating from several differentiation batches were included via a nested statistical analysis in this work. This hierarchical statistical methodology considers differentiation-batch-dependence of each data point and allows for a more reliable conclusion. In contrast, standard statistical tests underestimate the standard error due to large sample sizes and assumption of batch-independence of these data points.

CRISPR/Cas9 genetic engineering introduced another layer of complexity. In particular, the low efficiency of the homology-directed repair pathway is a major limitation of CRISPR-mediated gene editing of hiPSC. Numerous studies suggested absent expression of the target gene during the hiPSC state as a major limitation of CRISPR-based gene editing, as chromatin compaction around non-expressed genes limits the access of the Cas9 protein to the DNA target region (Daer et al. 2017). Published hiPSC expression profiles obtained from bulk RNA sequencing data indicate ubiquitous expression of *SLC22A5* in hiPSC (Chin et al. 2009; Churko et al. 2017). Moreover, the *in silico* gRNA design allowed an ideal cut-to-mutation distance of one base pair. Paquet and colleagues linked the editing efficiency of CRISPR/Cas9-mediated single base substitutions to this distance and showed that a low cut-to-mutation distance substantially improves successful introduction of homozygous point mutations (Paquet et al. 2016). Consequently, robust gene expression of *SLC22A5* during the hiPSC state and an optimal gRNA cutting site position might have contributed to the relatively high rate of biallelic editing in this study.

Besides technical aspects, the role of *SLC22A5* as a ubiquitously expressed gene (Longo et al. 2006) in hiPSC biology is not understood yet. RNA sequencing analysis data from Liu et al. (2017) demonstrated a continuous expression of *SLC22A5* among different stages of hiPSC cardiomyocyte differentiation, suggesting a possible involvement of carnitine metabolism. In line with this, it has been reported that the transition of anaerobic glycolytic metabolism into mitochondrial oxidative metabolism is necessary to ensure efficient cardiac specification of undifferentiated stem cells (Chung et al. 2007). OCTN2-defective hiPSC lines might therefore be compromised at both hiPSC state and during cardiac differentiation. Notably, the OCTN2 (+/+) control hiPSC line outperformed both OCTN2-defective hiPSC lines with respect to differentiation efficiency. While no difference could be observed between the respective genotypes regarding the proportion of cTNT-positive cells, OCTN2 (N32S) and OCTN2 (-/-) displayed significant lower differentiation efficiency (cardiomyocyte output in relation to the input of hiPSC).

5.1.1 Principal aspects of disease modeling: Clinically relevant point mutation versus complete knockout

This study aimed to model the PCD DCM phenotype by introducing a disease-related mutation into an established control hiPSC line. For this, the well-characterized OCTN2 (N32S) founder mutation was introduced at a homozygous state, reflecting a clinically relevant mutation. This approach is suited for well-established disease-relevant mutations which are characterized by high penetrance, implying a significant impact of the mutation on the phenotype. In contrast, for low penetrance mutations, the disease phenotype is likely more influenced by the patient-specific genetic profile or environmental factors (McNally and Mestroni 2017). Thus, modeling such a mutation in an unrelated control hiPSC line harbors the risk that additional genetic causes supersede the phenotype. Data from OCTN2 (N32S) patients indicate that the majority of untreated PCD patients remain asymptomatic until adulthood, but exhibit an increased risk of sudden cardiac death, suggesting a high penetrance of this mutation (Rasmussen et al. 2020). Nevertheless, given the long asymptomatic phase and the limitations of hiPSC-CM like immaturity and variability, it was unclear at the start of this project if a point mutation would allow reliable *in vitro* modeling of the PCD disease phenotype.

Accordingly, in addition to the desired OCTN2 (N32S) loss of function hiPSC line, a complete OCTN2 knockout was engineered and processed in parallel. This turned out to be beneficial since the concordant changes of several parameters (e.g. contractile parameters, protein expression of metabolic markers, clustering of (non)-cardiomyocyte subpopulations) in both lines validated the implication of OCTN2. Furthermore, for some parameters (force, extracellular matrix abundance), the effect size for OCTN2 (N32S) was smaller than in the full knockout OCTN2 (-/-), suggesting a correlation of these parameters with residual OCTN2 function as observed in OCTN2 (N32S) carrier PCD patients *in vivo* (Rasmussen et al. 2014a). In consequence, for some parameters differences were statistically significant only for OCTN2 (-/-) but not for OCTN2 (N32S).

5.2 Faithful reproduction of the PCD DCM phenotype in the hiPSC-CM model

Typical features of PCD DCM in both patients and established animal models (JVS mice) are markedly reduced tissue contents of different carnitine derivatives, functional impairment in glucose and lipid metabolism, myocardial steatosis and severe hyperglycemia. Several key aspects could be replicated in the hiPSC-CM model in this study: OCTN2-defective EHTs revealed intracellular lipid droplet accumulation, reduced acylcarnitine tissue content, a decline in force under fatty acid media conditions and proteomic alterations of different metabolic pathways.

5.2.1 Impact of carnitine supplementation on force development and contractile kinetics

OCTN2 (-/-) EHTs displayed lower force than control EHTs, accompanied by changes in contractile kinetics, specifically longer contraction and relaxation times and shorter resting length. The force and contraction parameters of OCTN2 (N32S) EHTs were concordantly altered, but due to smaller effect size and high data scatter, the analysis only revealed a significant difference in contraction.

The slower contraction kinetics match well findings in the proteomic screen: A higher MYH7 protein abundance and changes in the extracellular matrix protein composition. The slower myosin isoform MYH7 is abundant in the human adult heart and skeletal muscle fibers that exhibit slow-twitch contraction kinetics (Lompre et al. 1984). In addition, Sewanan and colleagues could show that extracellular matrix abnormalities provoke a prolonged contraction and time-to-peak by using healthy hiPSC cardiomyocytes grown on an extracellular matrix derived from a hypertrophic cardiomyopathy swine model (Sewanan et al. 2019). Accordingly, the underlying molecular cause of the increased contraction-time in OCTN2 (N32S) and OCTN2 (-/-) EHTs might be the higher MYH7 protein abundance and changes in the extracellular matrix protein composition.

Supplementation with L-carnitine (2 mM) increased force in all hiPSC-CM lines, including the control EHTs. This inotropic effect of carnitine on control EHTs is noteworthy. The observation is in concordance with several studies that reported a positive inotropic effect of carnitine in heart failure patients (Zhang et al. 2018b) and in cardiomyopathy animal models without specific alteration of carnitine metabolism (Micheletti et al. 1993; Maresca et al. 1995). Furthermore, Ferrari and colleagues could demonstrate that a long-term administration of propionyl-L-carnitine induced a positive inotropic effect in isolated rabbit hearts (Ferrari et al. 1991). The mechanism of inotropy of carnitine might be mediated by long-chain acylcarnitine (LCAC) since carnitine is a substrate for LCAC. LCACs promote a sarcolemmal late Na^+ current and inhibit the Na^+/K^+ -ATPase (Wu and Corr 1994, 1995). This leads to increased intracellular sodium concentration, extrusion via $\text{Na}^+/\text{Ca}^{2+}$ -exchange protein 1 (NCX) and secondary increased intracellular calcium concentration. In addition to this acute effect, cardioprotective effects mediated by carnitine are likely relevant. In this context, reduction of oxidative stress, inhibition of mitochondrial membrane permeability transition and the prevention of pro-apoptotic protein expression were described (Furuno et al. 2001; Tousson et al. 2016). Another relevant mechanism may be improved glucose utilization, which was also evident in this study and is discussed in chapter 5.4.3.

The positive inotropic effect of carnitine supplementation in the OCTN2-defective hiPSC-CM is compatible with the beneficial effect of lifetime carnitine supplementation in PCD patients. In addition, carnitine supplementation led to a longer resting length, but both parameters did

not reach baseline values of isogenic controls. Moreover, similar effects of carnitine supplementation could be observed in the isogenic control line. This data implies that hiPSC-CM in EHT format do not fully recapitulate the cardiomyocyte condition of newborn PCD patients. The limited effect of carnitine supplementation on EHT contractility might be related to the status of a fibroblast subpopulation in OCTN2-defective EHTs as discussed in detail in chapter 5.5.2. Apart from fibrosis, the difference in force between cell lines is likely the consequence of maladaptive changes in several aspects such as acylcarnitine-metabolism and alterations in mitochondrial function as discussed below.

5.3 Fibrosis phenotype in OCTN2-defective EHTs

Fibrosis is a hallmark of DCM and is mainly mediated by the secretion of extracellular matrix proteins by activated fibroblasts, leading to increased cardiac stiffness and dysfunction (Masci et al. 2013). Quantitative proteomics of OCTN2-defective EHTs revealed fibrotic remodeling, characterized by enrichment of proteins involved in the KEGG term *extracellular matrix interaction* and higher abundance of extracellular matrix proteins like COL1A1, FN1 and VTN. This finding was further supported by a lower resting length observed in OCTN2-defective EHTs, a parameter indicative of fibroblast activity. An impressive example in this context is the neonatal mouse EHT model, which is prepared from whole heart homogenate, including proliferative atrial fibroblasts. EHTs from this cell source only develop normally and are stable over time if the fibroblasts are mitotically inactivated and otherwise show progressive shortening and no force development (Stöhr et al. 2013). Notably, the cardiomyocyte purity of the input cell population (between 70-100%) showed a significant positive correlation with force and resting length for the OCTN2-defective genotypes while no such correlation could be observed for the isogenic control. This implies a relevant negative impact of fibroblasts, likely due to an activated state. The relevance of fibroblasts was also evident from the snRNA-seq analysis, which showed prominent fibroblast clusters in the OCTN2-defective genotypes (Chapter 5.5.2). This central role of fibroblasts in the hiPSC-EHT model is paralleled by the clinical findings of a strong myocardial fibrosis phenotype in PCD patients (Wang et al. 2014b; Tomlinson et al. 2018; Grünert et al. 2020).

Recently published data suggests that carnitine administration protects against arterial hypertension-related and angiotensin II-induced cardiac fibrosis (Chao et al. 2010; Zambrano et al. 2013). This could imply that one mechanism of prophylactic carnitine supplementation in patients is related to preventing fibroblast activation. Nevertheless, carnitine supplementation failed to significantly decrease the elevated *COL1A1* mRNA expression in OCNT2 (N32S) EHTs, suggesting that the treatment is insufficient in preventing fibroblast activation and extracellular matrix secretion in this model. This finding could indicate that fibroblast activation might have occurred already during the differentiation process and an effective carnitine

treatment might require an earlier starting point. Interestingly, a similar finding was reported for two homozygous N32S mutation carriers who developed myocardial scarring and replacement fibrosis although they received prophylactic carnitine treatment (Kyhl et al. 2019).

5.4 Metabolic remodeling

Genome-wide analysis (proteomics, snRNA-seq) of OCTN2-defective vs control EHTs revealed differential regulation of 4 enriched pathways related to metabolism and mitochondrial function, namely alteration of *fatty acid, propionyl-CoA, glucose and pyruvate metabolism*. These pathways can be directly linked to (acyl)-carnitine deprivation and have been previously described in PCD-animal models (Horiuchi et al. 1993, 1999; Spaniol et al. 2001; Jalil et al. 2006; Asai et al. 2006). Additionally, *cholesterol metabolism, ferroptosis* and the *hexosamine biosynthetic pathway* were discovered as novel pathophysiologically dysregulated pathways in this study. The interaction of these pathways and the link to cellular subpopulations identified by snRNA-seq will be discussed in detail in the following four chapters.

5.4.1 Lipid metabolism and tissue content of acylcarnitine

One obvious consequence of intracellular carnitine reduction is a decrease of acylcarnitine suitable for mitochondrial entry and subsequent beta-oxidation (Longo et al. 2006). Indeed, mass spectrometry analysis of EHT revealed lower tissue content of several LCACs (C16:1, C18:0, C18:1 and C18:2 acylcarnitines) in OCTN2 (N32S) EHTs compared to OCTN2 (+/+) EHTs. Furthermore, the declining force during 96 hours of cultivation in a medium only containing linoleic and oleic acid also suggested a defect in long-chain fatty acid (LCFA) metabolism in OCTN2-defective EHTs.

Notably, supplementing standard EHT media with carnitine increased EHT acylcarnitine content for OCTN2 (+/+) and OCTN2 (N32S), reaching up to 80% of OCTN2 (+/+) baseline values. While this is compatible with the inotropic effect in both lines, the discrepancy between a large increase in acylcarnitine content and a smaller inotropic effect for OCTN2 (N32S) points to additional factors. One possible explanation could be the fibroblast activity as discussed above (Chapter 5.3). Moreover, proteomic analysis of OCTN2-defective EHTs revealed an enrichment of proteins related to KEGG pathways associated with metabolism and mitochondrial function (*fatty acid metabolism, oxidative phosphorylation* and *PPAR signalling*), suggesting complex metabolic remodeling as a relevant disease phenotype. These findings were accompanied by dysregulation of beta-oxidation- and TCA-cycle-related proteins and upregulation of proteins involved in the carnitine shuttle system. These proteomic changes likely represent a compensatory upregulation in response to carnitine deprivation. This hypothesis is concordant with several other studies, which reported a compensatory

upregulation of *CPT1* on mRNA and protein level in the heart and skeletal muscle of secondary carnitine deficiency animal models (Degrace et al. 2004; Liepinsh et al. 2008; Li et al. 2017).

Quantitative qPCR revealed a lower expression of the essential high-affinity fatty acid transporter *CD36* in OCTN2-defective EHTs. This observation was in line with the lower abundance of not only *CD36* but also additional fatty acid membrane transporters like *FABP5* and *FABP3* on protein level. *CD36* is a membrane transporter highly expressed in the heart and facilitates myocardial uptake of LCFAs from albumin- and triglyceride (TAG)-rich lipoproteins (Abumrad and Goldberg 2016). Furthermore, *CD36* transduces intracellular signaling pathways by adjusting fatty acid oxidation to the intracellular lipid availability via the metabolic key regulator adenosine monophosphate-activated protein kinase (AMPK, Habets et al. 2007; Samovski et al. 2015). In congruence with this, high expression of *CD36* is often accompanied by an upregulation of fatty acid oxidation and recent studies identified *CD36* as a predictive marker for mitochondrial-rich and matured hiPSC-CM (Poon et al. 2020; Funakoshi et al. 2021). In contrast, it has been reported that *CD36* deficiency attenuates obesity-induced oxidative stress by enhancing glycolysis and decreasing NADPH-oxidase dependant ROS-production (Gharib et al. 2016). Thus, the lower expression of this transporter might not only underline immaturity of OCTN2-defective cardiomyocytes, but also demonstrate a compensatory response to reduce intracellular cytosolic lipid content and to prevent further cellular fatty acid entry.

Interestingly, OCTN2 (N32S) and OCTN2 (-/-) also showed a higher abundance of LDLR, VLDLR, receptors that are known to mediate endocytosis of cholesterol-rich LDLs (Goldstein and Brown 2009). This was accompanied by a higher abundance of LRP1, a protein responsible for the uptake of very low-density lipoprotein-cholesteryl ester (VLDL-CE) in cardiomyocytes (Cal et al. 2012). Although predominantly steroidogenic cells such as adrenocortical cells and ovarian granulosa store cholesteryl ester in lipid droplets (Shen et al. 2016), this finding could indicate an increased uptake of LDL and cholesteryl ester from the culture medium and could link cholesterol and cholesteryl ester metabolism to the observed formation of lipid droplets identified in OCTN2 (N32S) by electron microscopy. In addition, OCTN2-defective EHTs also showed a high abundance of *NCEH1*, a key enzyme that has been proposed to hydrolyze cholesteryl ester to form free cholesterol and suppress lipid droplet formation in macrophages (Igarashi et al. 2010), and *HSD17B12*, a protein that has been shown to catalyze the transformation of cholesterol derived estrone (E1) into the major female sex hormone estradiol (E2) (Van Luu et al. 2006). Interestingly, snRNA-seq analysis revealed that *NCEH1* was primarily expressed in a leukocyte cluster and to a minor extent in OCTN2-defective cardiomyocytes. The relevance of the leukocyte cluster identified by snRNA-seq is discussed in detail in chapter 5.5.3.

The enrichment of proteins related to cholesterol metabolism in OCTN2-defective EHTs is in line with data from Zhang et al., who found that high cholesterol content in the plasma membrane of HEK293 cells and proteoliposomes stimulates OCTN2-mediated carnitine uptake by enhancing the affinity towards L-carnitine. The authors suggested a possible protective effect of carnitine against cholesterol facilitated lipotoxicity (Zhang et al. 2021).

Moreover, OCTN2-defective EHTs displayed a lower abundance of proteins involved in propanoate metabolism. This pathway is directly linked to fatty acid oxidation since propanoate is the conjugate base of propionyl-CoA, the final product of odd-chain fatty acid beta-oxidation (Wongkittichote et al. 2017). However, a conclusion based on protein abundance is difficult. On the one hand, these proteomic alterations could be related to diminished oxidation of odd-numbered LCFA. On the other hand, these alterations may represent a compensatory response to a toxic accumulation of propionyl-CoA derived from excessive odd-numbered medium-chain fatty acid oxidation that by-pass carnitine-dependent fatty acid oxidation. For instance, the therapeutic effect of alternative lipid sources was demonstrated by Roe et al. who showed that treatment with medium-odd-chain fatty acids reverses chronic cardiomyopathy in children with LCFA oxidation disorder (Roe et al. 2002).

Changes in propanoate metabolism most likely further compromise the TCA-cycle since propionyl-CoA represents an important anaplerotic intermediate after succinate conversion (Wongkittichote et al. 2017). In line with this, OCTN2-defective cell lines displayed a reorganization of TCA-cycle participating proteins. Remarkably, cholesterol is another substrate for propionyl-CoA production, which is produced when cholesterol is metabolized to bile acids (Russell and Setchell 1992). The enrichment of proteins related to cholesterol metabolism in OCTN2 (N32S) and particularly the profile of proteins relevant for cholesterol internalization (VLDL, LDL, LRP1) might indicate that cholesterol uptake is upregulated in a compensatory manner.

The potential relevance of altered propionyl-CoA metabolism for the OCTN2 (N32S) phenotype is additionally indicated by the fact that it is closely linked to amino acid metabolism (Wongkittichote et al. 2017). Proteins related to amino acid metabolism were lower abundant in OCTN2 (N32S). Propionyl-CoA can also be produced via amino acid oxidation, suggesting that in OCTN2 (N32S) amino acid synthesis and decay are altered in a complex manner. Of note, chronic accumulation of branched-chain amino acids additionally inhibits glucose oxidation via inactivation of pyruvate dehydrogenase (PDH) and suppression of amino acid catabolism has indeed been linked to maladaptive remodeling in heart failure (Sun et al. 2016).

5.4.2 Consequences of acyl-CoA accumulation: Ceramides, TAG, ferroptosis

A second important effect of cytosolic carnitine deprivation is a local increase of acyl residues linked to coenzyme A (CoA). This thio-esterification represents the first step of LCFA metabolism after their entry into the cytosol (Watkins et al. 2007). Excessive acyl-CoA accumulation is an essential driver of several processes involved in inflammation and apoptosis (Li et al. 2010b). In this context, acyl-CoA serves as a building block for various metabolic intermediates such as ceramides, TAG and cholesteryl ester (Cooper et al. 2015).

Mass spectrometry analysis of different ceramide species did not reveal a difference between the genotypes and no effect of carnitine supplementation. One potential reason for the lack of a difference could be the time of cultivation (28 days) that was not long enough for ceramides to accumulate. Additionally, ceramides do not represent the final product but a metabolic intermediate that can be processed to other sphingolipid derivatives such as glucosylceramides and sphingomyelin (MacEyka and Spiegel 2014). For this conversion, ceramides are transported from the endoplasmic reticulum (ER) into the trans golgi apparatus by the ceramide transporter CERT (Bandet and Hajduch 2021). Remarkably, CERT was among the 10 most significantly more abundant proteins in OCTN2 (N32S) EHTs. In line with this, Bandet et al. found that CERT overexpression in palmitate-treated C2C12 myotubes as well as in the anterior tibial muscle of diabetic mice prevents the accumulation of several long-chain ceramides (C16, C22, C24 and C24:1-ceramides) and ameliorates insulin resistance in these systems (Bandet et al. 2018). This study indicates a protective role of CERT, which regulates ceramide tissue contents and facilitates a rapid turnover.

Several reports highlighted the relevance of ratios of long- versus short-chain ceramides as a sensitive predictor of adverse cardiac events in clinical trials (Laaksonen et al. 2016; Peterson et al. 2018). Here, the clinical ceramide test score (CERT1) considers that a high concentration of C16:0 ceramides increases the risk of cardiac events by inducing mitochondrial dysfunction via the inactivation of Akt/PKB, ROS generation and inhibition of the electron transport chain (Stratford et al. 2004; Field et al. 2020). In contrast, very long-chain ceramides (such as C24:0 and C24:1) are considered to be benign and decrease the score. Accordingly, similar ratios were calculated from ceramide tissue concentrations in this study. A higher C16:0/C24:1 ratio was observed in OCTN2 (N32S) EHTs compared to isogenic control, which was reduced by carnitine supplementation. However, the CERT1 score is based on plasma ceramide concentration, while in this study tissue ceramide concentrations were investigated, suggesting that ceramide scores in this study are not directly comparable to established risk scores.

Moreover, cellular lipid excess in the form of acyl-CoA accumulation is known to ultimately result in the production of cholesteryl ester and TAG. This process takes place in the ER and can subsequently result in storage in cytosolic lipid droplets (Wilfling et al. 2013). Rate-limiting

key enzymes involved in the initial step of fatty acid esterification into TAG, such as diglyceride acyltransferase (DGAT) and glycerol-3-phosphate O-acyltransferase (GPAT) were not detected by quantitative proteomics in this work. However, OCTN2-defective EHTs showed a higher abundance of fat storage-inducing transmembrane protein 1 (FITM1), a protein that directly binds to TAG and facilitates TAG-rich lipid droplet accumulation (Gross et al. 2011) and adipose differentiation-related protein 2 (PLIN2), an essential protein responsible for the localization of TAG- and cholesteryl ester-rich lipid droplets to the membrane of lysosomes (Kaushik and Cuervo 2015; Li et al. 2021). The higher abundance of these marker proteins is in line with a conspicuous accumulation of lipid droplets in OCTN2 (N32S) EHTs identified by electron transmission microscopy. Of note, carnitine supplementation prevented lipid accumulation in these tissues, emphasizing the effect of carnitine on mitochondrial fatty acid degradation. These findings are consistent with data published by Cooper et al., who demonstrated that carnitine treatment prevents myocardial TAG accumulation and lipotoxic cardiomyopathy in JVS mice (Cooper et al. 2015).

Accumulation of cytoplasmic fatty acids has been linked to lipotoxicity (Cooper et al. 2015). In this context, the enrichment of proteins related to the KEGG pathway *ferroptosis* in OCTN2 (N32S) is noteworthy. Ferroptosis is a programmed iron- and ROS-dependent type of cell death that was recently described (Dixon et al. 2012). It does not show typical characteristics of necrosis, autophagy, and apoptosis-like organelle swelling, autophagic vacuoles or chromatin condensation. In contrast, ferroptosis is mainly associated with a decline of mitochondria exhibiting increased membrane density and reduced mitochondrial cristae (Li et al. 2020) which is compatible with the morphology of mitochondria of OCTN2-defective EHTs as assessed by electron microscopy and mitochondria quantification by qPCR. In this context, ACSL4 has been proposed as a key enzyme of ferroptosis as it mediates the enrichment of long polyunsaturated ω 6 fatty acids in cell membranes (Doll et al. 2017). The products of the resulting membrane lipid peroxidation are a crucial source of ROS production and drive ferroptotic cell death. The degraded mitochondrial morphology and the enrichment of proteins involved in ferroptosis again point to the lipotoxic effect of unconjugated LCFAs in the presence of impaired beta-oxidation. Interestingly, snRNA-seq analysis revealed a high expression of *ACSL4* in non-cardiomyocytes, enriched in OCTN2-defective cell lines. Of note, ferroptosis can spread over adjacent cell populations resulting in a spatiotemporal pattern of cell damage (Katikaneni et al. 2020; Riegman et al. 2020).

5.4.3 Glucose and pyruvate metabolism

The proteomic alterations of oxidative metabolism in OCTN2-defective EHTs were accompanied by a lower abundance of proteins related to carbohydrate KEGG pathways such as *glycolysis*, *pyruvate metabolism* and *pentose phosphate pathway* in OCTN2 (N32S). The pentose phosphate pathway provides the essential reducing agent NADPH which is also required to synthesize non-essential amino acids (Wamelink et al. 2008; Ju et al. 2020). Therefore, reduced activity of this pathway might further compromise amino acid metabolism and explain the lower abundance of proteins involved in arginine, proline and cysteine metabolism in OCTN2 (N32S).

The reorganization of the glycolytic proteome was evident by a lower abundance of glycolytic key proteins PFK, GAPDH and PKM and a downregulation of genes encoding for glycolytic proteins *GAPDH* and *HK2* on mRNA level. Surprisingly, OCTN2 (N32S) EHTs displayed a higher glucose uptake from the cell culture medium than OCTN2 (+/+). This observation is on the one hand contradicting the diminished glycolytic protein abundance but on the other hand compatible with data from JVS mice. Here, Ushikai et al. (2011) could show a higher glucose uptake in the heart in comparison to control mice.

Cardiac work as a major factor for ATP consumption in EHT was calculated by multiplying spontaneous force and beating frequency. Since ATP storage capabilities in cardiomyocytes are low (Stanley et al. 2005), the ratio of glucose consumption divided by force or cardiac work (multiplication of force and spontaneous beating frequency) was calculated as a surrogate for the efficiency of ATP consumption from glucose. This ratio was considerably higher for OCTN2-defective EHTs, i.e. the OCTN2-defective EHTs needed more glucose to perform the same work. Since the delta lactate/delta glucose ratio was not different for the three genotypes, this finding likely is not related to a higher degree of inefficient anaerobic glycolysis. It could therefore be an indicator of defective mitochondrial metabolism and decreased pyruvate oxidation and anaplerosis. This hypothesis was supported by the lower number of mitochondria (as indicated by mitochondrial DNA quantification), the defective mitochondrial morphology (transmission electron microscopy) and the proteomic dysregulation of oxidative phosphorylation and TCA-cycle. Carnitine media supplementation of standard EHT medium resulted in a reduction of delta glucose, delta lactate values for all three genotypes and a reduction of the L/G ratio for OCTN2 (-/-). In addition, carnitine supplementation reduced the glucose consumption per cardiac work in OCTN2-defective EHTs, which could be associated with more efficient glucose utilization. However, it needs to be stated that carnitine supplementation was performed in the presence of serum (lipoprotein)-containing EHT medium. Thus, the changes could also be primarily related to improved fatty acid oxidation leading indirectly to less glucose consumption.

The hypothesis of impaired glucose oxidation is supported by qPCR analysis that revealed higher *PDK4* mRNA level. Notably, the higher *PDK4* expression was normalized by carnitine supplementation to the baseline level of the isogenic control, indicating that *PDK4* upregulation was directly linked to carnitine deprivation. This finding is in line with data published by Horiuchi et al., who could show that *PDK4* mRNA and protein is higher in the heart of JVS mice (Horiuchi et al. 1999). The *PDK4* protein has a critical role in inactivating PDH under pathological and physiological conditions by phosphorylation of the E1 alpha subunit of PDH (PDHE1 α) resulting in impaired pyruvate oxidation (Rardin et al. 2009). Numerous studies demonstrated that short- or long-term administration of high-fat diet induces upregulation of *PDK4* and increases cardiac fatty acid oxidation in the hearts of mice, which was associated with a diabetic-like metabolic inflexibility (Crewe et al. 2013; Sikder et al. 2018; Newhardt et al. 2019). Moreover, Mori et al. could demonstrate that a deletion of *PDK4* results in improved glucose oxidation and prevention of diastolic dysfunction in angiotensin II (Ang II) treated mice, underlining the key role of *PDK4* in cardiac metabolic flexibility (Mori et al. 2013).

PDK4 activation, as observed in OCTN2 (N32S) EHTs, is a well-described response to lipid accumulation and lipotoxicity. Although *PDK4* activation promotes lipid degradation, long-term suppression of the PDH complex by *PDK4* promotes metabolic inflexibility and inhibition of glucose metabolism.

Interestingly, it has been reported that carnitine-induced improvement of cardiac function of isolated rat hearts from a model of secondary carnitine deficiency was more related to an increase in glucose oxidation than to normalized fatty acid metabolism (Broderick et al. 1995). In line with this, Savic et al. proposed the improvement of glucose oxidation via PDH as a central mechanism of carnitine treatment of diabetic cardiomyopathy (Savic et al. 2021). The role of carnitine in glucose oxidation is important since acetylcarnitine formation via CRAT is necessary to buffer excessive acetyl-CoA under conditions where acetyl-CoA production exceeds consumption in the TCA cycle (Uziel et al. 1988; Arenas et al. 1994). Moreover, mitochondrial acetyl-CoA accumulation impairs PDH flux by activating PDK, thus directly linking the carnitine shuttle system to PDH activity (Holness and Sugden 2003). This mechanism might additionally contribute to the activation of *PDK4*, the lower abundance of proteins involved in pyruvate oxidation and the inefficient glucose uptake in OCTN2-defective EHTs. Nevertheless, the higher glucose uptake in parallel with impaired glucose oxidation in both, JVS mice and OCTN2 (N32S) EHTs, appears as a paradox and suggests a disproportionate distribution of glucose via ancillary anabolic pathways.

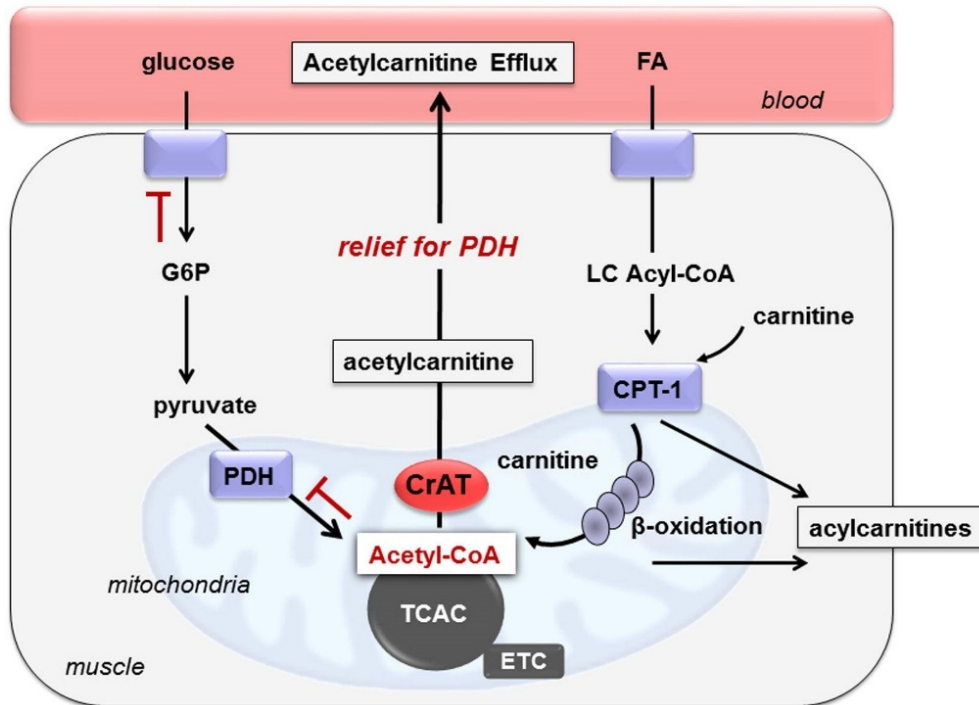


Figure 47: Role of carnitine and CRAT in regulating substrate switching and glucose tolerance. CRAT mediates acetylcarnitine efflux into the culture medium and therefore increases PDH activity by converting acetyl-CoA to acetylcarnitine ester. The red indicators depict the inhibitory effect of unbuffered acetyl-CoA on PDH and G6P conversion (Muio et al. 2012). G6P: Glucose-6-phosphate; PDH: Pyruvate dehydrogenase; TCAC: Tricarboxylic acid cycle; CRAT: Carnitine acetyltransferase; ETC: Electron transport chain; FA: Fatty acid; LC Acyl-CoA: Long-chain acyl-CoA; CPT-1: Carnitine palmitoyltransferase.

5.4.4 New aspects of PCD: O-linked β -N-acetylglucosamine pathway

Proteomic analysis revealed an enrichment of proteins related to KEGG pathways associated with the O-linked β -N-acetylglucosamine pathway in OCTN2-defective EHTs. Several proteins involved in O-linked- and N-linked-glycosylation were upregulated, including O-GlcNAc transferase and the rate-limiting enzyme GFPT1 which controls the flux of the hexosamine biosynthetic pathway. The hexosamine biosynthetic pathway is an alternative glucose metabolizing pathway resulting in uridine diphosphate N-acetylglucosamine (UDP-GlcNAc), a substrate for O-GlcNAcylation (Marshall et al. 1991; Chatham et al. 2008). O-GlcNAcylation in turn is a reversible post-translational modification controlled by O-GlcNAc transferase (OGT). It catalyzes the attachment of O-linked β -N-acetylglucosamine (O-GlcNAc) to serine and threonine amino acid residues. Conversely, O-GlcNAcase (OGA) catalyzes the removal of O-GlcNAc. OGT activity is required for postnatal cardiogenic maturation via mitochondrial protein modification and loss of OGT results in DCM and impaired coronary artery development in mice (Watson et al. 2014; Mu et al. 2020). Conversely, excessive O-GlcNAcylation induces

cardiac hypertrophy, arrhythmia and dysfunction via Ca²⁺/calmodulin-dependent protein kinase II (CaMKII) activation. The functional impact of O-linked-glycosylation end-products might be related to several O-GlcNAc modification sites of sarcomeric proteins such as troponin, actin and myosin (Ramirez-Correa et al. 2015). Importantly, elevated O-GlcNAcylation can also impair the function of proteins from the respiratory chain, disturbing mitochondrial function and promoting oxidative stress in the diabetic heart (Kaludercic and Di Lisa 2020). The additional relevance of fibroblasts and endocardium-like cells that potentially contribute to the activation of this pathway is discussed in chapter 5.5.2.

5.5 Single-nucleus RNA sequencing

In order to investigate cellular subclusters and the relevance of non-cardiomyocytes for the PCD DCM phenotype, single-nucleus RNA sequencing (snRNA-seq) was performed. This analysis revealed a smaller cardiomyocyte population, accompanied by an increased non-cardiomyocyte cluster containing cell types such as fibroblasts, endothelial cells, endocardium-like cells and leukocytes in OCTN2-defective cell lines.

5.5.1 Cardiomyocyte cluster definition and deviation in OCTN2-defective cell lines

Interestingly, snRNA-seq analysis results of OCTN2 (+/+) EHT show similarities to recent snRNA-seq analysis of the human heart with respect to heterogeneity and expression pattern of cardiomyocyte subpopulation: Several cardiomyocyte clusters identified in OCTN2 (+/+) EHTs were similar to clusters in the adult human heart (Litviňuková et al. 2020). Among these, one OCTN2 (+/+) cardiomyocyte population (CM6) shared the expression pattern of a specific ventricular cluster identified by Litviňuková et al. This cluster was characteristic for a high expression of *PRELID2*, a developmental molecule with unknown cardiac function, as well as *TBX20*, a transcription factor required for cardiac lineage specification and maturation of fetal cardiomyocytes (Chakraborty and Yutzey 2012). In contrast, one cardiomyocyte cluster enriched in OCTN2 (+/+) EHTs (CM8) displayed high expression of the atrial myosin isoform *MYL7* and recaptures the signature of an atrial population identified in the above-mentioned study. This cluster was furthermore characterized by high expression of *TBX5*, another transcriptional activator involved in cardiac development, which is highly expressed in the human atrium (Steimle and Moskowitz 2017). Another cluster with similar abundance in all OCTN2 genotypes (CM2) is analogous to a metabolically active ventricular population identified by Litviňuková et al. This cluster showed high expression of nuclear-encoded mitochondrial genes (*COX7C*, *ATP5F1B*), but also genes involved in cardiac contraction (*TNNC1*, *MYH7*, *MYL2*), and *CRYAB*, a heat shock protein with cytoprotective and antioxidant function (Fittipaldi et al. 2015).

The heterogeneity of hiPSC-CM identified in OCTN2 (+/+) EHT is in line with a study of Churko et al., who performed droplet-based scRNA-seq of 2D cultured hiPSC-CM. The authors found ventricular populations with strong *MYL2* expression and an immature atrial-like cardiomyocyte population with high expression of *TBX5* (similar to cluster CM8 in this study) underlining the heterogeneity and immaturity of hiPSC-CM (Churko et al. 2018). Not surprisingly, OCTN2 (+/+) EHTs similarly depict an enrichment of clusters pointing to immature atrial-like cardiomyocyte populations (CM8). Nevertheless, the high similarity of the cardiomyocyte clusters compared to the adult human heart underscores the relevance of this analysis.

On this basis, The OCTN2-defective EHTs were compared to OCTN2 (+/+) EHTs. While some clusters depicted a similar abundance in all OCTN2 genotypes (e.g. CM2) there were also 4 disease-specific cardiomyocyte clusters noted. Interestingly, these clusters were absent in OCTN2 (+/+) EHTs but similarly dominant in OCTN2 (N32S) and OCTN2 (-/-) EHTs. 3 of these 4 disease-specific clusters were not reflecting specific gene expression alterations associated with metabolism or pathological pathways previously identified in OCTN2-defective EHTs. In contrast, one cluster (CM1) showed an enrichment of genes involved in metabolism-associated terms such as *insulin secretion*, *cortisol synthesis* and *n-glycan biosynthesis*, matching well with the proteomic results.

A closer analysis of this cluster CM1 depicted the highest expression of *ACACB*, a mitochondrially located carboxylase that mediates the irreversible carboxylation of acetyl-CoA to malonyl-CoA (Cheng et al. 2007). In turn, malonyl-CoA is an allosteric inhibitor of CPT1b and therefore an essential inhibitor of beta-oxidation (Foster 2012). The high expression of this marker could be an indicator of accumulated acetyl-CoA in this cardiomyocyte population, a maladaptive consequence of diminished carnitine content as discussed in chapter 5.4.1. Interestingly, CM1 also exhibited high expression of *ESR1*, a receptor of the cholesterol-derived estrogen hormone estradiol (E2) (Klinge 2001) and the metabolic key regulator *FOXO1*. Notably, it has also been reported that high *ESR1* expression was associated with protection against apoptosis in mouse cardiomyocytes treated with hydrogen peroxide (Wang et al. 2010), suggesting a cardioprotective role of *ESR1*. Additionally, Zafirovic et al. demonstrated that E2 treatment diminishes nitric oxide synthase (iNOS) activity in the heart of high-fat treated rats via the PI3K/Akt signaling pathway, which was associated with a downregulation of CD36 protein (Zafirovic et al. 2017). A similar observation has been made by Zhang et al. who could show that *ESR1* activation results in diminished ROS production via the Akt-Nrf2 axis and decreased fibrosis via inhibition of the TGF β pathway in the heart of diabetic mice (Zhang et al. 2018a). Taken together, these findings further underscore unbuffered accumulation of acetyl-CoA as a disease phenotype and furthermore indicate that estrogen signaling might be upregulated in a compensatory manner in OCTN2-defective EHTs.

5.5.2 Fibroblast cluster and endocardium-like cluster

SnRNA-sequencing revealed a prominent fibroblasts cluster primarily in OCTN2 (-/-). Gene expression analysis between fibroblast clusters revealed a higher expression of *CCN2*, *POSTN*, and *FAP* in OCTN2-defective fibroblast. Of note, these genes are highly expressed in fibroblasts in infarcted hearts after injury (Humeres and Frangogiannis 2019). This was accompanied by lower expression of *TCF1*, a marker for quiescent fibroblasts, suggesting that OCTN2-defective fibroblasts exhibit an activated and proliferative phenotype. Additionally, OCTN2 (-/-) fibroblasts showed higher expression of *ACTA2* and *NOTCH3*, genes described in the context of infarct healing, when cardiac fibroblasts undergo a transition to a matrix-synthetic myofibroblast phenotype (Chen and Frangogiannis 2013). OCTN2-defective genotypes revealed a prominent endocardium-like cluster also characterized by genes involved in extracellular matrix synthesis. This was underlined by a high expression of the *HAPLN1* and *SERPINE1*, genes that were recently identified as early injury-response factors in the zebrafish endocardium (Münch et al. 2017) and injured neonatal mouse heart (Darehzereshki et al. 2015). This cluster most likely contributes to ECM formation in OCTN2-defective EHTs. Activation of ECM formation in OCTN2-defective EHTs is compatible with qPCR and proteomics results, indicating enrichment of ECM proteins and upregulation of fibroblast markers. It is important to point out that a fibrotic phenotype is not specific for PCD DCM and was recently demonstrated in DCM with different etiology by scRNA-seq. In this study the authors described an age-dependent increase of fibroblasts as well as a trend of an increased endothelial cell and leukocyte cluster in pediatric DCM failing heart samples across certain ages and DCM entities (Nicin et al. 2021).

Interestingly, snRNA-seq revealed that *GFPT1*, the rate-limiting enzyme of the hexosamine biosynthetic pathway, showed the highest expression in endocardium-like cells and fibroblasts enriched in OCTN2-defective EHTs, suggesting an important role of this pathway in non-cardiomyocytes. Apart from its impact on cardiomyocyte function, the hexosamine biosynthesis pathway also contributes to the synthesis of extracellular matrix as the production of proteoglycans and hyaluronic acid draws from a systolic pool of UDP-GlcNAc (Tran and Wang 2019). Moreover, Aguilar and colleagues demonstrated that high-glucose-induced protein O-GlcNAcylation stimulates cardiac fibroblast collagen synthesis, compatible with the higher glucose uptake and fibrotic phenotype of OCTN2-defective cell lines (Aguilar et al. 2014). Remarkably, it was also reported that the intermediate filament proteins vimentin and desmin demonstrate lectin-like GlcNAc-binding properties on the cell surface of cardiomyocytes and mediate the internalization of GlcNAc-modified molecules (Aso et al. 2007; Ise et al. 2010).

The hypothesis that this mechanism may be relevant in this PCD *in vitro* model is further supported by the observation that elevated O-GlcNAcylation is also known to activate the metabolic stress-responsive regulator *FOXO1* (Housley et al. 2008) which showed the highest expression in OCTN2-defective cardiomyocyte clusters in the snRNA-seq analysis.

FOXO1 was also found to be hyperactive in high-fat-induced obese mice and has recently emerged as a potential target for the treatment of diabetic cardiomyopathy as it is a direct activator of *PDK4* (Gopal et al. 2017). In line with this, *FOXO1* inhibition mediates cardioprotection in type-2-diabetes by enhancing *PDH* activity (Gopal et al. 2021). These studies link the hexosamine biosynthetic pathway with the inhibition of pyruvate metabolism and might indicate that non-cardiomyocytes in OCTN2-defective EHTs additionally contribute to metabolic dysfunction of cardiomyocytes via *FOXO1* activation. Consequently, both, *FOXO1* and *PDK4* might represent potential therapeutic targets to improve cardiac efficiency, attenuate fibrosis and prevent cardiac metabolic remodeling in this model.

5.5.3 Lipid metabolism and leukocytes

OCTN2-defective genotypes showed one additional myeloid progenitor cluster which was almost absent in the isogenic control. While this was an unexpected result at first glance, several studies provide a potential link between defects in carnitine- and lipid metabolism and myeloid cells. Interestingly, it has been shown that treatment with the *CPT1*-inhibitor malonyl-CoA promotes the expansion of hematopoietic stem progenitor cells and subsequently ameliorated blood reconstitution capacity by decreasing fatty acid oxidation and increasing *de novo* lipogenesis in these cells (Giger et al. 2020). An additional study suggested that long-term treatment with a high-fat diet not only increases the number and function of bone marrow progenitors but also skews their differentiation toward the myeloid lineage (Singer et al. 2014). In line with this, it was shown that supplementation of propionyl-L-carnitine ameliorates serum deprivation-induced impairment of mitochondrial beta-oxidation in a rat model of endothelial dysfunction and reduces adhesion of leukocytes to endothelial cells in this model (Igarashi et al. 2010). Thus, these studies provide evidence for the role of lipid metabolism in modulating hematopoietic stem cell biology and myeloid commitment, which might be the underlying mechanism causing the appearance of the myeloid cluster in OCTN2-defective EHTs.

5.6 Conclusion & outlook

In summary, EHTs generated from OCTN2-defective hiPSC-derived cardiomyocytes recapitulated hallmarks of PCD DCM and provided novel insights into the molecular and cellular mechanism of the disease. Impaired acylcarnitine formation was associated with lipid droplet accumulation, lower mitochondrial DNA abundance and alterations of proteins involved in mitochondrial metabolism and glycolysis. Quantitative proteomic analysis identified impairment of the PDH complex, and this was underlined by a higher mRNA abundance of *PDK4* in OCTN2-defective EHTs. In addition, proteomic analysis revealed ferroptosis and O-linked-glycosylation as novel pathways potentially contributing to metabolic remodeling in PCD. Carnitine supplementation normalized acylcarnitine tissue contents and *PDK4* abundance to levels of the isogenic control but had a minor effect on contractile parameters and could not decrease mRNA expression of the fibroblast marker *COL1A1*.

Cardiomyocyte subclusters identified in control EHTs recapitulated the gene expression patterns of a published single-cell transcriptomic analysis of the human heart, underlining the value of hiPSC-CM as an *in vitro* disease modeling platform. The enrichment of fetal- and atrial-like cardiomyocyte cell clusters in control EHTs emphasizes the immaturity of hiPSC derived cardiomyocytes and displays a major limitation of this model.

The different expression of metabolic key regulators revealed by single-nucleus RNA sequencing highlights the complexity of metabolic dysfunction-induced cardiomyopathy. In particular, the relevance of fibroblast biology was emphasized in this study and was relevant for the disease pathology. Implementing a multicellular EHT model with a defined proportion of different cardiac cell types or applying a cardiac organoid model as previously established might therefore be beneficial to investigate the pathomechanism of DCM systemically.

The pathways identified in this study were recently described in the context of different disease conditions and are therefore likely relevant therapeutic targets. Accordingly, this model provides the basis to analyze the effect of mitochondrial modulators (e.g., elamipretide, dichloroacetate), ferroptosis inhibitors (e.g., MAMC-3203, liproxstatin-1) or OGT/HBP inhibitors (e.g., Ac45S-GlcNAc, azaserine, OSMI-1) on the cardiomyopathy phenotype. In addition, the analysis of mitochondrial respiration rate and ATP production should confirm metabolic dysfunction of OCTN2-defective cardiomyocytes in future experiments.

6 Summary

Primary carnitine deficiency (PCD) is an autosomal recessive monogenic disorder caused by mutations in the gene *SLC22A5*, encoding for the plasmalemmal carnitine transporter OCTN2. PCD patients suffer from muscular weakness and dilated cardiomyopathy (DCM) due to reduced cellular carnitine uptake and require life-long oral L-carnitine supplementation. However, the initial disease mechanism of PCD is not clear, and predictive PCD *in vitro* models are required. Two principal mechanisms are considered relevant: (i) Impaired mitochondrial import of acylcarnitine leads to mitochondrial energy deprivation and (ii) reduced fatty acid metabolism results in cytoplasmic acyl-CoA accumulation, ceramide formation and lipotoxicity. To better characterize the molecular mechanism of PCD, CRISPR/Cas9 gene editing was used to generate hiPSC lines carrying a full OCTN2-knockout (OCTN2 (-/-)) and a homozygous point mutation (OCTN2 (N32S)) which is one of the most frequent OCTN2 mutations in PCD patients. The effect of the OCTN2 genotype on contractile force, proteome, single nuclear transcriptome and ultrastructural morphology was analyzed in a three-dimensional engineered heart tissue (EHT) model. In analogy to oral carnitine supplementation in PCD patients, the effect of carnitine media supplementation (2 mM) on contractile parameters and acylcarnitine and ceramide tissue content was studied.

OCTN2-defective genotypes exhibited lower cardiac differentiation efficiency (cardiomyocyte output over hiPSC input), but no difference in cardiomyocyte purity, demonstrated by a high percentage of cTNT-positive cells. OCTN2 (-/-) EHTs displayed lower force and resting length and higher contraction time under baseline conditions. While a similar trend was also observed for OCTN2 (N32S), this was not statistically significant due to high data scatter and smaller effect size. Unlike the isogenic control, force generation of both OCTN2-defective EHTs showed a positive correlation with cardiomyocyte purity (% of cTNT-positive cells), implicating a strong impact of non-cardiomyocytes on the disease phenotype in this model.

Apart from contractile readouts, OCTN2-defective EHTs showed molecular alterations which resembled characteristics of PCD animal models such as myocardial lipid droplet accumulation, higher glucose uptake and compensatory upregulation of proteins involved in the carnitine shuttle system. Further defects in mitochondrial metabolism were demonstrated by lower mitochondrial DNA abundance, degraded mitochondrial morphology and indirectly by a decline in force development in fatty acid medium. TMT-based proteomic analysis identified a lower abundance of proteins involved in glycolysis, pyruvate metabolism and dysregulation of proteins related to TCA-cycle and oxidative phosphorylation. Impairment of pyruvate metabolism was supported by upregulation of pyruvate dehydrogenase kinase 4 (*PDK4*) on mRNA level, reproducing an alteration described in the heart of a PCD animal model. A higher abundance of extracellular matrix- and fibrosis-related proteins implicated the relevance of

fibroblasts in this model, which was further supported by the strong representation of an activated fibroblast cluster in OCTN2-defective EHTs in single-nucleus RNA sequencing.

O-linked-glycosylation, a pathway recently described in the context of cardiac hypertrophy, was identified in the proteomic analysis as a mechanism that potentially contributes to metabolic remodeling in PCD. Moreover, ferroptosis was identified as a novel pathway in OCTN2-defective genotypes. This pathway describes an iron- and lipid-dependent cell death mechanism and linked the impairment of acylcarnitine metabolism with lipotoxicity.

Carnitine media supplementation normalized acylcarnitine tissue contents and *PDK4* transcript levels to isogenic control values and reduced lipid droplet accumulation and glucose consumption per cardiac workload. However, this intervention had only a minor effect on force development, and resting length and could not significantly decrease *COL1A1* mRNA expression in OCTN2 (N32S) EHTs, suggesting that the supplementation was ineffective in preventing all aspects of the disease phenotype.

Single-nuclear RNA sequencing revealed different clustering of cardiomyocyte subpopulations between isogenic control and OCTN2-defective EHTs with a higher expression of metabolic relevant regulators such as *FOXO1* and *ESR1* in the disease lines. Non-cardiomyocyte clusters like fibroblasts, endothelial cells and endocardium-like cells were enriched in OCTN2-defective EHTs. Additionally, the stronger representation of a leukocyte cluster in OCTN2-defective EHTs was compatible with a higher myeloid differentiation propensity of mesodermal progenitors.

Taken together, this study established a human *in vitro* model for PCD DCM which replicates several known PCD disease aspects and revealed disease-specific novel pathways and composition of cellular subclusters.

7 Zusammenfassung

Primäre Carnitindefizienz (PCD) ist eine autosomal rezessiv-vererbte monogenetische Erkrankung, die durch Mutationen im Gen *SLC22A5* verursacht wird. PCD-Patienten leiden unter Muskelschwäche und dilatativer Kardiomyopathie, welche durch eine verminderte zelluläre Carnitin-Aufnahme durch den *SLC22A5* codierten Transporter OCTN2 hervorgerufen wird. PCD-Patienten benötigen eine lebenslange orale L-Carnitin-Supplementation. Zwei Krankheitsmechanismen werden als relevant angesehen: Ein gestörter mitochondrialer Transport von Acylcarnitin führt zu verminderter mitochondrialer ATP-Produktion, und der reduzierte Fettsäurestoffwechsel führt zu zytoplasmatischer Acyl-CoA-Akkumulation, Ceramidbildung und Lipotoxizität. Die detaillierten Mechanismen der PCD sind jedoch unzureichend verstanden, weshalb prädiktive PCD-*In-vitro*-Modelle benötigt werden. In diesem Zusammenhang wurden im Rahmen dieser Arbeit zwei humane induzierte pluripotente Stammzell (hiPSC)-linien mittels CRISPR/Cas9-Genom-Editierung generiert, welche einen vollständigen OCTN2-Knockout (OCTN2 (-/-)) als auch eine klinisch relevante homozygote Punktmutation (OCTN2 (N32S)) tragen. Die isogene Kontroll-Zelllinie sowie die genomeditierten Zelllinien wurde zu Kardiomyozyten differenziert und dreidimensionale Herzgewebe (Engineered heart tissue, EHT) hergestellt. Die Auswirkung des OCTN2-Genotyps auf Kontraktionsparameter, das Proteom, das Einzel-Zell-Transkriptom und die ultrastrukturelle Morphologie wurden analysiert. In Analogie zur oralen L-Carnitin-Supplementation bei PCD-Patienten wurde der Effekt einer L-Carnitin-Medium-Supplementation (2 mM) auf kontraktile Parameter und den Acylcarnitin- sowie Ceramid-Gehalt des Gewebes untersucht.

OCTN2-defekte Genotypen zeigten eine geringere Effizienz der Kardiomyozyten Differenzierung (Kardiomyozyten-Output pro hiPSC-Input), aber keinen Unterschied in der Reinheit der Kardiomyozyten, was durch einen hohen prozentualen Anteil an cTNT-positiven Zellen gezeigt wurde. OCTN2 (-/-) EHTs wiesen unter Ausgangsbedingungen eine geringere Kraft und Länge im relaxierten Zustand, sowie eine längere Kontraktionszeit auf. Ein ähnlicher Trend wurde auch für OCTN2 (N32S) beobachtet, der jedoch aufgrund der großen Datenstreuung und der geringeren Effektgröße keine Signifikanz erreichte. Im Gegensatz zur isogenen Kontrolle, wies die Kraftentwicklung beider OCTN2-defekten EHTs eine positive Korrelation mit der Kardiomyozytenreinheit (% der TNT-positiven Zellen) auf, was auf einen starken Einfluss der Nicht-Kardiomyozyten auf den Krankheitsphänotyp in diesem Modell hindeutet.

OCTN2-defekte EHTs zeigten molekulare Veränderungen, die den Merkmalen von beschriebene PCD-Tiermodellen ähneln, wie z. B. die Akkumulation von Lipidtröpfchen im Myokard, eine höhere Glukoseaufnahme und eine kompensatorische Hochregulierung von Proteinen, die am Carnitin-Shuttle-System beteiligt sind. Weitere Defekte im mitochondrialen

Stoffwechsel wurden durch eine geringere mitochondriale DNA-Abundanz, eine defekte mitochondriale Morphologie und indirekt durch eine verminderte Kraftentwicklung in Fettsäuremedium im Zeitverlauf nachgewiesen. Eine TMT-basierte Proteomanalyse ergab eine geringere Abundanz von Proteinen, die an der Glykolyse und dem Pyruvat-Stoffwechsel beteiligt sind, sowie eine Dysregulation von Proteinen, die mit dem Citratzyklus und der oxidativen Phosphorylierung assoziiert sind. Die Beeinträchtigung des Pyruvat-Stoffwechsels wurde durch eine Hochregulierung der Pyruvat-Dehydrogenase-Kinase 4 (*PDK4*) auf mRNA-Ebene unterstützt. Weiterhin deutete eine höhere Abundanz von extrazellulären Matrix-Proteinen auf die Relevanz von Fibroblasten in diesem Modell hin, was durch ein prominentes Cluster von aktivierten Fibroblasten in OCTN2-defekten EHTs in der Einzelkern-RNA-Sequenzierung unterstützt wurde.

Die O-verknüpfte Glykosylierung, eine posttranslationale Modifizierung, die kürzlich im Zusammenhang mit kardialer Hypertrophie beschrieben wurde, wurde in der Proteomanalyse als ein Mechanismus identifiziert, der möglicherweise zur metabolischen Remodelierung von PCD beiträgt. Darüber hinaus wurde der eisen- und lipidabhängige Zelltodmechanismus Ferroptose als neuer Signalweg in OCTN2-defekten Genotypen identifiziert.

L-Carnitin-Medium- Supplementation normalisierte den Acylcarnitin-Gehalt im Gewebe und *PDK4*-Transkriptionswerte auf Werte der isogenen Kontrolle, und verringerte die Akkumulation von Lipidtröpfchen sowie den Glukoseverbrauch normalisiert zur kontraktilen Arbeit der EHTs. Diese Intervention hatte jedoch nur eine geringe Auswirkung auf die Kraftentwicklung und die Länge im relaxierten Zustand der EHTs und konnte die *COL1A1*-mRNA-expression in OCTN2 (N32S) EHTs nicht signifikant verringern, was darauf hindeutet, dass die Supplementation nicht alle Aspekte des Krankheitsphänotyps verhindern konnte.

Die Einzelkern-RNA-Sequenzierung ergab zusätzlich eine unterschiedliche Clusterbildung von Kardiomyozyten-Subpopulationen zwischen isogenen Kontroll- und OCTN2-defekten EHTs. Weiterhin zeigten sich unterschiedliche Expression von Stoffwechsel-relevanten Modulatoren wie *FOXO1* und *ESR1*. Nicht-Kardiomyozyten-Populationen wie Fibroblasten, Endothelzellen und Endokard-ähnliche Zellen waren in OCTN2-defekten EHTs angereichert. Darüber hinaus war die stärkere Repräsentation eines Leukozyten-Clusters in OCTN2-defekten EHTs mit einer höheren myeloischen Differenzierungsneigung der mesodermalen Vorläuferzellen vereinbar.

Insgesamt wurde in dieser Studie ein humanes *In-vitro*-Modell für PCD DCM entwickelt, das mehrere bekannte PCD-Krankheitsaspekte nachbildet und neue krankheits-spezifische Signalwege sowie die Zusammensetzung von zellulären Subpopulationen identifizieren konnte.

8 References

- Abumrad NA, Goldberg IJ (2016) CD36 actions in the heart: Lipids, calcium, inflammation, repair and more? *Biochim Biophys Acta - Mol Cell Biol Lipids* 1861:1442–1449. <https://doi.org/10.1016/j.bbalip.2016.03.015>
- Adikusuma F, Piltz S, Corbett MA, et al (2018) Large deletions induced by Cas9 cleavage. *Nature* 560:E8–E9. <https://doi.org/10.1038/s41586-018-0380-z>
- Aguilar H, Fricovsky E, Ihm S, et al (2014) Role for high-glucose-induced protein O-GlcNAcylation in stimulating cardiac fibroblast collagen synthesis. *Am J Physiol - Cell Physiol* 306:794–804. <https://doi.org/10.1152/ajpcell.00251.2013>
- Alpert NR, Brosseau C, Federico A, et al (2002) Molecular mechanics of mouse cardiac myosin isoforms. *Am J Physiol - Hear Circ Physiol* 283:1446–1454. <https://doi.org/10.1152/ajpheart.00274.2002>
- Amezquita RA, Lun ATL, Becht E, et al (2020) Orchestrating single-cell analysis with Bioconductor. *Nat Methods* 17:137–145. <https://doi.org/10.1038/s41592-019-0654-x>
- Amoasii L, Hildyard JCW, Li H, et al (2018) Gene editing restores dystrophin expression in a canine model of Duchenne muscular dystrophy. *Science (80-)* 362:86–91. <https://doi.org/10.1126/SCIENCE.AAU1549>
- Aravamudhan S, Türk C, Bock T, et al (2021) Phosphoproteomics of the developing heart identifies PERM1 - An outer mitochondrial membrane protein. *J Mol Cell Cardiol* 154:41–59. <https://doi.org/10.1016/j.yjmcc.2021.01.010>
- Arbustini E, Diegoli M, Fasani R, et al (1998) Mitochondrial DNA mutations and mitochondrial abnormalities in dilated cardiomyopathy. *Am J Pathol* 153:1501–1510. [https://doi.org/10.1016/S0002-9440\(10\)65738-0](https://doi.org/10.1016/S0002-9440(10)65738-0)
- Arenas J, Huertas R, Campos Y, et al (1994) Effects of l-carnitine on the pyruvate dehydrogenase complex and carnitine palmitoyl transferase activities in muscle of endurance athletes. *FEBS Lett* 341:91–93. [https://doi.org/10.1016/0014-5793\(94\)80246-7](https://doi.org/10.1016/0014-5793(94)80246-7)
- Asai T, Okumura K, Takahashi R, et al (2006) Combined therapy with PPAR α agonist and l-carnitine rescues lipotoxic cardiomyopathy due to systemic carnitine deficiency. *Cardiovasc Res* 70:566–577. <https://doi.org/10.1016/j.cardiores.2006.02.005>
- Aso S, Ise H, Takahashi M, et al (2007) Effective uptake of N-acetylglucosamine-conjugated liposomes by cardiomyocytes in vitro. *J Control Release* 122:189–198. <https://doi.org/10.1016/j.jconrel.2007.07.003>

- Bacigalupa ZA, Bhadiadra CH, Reginato MJ (2018) O-GlcNAcylation: key regulator of glycolytic pathways. *J Bioenerg Biomembr* 50:189–198. <https://doi.org/10.1007/s10863-018-9742-3>
- Balaban RS (2009) Domestication of the cardiac mitochondrion for energy conversion. *J Mol Cell Cardiol* 46:832–841. <https://doi.org/10.1016/j.yjmcc.2009.02.018>
- Bandet CL, Hajduch E (2021) CERT-Dependent Ceramide Transport, A Crucial Process in Cells. *J Diabetes Clin Res* 3:40–45. <https://doi.org/10.33696/diabetes.3.036>
- Bandet CL, Mahfouz R, Véret J, et al (2018) Ceramide Transporter CERT Is Involved in Muscle Insulin Signaling Defects Under Lipotoxic Conditions. *Diabetes* 67:1258–1271. <https://doi.org/10.2337/DB17-0901>
- Belke DD, Larsen TS, Lopaschuk GD, Severson DL (1999) Glucose and fatty acid metabolism in the isolated working mouse heart. *Am J Physiol - Regul Integr Comp Physiol* 277:1210–1217. <https://doi.org/10.1152/ajpregu.1999.277.4.r1210>
- Bertero E, Maack C (2018) Metabolic remodelling in heart failure. *Nat Rev Cardiol* 15:457–470. <https://doi.org/10.1038/s41569-018-0044-6>
- Boch J, Scholze H, Schornack S, et al (2009) Breaking the code of DNA binding specificity of TAL-type III effectors. *Science* (80-) 326:1509–1512. <https://doi.org/10.1126/SCIENCE.1178811>
- Braunwald E (2013) Heart failure. *JACC Hear Fail* 1:1–20. <https://doi.org/10.1016/j.jchf.2012.10.002>
- Breckwoldt K, Letuffe-Brenière D, Mannhardt I, et al (2017) Differentiation of cardiomyocytes and generation of human engineered heart tissue. *Nat Protoc* 12:1177–1197. <https://doi.org/10.1038/nprot.2017.033>
- Brinkman EK, Kousholt AN, Harmsen T, et al (2018) Easy quantification of template-directed CRISPR/Cas9 editing. *Nucleic Acids Res* 46:e58. <https://doi.org/10.1093/nar/gky164>
- Broderick TL, Panagakis G, DiDomenico D, et al (1995) L-carnitine improvement of cardiac function is associated with a stimulation in glucose but not fatty acid metabolism in carnitine-deficient hearts. *Cardiovasc Res* 30:815–820. [https://doi.org/10.1016/S0008-6363\(95\)00111-5](https://doi.org/10.1016/S0008-6363(95)00111-5)
- Bruyneel AA, McKeithan WL, Feyen DA, Mercola M (2018) Will iPSC-cardiomyocytes revolutionize the discovery of drugs for heart disease? *Curr Opin Pharmacol* 42:55–61. <https://doi.org/10.1016/j.coph.2018.07.003>

- Burkart AM, Tan K, Warren L, et al (2016) Insulin Resistance in Human iPS Cells Reduces Mitochondrial Size and Function. *Sci Rep* 6:1–12. <https://doi.org/10.1038/srep22788>
- Burridge PW, Anderson D, Priddle H, et al (2007) Improved Human Embryonic Stem Cell Embryoid Body Homogeneity and Cardiomyocyte Differentiation from a Novel V-96 Plate Aggregation System Highlights Interline Variability. *Stem Cells* 25:929–938. <https://doi.org/10.1634/stemcells.2006-0598>
- Burridge PW, Keller G, Gold JD, Wu JC (2012) Production of de novo cardiomyocytes: Human pluripotent stem cell differentiation and direct reprogramming. *Cell Stem Cell* 10:16–28. <https://doi.org/10.1016/j.stem.2011.12.013>
- Burridge PW, Matsa E, Shukla P, et al (2014) Chemically defined generation of human cardiomyocytes. *Nat Methods* 11:855–860. <https://doi.org/10.1038/nMeth.2999>
- Cal R, Castellano J, Revuelta-López E, et al (2012) Low-density lipoprotein receptor-related protein 1 mediates hypoxia-induced very low density lipoprotein-cholesterol uptake and accumulation in cardiomyocytes. *Cardiovasc Res* 94:469–479. <https://doi.org/10.1093/cvr/cvs136>
- Camman M, Joanne P, Agbulut O, Hélarly C (2022) 3D models of dilated cardiomyopathy: Shaping the chemical, physical and topographical properties of biomaterials to mimic the cardiac extracellular matrix. *Bioact Mater* 7:275–291. <https://doi.org/10.1016/j.bioactmat.2021.05.040>
- Chabowski A, Gorski J, Glatz J, et al (2008) Protein-mediated Fatty Acid Uptake in the Heart. *Curr Cardiol Rev* 4:12–21. <https://doi.org/10.2174/157340308783565429>
- Chaiyawat P, Chokchaichamnankit D, Lirdprapamongkol K, et al (2015) Alteration of O-GlcNAcylation affects serine phosphorylation and regulates gene expression and activity of pyruvate kinase M2 in colorectal cancer cells. *Oncol Rep* 34:1933–1942. <https://doi.org/10.3892/or.2015.4178>
- Chakraborty S, Yutzey KE (2012) Tbx20 regulation of cardiac cell proliferation and lineage specialization during embryonic and fetal development in vivo. *Dev Biol* 363:234–246. <https://doi.org/10.1016/J.YDBIO.2011.12.034>
- Chao HH, Chen CH, Liu JC, et al (2010) L-Carnitine attenuates angiotensin II-induced proliferation of cardiac fibroblasts: Role of NADPH oxidase inhibition and decreased sphingosine-1-phosphate generation. *J Nutr Biochem* 21:580–588. <https://doi.org/10.1016/j.jnutbio.2009.03.003>
- Chatham JC, Nöt LG, Fülöp N, Marchase RB (2008) Hexosamine biosynthesis and protein

- O-glycosylation: The first line of defense against stress, ischemia, and trauma. *Shock* 29:431–440. <https://doi.org/10.1097/SHK.0b013e3181598bad>
- Chen F, Pruett-Miller SM, Huang Y, et al (2011) High-frequency genome editing using ssDNA oligonucleotides with zinc-finger nucleases. *Nat Methods* 8:753–757. <https://doi.org/10.1038/nmeth.1653>
- Chen W, Frangogiannis NG (2013) Fibroblasts in post-infarction inflammation and cardiac repair. *Biochim Biophys Acta - Mol Cell Res* 1833:945–953. <https://doi.org/10.1016/J.BBAMCR.2012.08.023>
- Cheng D, Chu CH, Chen L, et al (2007) Expression, purification, and characterization of human and rat acetyl cenzyme A carboxylase (ACC) isozymes. *Protein Expr Purif* 51:11–21. <https://doi.org/10.1016/j.pep.2006.06.005>
- Chin MH, Mason MJ, Xie W, et al (2009) Induced Pluripotent Stem Cells and Embryonic Stem Cells Are Distinguished by Gene Expression Signatures. *Cell Stem Cell* 5:111–123. <https://doi.org/10.1016/J.STEM.2009.06.008>
- Cho SW, Kim S, Kim JM, Kim JS (2013) Targeted genome engineering in human cells with the Cas9 RNA-guided endonuclease. *Nat Biotechnol* 31:230–232. <https://doi.org/10.1038/nbt.2507>
- Chung S, Dzeja PP, Faustino RS, et al (2007) Mitochondrial oxidative metabolism is required for the cardiac differentiation of stem cells. *Nat Clin Pract Cardiovasc Med* 2007 41 4:S60–S67. <https://doi.org/10.1038/ncpcardio0766>
- Churko JM, Garg P, Treutlein B, et al (2018) Defining human cardiac transcription factor hierarchies using integrated single-cell heterogeneity analysis. *Nat Commun* 9. <https://doi.org/10.1038/s41467-018-07333-4>
- Churko JM, Lee J, Ameen M, et al (2017) Transcriptomic and epigenomic differences in human induced pluripotent stem cells generated from six reprogramming methods. *Nat Biomed Eng* 2017 110 1:826–837. <https://doi.org/10.1038/s41551-017-0141-6>
- Concordet JP, Haeussler M (2018) CRISPOR: Intuitive guide selection for CRISPR/Cas9 genome editing experiments and screens. *Nucleic Acids Res* 46:W242–W245. <https://doi.org/10.1093/nar/gky354>
- Cooper DE, Young PA, Klett EL, Coleman RA (2015) Physiological consequences of compartmentalized acyl-CoA metabolism. *J Biol Chem* 290:20023–20031. <https://doi.org/10.1074/jbc.R115.663260>
- Correia C, Koshkin A, Duarte P, et al (2017) Distinct carbon sources affect structural and

- functional maturation of cardiomyocytes derived from human pluripotent stem cells. *Sci Rep* 7:1–17. <https://doi.org/10.1038/s41598-017-08713-4>
- Crewe C, Kinter M, Szweda LI (2013) Rapid Inhibition of Pyruvate Dehydrogenase: An Initiating Event in High Dietary Fat-Induced Loss of Metabolic Flexibility in the Heart. *PLoS One* 8:1–15. <https://doi.org/10.1371/journal.pone.0077280>
- Daer RM, Cutts JP, Brafman DA, Haynes KA (2017) The Impact of Chromatin Dynamics on Cas9-Mediated Genome Editing in Human Cells. *ACS Synth Biol* 6:428–438. <https://doi.org/10.1021/acssynbio.5b00299>
- Darehzereshki A, Rubin N, Gamba L, et al (2015) Differential regenerative capacity of neonatal mouse hearts after cryoinjury. *Dev Biol* 399:91–99. <https://doi.org/10.1016/J.YDBIO.2014.12.018>
- De Korte T, Katili PA, Mohd Yusof NAN, et al (2020) Unlocking personalized biomedicine and drug discovery with human induced pluripotent stem cell-derived cardiomyocytes: Fit for purpose or forever elusive? *Annu Rev Pharmacol Toxicol* 60:529–551. <https://doi.org/10.1146/annurev-pharmtox-010919-023309>
- Degrace P, Demizieux L, Gresti J, et al (2004) Fatty acid oxidation and related gene expression in heart depleted of carnitine by mildronate treatment in the rat. *Mol Cell Biochem* 258:171–182. <https://doi.org/10.1023/B:MCBI.0000012853.20116.06>
- Deltcheva E, Chylinski K, Sharma CM, et al (2011) CRISPR RNA maturation by trans-encoded small RNA and host factor RNase III. *Nature* 471:602–607. <https://doi.org/10.1038/nature09886>
- Dixon SJ, Lemberg KM, Lamprecht MR, et al (2012) Ferroptosis: An iron-dependent form of nonapoptotic cell death. *Cell* 149:1060–1072. <https://doi.org/10.1016/j.cell.2012.03.042>
- Doenst T, Nguyen TD, Abel ED (2013) Cardiac metabolism in heart failure: Implications beyond atp production. *Circ Res* 113:709–724. <https://doi.org/10.1161/CIRCRESAHA.113.300376>
- Doll S, Proneth B, Tyurina YY, et al (2017) ACSL4 dictates ferroptosis sensitivity by shaping cellular lipid composition. *Nat Chem Biol* 13:91–98. <https://doi.org/10.1038/nchembio.2239>
- Eschenhagen T, Carrier L (2019) Cardiomyopathy phenotypes in human-induced pluripotent stem cell-derived cardiomyocytes—a systematic review. *Pflugers Arch Eur J Physiol* 471:755–768. <https://doi.org/10.1007/s00424-018-2214-0>
- Eschenhagen T, Fink C, Remmers U, et al (1997) Three-dimensional reconstitution of

- embryonic cardiomyocytes in a collagen matrix: a new heart muscle model system. *FASEB J* 11:683–694. <https://doi.org/10.1096/fasebj.11.8.9240969>
- Evans AM, Fornasini G (2003) Pharmacokinetics of L-carnitine. *Clin Pharmacokinet* 42:941–967. <https://doi.org/10.2165/00003088-200342110-00002>
- Fairweather DL, Cooper LT, Blauwet LA (2013) Sex and Gender Differences in Myocarditis and Dilated Cardiomyopathy. *Curr Probl Cardiol* 38:7–46. <https://doi.org/10.1016/j.cpcardiol.2012.07.003>
- Fang Y, Lai KS, She P, et al (2020) Tbx20 Induction Promotes Zebrafish Heart Regeneration by Inducing Cardiomyocyte Dedifferentiation and Endocardial Expansion. *Front Cell Dev Biol* 8:1–17. <https://doi.org/10.3389/fcell.2020.00738>
- Ferrari R, Pasini E, Condorelli E, et al (1991) Effect of propionyl-L-carnitine on mechanical function of isolated rabbit heart. *Cardiovasc drugs Ther* 5 Suppl 1:17–23. <https://doi.org/10.1007/BF00128239>
- Feyen DAM, McKeithan WL, Bruyneel AAN, et al (2020) Metabolic Maturation Media Improve Physiological Function of Human iPSC-Derived Cardiomyocytes. *Cell Rep* 32:. <https://doi.org/10.1016/j.celrep.2020.107925>
- Field BC, Gordillo R, Scherer PE (2020) The Role of Ceramides in Diabetes and Cardiovascular Disease Regulation of Ceramides by Adipokines. *Front Endocrinol (Lausanne)* 0:763. <https://doi.org/10.3389/FENDO.2020.569250>
- Fittipaldi S, Mercatelli N, Dimaur- I, et al (2015) Alpha B-crystallin induction in skeletal muscle cells under redox imbalance is mediated by a JNK-dependent regulatory mechanism. *Free Radic Biol Med*. <https://doi.org/10.1016/j.freeradbiomed.2015.05.035>
- Foster DW (2012) Malonyl-CoA: The regulator of fatty acid synthesis and oxidation. *J Clin Invest* 122:1958–1959. <https://doi.org/10.1172/JCI63967>
- Funakoshi S, Fernandes I, Mastikhina O, et al (2021) Generation of mature compact ventricular cardiomyocytes from human pluripotent stem cells. *Nat Commun* 12:. <https://doi.org/10.1038/s41467-021-23329-z>
- Furuno T, Kanno T, Arita K, et al (2001) Roles of long chain fatty acids and carnitine in mitochondrial membrane permeability transition. *Biochem Pharmacol* 62:1037–1046. [https://doi.org/10.1016/S0006-2952\(01\)00745-6](https://doi.org/10.1016/S0006-2952(01)00745-6)
- Garbern JC, Lee RT (2021) Mitochondria and metabolic transitions in cardiomyocytes: lessons from development for stem cell-derived cardiomyocytes. *Stem Cell Res Ther* 2021 121 12:1–25. <https://doi.org/10.1186/S13287-021-02252-6>

- Garneau JE, Dupuis MÈ, Villion M, et al (2010) The CRISPR/cas bacterial immune system cleaves bacteriophage and plasmid DNA. *Nature* 468:67–71.
<https://doi.org/10.1038/nature09523>
- Geraets IME, Glatz JFC, Luiken JJFP, Nabben M (2019) Pivotal role of membrane substrate transporters on the metabolic alterations in the pressure-overloaded heart. *Cardiovasc Res* 115:1000–1012. <https://doi.org/10.1093/cvr/cvz060>
- Gharib M, Tao H, Fungwe T V., Hajri T (2016) Cluster Differentiating 36 (CD36) Deficiency Attenuates Obesity-Associated Oxidative Stress in the Heart. *PLoS One* 11:e0155611.
<https://doi.org/10.1371/JOURNAL.PONE.0155611>
- Giesbertz P, Ecker J, Haag A, et al (2015) An LC-MS/MS method to quantify acylcarnitine species including isomeric and odd-numbered forms in plasma and tissues. *J Lipid Res* 56:2029–2039. <https://doi.org/10.1194/jlr.D061721>
- Giger S, Kovtonyuk L V., Utz SG, et al (2020) A Single Metabolite which Modulates Lipid Metabolism Alters Hematopoietic Stem/Progenitor Cell Behavior and Promotes Lymphoid Reconstitution. *Stem Cell Reports* 15:566–576.
<https://doi.org/10.1016/j.stemcr.2020.07.021>
- Godier-Furnémont AFG, Tiburcy M, Wagner E, et al (2015) Physiologic force-frequency response in engineered heart muscle by electromechanical stimulation. *Biomaterials* 60:82–91. <https://doi.org/10.1016/J.BIOMATERIALS.2015.03.055>
- Goldstein JL, Brown MS (2009) The LDL receptor. *Arterioscler Thromb Vasc Biol* 29:431–438. <https://doi.org/10.1161/ATVBAHA.108.179564>
- Gopal K, Al Batran R, Altamimi TR, et al (2021) FoxO1 inhibition alleviates type 2 diabetes-related diastolic dysfunction by increasing myocardial pyruvate dehydrogenase activity. *Cell Rep* 35:. <https://doi.org/10.1016/j.celrep.2021.108935>
- Gopal K, Saleme B, Batran R Al, et al (2017) FoxO1 regulates myocardial glucose oxidation rates via transcriptional control of pyruvate dehydrogenase kinase 4 expression. *Am J Physiol - Hear Circ Physiol* 313:H479–H490.
<https://doi.org/10.1152/ajpheart.00191.2017>
- Gross DA, Zhan C, Silver DL (2011) Direct binding of triglyceride to fat storage-inducing transmembrane proteins 1 and 2 is important for lipid droplet formation. *Proc Natl Acad Sci* 108:19581–19586. <https://doi.org/10.1073/PNAS.1110817108>
- Grünert SC, Tucci S, Schumann A, et al (2020) Primary carnitine deficiency-diagnosis after heart transplantation: Better late than never! *Orphanet J Rare Dis* 15:4–9.

<https://doi.org/10.1186/s13023-020-01371-2>

Guo Q, Mintier G, Ma-Edmonds M, et al (2018) “Cold shock” increases the frequency of homology directed repair gene editing in induced pluripotent stem cells. *Sci Rep* 8:1–11. <https://doi.org/10.1038/s41598-018-20358-5>

Habets DDJ, Coumans WA, Voshol PJ, et al (2007) AMPK-mediated increase in myocardial long-chain fatty acid uptake critically depends on sarcolemmal CD36. *Biochem Biophys Res Commun* 355:204–210. <https://doi.org/10.1016/j.bbrc.2007.01.141>

Hansen A, Eder A, Bönstrup M, et al (2010) Development of a drug screening platform based on engineered heart tissue. *Circ Res* 107:35–44. <https://doi.org/10.1161/CIRCRESAHA.109.211458>

Hashem SI, Murphy AN, Divakaruni AS, et al (2017) Impaired mitophagy facilitates mitochondrial damage in Danon disease. *J Mol Cell Cardiol* 108:86–94. <https://doi.org/10.1016/j.yjmcc.2017.05.007>

Haurwitz RE, Jinek M, Wiedenheft B, et al (2010) Sequence- and structure-specific RNA processing by a CRISPR endonuclease. *Science* (80-) 329:1355–1358. <https://doi.org/10.1126/science.1192272>

Hershberger RE (2010) A Glimpse Into Multigene Rare Variant Genetics. Triple Mutations in Hypertrophic Cardiomyopathy. *J Am Coll Cardiol* 55:1454–1455. <https://doi.org/10.1016/j.jacc.2009.12.025>

Hew KW, Keller KA (2003) Postnatal anatomical and functional development of the heart: A species comparison. *Birth Defects Res Part B - Dev Reprod Toxicol* 68:309–320. <https://doi.org/10.1002/bdrb.10034>

Hick A, Wattenhofer-Donzé M, Chintawar S, et al (2013) Neurons and cardiomyocytes derived from induced pluripotent stem cells as a model for mitochondrial defects in Friedreich’s ataxia. *DMM Dis Model Mech* 6:608–621. <https://doi.org/10.1242/dmm.010900>

Hirt MN, Boeddinghaus J, Mitchell A, et al (2014) Functional improvement and maturation of rat and human engineered heart tissue by chronic electrical stimulation. *J Mol Cell Cardiol* 74:151–161. <https://doi.org/10.1016/j.yjmcc.2014.05.009>

Hirt MN, Sörensen NA, Bartholdt LM, et al (2012) Increased afterload induces pathological cardiac hypertrophy: A new in vitro model. *Basic Res Cardiol* 107:. <https://doi.org/10.1007/s00395-012-0307-z>

Holness MJ, Sugden MC (2003) Regulation of pyruvate dehydrogenase complex activity by

- reversible phosphorylation. *Biochem Soc Trans* 31:1143–1151.
<https://doi.org/10.1042/BST0311143>
- Horikoshi Y, Yan Y, Terashvili M, et al (2019) Cardiomyocyte-Like Energy Metabolism Phenotypes. *Cells* 8:
- Horiuchi M, Kobayashi K, Masuda M, et al (1999) Pyruvate dehydrogenase kinase 4 mRNA is increased in the hypertrophied ventricles of carnitine-deficient juvenile visceral steatosis (JVS) mice. *BioFactors* 10:301–309. <https://doi.org/10.1002/biof.5520100232>
- Horiuchi M, Yoshida H, Kobayashi K, et al (1993) Cardiac hypertrophy in juvenile visceral steatosis (jvs) mice with systemic carnitine deficiency. *FEBS Lett* 326:267–271.
[https://doi.org/10.1016/0014-5793\(93\)81805-A](https://doi.org/10.1016/0014-5793(93)81805-A)
- Houser SR, Margulies KB, Murphy AM, et al (2012) Animal Models of Heart Failure. *Circ Res* 78–94. <https://doi.org/10.1161/RES.0B013E3182582523>
- Housley MP, Rodgers JT, Udeshi ND, et al (2008) O-GlcNAc regulates FoxO activation in response to glucose. *J Biol Chem* 283:16283–16292.
<https://doi.org/10.1074/jbc.M802240200>
- Humeres C, Frangogiannis NG (2019) Fibroblasts in the Infarcted, Remodeling, and Failing Heart. *JACC Basic to Transl Sci* 4:449–467. <https://doi.org/10.1016/j.jacbts.2019.02.006>
- Huo J, Kamalakar A, Yang X, et al (2017) Evaluation of batch variations in induced pluripotent stem cell-derived human cardiomyocytes from 2 major suppliers. *Toxicol Sci* 156:25–38. <https://doi.org/10.1093/toxsci/kfw235>
- Hwang HS, Kryshnal DO, Feaster TK, et al (2015) Comparable calcium handling of human iPSC-derived cardiomyocytes generated by multiple laboratories. *J Mol Cell Cardiol* 85:79–88. <https://doi.org/10.1016/j.yjmcc.2015.05.003>
- Igarashi M, Osuga JI, Uozaki H, et al (2010) The critical role of neutral cholesterol ester hydrolase 1 in cholesterol removal from human macrophages. *Circ Res* 107:1387–1395.
<https://doi.org/10.1161/CIRCRESAHA.110.226613>
- Ise H, Kobayashi S, Goto M, et al (2010) Vimentin and desmin possess GlcNAc-binding lectin-like properties on cell surfaces. *Glycobiology* 20:843–864.
<https://doi.org/10.1093/glycob/cwq039>
- Jalil MA, Horiuchi M, Wakamatsu M, et al (2006) Attenuation of cardiac hypertrophy in carnitine-deficient juvenile visceral steatosis (JVS) mice achieved by lowering dietary lipid. *J Biochem* 139:263–270. <https://doi.org/10.1093/jb/mvj032>

- Jaswal JS, Keung W, Wang W, et al (2011) Targeting fatty acid and carbohydrate oxidation - A novel therapeutic intervention in the ischemic and failing heart. *Biochim Biophys Acta - Mol Cell Res* 1813:1333–1350. <https://doi.org/10.1016/j.bbamcr.2011.01.015>
- Jinek M, Chylinski K, Fonfara I, et al (2012) A Programmable Dual-RNA–Guided DNA Endonuclease in Adaptive Bacterial Immunity — Supplementary Materials. 337:816–821
- Ju HQ, Lin JF, Tian T, et al (2020) NADPH homeostasis in cancer: functions, mechanisms and therapeutic implications. *Signal Transduct Target Ther* 5:1–12. <https://doi.org/10.1038/s41392-020-00326-0>
- Kaludercic N, Di Lisa F (2020) Mitochondrial ROS Formation in the Pathogenesis of Diabetic Cardiomyopathy. *Front Cardiovasc Med* 7:1–15. <https://doi.org/10.3389/fcvm.2020.00012>
- Kapelko VI (2001) Extracellular matrix alterations in cardiomyopathy: The possible crucial role in the dilative form. *Exp Clin Cardiol* 6:41–49
- Karamanlidis G, Lee CF, Garcia-Menendez L, et al (2013) Mitochondrial Complex I Deficiency Increases Protein Acetylation and Accelerates Heart Failure. *Cell Metab* 18:239–250. <https://doi.org/10.1016/J.CMET.2013.07.002>
- Katikaneni A, Jelcic M, Gerlach GF, et al (2020) Lipid peroxidation regulates long-range wound detection through 5-lipoxygenase in zebrafish. *Nat Cell Biol* 22:1049–1055. <https://doi.org/10.1038/s41556-020-0564-2>
- Kaushik S, Cuervo AM (2015) Degradation of lipid droplet-associated proteins by chaperone-mediated autophagy facilitates lipolysis. *Nat Cell Biol* 17:759–770. <https://doi.org/10.1038/ncb3166>
- Kaushik VK, Kavana M, Volz JM, et al (2009) Characterization of recombinant human acetyl-CoA carboxylase-2 steady-state kinetics. *Biochim Biophys Acta - Proteins Proteomics* 1794:961–967. <https://doi.org/10.1016/j.bbapap.2009.02.004>
- Kilic M, Özgül RK, Coşkun T, et al (2011) Identification of Mutations and Evaluation of Cardiomyopathy in Turkish Patients with Primary Carnitine Deficiency. *JIMD Rep* 3:17–23. https://doi.org/10.1007/8904_2011_36
- Kilpinen H, Goncalves A, Leha A, et al (2017) Common genetic variation drives molecular heterogeneity in human iPSCs. *Nat* 546:370–375. <https://doi.org/10.1038/nature22403>
- Kim C, Wong J, Wen J, et al (2013) Studying arrhythmogenic right ventricular dysplasia with

- patient-specific iPSCs. *Nature* 494:105–110. <https://doi.org/10.1038/nature11799>
- Kim YG, Cha J, Chandrasegaran S (1996) Hybrid restriction enzymes: Zinc finger fusions to Fok I cleavage domain. *Proc Natl Acad Sci U S A* 93:1156–1160. <https://doi.org/10.1073/pnas.93.3.1156>
- Klinge CM (2001) Estrogen receptor interaction with estrogen response elements. *Nucleic Acids Res* 29:2905–2919. <https://doi.org/10.1093/nar/29.14.2905>
- Knottnerus SJG, Mengarelli I, Wüst RCI, et al (2020) Electrophysiological Abnormalities in VLCAD Deficient hiPSC-Cardiomyocytes Can Be Improved by Lowering Accumulation of Fatty Acid Oxidation Intermediates. *Int J Mol Sci* 21:2589. <https://doi.org/10.3390/IJMS21072589>
- Koizumi T, Nikaido H, Nonomura A, Yoneda T (1988) Infantile disease with microvesicular fatty infiltration of viscera spontaneously occurring in the C3H-H-2° strain of mouse with similarities to Reye's syndrome. *Lab Anim* 22:83–87. <https://doi.org/10.1258/002367788780746511>
- Kolwicz SC, Purohit S, Tian R (2013) Cardiac metabolism and its interactions with contraction, growth, and survival of cardiomyocytes. *Circ Res* 113:603–616. <https://doi.org/10.1161/CIRCRESAHA.113.302095>
- Kosicki M, Tomberg K, Bradley A (2018) Repair of double-strand breaks induced by CRISPR–Cas9 leads to large deletions and complex rearrangements. *Nat Biotechnol* 36:. <https://doi.org/10.1038/nbt.4192>
- Krenz M, Sanbe A, Bouyer-Dalloz F, et al (2003) Analysis of myosin heavy chain functionality in the heart. *J Biol Chem* 278:17466–17474. <https://doi.org/10.1074/jbc.M210804200>
- Kyhl K, Róin T, Lund A, et al (2019) Cardiac function and incidence of unexplained myocardial scarring in patients with primary carnitine deficiency - a cardiac magnetic resonance study. *Sci Rep* 9:13909. <https://doi.org/10.1038/s41598-019-50458-9>
- Laaksonen R, Ekroos K, Sysi-Aho M, et al (2016) Plasma ceramides predict cardiovascular death in patients with stable coronary artery disease and acute coronary syndromes beyond LDL-cholesterol. *Eur Heart J* 37:1967–1976. <https://doi.org/10.1093/eurheartj/ehw148>
- Laco F, Woo TL, Zhong Q, et al (2018) Unraveling the Inconsistencies of Cardiac Differentiation Efficiency Induced by the GSK3β Inhibitor CHIR99021 in Human Pluripotent Stem Cells. *Stem Cell Reports* 10:1851–1866. <https://doi.org/10.1016/J.STEMCR.2018.03.023>

- Lamhonwah AM, Olpin SE, Pollitt RJ, et al (2002) Novel OCTN2 mutations: No genotype-phenotype correlations: Early carnitine therapy prevents cardiomyopathy. *Am J Med Genet* 111:271–284. <https://doi.org/10.1002/ajmg.10585>
- Lamhonwah AM, Tein I (2006) Novel localization of OCTN1, an organic cation/carnitine transporter, to mammalian mitochondria. *Biochem Biophys Res Commun* 345:1315–1325. <https://doi.org/10.1016/j.bbrc.2006.05.026>
- Lecina M, Ting S, Choo A, et al (2010) Scalable platform for human embryonic stem cell differentiation to cardiomyocytes in suspended microcarrier cultures. *Tissue Eng - Part C Methods* 16:1609–1619. <https://doi.org/10.1089/ten.tec.2010.0104>
- Li F, Wang X, Capasso JM, Gerdes AM (1996) Rapid transition of cardiac myocytes from hyperplasia to hypertrophy during postnatal development. *J Mol Cell Cardiol* 28:1737–1746. <https://doi.org/10.1006/jmcc.1996.0163>
- Li FY, El-Hattab AW, Bawle E V., et al (2010a) Molecular spectrum of SLC22A5 (OCTN2) gene mutations detected in 143 subjects evaluated for systemic carnitine deficiency. *Hum Mutat* 31:. <https://doi.org/10.1002/humu.21311>
- Li HL, Fujimoto N, Sasakawa N, et al (2015) Precise correction of the dystrophin gene in duchenne muscular dystrophy patient induced pluripotent stem cells by TALEN and CRISPR-Cas9. *Stem Cell Reports* 4:143–154. <https://doi.org/10.1016/j.stemcr.2014.10.013>
- Li J, Cao F, Yin H liang, et al (2020) Ferroptosis: past, present and future. *Cell Death Dis* 11:. <https://doi.org/10.1038/s41419-020-2298-2>
- Li JM, Li LY, Qin X, et al (2017) Systemic regulation of L-carnitine in nutritional metabolism in zebrafish, *Danio rerio*. *Sci Rep* 7:. <https://doi.org/10.1038/srep40815>
- Li LO, Klett EL, Coleman RA (2010b) Acyl-CoA synthesis, lipid metabolism and lipotoxicity. *Biochim Biophys Acta - Mol Cell Biol Lipids* 1801:246–251. <https://doi.org/10.1016/j.bbalip.2009.09.024>
- Li Y, Khanal P, Norheim F, et al (2021) Plin2 deletion increases cholesteryl ester lipid droplet content and disturbs cholesterol balance in adrenal cortex. *J Lipid Res* 62:100048. <https://doi.org/10.1016/J.JLR.2021.100048>
- Lian X, Zhang J, Azarin SM, et al (2013) Directed cardiomyocyte differentiation from human pluripotent stem cells by modulating Wnt/ β -catenin signaling under fully defined conditions. *Nat Protoc* 8:162–175. <https://doi.org/10.1038/nprot.2012.150>
- Liao Y, Wang J, Jaehnig EJ, et al (2019) WebGestalt 2019: gene set analysis toolkit with

- revamped UIs and APIs. *Nucleic Acids Res* 47:W199–W205.
<https://doi.org/10.1093/nar/gkz401>
- Liepinsh E, Kuka J, Svalbe B, et al (2009) Effects of Long-Term Mildronate Treatment on Cardiac and Liver Functions in Rats. *Basic Clin Pharmacol Toxicol* 105:387–394.
<https://doi.org/10.1111/J.1742-7843.2009.00461.X>
- Liepinsh E, Vilskersts R, Skapare E, et al (2008) Mildronate decreases carnitine availability and up-regulates glucose uptake and related gene expression in the mouse heart. *Life Sci* 83:613–619. <https://doi.org/10.1016/j.lfs.2008.08.008>
- Lin S, Staahl BT, Alla RK, Doudna JA (2014) Enhanced homology-directed human genome engineering by controlled timing of CRISPR/Cas9 delivery. *Elife* 3:e04766.
<https://doi.org/10.7554/eLife.04766>
- Lin Y, Zhang W, Huang C, et al (2021) Increased detection of primary carnitine deficiency through second-tier newborn genetic screening. *Orphanet J Rare Dis* 16:1–7.
<https://doi.org/10.1186/s13023-021-01785-6>
- Litviňuková M, Talavera-López C, Maatz H, et al (2020) Cells of the adult human heart. *Nature* 588:466–472. <https://doi.org/10.1038/s41586-020-2797-4>
- Liu Q, Jiang C, Xu J, et al (2017) Genome-Wide Temporal Profiling of Transcriptome and Open Chromatin of Early Cardiomyocyte Differentiation Derived from hiPSCs and hESCs. *Circ Res* 121:376–391. <https://doi.org/10.1161/CIRCRESAHA.116.310456>
- Lloyd DFA, Vara R, Mathur S (2017) Cardiac manifestations of inherited metabolic disease in children. *Pediatr. Int.* 59:525–529
- Loeber JG, Platis D, Zetterström RH, Schielen PJCI (2021) Neonatal screening in Europe revisited: An ISNS-perspective on the current state and developments since 2010. *Medecine/Sciences* 37:441–456. <https://doi.org/10.1051/medsci/2021059>
- Lompre AM, Nadal-Ginard B, Mahdavi V (1984) Expression of the cardiac ventricular α - and β -myosin heavy chain genes is developmentally and hormonally regulated. *J Biol Chem* 259:6437–6446. [https://doi.org/10.1016/s0021-9258\(20\)82162-0](https://doi.org/10.1016/s0021-9258(20)82162-0)
- Longo N, Amat Di San Filippo C, Pasquali M, et al (2006) Disorders of carnitine transport and the carnitine cycle. *Am J Med Genet - Semin Med Genet* 142 C:77–85.
<https://doi.org/10.1002/ajmg.c.30087>
- Longo N, Frigeni M, Pasquali M (2016) Carnitine transport and fatty acid oxidation. *Biochim Biophys Acta - Mol Cell Res* 1863:2422–2435.
<https://doi.org/10.1016/j.bbamcr.2016.01.023>

- Lopaschuk GD, Spafford MA, Marsh DR (1991) Glycolysis is predominant source of myocardial ATP production immediately after birth. *Am J Physiol - Hear Circ Physiol* 261:1698–1705. <https://doi.org/10.1152/ajpheart.1991.261.6.h1698>
- Lopaschuk GD, Ussher JR, Folmes CDLL, et al (2010) Myocardial fatty acid metabolism in health and disease. *Physiol Rev* 90:207–258. <https://doi.org/10.1152/physrev.00015.2009>
- Louzao-Martinez L, Vink A, Harakalova M, et al (2016) Characteristic adaptations of the extracellular matrix in dilated cardiomyopathy. Elsevier
- Lund RJ, Närvä E, Lahesmaa R (2012) Genetic and epigenetic stability of human pluripotent stem cells. *Nat Rev Genet* 13:732–744. <https://doi.org/10.1038/nrg3271>
- Lundy SD, Zhu W-Z, Regnier M, Laflamme MA (2013) Structural and Functional Maturation of Cardiomyocytes Derived from Human Pluripotent Stem Cells. <https://home.liebertpub.com/scd> 22:1991–2002. <https://doi.org/10.1089/SCD.2012.0490>
- MacEyka M, Spiegel S (2014) Sphingolipid metabolites in inflammatory disease. *Nature* 510:58–67. <https://doi.org/10.1038/nature13475>
- Maekawa S, Mori D, Nishiya T, et al (2007) OCTN2VT, a splice variant of OCTN2, does not transport carnitine because of the retention in the endoplasmic reticulum caused by insertion of 24 amino acids in the first extracellular loop of OCTN2. *Biochim Biophys Acta - Mol Cell Res* 1773:1000–1006. <https://doi.org/10.1016/j.bbamcr.2007.04.005>
- Magoulas PL, El-Hattab AW (2012) Systemic primary carnitine deficiency: An overview of clinical manifestations, diagnosis, and management. *Orphanet J. Rare Dis.* 7
- Mali P, Yang L, Esvelt KM, et al (2013) RNA-guided human genome engineering via Cas9. *Science* (80-) 339:823–826. <https://doi.org/10.1126/SCIENCE.1232033>
- Mannhardt I, Breckwoldt K, Letuffe-Brenière D, et al (2016) Human Engineered Heart Tissue: Analysis of Contractile Force. *Stem Cell Reports* 7:29–42. <https://doi.org/10.1016/j.stemcr.2016.04.011>
- Mannhardt I, Saleem U, Mosqueira D, et al (2020) Comparison of 10 Control hPSC Lines for Drug Screening in an Engineered Heart Tissue Format. *Stem Cell Reports* 15:983–998. <https://doi.org/10.1016/j.stemcr.2020.09.002>
- Mao Z, Bozzella M, Seluanov A, Gorbunova V (2008) DNA repair by nonhomologous end joining and homologous recombination during cell cycle in human cells. *Cell Cycle* 7:2902–2906. <https://doi.org/10.4161/cc.7.18.6679>

- Maresca P, Mancinelli R, Corsico N, et al (1995) Positive action of propionyl-L-carnitine on mechanical performance of papillary muscle from Syrian hamsters with hereditary dilated cardiomyopathy. *Eur J Pharmacol* 287:303–307. [https://doi.org/10.1016/0014-2999\(95\)00699-0](https://doi.org/10.1016/0014-2999(95)00699-0)
- Maron BJ, Towbin JA, Thiene G, et al (2006) Contemporary definitions and classification of the cardiomyopathies: An American Heart Association Scientific Statement from the Council on Clinical Cardiology, Heart Failure and Transplantation Committee; Quality of Care and Outcomes Research and Functio. *Circulation* 113:1807–1816. <https://doi.org/10.1161/CIRCULATIONAHA.106.174287>
- Marshall S, Bacote V, Traxinger RR (1991) Discovery of a metabolic pathway mediating glucose-induced desensitization of the glucose transport system: role of hexosamine in the induction of insulin resistance. *J Biol Chem* 266:4706–4712. [https://doi.org/10.1016/s0021-9258\(19\)67706-9](https://doi.org/10.1016/s0021-9258(19)67706-9)
- Masci PG, Schuurman R, Andrea B, et al (2013) Myocardial fibrosis as a key determinant of left ventricular remodeling in idiopathic dilated cardiomyopathy: A contrast-enhanced cardiovascular magnetic study. *Circ Cardiovasc Imaging* 6:790–799. <https://doi.org/10.1161/CIRCIMAGING.113.000438>
- Mazzarotto F, Tayal U, Buchan RJ, et al (2020) Reevaluating the Genetic Contribution of Monogenic Dilated Cardiomyopathy. *Circulation* 387–398. <https://doi.org/10.1161/CIRCULATIONAHA.119.037661>
- McNally EM, Mestroni L (2017) Dilated Cardiomyopathy. *Circ Res* 121:731–748. <https://doi.org/10.1161/CIRCRESAHA.116.309396>
- Miao Y, Tian L, Martin M, et al (2020) Intrinsic Endocardial Defects Contribute to Hypoplastic Left Heart Syndrome. *Cell Stem Cell* 27:574-589.e8. <https://doi.org/10.1016/J.STEM.2020.07.015>
- Micheletti R, Di Paola ED, Schiavone A, et al (1993) Propionyl-L-carnitine limits chronic ventricular dilation after myocardial infarction in rats. *Am J Physiol - Hear Circ Physiol* 264:. <https://doi.org/10.1152/ajpheart.1993.264.4.h1111>
- Milani-Nejad N, Janssen PML (2014) Small and large animal models in cardiac contraction research: Advantages and disadvantages. *Pharmacol Ther* 141:235–249. <https://doi.org/10.1016/j.pharmthera.2013.10.007>
- Miyaoka Y, Berman JR, Cooper SB, et al (2016) Systematic quantification of HDR and NHEJ reveals effects of locus, nuclease, and cell type on genome-editing. *Sci Rep* 6:1–12. <https://doi.org/10.1038/srep23549>

- Moretti A, Bellin M, Welling A, et al (2010) Patient-Specific Induced Pluripotent Stem-Cell Models for Long-QT Syndrome. *N Engl J Med* 363:1397–1409.
<https://doi.org/10.1056/NEJMOA0908679>
- Mori J, Alrob OA, Wagg CS, et al (2013) ANG II causes insulin resistance and induces cardiac metabolic switch and inefficiency: A critical role of PDK4. *Am J Physiol - Hear Circ Physiol* 304:1103–1113. <https://doi.org/10.1152/ajpheart.00636.2012>
- Mu Y, Yu H, Wu T, et al (2020) O-linked β -N-acetylglucosamine transferase plays an essential role in heart development through regulating angiopoietin-1. *PLoS Genet* 16:.
<https://doi.org/10.1371/journal.pgen.1008730>
- Mummery C, Ward D, Van Den Brink CE, et al (2002) Cardiomyocyte differentiation of mouse and human embryonic stem cells. *J Anat* 200:233–242.
<https://doi.org/10.1046/j.1469-7580.2002.00031.x>
- Münch J, Grivas D, González-Rajal Á, et al (2017) Notch signalling restricts inflammation and *Serpine1* expression in the dynamic endocardium of the regenerating zebrafish heart. *Dev* 144:1425–1440. <https://doi.org/10.1242/dev.143362>
- Muoio DM, Noland RC, Kovalik JP, et al (2012) Muscle-specific deletion of carnitine acetyltransferase compromises glucose tolerance and metabolic flexibility. *Cell Metab* 15:764–777. <https://doi.org/10.1016/j.cmet.2012.04.005>
- Nakanishi T, Hatanaka T, Huang W, et al (2001) Na⁺ - and Cl⁻ -coupled active transport of carnitine by the amino acid transporter ATB_{0,+} from mouse colon expressed in HRPE cells and *Xenopus* oocytes. *J Physiol* 532:297–304. <https://doi.org/10.1111/j.1469-7793.2001.0297f.x>
- Newhardt MF, Batushansky La, Matsuzaki S, et al (2019) Enhancing cardiac glycolysis causes an increase in PDK4 content in response to short-term high-fat diet. *J Biol Chem* 294:16831–16845. <https://doi.org/10.1074/jbc.RA119.010371>
- Nicin L, Abplanalp WT, Schänzer A, et al (2021) Single Nuclei Sequencing Reveals Novel Insights into the Regulation of Cellular Signatures in Children with Dilated Cardiomyopathy. *Circulation* 1704–1719.
<https://doi.org/10.1161/CIRCULATIONAHA.120.051391>
- Nunes SS, Miklas JW, Liu J, et al (2013) Biowire: A platform for maturation of human pluripotent stem cell-derived cardiomyocytes. *Nat Methods* 10:781–787.
<https://doi.org/10.1038/nmeth.2524>
- Pan Z, Ebert A, Liang P (2021) Human-induced pluripotent stem cells as models for rare

- cardiovascular diseases: from evidence-based medicine to precision medicine. *Pflugers Arch Eur J Physiol* 473:1151–1165. <https://doi.org/10.1007/s00424-020-02486-y>
- Paquet D, Kwart D, Chen A, et al (2016) Efficient introduction of specific homozygous and heterozygous mutations using CRISPR/Cas9. *Nat* 2016 5337601 533:125–129. <https://doi.org/10.1038/nature17664>
- Parikh BA, Beckman DL, Patel SJ, et al (2015) Detailed phenotypic and molecular analyses of genetically modified mice generated by CRISPR-Cas9-mediated editing. *PLoS One* 10:1–28. <https://doi.org/10.1371/journal.pone.0116484>
- Park S, Jeon JH, Min BK, et al (2018) Role of the pyruvate dehydrogenase complex in metabolic remodeling: Differential pyruvate dehydrogenase complex functions in metabolism. *Diabetes Metab J* 42:270–281. <https://doi.org/10.4093/dmj.2018.0101>
- Peterson LR, Xanthakis V, Duncan MS, et al (2018) Ceramide remodeling and risk of cardiovascular events and mortality. *J Am Heart Assoc* 7:. <https://doi.org/10.1161/JAHA.117.007931>
- Pirillo A, Svecla M, Catapano AL, et al (2021) Impact of protein glycosylation on lipoprotein metabolism and atherosclerosis. *Cardiovasc Res* 117:1033–1045. <https://doi.org/10.1093/CVR/CVAA252>
- Pohjoismäki JL., Goffart S, Taylor RW, et al (2010) Developmental and Pathological Changes in the Human Cardiac Muscle Mitochondrial DNA Organization , Replication and Copy Number. 5:. <https://doi.org/10.1371/journal.pone.0010426>
- Poon ENY, Luo X ling, Webb SE, et al (2020) The cell surface marker CD36 selectively identifies matured, mitochondria-rich hPSC-cardiomyocytes. *Cell Res* 30:626–629. <https://doi.org/10.1038/s41422-020-0292-y>
- Puzianowska-Kuznicka M (2012) ESR1 in myocardial infarction. *Clin. Chim. Acta* 413:81–87
- Ramirez-Correa GA, Ma J, Slawson C, et al (2015) Removal of abnormal myofilament O-GlcNAcylation restores Ca²⁺ sensitivity in diabetic cardiac muscle. *Diabetes* 64:3573–3587. <https://doi.org/10.2337/db14-1107>
- Ran FA, Hsu PD, Wright J, et al (2013) Genome engineering using the CRISPR-Cas9 system. *Nat Protoc* 8:2281–2308. <https://doi.org/10.1038/nprot.2013.143>
- Randle PJ, Garland PB, Hales CN, Newsholme EA (1963) The glucose fatty-acid cycle and its role in insulin sensivity and the metabolic disturbances of diabetes mellitus. *Lancet* 281:785–789. [https://doi.org/10.1016/S0140-6736\(63\)91500-9](https://doi.org/10.1016/S0140-6736(63)91500-9)

- Rardin MJ, Wiley SE, Naviaux RK, et al (2009) Monitoring phosphorylation of the pyruvate dehydrogenase complex. *Anal Biochem* 389:157–164.
<https://doi.org/10.1016/J.AB.2009.03.040>
- Rasmussen J, Dunø M, Lund AM, et al (2020) Increased risk of sudden death in untreated primary carnitine deficiency. *J Inherit Metab Dis* 43:290–296.
<https://doi.org/10.1002/jimd.12158>
- Rasmussen J, Lund AM, Risom L, et al (2014a) Residual OCTN2 transporter activity, carnitine levels and symptoms correlate in patients with primary carnitine deficiency. *Mol Genet Metab Reports* 1:241–248. <https://doi.org/10.1016/j.ymgmr.2014.04.008>
- Rasmussen J, Nielsen OW, Janzen N, et al (2014b) Carnitine levels in 26,462 individuals from the nationwide screening program for primary carnitine deficiency in the Faroe Islands. *J Inherit Metab Dis* 37:215–222. <https://doi.org/10.1007/s10545-013-9606-2>
- Raval KK, Tao R, White BE, et al (2015) Pompe disease results in a Golgi-based glycosylation deficit in human induced pluripotent stem cell-derived cardiomyocytes. *J Biol Chem* 290:3121–3136. <https://doi.org/10.1074/jbc.M114.628628>
- Rebouche CJ (2004) Kinetics, pharmacokinetics, and regulation of L-carnitine and acetyl-L-carnitine metabolism. *Ann N Y Acad Sci* 1033:30–41.
<https://doi.org/10.1196/annals.1320.003>
- Rebouche CJ, Engel AG (1980) Tissue distribution of carnitine biosynthetic enzymes in man. *BBA - Gen Subj* 630:22–29. [https://doi.org/10.1016/0304-4165\(80\)90133-6](https://doi.org/10.1016/0304-4165(80)90133-6)
- Riegman M, Sagie L, Galed C, et al (2020) Ferroptosis occurs through an osmotic mechanism and propagates independently of cell rupture. *Nat Cell Biol* 22:1042–1048.
<https://doi.org/10.1038/s41556-020-0565-1>
- Roe CR, Sweetman L, Roe DS, et al (2002) Treatment of cardiomyopathy and rhabdomyolysis in long-chain fat oxidation disorders using an anaplerotic odd-chain triglyceride. *J Clin Invest* 110:259–269. <https://doi.org/10.1172/JCI0215311>
- Rohani L, Machiraju P, Sabouny R, et al (2020) Reversible Mitochondrial Fragmentation in iPSC-Derived Cardiomyocytes From Children With DCMA, a Mitochondrial Cardiomyopathy. *Can J Cardiol* 36:554–563. <https://doi.org/10.1016/j.cjca.2019.09.021>
- Rose EC, di San Filippo CA, Ndukwe Erlingsson UC, et al (2012) Genotype-phenotype correlation in primary carnitine deficiency. *Hum Mutat* 33:118–123.
<https://doi.org/10.1002/humu.21607>
- Rotoli BM, Visigalli R, Barilli A, et al (2020) Functional analysis of OCTN2 and ATB0,+ in

- normal human airway epithelial cells. *PLoS One* 15:e0228568.
<https://doi.org/10.1371/JOURNAL.PONE.0228568>
- Rudolph M, Heymann MA, Rudolph AM (1975) Control of the Ductus Arteriosus. *Physiol Rev* 55:62–78. <https://doi.org/10.1152/PHYSREV.1975.55.1.62>
- Russell DW, Setchell KDR (1992) Bile Acid Biosynthesis. *Biochemistry* 31:4737–4749.
<https://doi.org/https://doi.org/10.1021/bi00135a001>
- Saburi Y, Okumura K, Matsui H, et al (2003) Changes in distinct species of 1,2-diacylglycerol in cardiac hypertrophy due to energy metabolic disorder. *Cardiovasc Res* 57:92–100.
[https://doi.org/10.1016/S0008-6363\(02\)00608-9](https://doi.org/10.1016/S0008-6363(02)00608-9)
- Samovski D, Sun J, Pietka T, et al (2015) Regulation of AMPK activation by CD36 links fatty acid uptake to β -oxidation. *Diabetes* 64:353–359. <https://doi.org/10.2337/db14-0582>
- Satin J, Itzhaki I, Rapoport S, et al (2008) Calcium Handling in Human Embryonic Stem Cell-Derived Cardiomyocytes. *Stem Cells* 26:1961–1972.
<https://doi.org/10.1634/stemcells.2007-0591>
- Sato Y, Kobayashi H, Higuchi T, et al (2017) Metabolomic Profiling of Pompe Disease-Induced Pluripotent Stem Cell-Derived Cardiomyocytes Reveals That Oxidative Stress Is Associated with Cardiac and Skeletal Muscle Pathology. *Stem Cells Transl Med* 6:31–39. <https://doi.org/10.5966/sctm.2015-0409>
- Savic D, Ball V, Curtis MK, et al (2021) L-Carnitine Stimulates In Vivo Carbohydrate Metabolism in the Type 1 Diabetic Heart as Demonstrated by Hyperpolarized MRI. *Metab* 2021, Vol 11, Page 191 11:191. <https://doi.org/10.3390/METABO11030191>
- Scaglia F, Wang Y, Singh RH, et al (1998) Defective urinary carnitine transport in heterozygotes for primary carnitine deficiency. *Genet Med* 1:34–39.
<https://doi.org/10.1097/00125817-199811000-00008>
- Schaaf S, Shibamiya A, Mewe M, et al (2011) Human engineered heart tissue as a versatile tool in basic research and preclinical toxicology. *PLoS One* 6:.
<https://doi.org/10.1371/journal.pone.0026397>
- Schönfeld P, Wojtczak L (2016) Short- and medium-chain fatty acids in energy metabolism: The cellular perspective. *J Lipid Res* 57:943–954. <https://doi.org/10.1194/jlr.R067629>
- Schultheiss HP, Fairweather DL, Caforio ALP, et al (2019) Dilated cardiomyopathy. *Nat Rev Dis Prim* 5:.
<https://doi.org/10.1038/s41572-019-0084-1>
- Schupp JC, Adams TS, Jr CC, et al (2021) Integrated Single-Cell Atlas of Endothelial Cells of

- the Human Lung. *Circulation* 144:286–302.
<https://doi.org/10.1161/CIRCULATIONAHA.120.052318>
- Schwamb J, Feldhaus V, Baumann M, et al (2012) B-cell receptor triggers drug sensitivity of primary CLL cells by controlling glucosylation of ceramides. *Blood* 120:3978–3985.
<https://doi.org/10.1182/blood-2012-05-431783>
- Sewanan LR, Schwan J, Kluger J, et al (2019) Extracellular Matrix From Hypertrophic Myocardium Provokes Impaired Twitch Dynamics in Healthy Cardiomyocytes. *JACC Basic to Transl Sci* 4:495–505. <https://doi.org/10.1016/j.jacbts.2019.03.004>
- Shen WJ, Azhar S, Kraemer FB (2016) Lipid droplets and steroidogenic cells. *Exp Cell Res* 340:209–214. <https://doi.org/10.1016/j.yexcr.2015.11.024>
- Shibamiya A, Schulze E, Krauß D, et al (2020) Cell Banking of hiPSCs: A Practical Guide to Cryopreservation and Quality Control in Basic Research. *Curr Protoc Stem Cell Biol* 55:1–26. <https://doi.org/10.1002/cpsc.127>
- Shin HY, Wang C, Lee HK, et al (2017) CRISPR/Cas9 targeting events cause complex deletions and insertions at 17 sites in the mouse genome. *Nat Commun* 8:1–10.
<https://doi.org/10.1038/ncomms15464>
- Sikder K, Shukla SK, Patel N, et al (2018) High Fat Diet Upregulates Fatty Acid Oxidation and Ketogenesis via Intervention of PPAR- γ . *Cell Physiol Biochem* 48:1317–1331.
<https://doi.org/10.1159/000492091>
- Singer K, DelProposto J, Lee Morris D, et al (2014) Diet-induced obesity promotes myelopoiesis in hematopoietic stem cells. *Mol Metab* 3:664–675.
<https://doi.org/10.1016/j.molmet.2014.06.005>
- Skryabin B V., Kummerfeld DM, Gubar L, et al (2020) Pervasive head-to-tail insertions of DNA templates mask desired CRISPR-Cas9-mediated genome editing events. *Sci Adv* 6:. <https://doi.org/10.1126/sciadv.aax2941>
- Spaniol M, Brooks H, Auer L, et al (2001) Development and characterization of an animal model of carnitine deficiency. *Eur J Biochem* 268:1876–1887.
<https://doi.org/10.1080/00016480510038149>
- Spiekerkoetter U, Huener G, Baykal T, et al (2003) Silent and symptomatic primary carnitine deficiency within the same family due to identical mutations in the organic cation/carnitine transporter OCTN2. *J Inherit Metab Dis* 26:613–615.
<https://doi.org/10.1023/A:1025968502527>
- Stanley CA (2004) Carnitine deficiency disorders in children. *Ann N Y Acad Sci* 1033:42–51.

<https://doi.org/10.1196/annals.1320.004>

Stanley WC, Recchia FA, Lopaschuk GD (2005) Myocardial substrate metabolism in the normal and failing heart. *Physiol Rev* 85:1093–1129.

<https://doi.org/10.1152/physrev.00006.2004>

Steimle JD, Moskowitz IP (2017) TBX5: A Key Regulator of Heart Development. In: *Current Topics in Developmental Biology*. Academic Press, pp 195–221

Steuerwald U, Lund AM, Rasmussen J, et al (2017) Neonatal screening for primary carnitine deficiency: Lessons learned from the Faroe Islands. *Int J Neonatal Screen* 3:1–10.

<https://doi.org/10.3390/ijns3010001>

Stöhr A, Friedrich FW, Flenner F, et al (2013) Contractile abnormalities and altered drug response in engineered heart tissue from Mybpc3-targeted knock-in mice. *J Mol Cell Cardiol* 63:189–198. <https://doi.org/10.1016/j.jmcc.2013.07.011>

Stratford S, Hoehn KL, Liu F, Summers SA (2004) Regulation of insulin action by ceramide: Dual mechanisms linking ceramide accumulation to the inhibition of Akt/protein kinase B. *J Biol Chem* 279:36608–36615. <https://doi.org/10.1074/jbc.M406499200>

Sun H, Olson KC, Gao C, et al (2016) Catabolic defect of branched-chain amino acids promotes heart failure. *Circulation* 133:2038–2049.

<https://doi.org/10.1161/CIRCULATIONAHA.115.020226>

Taegtmeyer H, Golfman L, Sharma S, et al (2004) Linking gene expression to function: Metabolic flexibility in the normal and diseased heart. *Ann N Y Acad Sci* 1015:202–213.

<https://doi.org/10.1196/annals.1302.017>

Taegtmeyer H, Young ME, Lopaschuk GD, et al (2016) Assessing Cardiac Metabolism. *Circ Res* 118:1659–1701. <https://doi.org/10.1161/RES.0000000000000097>

Takahashi K, Tanabe K, Ohnuki M, et al (2007a) Induction of Pluripotent Stem Cells from Adult Human Fibroblasts by Defined Factors. *Cell* 131:861–872.

<https://doi.org/10.1016/j.cell.2007.11.019>

Takahashi K, Yamanaka S (2006) Induction of Pluripotent Stem Cells from Mouse Embryonic and Adult Fibroblast Cultures by Defined Factors. *Cell* 126:663–676.

<https://doi.org/10.1016/j.cell.2006.07.024>

Takahashi R, Asai T, Murakami H, et al (2007b) Pressure overload-induced cardiomyopathy in heterozygous carrier mice of carnitine transporter gene mutation. *Hypertension* 50:497–502. <https://doi.org/10.1161/HYPERTENSIONAHA.107.088609>

- Tamai I, Ohashi R, Nezu JI, et al (1998) Molecular and functional identification of sodium ion-dependent, high affinity human carnitine transporter OCTN2. *J Biol Chem* 273:20378–20382. <https://doi.org/10.1074/jbc.273.32.20378>
- Tan J, Wagner M, Stenton SL, et al (2020) Lifetime risk of autosomal recessive mitochondrial disorders calculated from genetic databases. *EBioMedicine* 54:102730. <https://doi.org/10.1016/j.ebiom.2020.102730>
- Tang NLS, Ganapathy V, Wu X, et al (1999) Mutations of OCTN2, an organic cation/carnitine transporter lead to deficient cellular carnitine uptake in primary carnitine deficiency. *Hum Mol Genet* 8:655–660. <https://doi.org/10.1093/hmg/8.4.655>
- Therrell BL, Lloyd-Puryear MA, Camp KM, Mann MY (2014) Inborn errors of metabolism identified via newborn screening: Ten-year incidence data and costs of nutritional interventions for research agenda planning. *Mol Genet Metab* 113:14–26. <https://doi.org/10.1016/j.ymgme.2014.07.009>
- Tirziu D, Giordano FJ, Simons M (2010) Cell communications in the heart. *Circulation* 122:928–937. <https://doi.org/10.1161/CIRCULATIONAHA.108.847731>
- Tomlinson S, Atherton J, Prasad S (2018) Primary Carnitine Deficiency: A Rare, Reversible Metabolic Cardiomyopathy. *Case Reports Cardiol* 2018:1–3. <https://doi.org/10.1155/2018/3232105>
- Tomomura M, Imamura Y, Horiuchi M, et al (1992) Abnormal expression of urea cycle enzyme genes in juvenile visceral steatosis (jvs) mice. *Biochim Biophys Acta - Mol Basis Dis* 1138:167–171. [https://doi.org/10.1016/0925-4439\(92\)90058-U](https://doi.org/10.1016/0925-4439(92)90058-U)
- Tousson E, Hafez E, Zaki S, Gad A (2016) The cardioprotective effects of L-carnitine on rat cardiac injury , apoptosis , and oxidative stress caused by amethopterin. *Environ Sci Pollut Res* 20600–20608. <https://doi.org/10.1007/s11356-016-7220-1>
- Towbin JA, Lowe AM, Colan SD, et al (2006) Incidence, Causes, and Outcomes of Dilated Cardiomyopathy in Children. *J Am Med Assoc* 296:1867–1876. <https://doi.org/10.1001/jama.296.15.1867>
- Tran DH, Wang Z V. (2019) Glucose Metabolism in Cardiac Hypertrophy and Heart Failure. *J Am Heart Assoc* 8:1–18. <https://doi.org/10.1161/JAHA.119.012673>
- Ulmer BM, Eschenhagen T (2020) Human pluripotent stem cell-derived cardiomyocytes for studying energy metabolism. *Biochim Biophys Acta - Mol Cell Res* 1867:118471. <https://doi.org/10.1016/j.bbamcr.2019.04.001>
- Ulmer BM, Stoehr A, Schulze ML, et al (2018) Contractile Work Contributes to Maturation of

- Energy Metabolism in hiPSC-Derived Cardiomyocytes. *Stem Cell Reports* 10:834–847. <https://doi.org/10.1016/j.stemcr.2018.01.039>
- Urban TJ, Gallagher RC, Brown C, et al (2006) Functional genetic diversity in the high-affinity carnitine transporter OCTN2 (SLC22A5). *Mol Pharmacol* 70:1602–1611. <https://doi.org/10.1124/mol.106.028126>
- Ushikai M, Horiuchi M, Kobayashi K, et al (2011) Induction of PDK4 in the heart muscle of JVS mice, an animal model of systemic carnitine deficiency, does not appear to reduce glucose utilization by the heart. *Mol Genet Metab* 102:349–355. <https://doi.org/10.1016/j.ymgme.2010.11.167>
- Uziel G, Garavaglia B, Di Donato S (1988) Carnitine stimulation of pyruvate dehydrogenase complex (PDHC) in isolated human skeletal muscle mitochondria. *Muscle Nerve* 11:720–724. <https://doi.org/10.1002/mus.880110708>
- Van Luu T, Tremblay P, Labrie F (2006) Characterization of type 12 17 β -hydroxysteroid dehydrogenase, an isoform of type 3 17 β -hydroxysteroid dehydrogenase responsible for estradiol formation in women. *Mol Endocrinol* 20:437–443. <https://doi.org/10.1210/me.2005-0058>
- Vaz FM, Wanders RJA (2002) Carnitine biosynthesis in mammals. *Biochem J* 361:417–429. <https://doi.org/10.1042/0264-6021:3610417>
- Verkerk AO, Knottnerus SJGG, Portero V, et al (2021) Electrophysiological Abnormalities in VLCAD Deficient hiPSC-Cardiomyocytes Do not Improve with Carnitine Supplementation. *Front Pharmacol* 11:. <https://doi.org/10.3389/fphar.2020.616834>
- Wagner CA, Lükewille U, Kaltenbach S, et al (2000) Functional and pharmacological characterization of human Na⁺-carnitine cotransporter hOCTN2. *Am J Physiol - Ren Physiol* 279:. <https://doi.org/10.1152/ajprenal.2000.279.3.f584>
- Wamelink MMC, Struys EA, Jakobs C (2008) The biochemistry, metabolism and inherited defects of the pentose phosphate pathway: A review. *J Inherit Metab Dis* 31:703–717. <https://doi.org/10.1007/s10545-008-1015-6>
- Wang F, He Q, Sun Y, et al (2010) Female Adult Mouse Cardiomyocytes Are Protected Against Oxidative Stress. *Hypertension* 55:1172–1178. <https://doi.org/10.1161/HYPERTENSIONAHA.110.150839>
- Wang G, McCain ML, Yang L, et al (2014a) Modeling the mitochondrial cardiomyopathy of Barth syndrome with induced pluripotent stem cell and heart-on-chip technologies. *Nat Med* 20:616–623. <https://doi.org/10.1038/nm.3545>

- Wang SS, Rao J, Li YF, et al (2014b) Primary carnitine deficiency cardiomyopathy. *Int J Cardiol* 174:171–173. <https://doi.org/10.1016/j.ijcard.2014.03.190>
- Watkins PA, Maignel D, Jia Z, Pevsner J (2007) Evidence for 26 distinct acyl-coenzyme A synthetase genes in the human genome. *J Lipid Res* 48:2736–2750. <https://doi.org/10.1194/jlr.M700378-JLR200>
- Watson LJ, Long BW, DeMartino AM, et al (2014) Cardiomyocyte Ogt is essential for postnatal viability. *Am J Physiol - Hear Circ Physiol* 306:142–153. <https://doi.org/10.1152/ajpheart.00438.2013>
- Weintraub RG, Semsarian C, Macdonald P (2017) Dilated cardiomyopathy. *Lancet* 390:400–414. [https://doi.org/10.1016/S0140-6736\(16\)31713-5](https://doi.org/10.1016/S0140-6736(16)31713-5)
- Weterings E, Chen DJ (2008) The endless tale of non-homologous end-joining. *Cell Res* 18:114–124. <https://doi.org/10.1038/cr.2008.3>
- Wilcken B, Wiley V, Hammond J, Carpenter K (2003) Screening Newborns for Inborn Errors of Metabolism by Tandem Mass Spectrometry. *N Engl J Med* 348:2304–2312. <https://doi.org/10.1056/nejmoa025225>
- Wilfling F, Wang H, Haas JT, et al (2013) Triacylglycerol synthesis enzymes mediate lipid droplet growth by relocating from the ER to lipid droplets. *Dev Cell* 24:384–399. <https://doi.org/10.1016/j.devcel.2013.01.013>
- Wongkittichote P, Ah Mew N, Chapman KA (2017) Propionyl-CoA carboxylase – A review. *Mol Genet Metab* 122:145–152. <https://doi.org/10.1016/j.ymgme.2017.10.002>
- Wu J, Corr PB (1994) Palmitoyl transient carnitine modifies sodium currents and induces inward current in ventricular myocytes. *Am J Physiol* 266:1034–1046.
- Wu J, Corr PB (1995) Palmitoylcarnitine transient inward increases $[Na^+]_i$ and initiates current in adult ventricular myocytes. *Am J Physiol* 268:2405–2417
- Wu X, Prasad PD, Leibach FH, Ganapathy V (1998) cDNA Sequence, Transport Function, and Genomic Organization of Human OCTN2, a New Member of the Organic Cation Transporter Family. *Biochem Biophys Res Commun* 246:589–595. <https://doi.org/10.1006/BBRC.1998.8669>
- Xiong Y, Guan KL (2012) Mechanistic insights into the regulation of metabolic enzymes by acetylation. *J Cell Biol* 198:155–164. <https://doi.org/10.1083/jcb.201202056>
- Yang X, Li Q, Wang F, et al (2021) Newborn Screening and Genetic Analysis Identify Six Novel Genetic Variants for Primary Carnitine Deficiency in Ningbo Area, China. *Front*

- Genet 12:1–8. <https://doi.org/10.3389/fgene.2021.686137>
- Yang X, Pabon L, Murry CE (2014) Engineering adolescence: Maturation of human pluripotent stem cell-derived cardiomyocytes. *Circ Res* 114:511–523. <https://doi.org/10.1161/CIRCRESAHA.114.300558>
- Ye L, Zhang S, Greder L, et al (2013) Effective Cardiac Myocyte Differentiation of Human Induced Pluripotent Stem Cells Requires VEGF. *PLoS One* 8:. <https://doi.org/10.1371/journal.pone.0053764>
- Yoshimine K, Horiuchi M, Suzuki S, et al (1997) Altered Expression of Atrial Natriuretic Peptide and Contractile Protein Genes in Hypertrophied Ventricle of JVS Mice with Systemic Carnitine Deficiency. *J Mol Cell Cardiol* 29:571–578. <https://doi.org/10.1006/JMCC.1996.0300>
- Zafirovic S, Obradovic M, Sudar-Milovanovic E, et al (2017) 17 β -Estradiol protects against the effects of a high fat diet on cardiac glucose, lipid and nitric oxide metabolism in rats. *Mol Cell Endocrinol* 446:12–20. <https://doi.org/10.1016/J.MCE.2017.02.001>
- Zambrano S, Blanca AJ, Ruiz-Armenta M V., et al (2013) L-Carnitine protects against arterial hypertension-related cardiac fibrosis through modulation of PPAR- γ expression. *Biochem Pharmacol* 85:937–944. <https://doi.org/10.1016/j.bcp.2012.12.021>
- Zhang B, Zhang J, Zhang C, et al (2018a) Notoginsenoside R1 Protects Against Diabetic Cardiomyopathy Through Activating Estrogen Receptor α and Its Downstream Signaling. *Front Pharmacol* 0:1227. <https://doi.org/10.3389/FPHAR.2018.01227>
- Zhang J, Klos M, Wilson GF, et al (2012) Extracellular matrix promotes highly efficient cardiac differentiation of human pluripotent stem cells: The matrix sandwich method. *Circ Res* 111:1125–1136. <https://doi.org/10.1161/CIRCRESAHA.112.273144>
- Zhang L, Gui T, Console L, et al (2021) Cholesterol stimulates the cellular uptake of L-carnitine by the carnitine/organic cation transporter novel 2 (OCTN2). *J Biol Chem* 296:100204. <https://doi.org/doi:10.1074/jbc.RA120.015175>
- Zhang S, Hulver MW, McMillan RP, et al (2014) The pivotal role of pyruvate dehydrogenase kinases in metabolic flexibility. *Nutr Metab* 11:1–9. <https://doi.org/10.1186/1743-7075-11-10>
- Zhang X, Cheng H-J, Ukai T, et al (2018b) Abstract 11242: Enhanced Cardiac and Vascular Responses of L-Carnitine in Heart Failure: Assessment by Left Ventricular Pressure-Volume Analysis. *Circulation* 138:A11242–A11242
- Zhang Y, Guallar E, Ashar FN, et al (2017) Association between mitochondrial DNA copy

number and sudden cardiac death: Findings from the Atherosclerosis Risk in Communities study (ARIC). *Eur Heart J* 38:3443–3448.
<https://doi.org/10.1093/eurheartj/ehx354>

Zhao Y, Rafatian N, Feric NT, et al (2019) A Platform for Generation of Chamber-Specific Cardiac Tissues and Disease Modeling. *Cell* 176:913-927.e18.
<https://doi.org/10.1016/j.cell.2018.11.042>

Zimmermann WH, Fink C, Kralisch D, et al (2000) Three-dimensional engineered heart tissue from neonatal rat cardiac myocytes. *Biotechnol Bioeng* 68:106–114.
[https://doi.org/doi: 10.1002/\(SICI\)1097-0290\(20000405\)6](https://doi.org/doi:10.1002/(SICI)1097-0290(20000405)6)

Zuurbier CJ, Bertrand L, Beauloye CR, et al (2020) Cardiac metabolism as a driver and therapeutic target of myocardial infarction. *J Cell Mol Med* 24:5937–5954.
<https://doi.org/10.1111/jcmm.15180>

9 Supplement

9.1 Supplementary figures and tables

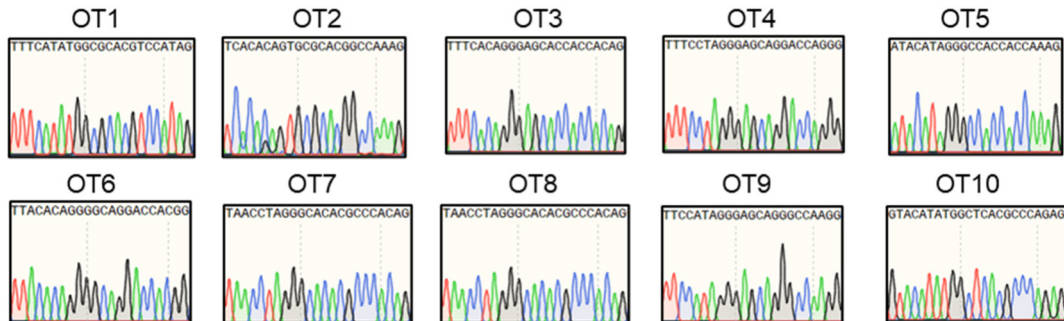
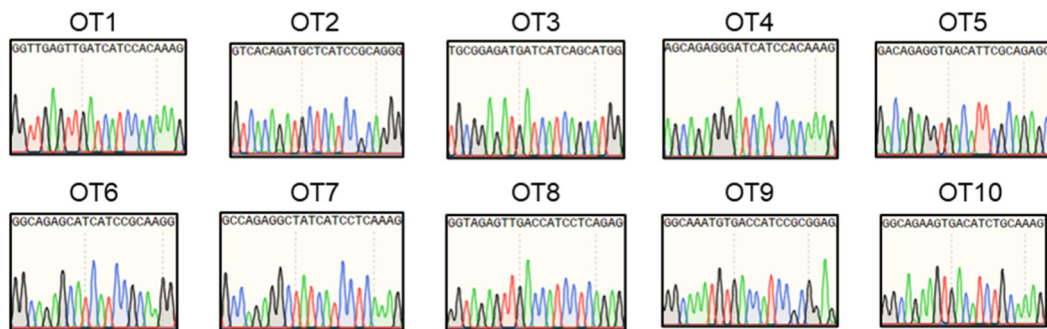
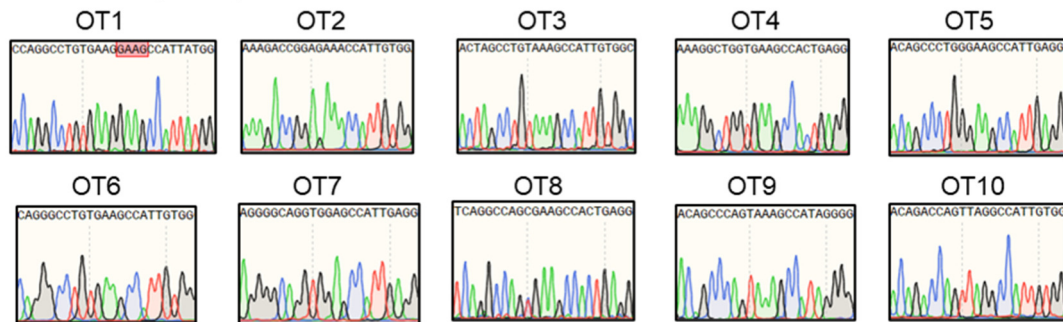
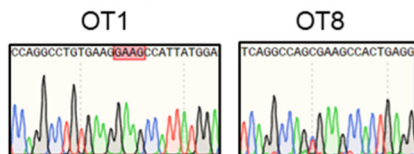
A OCTN2 (-/-): gRNA1**B OCTN2 (-/-): gRNA2****C OCTN2 (N32S)****OCTN2 (+/+), isogenic control**

Figure S1: Sanger sequencing of the Top10 off-targets after genome editing to generate OCTN2-defective hiPSC lines. A: OCTN2 (-/-) – gRNA1; B: OCTN2 (-/-) – gRNA2. C: OCTN2 (N32S). Traces were aligned to wildtype region. Indels/ single nucleotide polymorphism as detected in the regions of OT1 and OT8 of OCTN2 (N32S) were also present in the isogenic control indicating the absence of CRISPR-induced alterations in all sequenced off-target regions. OT: Off-target.

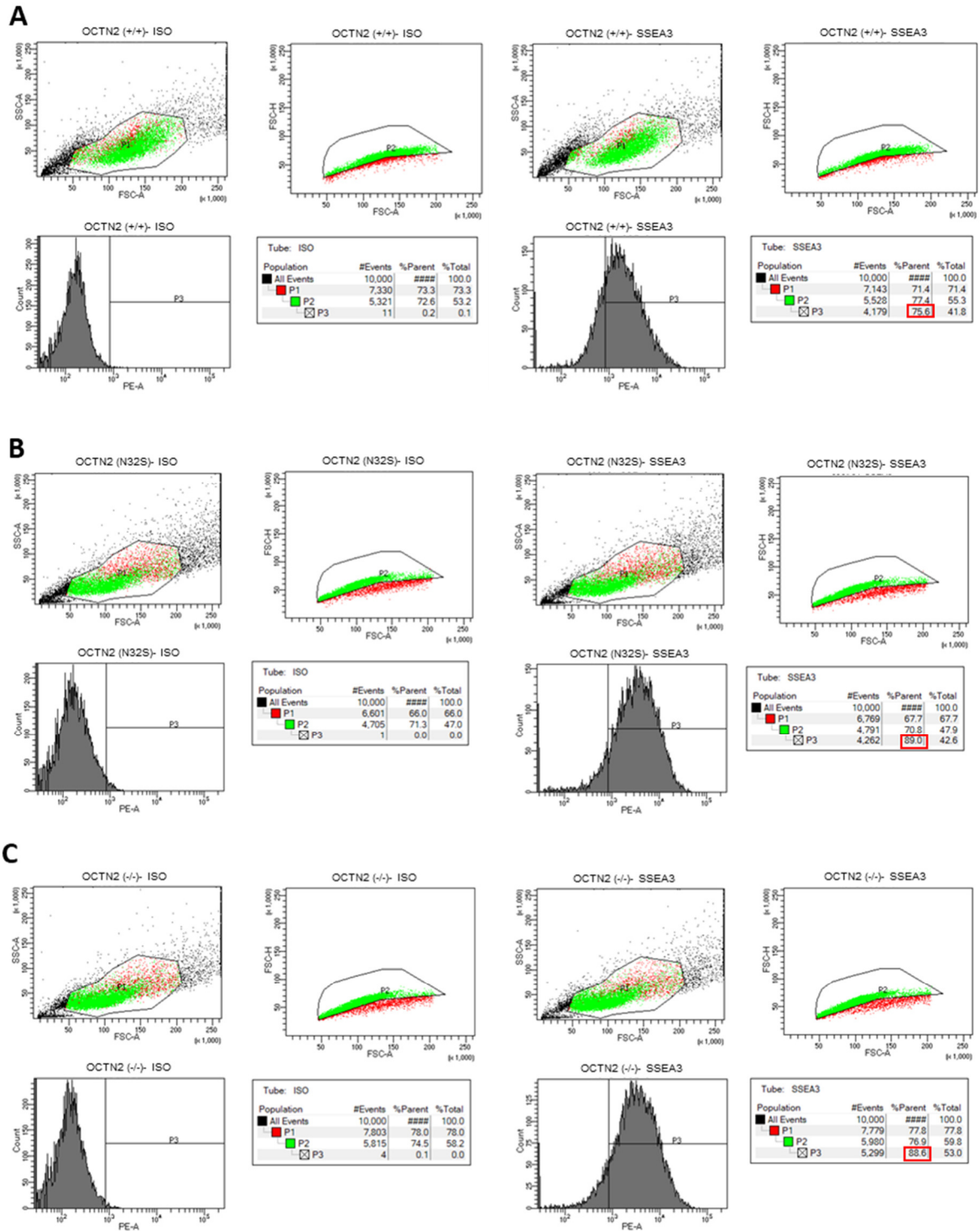


Figure S2: Flow cytometric SSEA-3 analysis of hiPSCs. A: OCTN2 (+/+); B: OCTN2 (N32S); C: OCTN2 (-/-). First, forward scatter (FSC) and sideward scatter (SSC) were used to exclude cell debris based on size and granularity. To only include single cells in the analysis, doublets were gated out subsequently. Proportion of SSEA3-positive cells was determined by adjusting gate P3 according to PE staining of the isotype control (C). The red box indicates the percentage of SSEA3-positive hiPSCs.

Table S1: KEGG Enrichment analysis of proteins with significant higher abundance in OCTN2 (N32) vs OCTN2 (+/+).

Description	GeneSet	Size	Overlap	Enrichment-Ratio	pValue	FDR	Protein
Ribosome	hsa03010	134	42	12.39	0.00E+00	0.00E+00	RPS16;RPL37A;RPS15;RPL18A;RPS24;RPS3;RPS11;RPS15A;RPS2;RPL11;RPS18;RPL9;MRPS15;RPS3A;RPS7;RPL35;MRPS5;RPL3;RPL36A;RPL32;MRPL24;RPS9;RPS29;RPL6;RPL35A;RPL21;RPS13;RPL31;RPL10;RPS8;RPS14;MRPS7;RPS6;MRPS14;RPL13A;RPL24;RPL18;RPL30;RPL27A;MRPS11;RPS4X;MRPS2
Other types of O-glycan biosynthesis	hsa00514	22	5	8.98	1.82E-04	9.77E-03	ST6GAL1;PLOD3;POFUT2;EOGT;POGLUT1
N-Glycan biosynthesis	hsa00510	49	10	8.06	2.94E-07	3.95E-05	MAN1C1;ST6GAL1;STT3A;RPN2;RPN1;MAN1A2;DDOST;STT3B;ALG12;MOGS
Ferroptosis	hsa04216	40	5	4.94	3.15E-03	9.39E-02	ACSL4;SLC3A2;LPCAT3;CP;VDAC3
Cholesterol metabolism	hsa04979	50	6	4.74	1.52E-03	5.84E-02	APOA1;APOE;NCEH1;VDAC1;VDAC3;LDLR
Complement and coagulation cascades	hsa04610	79	9	4.50	1.57E-04	9.77E-03	F13A1;VTN;C1QB;FGB;A2M;SERPINA1;FGG;PROS1;C7
Fatty acid metabolism	hsa01212	48	5	4.12	6.97E-03	1.70E-01	CPT1A;ACSL4;HSD17B12;CPT1B;TECR
Oxidative phosphorylation	hsa00190	133	13	3.86	2.87E-05	2.57E-03	COX7A1;ATP6;UQCRC10;NDUFA10;NDUFA13;NDUFB5;ATP6V0D1;NDUFA4;COX6C;ATP6V0A1;NDUFB9;NDUFB4;NDUFB7
ECM-receptor interaction	hsa04512	82	8	3.86	1.04E-03	4.65E-02	COL1A1;THBS1;COL6A1;FN1;VTN;ITGB5;ITGA3;ITGAV
PPAR signaling pathway	hsa03320	74	7	3.74	2.55E-03	8.55E-02	CPT1A;ACSL4;APOA1;SLC27A6;PLIN2;CPT1B;SLC27A1
Arrhythmogenic right ventricular cardiomyopathy (ARVC)	hsa05412	72	6	3.29	9.49E-03	2.12E-01	ACTB;DES;ITGB5;ACTN2;ITGA3;ITGAV
Systemic lupus erythematosus	hsa05322	133	9	2.67	6.44E-03	1.70E-01	ACTN4;ACTN1;H2AFY;HIST1H2AC;H2AFY2;C1QB;HIST1H2BL;HIST2H2BE;C7

Table S2: KEGG Enrichment analysis of proteins with significant lower abundance in OCTN2 (N32) vs OCTN2 (+/+).

Description	Gene Set	Size	Overlap	Enrichment-Ratio	pValue	FDR	Protein
Pyruvate metabolism	hsa00620	39	7	17.64	1.00E-07	1.35E-05	ACYP1;MDH1;ACAT2;GLO1;LDHB;ACSS1;ME1
Propanoate metabolism	hsa00640	32	5	15.35	1.55E-05	1.04E-03	ACAT2;ACSS3;LDHB;ABAT;ACSS1
Arginine biosynthesis	hsa00220	21	3	14.04	1.18E-03	2.83E-02	ACY1;GOT1;ARG2
Pentose phosphate pathway	hsa00030	30	4	13.10	2.22E-04	7.43E-03	GPI;ALDOA;RPE;ALDOC
Glyoxylate and dicarboxylate metabolism	hsa00630	30	4	13.10	2.22E-04	7.43E-03	MDH1;ACAT2;ACSS1;SHMT2
Biosynthesis of amino acids	hsa01230	75	8	10.48	7.65E-07	6.83E-05	ALDOA;RPE;PHGDH;ACY1;GOT1;SHMT2;ALDOC;ARG2
Carbon metabolism	hsa01200	116	12	10.16	1.46E-09	3.92E-07	GPI;ALDOA;MDH1;RPE;ADH5;ACAT2;PHGDH;ACSS1;GOT1;SHMT2;ALDOC;ME1
Arginine and proline metabolism	hsa00330	50	5	9.83	1.41E-04	6.31E-03	OAT;GOT1;SMS;MAOB;ARG2
Glycolysis / Gluconeogenesis	hsa00010	68	6	8.67	6.01E-05	3.22E-03	GPI;ALDOA;ADH5;LDHB;ACSS1;ALDOC
Cysteine and methionine metabolism	hsa00270	47	4	8.36	1.27E-03	2.83E-02	MDH1;LDHB;GOT1;SMS
Arrhythmogenic right ventricular cardiomyopathy (ARVC)	hsa05412	72	5	6.82	7.84E-04	2.34E-02	DAG1;GJA1;CACNA2D2;SGCB;SGCD
PPAR signaling pathway	hsa03320	74	5	6.64	8.89E-04	2.38E-02	SORBS1;SCP2;ME1;FABP5;CD36

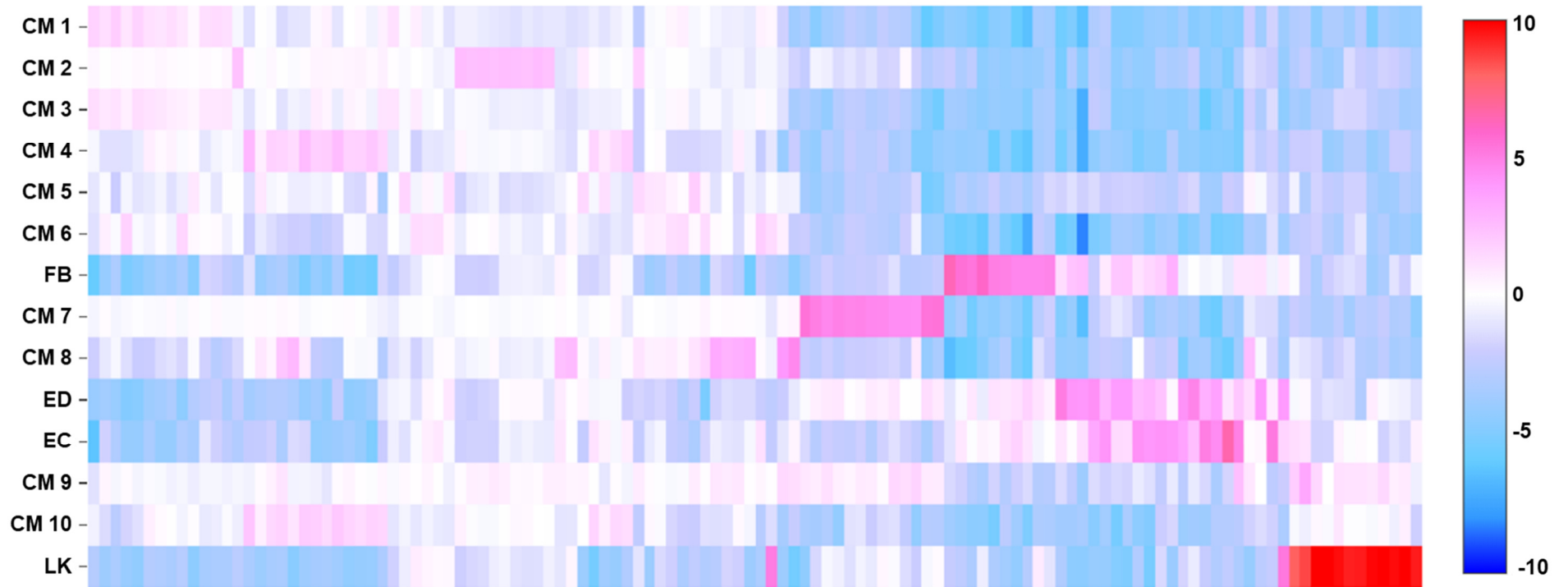


Figure S3: Heatmap panel of snRNA-seq analysis. Depicted is the differential gene log₂ fold change of the top 10 upregulated genes per cluster (average expression within the cluster compared to the rest of the dataset). CM: cardiomyocytes; FB: fibroblast; ED: endocardium-like-; EC: endothelial cells; LK: leukocytes.

Table S3: 100 most strongly expressed genes per subcluster (CM1, CM2, CM3) identified by snRNA-seq. Genes are ranked according to their log2 fold change vs average expression of entire dataset.

	CM1 Gene	CM1 Average	CM1 Log2 FC	CM1 P-Value	CM2 Gene	CM2 Average	CM2 Log2 FC	CM2 P-Value	CM3 Gene	CM3 Average	CM3 Log2 FC	CM3 P-Value
1	ANGPT1	4.095	2.061	1.48E-18	MT-CYB	2.025	2.593	2.02E-18	LINC01182	4.705	1.344	6.38E-03
2	LINC01182	4.827	1.938	1.34E-15	MB	2.096	2.578	2.83E-18	SORCS3	2.012	1.322	5.75E-03
3	SORCS3	2.029	1.843	6.08E-15	TNNC1	6.048	2.561	2.02E-18	ANGPT1	3.397	1.156	3.61E-02
4	ESR1	1.133	1.443	5.79E-09	MT-ATP6	1.038	2.558	1.96E-17	AC124947.1	1.934	1.139	3.69E-02
5	ADAMTSL1	2.240	1.434	5.71E-09	TNNI1	4.407	2.486	2.30E-17	SLC9C1	1.032	1.084	7.22E-02
6	GRID1	1.910	1.362	4.72E-08	MT-CO2	2.391	2.472	1.08E-16	OPCML	1.004	1.040	1.47E-01
7	CACHD1	1.941	1.344	9.01E-08	CRYAB	1.203	2.419	1.08E-15	AC108058.1	2.841	0.988	1.33E-01
8	AC113414.1	2.091	1.334	1.21E-07	MT-CO3	2.049	2.407	7.32E-16	GRID1	1.885	0.982	1.44E-01
9	FHL2	21.544	1.289	2.35E-07	MYH7	8.549	2.407	5.54E-16	ADAMTSL1	2.057	0.947	1.86E-01
10	AC124947.1	1.728	1.259	7.33E-07	PRDX2	1.093	2.397	1.34E-15	CACHD1	1.842	0.929	2.16E-01
11	AC010967.1	1.004	1.256	1.46E-06	ACTC1	15.785	2.356	1.34E-15	AC113414.1	1.913	0.888	2.77E-01
12	SLC9C1	0.959	1.248	1.57E-06	MYL2	7.129	2.270	3.75E-14	FHL2	20.741	0.875	2.76E-01
13	SLC22A23	1.338	1.218	2.07E-06	MT-CO1	2.011	2.263	8.87E-14	RAPGEF4	1.314	0.862	3.20E-01
14	TRIQQ	1.335	1.218	2.39E-06	GAPDH	3.930	2.227	2.21E-13	AC117834.1	1.267	0.843	3.59E-01
15	KCNQ3	1.437	1.175	6.68E-06	ENO3	1.642	2.203	5.71E-13	AC011389.1	1.370	0.839	3.59E-01
16	AC108058.1	2.642	1.168	5.83E-06	NPPA	7.439	2.140	3.09E-12	AP001021.3	1.539	0.813	4.13E-01
17	GAREM1	1.603	1.113	2.25E-05	SRP14	1.266	2.102	1.13E-11	PHACTR1	1.498	0.793	4.58E-01
18	RAPGEF4	1.317	1.104	3.01E-05	RPL8	1.554	2.069	2.35E-11	FBN2	16.871	0.782	4.58E-01
19	FBN2	17.316	1.096	2.53E-05	LDHA	1.683	2.053	5.61E-11	AP001825.1	1.242	0.775	4.97E-01
20	PLCXD3	2.287	1.092	3.66E-05	HSP90AB1	2.162	2.053	3.66E-11	NUDT4	2.608	0.771	4.90E-01
21	MGAT4C	2.448	1.086	4.05E-05	ATP5F1B	1.157	2.046	5.67E-11	KCNQ3	1.334	0.768	5.19E-01
22	CORIN	4.509	1.066	5.10E-05	HSP90AA1	2.023	2.015	1.04E-10	MAN1C1	2.698	0.766	5.03E-01
23	ARHGEF9	1.058	1.060	7.27E-05	UBC	1.301	2.015	1.21E-10	CORIN	4.394	0.753	5.32E-01
24	RBFOX1	1.784	1.045	1.01E-04	ATP5MC3	1.676	2.008	9.79E-11	PLCXD3	2.162	0.741	5.77E-01
25	PCAT1	1.489	1.022	1.67E-04	MIF	1.441	1.995	1.95E-10	SH3PXD2A	2.091	0.738	5.70E-01
26	NUDT4	2.527	1.005	1.80E-04	CKM	1.247	1.979	3.08E-10	FAM189A2	1.819	0.735	5.86E-01
27	ITGA9	0.849	1.001	2.56E-04	RPS15	1.012	1.962	5.07E-10	AC092640.1	3.124	0.735	5.77E-01
28	ERBB4	10.776	0.996	2.08E-04	NDUFA13	1.306	1.961	3.94E-10	ACACB	1.542	0.731	5.93E-01
29	MAN1C1	2.660	0.996	2.22E-04	COX6B1	1.098	1.938	7.75E-10	LINC02069	0.622	0.729	5.32E-01
30	GPRIN3	0.827	0.981	3.78E-04	COX4I1	1.345	1.911	1.39E-09	PRDM16	0.843	0.725	5.16E-01
31	PACRG	0.909	0.958	5.81E-04	NDUFA4	1.407	1.906	1.39E-09	STARD4-AS1	4.118	0.725	6.04E-01
32	SLIT3	15.516	0.944	5.32E-04	TNNI3	1.114	1.886	4.06E-09	ESR1	0.911	0.721	6.46E-01
33	LINC01505	1.415	0.927	9.62E-04	COX7C	1.491	1.869	3.46E-09	SLC22A23	1.189	0.720	6.38E-01
34	DLG2	11.164	0.911	1.00E-03	RPL3	1.368	1.863	4.78E-09	AP000462.1	1.064	0.715	6.55E-01
35	TRDN-AS1	6.594	0.898	1.24E-03	H3F3A	1.529	1.857	4.91E-09	AL390783.1	1.954	0.714	6.43E-01
36	ACACB	1.503	0.896	1.38E-03	SLC25A4	1.934	1.836	6.88E-09	AL450384.2	0.923	0.713	6.61E-01
37	AC011389.1	1.270	0.889	1.67E-03	CSR3P	2.991	1.826	8.00E-09	XPO4	2.853	0.701	6.70E-01
38	AC117834.1	1.155	0.888	1.83E-03	NPPB	1.876	1.825	8.09E-08	SLIT3	15.103	0.700	6.68E-01
39	LINC00881	1.113	0.887	1.75E-03	RPS23	1.168	1.819	1.35E-08	GUCY1A1	1.725	0.693	7.19E-01
40	CCDC146	1.149	0.882	1.98E-03	RPLP1	2.211	1.803	1.49E-08	FGF12-AS1	1.166	0.688	7.28E-01
41	TMEM163	1.347	0.874	2.24E-03	RPL18	1.035	1.798	2.43E-08	MTSS1	3.283	0.683	7.20E-01
42	AC138305.1	1.442	0.862	2.75E-03	COX6C	1.314	1.767	3.91E-08	SYT2	1.617	0.681	7.38E-01
43	AC107068.2	3.329	0.861	3.46E-03	RPS4X	1.416	1.765	4.34E-08	PDZD2	1.426	0.676	7.52E-01
44	PDZD2	1.424	0.860	2.64E-03	SLC25A3	1.511	1.761	4.24E-08	GAREM1	1.419	0.667	7.83E-01
45	SCN5A	1.395	0.858	2.70E-03	RPS14	1.087	1.760	5.55E-08	A2M	2.150	0.665	7.80E-01
46	L3MBTL4	2.072	0.855	2.77E-03	MYL4	7.322	1.742	4.39E-08	TRIQQ	1.149	0.663	8.02E-01
47	MTSS1	3.203	0.852	2.78E-03	RPL15	1.096	1.727	1.16E-07	ABHD18	1.589	0.645	8.30E-01
48	SH3PXD2A	1.964	0.846	3.03E-03	COX5B	1.364	1.719	1.10E-07	MROH7	2.045	0.643	8.36E-01
49	AL136171.2	4.123	0.846	3.01E-03	RPL7A	1.254	1.707	1.63E-07	SLC27A6	3.645	0.638	8.51E-01
50	BMP7	1.003	0.844	3.53E-03	RPL11	1.365	1.700	1.74E-07	CCDC146	1.115	0.634	8.68E-01
51	CCDC141	2.687	0.838	3.43E-03	B2M	1.276	1.699	1.95E-07	AL133257.1	1.776	0.630	8.68E-01
52	ST6GAL1	2.993	0.820	4.54E-03	RPS3A	1.325	1.699	1.93E-07	ARHGEF9	0.946	0.629	8.68E-01
53	FAM189A2	1.687	0.818	5.05E-03	RPS27A	1.376	1.682	2.79E-07	AL355612.1	6.743	0.627	8.68E-01
54	LDLRAD4	4.896	0.808	5.32E-03	ATP5PF	1.212	1.674	3.02E-07	PACRG	0.845	0.626	7.85E-01

Supplement — 141

55	FGF12	24.583	0.806	5.50E-03	RPS24	1.598	1.669	3.25E-07	ITGA9	0.767	0.616	8.04E-01
56	TNNI3K	3.680	0.803	5.91E-03	KRT18	1.033	1.663	9.10E-07	PBX1	8.512	0.616	8.70E-01
57	B4GALNT3	2.442	0.802	6.01E-03	HSPB7	1.323	1.653	4.54E-07	GRAMD1B	3.806	0.615	8.82E-01
58	MROH7	1.999	0.800	6.26E-03	RPS28	1.174	1.651	5.11E-07	EDA	3.907	0.613	8.89E-01
59	EDA	3.866	0.787	7.84E-03	COX7B	1.253	1.644	5.34E-07	MGAT4C	2.129	0.613	8.94E-01
60	AP001825.1	1.111	0.784	8.72E-03	RPS2	1.179	1.630	8.27E-07	ST6GAL1	2.945	0.612	8.86E-01
61	HDAC9	5.038	0.783	7.63E-03	RPL34	1.086	1.628	9.28E-07	TNNI3K	3.664	0.610	8.92E-01
62	KLHL13	1.226	0.778	9.73E-03	SMPX	2.958	1.616	7.56E-07	DISC1	5.767	0.608	8.92E-01
63	ALPK2	3.365	0.777	8.35E-03	RPS18	1.108	1.593	1.76E-06	TMEM65	2.135	0.603	9.12E-01
64	MIR99AHG	1.782	0.774	9.37E-03	TNNT2	12.865	1.589	1.11E-06	MLIP-AS1	2.253	0.599	9.20E-01
65	ADCY5	1.403	0.772	9.67E-03	COX5A	1.058	1.587	1.82E-06	ALPK2	3.370	0.594	9.27E-01
66	ARHGEF3	1.843	0.771	9.58E-03	EEF1A1	1.736	1.584	1.73E-06	SLC8A1-AS1	18.279	0.592	9.30E-01
67	SFMBT2	2.644	0.767	9.99E-03	RPL5	1.307	1.545	3.94E-06	LINC00881	1.093	0.588	9.56E-01
68	SIPA1L2	1.540	0.752	1.26E-02	RPS7	1.077	1.544	4.53E-06	C15orf41	1.675	0.585	9.55E-01
69	CTNND2	2.275	0.750	1.27E-02	RPS19	1.338	1.539	4.67E-06	ERBB4	9.640	0.583	9.55E-01
70	BBOX1-AS1	0.667	0.749	2.06E-02	RPL37A	1.134	1.534	5.23E-06	BMP7	1.008	0.583	9.70E-01
71	KCNN2	1.863	0.747	1.33E-02	FTH1	0.732	1.526	8.60E-06	PCAT1	1.289	0.583	9.75E-01
72	AP001021.3	1.333	0.745	1.46E-02	ATP5MG	1.031	1.519	6.79E-06	AC005358.1	3.441	0.581	9.56E-01
73	MLIP	7.442	0.745	1.27E-02	MYH6	11.429	1.507	6.12E-06	CACNB2	9.294	0.579	9.60E-01
74	STK33	1.565	0.738	1.48E-02	ATP5F1A	1.095	1.507	8.38E-06	HDAC9	4.947	0.576	9.72E-01
75	TRDN	8.710	0.738	1.40E-02	MDH1	1.837	1.497	8.21E-06	DLG2	10.304	0.573	9.77E-01
76	SLC27A6	3.427	0.726	1.80E-02	RPL13	1.250	1.480	1.33E-05	LDLRAD4	4.763	0.565	9.99E-01
77	PBX1	8.172	0.724	1.72E-02	ATP5IF1	1.206	1.468	1.66E-05	AC010967.1	0.792	0.548	9.63E-01
78	TMEM65	2.081	0.723	1.82E-02	RPL10	1.732	1.443	2.39E-05	GPRIN3	0.729	0.538	9.72E-01
79	SMYD1	1.406	0.718	1.98E-02	RPL6	1.002	1.438	3.27E-05	RNF207	1.266	0.486	1.00E+00
80	GCNT2	2.166	0.715	2.03E-02	CD63	1.041	1.411	5.80E-05	PIK3R3	1.470	0.350	1.00E+00
81	GRK5	1.461	0.715	2.09E-02	MGST3	1.727	1.410	3.96E-05	ATP5IF1	0.632	0.334	1.00E+00
82	PLCB4	1.806	0.714	2.04E-02	TPM1	20.677	1.377	5.84E-05	VPS13D	1.143	0.230	1.00E+00
83	SYT2	1.489	0.712	2.22E-02	RPL41	1.838	1.300	2.57E-04	PHC2	0.501	0.226	1.00E+00
84	PPP1R9A	1.406	0.710	2.18E-02	PGK1	1.109	1.291	3.75E-04	KAZN	1.018	0.222	1.00E+00
85	XPO4	2.601	0.707	2.17E-02	SELENOW	1.442	1.215	9.51E-04	TMEM51	0.245	0.203	1.00E+00
86	GRAMD1B	3.595	0.706	2.22E-02	SH3BGR	1.132	1.091	5.30E-03	OSBPL9	1.106	0.192	1.00E+00
87	SGIP1	2.389	0.704	2.30E-02	TGM2	1.557	1.087	5.38E-03	AL513327.1	0.551	0.186	1.00E+00
88	CTNNA3	24.660	0.703	2.17E-02	MYL6	1.406	1.059	7.51E-03	HSPB7	0.569	0.174	1.00E+00
89	PLCL2	1.663	0.703	2.37E-02	MYL9	1.553	1.019	1.18E-02	PHACTR4	1.556	0.128	1.00E+00
90	AMMECR1	1.461	0.702	2.53E-02	FTL	0.447	0.959	2.67E-02	MKNK1	0.168	0.108	1.00E+00
91	OPCML	0.712	0.701	4.62E-02	MYL7	22.434	0.943	2.51E-02	MAST2	0.915	0.092	1.00E+00
92	PHACTR1	1.296	0.700	2.68E-02	ATP1A1	1.697	0.930	3.02E-02	HIVEP3	0.743	0.041	1.00E+00
93	STK39	3.936	0.700	2.33E-02	TTN	41.372	0.926	2.91E-02	SCMH1	2.255	0.040	1.00E+00
94	AC092640.1	2.772	0.696	2.51E-02	ATP1B1	2.288	0.922	3.20E-02	SRSF10	0.742	0.032	1.00E+00
95	NFIA	2.958	0.695	2.53E-02	DDX24	1.141	0.900	4.19E-02	EIF4G3	2.580	0.031	1.00E+00
96	CACNA1C	18.385	0.694	2.46E-02	DSTN	0.947	0.862	6.16E-02	EPS15	1.042	0.024	1.00E+00
97	C15orf41	1.634	0.691	2.73E-02	PLN	5.126	0.824	7.93E-02	NRDC	0.907	0.023	1.00E+00
98	NFXL1	1.275	0.688	3.65E-02	MYL3	5.762	0.815	8.61E-02	AGO3	0.988	0.007	1.00E+00
99	CLIC5	0.963	0.686	3.10E-02	ANKRD1	5.405	0.804	1.02E-01	PUM1	1.052	0.006	1.00E+00
100	GHR	1.274	0.681	3.24E-02	SEPTIN7	1.640	0.762	1.37E-01	KIF1B	0.912	0.003	1.00E+00

Table S4: 100 most strongly expressed genes per subcluster (CM4, CM5, CM6) identified by snRNA-seq. Genes are ranked according to their log2 fold change vs average expression of entire dataset.

	CM4 Gene	CM4 Average	CM4 Log2 FC	CM4 P-Value	CM5 Gene	CM5 Average	CM5 Log2 FC	CM5 P-Value	CM6 Gene	CM6 Average	CM6 Log2 FC	CM6 P-Value
1	ERVMER61-1	1.522	2.842	5.84E-22	STAT4	1.564	1.922	1.33E-10	PDGFD	1.725	1.949	9.25E-08
2	GALNT17	3.635	2.592	4.16E-20	OPHN1	2.247	1.632	1.01E-07	MGAT4C	4.205	1.784	1.55E-06
3	RGS6	1.909	2.635	1.31E-19	ANKRD1	7.800	1.542	7.01E-07	PACRG	1.496	1.600	4.81E-05
4	AL590814.1	1.231	2.201	7.40E-13	NPPB	1.538	1.524	6.26E-06	CD36	0.381	1.420	2.21E-03
5	AC107294.2	1.404	1.917	3.34E-10	CREB5	1.213	1.389	2.52E-05	TBX20	2.502	1.414	6.71E-04
6	LRRTM4	1.960	1.961	3.76E-10	CLSTN2	1.230	1.236	4.42E-04	KCNH7	1.756	1.405	1.03E-03
7	LINC02069	1.110	1.847	2.90E-09	AC139720.1	2.436	1.041	5.35E-03	PHACTR1	2.096	1.366	1.38E-03
8	EPHA4	5.037	1.790	5.69E-09	INPP4B	4.541	0.968	1.25E-02	HIF1A-AS3	2.354	1.320	2.30E-03
9	BRINP3	4.290	1.797	7.23E-09	AC108472.1	1.753	0.957	1.47E-02	FSD2	1.364	1.307	2.85E-03
10	CADPS	5.974	1.747	1.53E-08	MID1	12.831	0.934	1.86E-02	GUCY1A2	1.140	1.261	6.11E-03
11	AL354771.1	1.774	1.782	1.60E-08	PHLDB2	1.519	0.900	3.00E-02	LINC02552	4.490	1.212	7.91E-03
12	CRNDE	2.865	1.738	2.08E-08	AC020909.2	9.510	0.866	3.98E-02	HAND2-AS1	1.290	1.202	9.32E-03
13	AC010967.1	1.510	1.752	3.03E-08	PTPRB	0.901	0.852	6.01E-02	DAB1	4.591	1.125	2.00E-02
14	GABRB2	0.913	1.697	1.69E-07	ROR1	8.664	0.817	6.50E-02	AC109466.1	1.135	1.120	3.14E-02
15	SYNPO2	1.234	1.676	1.80E-07	SORBS2	16.419	0.816	6.58E-02	HIF1A	2.318	1.119	2.11E-02
16	PPP2R2B	3.518	1.632	2.65E-07	ARHGAP24	1.507	0.806	7.95E-02	IL1RAPL1	7.416	1.112	2.20E-02
17	MIR100HG	10.387	1.602	4.24E-07	AKAP13	9.130	0.789	8.37E-02	GLCCI1	1.553	1.041	4.58E-02
18	NFXL1	2.262	1.572	1.81E-06	XRCC4	2.346	0.816	8.43E-02	PRDM16	1.007	1.024	5.45E-02
19	AC107068.2	5.439	1.560	2.04E-06	NCKAP5	1.454	0.805	9.05E-02	PDE5A	2.703	1.018	5.25E-02
20	OPCML	1.327	1.625	2.25E-06	ADAM19	0.843	0.793	9.24E-02	PITPNC1	1.313	1.015	6.03E-02
21	CCBE1	1.654	1.538	3.50E-06	MYOZ2	1.291	0.782	9.58E-02	FGF13	1.262	0.992	7.41E-02
22	BBOX1-AS1	1.110	1.537	5.81E-06	PURPL	1.603	0.796	9.58E-02	LINC01505	1.651	0.990	7.25E-02
23	Z85996.3	0.822	1.459	1.94E-05	COLQ	0.991	0.777	1.03E-01	SDK1	2.495	0.989	6.85E-02
24	SGCD	0.887	1.461	2.38E-05	TRIM55	1.472	0.769	1.06E-01	RYR2	35.557	0.982	6.78E-02
25	SLIT2	13.714	1.410	2.50E-05	ROR1-AS1	1.378	0.745	1.31E-01	PHLDB2	1.662	0.982	7.58E-02
26	GRAMD1B	5.745	1.381	3.36E-05	MTUS2	5.462	0.737	1.36E-01	THSD4	2.482	0.977	7.49E-02
27	KCNJ3	0.621	1.363	1.58E-04	ADGRL3	1.421	0.746	1.41E-01	PTPRK	3.998	0.956	8.65E-02
28	SEMA3A	1.804	1.279	2.49E-04	LRIG2-DT	1.193	0.732	1.49E-01	LAMA2	9.408	0.952	8.71E-02
29	EDA	5.400	1.215	6.24E-04	LINC02552	3.242	0.721	1.62E-01	ENO1	1.069	0.933	1.11E-01
30	STARD13	2.257	1.175	1.17E-03	ST3GAL6	1.091	0.718	1.66E-01	FGF12-AS1	1.347	0.931	1.14E-01
31	MAN1A1	2.163	1.166	1.35E-03	ABCC4	0.285	0.709	1.86E-01	BMP5	4.335	0.913	1.20E-01
32	DGKI	2.946	1.151	1.66E-03	SYTL5	1.048	0.703	1.92E-01	AC107021.1	1.214	0.896	1.49E-01
33	STARD13-AS	1.437	1.107	3.22E-03	KCNQ5	1.977	0.699	2.08E-01	GBE1	2.190	0.893	1.46E-01
34	DPY19L2	1.201	1.087	4.26E-03	EMC10	36.245	0.682	2.11E-01	ABLIM1	6.598	0.892	1.38E-01
35	TMTC1	1.728	1.086	4.30E-03	PCDH7	2.498	0.690	2.14E-01	LTBP1	6.002	0.876	1.55E-01
36	VWC2	1.194	1.086	4.69E-03	RBM20	7.011	0.677	2.19E-01	TMTC2	0.744	0.862	1.58E-01
37	SPHKAP	1.750	1.082	4.75E-03	AC008496.2	2.053	0.679	2.22E-01	KCNN2	2.185	0.861	1.78E-01
38	XYLT1	1.043	1.076	5.75E-03	AC087286.2	1.453	0.677	2.25E-01	KCNQ5	2.241	0.855	2.02E-01
39	SLC27A6	4.537	1.054	5.99E-03	MYO18B	5.973	0.671	2.27E-01	TMEM65	2.476	0.849	1.91E-01
40	LDLRAD4	6.071	1.015	9.19E-03	FLNB	0.931	0.689	2.29E-01	GOLGA8A	1.157	0.837	2.12E-01
41	AFF3	3.294	1.006	1.08E-02	GRIP1	0.953	0.677	2.38E-01	DECR1	1.343	0.835	2.12E-01
42	SHROOM4	1.210	1.015	1.13E-02	ACTN2	3.952	0.659	2.49E-01	AC139720.1	2.258	0.834	2.19E-01
43	CPNE5	1.380	1.010	1.14E-02	NEAT1	37.046	0.652	2.58E-01	FGF12	28.174	0.828	2.15E-01
44	LIMCH1	0.531	0.994	1.38E-02	EDNRA	1.522	0.658	2.60E-01	PGK1	0.861	0.815	2.56E-01
45	MAST4	9.043	0.965	1.65E-02	FGF13	1.006	0.664	2.63E-01	RNF150	2.906	0.802	2.56E-01
46	ERC2	2.600	0.961	1.82E-02	PRICKLE1	11.183	0.644	2.71E-01	AGL	1.504	0.799	2.64E-01
47	ICA1	1.630	0.960	1.88E-02	P2RY6	0.052	0.766	2.76E-01	FIGN	1.956	0.798	2.62E-01
48	ADCY5	1.725	0.952	2.03E-02	SLC16A1-AS1	2.060	0.642	2.77E-01	SLC8A1-AS1	20.656	0.795	2.61E-01
49	GREB1L	0.843	0.964	2.07E-02	NLGN1	2.259	0.646	2.83E-01	ERBB4	10.943	0.793	2.66E-01
50	AC109466.1	1.013	0.975	2.42E-02	JPH2	1.473	0.639	2.85E-01	PLOD2	1.104	0.788	2.90E-01
51	FLT1	0.847	0.952	3.02E-02	DDX60L	2.724	0.634	2.93E-01	AC093879.1	1.431	0.788	2.82E-01
52	KIFAP3	3.642	0.910	3.07E-02	ATP2B4	2.048	0.631	3.02E-01	TLN2	1.243	0.787	2.84E-01
53	AUTS2	19.972	0.905	3.11E-02	SHROOM3	2.191	0.629	3.06E-01	RBM24	1.714	0.768	3.12E-01

Supplement — 143

54	FOXO1	4.544	0.906	3.17E-02	ACTN4	1.451	0.621	3.21E-01	WDR60	1.182	0.767	3.17E-01
55	CERS6	2.535	0.897	3.50E-02	DENND5A	2.036	0.615	3.30E-01	LAMA4	1.013	0.762	3.32E-01
56	SCN5A	1.589	0.901	3.53E-02	RICTOR	1.041	0.605	3.62E-01	TECRL	7.224	0.761	3.18E-01
57	AMZ1	0.811	0.907	3.54E-02	SLMAP	1.887	0.595	3.74E-01	CREM	1.028	0.756	3.39E-01
58	AMMECR1	1.739	0.864	5.23E-02	AKAP6	4.244	0.593	3.76E-01	NAV3	0.513	0.750	3.25E-01
59	P3H2	1.327	0.862	5.34E-02	PDE10A	1.009	0.604	3.84E-01	SLC8A1	74.077	0.744	3.42E-01
60	PLEKHA5	8.653	0.848	5.52E-02	GCNT2	2.140	0.573	4.26E-01	CCSER1	1.831	0.744	3.59E-01
61	OSBP2	1.270	0.846	6.09E-02	PALM2- AKAP2	5.005	0.570	4.26E-01	MB21D2	0.772	0.743	2.98E-01
62	L3MBTL4	2.238	0.838	6.44E-02	XPR1	1.878	0.569	4.34E-01	GCNT2	2.425	0.738	3.61E-01
63	CLSTN2	1.017	0.852	7.03E-02	SH3D19	2.085	0.558	4.58E-01	SYNE2	0.793	0.736	3.11E-01
64	PBX1	9.375	0.813	7.71E-02	NT5C2	1.648	0.556	4.65E-01	SPHKAP	1.466	0.736	3.80E-01
65	TRDN-AS1	7.004	0.810	7.90E-02	CMYA5	4.958	0.549	4.77E-01	RCAN2	1.728	0.732	3.75E-01
66	AC138305.1	1.553	0.817	8.13E-02	SLC20A2	1.753	0.551	4.78E-01	MYBPC3	5.160	0.723	3.83E-01
67	FRS2	1.660	0.810	8.36E-02	CPEB4	1.666	0.550	4.79E-01	MARCH1	0.310	0.720	3.88E-01
68	SLC22A23	1.226	0.811	8.53E-02	MALAT1	554.747	0.542	4.85E-01	INPP4B	4.083	0.718	3.98E-01
69	ARHGAP26	1.936	0.799	9.01E-02	IPO9-AS1	4.414	0.540	4.98E-01	KDM4C	1.490	0.718	4.01E-01
70	INTS6L	1.250	0.794	9.69E-02	ARHGAP42	1.623	0.534	5.14E-01	ALOX5	0.032	0.695	8.51E-01
71	MTSS1	3.385	0.770	1.15E-01	MB21D2	0.667	0.540	5.19E-01	TMEM163	1.351	0.683	4.80E-01
72	SFMBT2	2.849	0.754	1.32E-01	INSR	0.956	0.535	5.19E-01	RNPC3	1.423	0.679	4.77E-01
73	AL136171.2	4.307	0.748	1.36E-01	NBEA	1.019	0.533	5.24E-01	TNNI3	0.582	0.676	4.28E-01
74	MACROD2	2.674	0.749	1.37E-01	FSD2	0.838	0.532	5.33E-01	PDZRN3	2.584	0.653	5.29E-01
75	MLIP	8.145	0.742	1.39E-01	ABHD15- AS1	1.132	0.527	5.38E-01	RBFOX1	1.613	0.650	5.45E-01
76	PDLIM5	20.471	0.741	1.40E-01	MYOM1	5.795	0.522	5.38E-01	AC113414.1	1.644	0.645	5.59E-01
77	TECRL	6.982	0.737	1.47E-01	ABTB2	1.653	0.525	5.40E-01	PRELID2	0.725	0.644	4.82E-01
78	TRIQK	1.177	0.738	1.58E-01	GFOD1	1.287	0.518	5.63E-01	KDM6A	1.706	0.639	5.60E-01
79	TRIM2	1.123	0.731	1.59E-01	SYT2	1.426	0.516	5.68E-01	FASTKD1	1.204	0.636	5.67E-01
80	DAB1	3.535	0.721	1.72E-01	PALLD	22.231	0.506	5.75E-01	NRP1	2.976	0.636	5.70E-01
81	SLC24A3	0.389	0.725	1.74E-01	ATF7IP2	1.592	0.510	5.76E-01	RAPGEF4	1.140	0.635	5.80E-01
82	DOCK9	1.078	0.719	1.77E-01	TNNI3	0.518	0.523	5.77E-01	PDZD2	1.386	0.634	5.75E-01
83	MIR99AHG	1.879	0.711	1.84E-01	CAMK2D	6.320	0.500	5.95E-01	INSR	1.038	0.632	5.80E-01
84	PPARGC1A	1.287	0.710	1.87E-01	SAMD4A	3.874	0.500	5.97E-01	TMEM161B- AS1	1.116	0.629	5.88E-01
85	RASSF8	1.466	0.708	1.90E-01	TTN-AS1	10.465	0.497	6.02E-01	AL450384.2	0.873	0.626	6.00E-01
86	CPVL	2.153	0.701	1.95E-01	TRIO	3.309	0.499	6.03E-01	LRRC39	1.006	0.625	5.98E-01
87	AP001021.3	1.406	0.700	2.02E-01	MARCH3	1.309	0.501	6.11E-01	SLC8A3	0.240	0.624	6.34E-01
88	NRXN1	0.272	0.723	2.04E-01	PKP2	1.879	0.491	6.28E-01	DCP1B	3.072	0.623	5.89E-01
89	STRBP	1.270	0.694	2.06E-01	HECW2	1.302	0.499	6.34E-01	EPB41L3	0.813	0.607	6.40E-01
90	MANBA	1.090	0.694	2.07E-01	MAP4	3.448	0.485	6.35E-01	LDHA	0.776	0.604	5.74E-01
91	ATP1B1	1.989	0.690	2.08E-01	PRKAG2	1.775	0.483	6.46E-01	TAB2	1.341	0.603	6.40E-01
92	BACH2	1.572	0.691	2.10E-01	FGD6	1.641	0.482	6.47E-01	PRKAA2	1.206	0.599	6.40E-01
93	GRK5	1.558	0.690	2.12E-01	ERC2	1.951	0.480	6.55E-01	WNK1	2.405	0.598	6.40E-01
94	BMP7	1.054	0.688	2.17E-01	TBC1D8	0.857	0.479	6.56E-01	DST	3.639	0.597	6.40E-01
95	AC124947.1	1.439	0.685	2.21E-01	ALPK3	1.273	0.476	6.57E-01	FGD4	0.631	0.596	5.81E-01
96	TRDN	9.405	0.672	2.29E-01	DMD	23.639	0.471	6.60E-01	AC106845.1	0.464	0.593	6.07E-01
97	MID1	11.207	0.670	2.38E-01	CELF2	2.072	0.468	6.76E-01	RNF207	1.346	0.588	6.59E-01
98	ESRRG	3.689	0.668	2.40E-01	PACS1	2.008	0.466	6.80E-01	TACC2	1.868	0.587	6.59E-01
99	ELL2	1.541	0.669	2.45E-01	NRXN3	1.267	0.492	6.86E-01	MLLT3	1.640	0.584	6.67E-01
100	HOMER1	1.541	0.667	2.45E-01	ATP13A3	2.241	0.463	6.87E-01	CACNA1C	18.773	0.575	6.76E-01

Table S5: 100 most strongly expressed genes per subcluster (FB, CM7, CM8) identified by snRNA-seq. Genes are ranked according to their log2 fold change vs average expression of entire dataset.

	FB Gene	FB Average	FB Log2 FC	FB P-Value	CM7 Gene	CM7 Average	CM7 Log2 FC	CM7 P-Value	CM8 Gene	CM8 Average	CM8 Log2 FC	CM8 P-Value
1	TDO2	1.056	6.402	2.19E-93	APOLD1	2.167	5.503	6.70E-90	ZNF385B	5.391	4.663	2.68E-51
2	DKK2	1.670	6.080	7.83E-73	CIT	1.130	5.503	6.70E-90	SLC8A3	1.423	4.039	2.04E-34
3	KCNE4	1.249	5.598	5.22E-91	KIF18B	1.072	5.440	5.56E-88	TRPM3	2.115	3.349	5.78E-23
4	COL6A3	4.728	5.401	2.58E-99	TOP2A	2.332	5.056	1.72E-78	HCN1	1.051	3.323	4.28E-21
5	LINGO2	2.648	5.077	3.84E-74	TPX2	1.239	4.944	1.15E-74	PAM	18.064	2.978	9.58E-19
6	LINC00632	1.195	4.975	9.69E-77	BUB1	1.085	4.874	1.53E-73	NRXN1	1.071	3.126	3.41E-18
7	MIR503HG	6.237	4.818	4.50E-77	NUSAP1	1.609	4.780	4.66E-72	RABGAP1L	9.067	2.655	4.68E-14
8	FAP	2.076	4.764	9.41E-73	ANLN	1.384	4.703	6.89E-70	KCNJ3	1.434	2.755	4.68E-14
9	TEX41	1.119	4.753	5.37E-60	POLQ	1.195	4.682	2.38E-69	NRXN3	4.544	2.636	2.72E-12
10	PDGFRB	1.717	4.730	3.58E-71	ASPM	1.075	4.722	6.66E-65	PLCB1	5.048	2.487	1.42E-11
11	AL390957.1	4.912	4.720	8.13E-65	ARHGAP11B	1.047	4.490	4.54E-61	GABRB2	1.355	2.236	2.01E-08
12	AP002518.2	1.515	4.557	5.23E-65	BRIP1	1.896	4.254	6.01E-56	COL4A6	1.338	2.107	3.20E-07
13	KCND2	2.871	4.411	2.48E-53	CENPF	1.622	4.487	4.27E-54	CACNA1D	2.033	2.105	3.51E-07
14	COL5A1	5.501	4.365	3.95E-65	C21orf58	1.317	4.149	9.05E-54	TBX5	3.738	2.041	3.65E-07
15	LINC01239	1.125	4.341	8.77E-50	MIR924HG	1.139	4.385	3.86E-51	CADPS2	1.164	2.069	8.51E-07
16	COL1A2	9.235	4.316	8.80E-59	RFC3	1.349	3.758	4.70E-43	Z85996.3	1.211	2.001	2.14E-06
17	SRPX2	1.414	4.308	1.60E-58	SMC4	1.700	3.497	1.40E-37	EFNA5	1.381	1.766	1.64E-04
18	COL1A1	11.448	4.236	7.93E-55	CEP128	1.169	3.384	1.72E-33	KCNIP4	2.904	1.897	2.03E-04
19	PAPSS2	1.108	4.226	4.64E-55	ECT2	1.038	3.256	7.32E-31	KCNH7	2.142	1.697	2.29E-04
20	MSC-AS1	1.877	4.202	4.22E-56	DIAPH3	4.282	3.148	1.07E-29	VAV3	0.204	1.743	3.18E-03
21	LMCD1	2.001	4.132	8.73E-52	ATAD2	1.803	2.915	9.30E-25	PDE4B	0.487	1.373	9.11E-03
22	SULF2	1.657	4.096	6.50E-53	EZH2	1.285	2.826	9.78E-23	CPNE5	1.804	1.375	9.11E-03
23	SERPINE2	1.576	4.036	1.15E-45	CENPP	1.773	2.780	7.92E-22	AC009264.1	10.861	1.358	9.19E-03
24	COL3A1	7.511	3.993	6.79E-47	MMS22L	1.044	2.526	3.70E-17	GRIP1	1.501	1.349	1.23E-02
25	TNC	3.919	3.983	1.07E-42	LINC01572	1.250	2.195	1.67E-12	MYL7	29.421	1.328	1.24E-02
26	PIEZO2	3.134	3.946	2.85E-49	BARD1	1.202	2.135	6.84E-12	AC008496.2	3.179	1.322	1.39E-02
27	COL6A2	2.009	3.937	4.87E-49	TRIM13	2.711	2.075	2.51E-11	CHRM2	7.221	1.285	1.89E-02
28	KCTD16	2.844	3.901	7.06E-42	SLC4A8	0.253	2.174	1.11E-10	ZNF608	1.791	1.257	2.63E-02
29	CLMAT3	1.026	3.873	1.82E-46	DLEU2	4.951	1.924	1.55E-09	NEDD4L	1.047	1.218	2.80E-02
30	CCDC102B	1.415	3.847	7.49E-42	ZNF43	1.065	1.921	2.73E-09	EDNRA	2.280	1.248	2.81E-02
31	AL137024.1	2.197	3.831	7.21E-43	RGS3	1.084	1.906	4.35E-09	CAMK1D	1.625	1.177	5.59E-02
32	MYO10	2.108	3.822	2.32E-44	NSD2	1.773	1.748	1.23E-07	RORA	1.891	1.161	6.63E-02
33	PAPPA	7.914	3.810	2.46E-45	SKA2	1.058	1.692	5.60E-07	LRMDA	1.487	1.151	7.46E-02
34	MRC2	1.674	3.799	1.40E-45	SCLT1	1.833	1.615	2.35E-06	COL4A5	4.586	1.114	8.15E-02
35	AP000331.1	1.686	3.791	2.22E-44	CKAP5	1.140	1.613	2.80E-06	COL8A1	0.749	1.162	8.95E-02
36	TIMP1	11.411	3.773	6.59E-35	POLA1	1.803	1.574	5.06E-06	AC020909.2	11.535	1.091	9.81E-02
37	DEC1	4.586	3.771	2.79E-36	LINC01515	1.706	1.565	6.57E-06	CMYA5	7.162	1.087	9.96E-02
38	RUNX1	3.848	3.744	1.94E-44	LCORL	1.638	1.561	6.70E-06	SOX5	0.877	1.077	1.05E-01
39	ADGRB3	1.308	3.566	3.09E-34	SYNE2	1.205	1.477	3.78E-05	STAT4	1.126	1.107	1.12E-01
40	ITGA11	4.875	3.558	2.05E-40	SPATA5	1.065	1.417	1.05E-04	EMC10	47.245	1.042	1.33E-01
41	ST6GAL2	1.404	3.555	8.01E-37	EPB41L3	1.287	1.408	1.25E-04	PLCL1	2.085	1.030	1.55E-01
42	BCAT1	1.276	3.503	4.74E-37	AL591519.1	1.363	1.400	1.57E-04	ARHGAP24	1.815	1.027	1.62E-01
43	ADAM12	1.853	3.485	8.14E-35	CACNA1D	1.277	1.374	3.64E-04	BMP5	4.685	1.014	1.64E-01
44	ITGA1	4.939	3.464	2.95E-37	MPHOSPH9	1.503	1.241	1.35E-03	BMP2K	0.820	0.958	1.90E-01
45	PRAG1	1.330	3.459	1.99E-34	NUCKS1	1.261	1.204	2.36E-03	NPPB	1.289	1.048	2.01E-01
46	GRIK2	2.111	3.452	1.04E-34	GREB1L	0.985	1.205	2.66E-03	SIK2	1.171	0.988	2.04E-01
47	CTHRC1	1.008	3.444	2.94E-34	CEP112	1.402	1.112	7.46E-03	RGS3	0.653	0.939	2.18E-01
48	GAS7	1.645	3.433	8.02E-35	ZRANB3	1.431	1.106	7.81E-03	TENM4	0.478	0.979	2.22E-01
49	ANOS1	1.254	3.420	1.75E-32	HP1BP3	1.378	1.074	1.14E-02	FRMD4B	1.790	0.971	2.28E-01
50	BNC2	2.029	3.383	1.58E-33	RANBP17	1.781	1.062	1.35E-02	ST6GALNAC3	0.932	0.924	2.31E-01
51	SPARC	2.686	3.370	1.59E-34	FRMD4B	1.806	1.034	1.95E-02	MYH6	8.686	0.946	2.48E-01
52	LMCD1-AS1	2.898	3.306	1.72E-32	AC005400.1	1.175	1.030	1.96E-02	MID1	13.618	0.936	2.62E-01
53	AP002989.1	2.881	3.304	1.37E-31	SRSF10	1.351	1.017	2.16E-02	TECRL	8.121	0.929	2.70E-01
54	NOX4	0.946	3.266	8.54E-28	RAD51B	0.941	1.008	2.82E-02	EPB41L3	0.970	0.873	2.97E-01

Supplement — 145

55	FRMD6	2.111	3.256	2.83E-30	MAGI3	1.051	0.943	4.87E-02	DOCK9	1.250	0.907	3.15E-01
56	FBN1	2.266	3.242	1.33E-31	SDK1	2.372	0.922	5.65E-02	SEMA3A	1.527	0.907	3.18E-01
57	SPATS2L	2.417	3.216	1.08E-31	DLG2	12.310	0.883	7.61E-02	RALGAPA2	0.947	0.819	3.82E-01
58	NHS	1.804	3.206	2.77E-29	ZNF704	1.298	0.882	8.25E-02	ST3GAL1	2.098	0.861	3.84E-01
59	TFPI	1.246	3.194	3.39E-29	MIR133A1HG	1.134	0.881	8.39E-02	FGD4	0.734	0.822	3.88E-01
60	ST6GALNAC5	3.199	3.180	1.07E-27	ST3GAL3	1.067	0.862	9.76E-02	LIPA	0.287	0.833	4.14E-01
61	AC022126.1	1.372	3.171	4.58E-28	ZNF83	0.861	0.863	1.01E-01	COLQ	1.051	0.797	4.20E-01
62	TNS3	2.780	3.151	1.58E-30	NAV2	3.269	0.840	1.12E-01	RGS6	0.807	0.825	4.24E-01
63	FN1	16.877	3.108	3.11E-29	AP001825.1	1.269	0.830	1.28E-01	PRELID2	0.807	0.799	4.29E-01
64	ACTA2	2.538	3.105	7.63E-28	NNT	1.252	0.818	1.37E-01	AC107021.1	1.195	0.847	4.34E-01
65	SULF1	4.163	3.082	1.80E-25	AFF3	2.989	0.812	1.40E-01	C1orf21	1.023	0.780	4.58E-01
66	LDB2	0.861	3.069	3.21E-20	PKP4	1.075	0.810	1.47E-01	MIR924HG	0.256	0.850	5.35E-01
67	RRBP1	1.333	3.061	3.93E-28	MCTP1	0.120	0.874	1.50E-01	INTS6L	1.291	0.792	5.36E-01
68	INHBA	1.438	3.051	2.99E-26	CDK19	1.002	0.808	1.50E-01	AL390783.1	2.059	0.784	5.50E-01
69	DCLK1	2.039	3.019	6.39E-25	MAP3K20	1.511	0.791	1.66E-01	CDK8	1.852	0.772	5.78E-01
70	SEPTIN11	2.671	3.012	2.13E-27	AP001011.1	1.099	0.789	1.71E-01	ERC2	2.412	0.772	5.79E-01
71	RAB31	0.584	3.006	1.57E-24	AP003086.1	0.810	0.787	1.86E-01	FSD2	0.972	0.720	5.85E-01
72	TRPS1	3.483	2.990	3.59E-27	KDM6A	1.832	0.769	1.93E-01	SPOCK1	0.649	0.719	6.40E-01
73	SPATA13	1.030	2.971	6.27E-25	CDC27	1.156	0.754	2.15E-01	PTPRB	0.868	0.711	6.40E-01
74	PDLIM3	2.546	2.965	2.56E-25	KLHL13	1.317	0.752	2.26E-01	SYNE2	0.785	0.701	6.41E-01
75	INSYN2B	0.470	2.964	1.43E-21	RSRC1	0.863	0.738	2.45E-01	ZFYVE16	1.001	0.693	6.43E-01
76	EDIL3	2.987	2.962	4.33E-25	PRKDC	1.035	0.720	2.71E-01	ADGRL3	1.488	0.749	6.58E-01
77	MYOF	1.613	2.952	1.82E-25	SNTA1	1.622	0.708	2.85E-01	AC011287.1	1.601	0.743	6.73E-01
78	C2orf27A	1.231	2.928	2.36E-24	PDS5B	1.202	0.701	3.01E-01	MAST4	8.107	0.721	6.92E-01
79	TENM3	3.169	2.926	1.71E-24	SMCHD1	1.162	0.695	3.11E-01	AC008771.1	1.663	0.716	7.00E-01
80	UACA	4.557	2.910	1.77E-25	ASXL1	1.498	0.687	3.25E-01	ADAM19	0.813	0.659	7.07E-01
81	GRIA3	1.541	2.907	3.39E-24	KCNQ5	2.016	0.693	3.33E-01	SLIT2	9.525	0.702	7.27E-01
82	APBB2	3.752	2.906	2.76E-25	NUP98	0.837	0.672	3.57E-01	ROR2	1.460	0.689	7.60E-01
83	CCDC80	2.754	2.905	2.88E-23	ATF7IP	1.044	0.665	3.67E-01	PLOD2	1.014	0.635	7.62E-01
84	SASH1	2.846	2.861	4.61E-24	PCM1	1.417	0.658	3.76E-01	SDK1	2.093	0.682	7.69E-01
85	PLXDC2	3.230	2.854	2.51E-23	HNRNPA2B1	1.199	0.658	3.79E-01	AL591519.1	0.885	0.629	7.86E-01
86	IL1R1	1.054	2.838	1.16E-21	PHACTR4	2.141	0.648	3.93E-01	FNBP1L	0.423	0.639	7.87E-01
87	DYNC2H1	2.742	2.800	1.91E-22	CALM2	1.164	0.645	4.05E-01	RAP1GAP2	1.268	0.677	7.93E-01
88	CDH11	6.925	2.798	1.01E-23	CRLF3	1.505	0.641	4.08E-01	SLC2A13	0.651	0.651	7.93E-01
89	SMYD3	16.884	2.724	2.20E-22	PHIP	1.042	0.636	4.25E-01	ST7-AS2	1.104	0.669	8.11E-01
90	MMP16	1.231	2.691	1.20E-19	C1orf21	0.919	0.637	4.31E-01	ATP2A2	4.493	0.657	8.19E-01
91	CALD1	25.180	2.655	5.88E-21	FUS	1.103	0.624	4.47E-01	TNNI3	0.561	0.601	8.67E-01
92	DDAH1	3.094	2.643	4.48E-19	ROR2	1.374	0.619	4.63E-01	HAND2-AS1	0.897	0.584	8.80E-01
93	PRKG1	10.159	2.632	1.54E-20	WWOX	2.179	0.614	4.67E-01	MARCH3	1.466	0.635	8.92E-01
94	SEC24D	2.048	2.626	3.62E-20	FANCC	1.015	0.605	4.92E-01	GRK3	0.315	0.594	8.94E-01
95	GPC6	13.452	2.621	2.35E-20	CDKAL1	1.347	0.597	5.06E-01	RC3H1	1.347	0.611	9.30E-01
96	CYTOR	1.971	2.620	1.33E-19	TNNI3K	3.583	0.587	5.27E-01	INPP4B	3.850	0.608	9.30E-01
97	AC083870.1	10.386	2.591	1.15E-19	DGKH	1.323	0.585	5.38E-01	AC139720.1	1.980	0.604	9.30E-01
98	FLT1	1.994	2.584	1.69E-18	RBMX	2.196	0.576	5.48E-01	CPEB4	1.780	0.606	9.30E-01
99	COL4A1	6.201	2.571	2.33E-19	FGD4	0.609	0.547	5.57E-01	AC005400.1	0.898	0.555	9.30E-01
100	KALRN	4.435	2.544	6.84E-19	LPAR6	0.314	0.555	5.57E-01	PRKAG2	1.960	0.597	9.30E-01

Table S6: 100 most strongly expressed genes per subcluster (ED, EC, CM9) identified by snRNA-seq. Genes are ranked according to their log2 fold change vs average expression of entire dataset.

	ED Gene	ED Average	ED Log2 FC	ED P-Value	EC Gene	EC Average	EC Log2 FC	EC P-Value	CM9 Gene	CM9 Average	CM9 Log2 FC	CM9 P-Value
1	MIR31HG	1.145	5.088	3.68E-49	PKHD1L1	1.359	6.601	6.52E-55	FYB1	0.114	3.469	1.00E+00
2	SERPINE1	9.100	4.185	3.91E-40	EBF1	1.610	4.983	6.46E-31	EBF1	0.571	2.493	1.00E+00
3	AKAP12	1.788	4.027	2.62E-34	ACSM3	1.806	5.199	5.25E-30	MGAM	0.019	1.961	1.00E+00
4	HMGA2	5.833	3.880	5.99E-34	PDE3A	10.149	4.306	8.94E-29	MIR924HG	0.476	1.719	1.00E+00
5	HMGA2-AS1	2.601	3.871	3.51E-33	EMCN	1.687	5.073	1.02E-27	ARHGAP11B	0.381	1.566	1.00E+00
6	AADAACL2-AS1	1.100	4.839	7.42E-32	MECOM	4.454	4.181	3.82E-27	CD86	0.000	1.551	1.00E+00
7	LINC01592	2.233	4.062	3.43E-31	CASC15	4.936	4.086	2.80E-26	VSIG4	0.000	1.521	1.00E+00
8	CRIM1	3.100	3.613	5.75E-30	BMP6	2.377	4.523	9.77E-25	SLC8A3	0.438	1.474	1.00E+00
9	SULT1E1	1.838	4.348	1.66E-29	PTGIS	2.019	3.986	1.04E-22	CENPF	0.514	1.346	1.00E+00
10	HAPLN1	1.063	4.294	2.82E-29	CFH	1.017	4.015	4.52E-22	ZNF385B	1.276	1.335	1.00E+00
11	NTM	3.508	3.584	2.17E-28	LDB2	1.885	4.112	4.17E-21	STAB1	0.000	1.214	1.00E+00
12	LINC02694	1.342	3.707	1.58E-26	EFNB2	1.126	3.681	1.26E-19	ASPM	0.286	1.201	1.00E+00
13	POSTN	2.458	3.634	3.21E-26	ITGA8	1.146	4.251	1.66E-19	HCK	0.000	1.144	1.00E+00
14	ITGA2	1.585	3.535	4.63E-26	RALYL	1.200	3.911	4.01E-19	ITGAX	0.000	1.144	1.00E+00
15	NEGR1	1.181	3.524	1.23E-25	C7	1.351	3.794	1.00E-18	CEP128	0.438	1.144	1.00E+00
16	TGFBI	1.365	3.391	1.38E-23	LRIG3	1.014	3.611	1.37E-18	KDM6A	2.533	1.141	1.00E+00
17	NABP1	0.551	3.476	1.70E-23	AC015522.1	4.091	3.866	1.85E-18	HS3ST2	0.000	1.087	1.00E+00
18	PCED1B	1.370	3.353	2.04E-23	SNTB1	0.662	3.866	2.47E-18	ITGA2	0.457	1.087	1.00E+00
19	DDAH1	4.687	3.279	2.57E-23	FLI1	1.200	3.535	6.19E-18	GABRB2	0.724	1.071	1.00E+00
20	CCN2	1.971	3.357	3.20E-23	KCNT2	1.361	3.488	7.46E-17	RPL18	0.724	0.985	1.00E+00
21	COL8A1	2.440	3.406	4.60E-23	SLC2A13	3.392	3.391	1.65E-16	SAMSN1	0.019	0.981	1.00E+00
22	EDIL3	3.932	3.259	4.65E-23	IQGAP2	0.536	3.717	3.51E-16	RAPGEF6	1.429	0.979	1.00E+00
23	FAM155A	2.724	3.321	1.02E-22	AC079465.1	1.439	3.333	6.08E-16	CLECTA	0.000	0.971	1.00E+00
24	KCNMA1	0.627	3.969	1.06E-22	MGP	1.070	3.897	1.35E-15	RPS3A	0.971	0.970	1.00E+00
25	AL078459.1	3.325	3.220	2.35E-22	C12orf40	1.948	3.229	4.15E-14	APOLD1	0.438	0.957	1.00E+00
26	EGFR	1.009	3.303	2.67E-22	AC078923.1	1.045	3.428	2.33E-13	PRELID2	0.933	0.956	1.00E+00
27	FN1	20.082	3.157	4.28E-22	ZNF385D	2.132	3.139	4.74E-13	AC022126.1	0.495	0.956	1.00E+00
28	FRMD6	2.481	3.251	4.42E-22	LINC01091	1.285	3.118	8.04E-13	NRXN3	1.829	0.942	1.00E+00
29	COL25A1	1.211	3.454	6.58E-22	HAPLN1	1.000	3.622	9.28E-13	NRXN1	0.324	0.935	1.00E+00
30	AC013652.1	1.455	3.299	1.36E-21	PRKCB	0.431	3.444	1.47E-12	TRPM3	0.590	0.926	1.00E+00
31	FLI1	0.887	3.221	3.55E-21	FLRT2	4.359	3.010	2.78E-12	ST18	0.000	0.921	1.00E+00
32	BMP6	1.368	3.658	1.86E-20	ST8SIA4	0.326	3.552	5.58E-12	VAV3	0.114	0.921	1.00E+00
33	ITGA4	0.794	3.193	2.91E-20	LSAMP	6.056	2.993	9.77E-12	SLC25A3	1.029	0.907	1.00E+00
34	ST6GALNAC5	3.738	3.176	3.86E-20	AC007319.1	1.883	2.990	1.50E-11	CDC42SE2	0.800	0.867	1.00E+00
35	TGFB2	2.180	3.103	6.31E-20	UNC5C	1.596	2.944	2.62E-11	CRYAB	0.571	0.858	1.00E+00
36	SYT1	1.235	3.289	1.91E-19	LRP1B	1.126	3.218	3.03E-11	SPOCK1	0.724	0.837	1.00E+00
37	FRMD4A	3.771	2.972	9.80E-19	NOX4	1.136	3.024	3.04E-11	RPS4X	0.914	0.837	1.00E+00
38	INHBA	1.605	2.970	8.81E-18	NRG1	2.491	3.138	3.09E-11	TRPM2	0.000	0.835	1.00E+00
39	THBS1	1.808	2.981	8.82E-18	KCNIP4	6.231	3.132	4.54E-11	RPL3	0.838	0.834	1.00E+00
40	CDH13	4.288	2.889	2.48E-17	SULT1E1	1.546	3.428	6.08E-11	KIF18B	0.190	0.833	1.00E+00
41	PVT1	2.448	2.867	2.81E-17	COL25A1	1.159	3.057	8.17E-11	BUB1	0.210	0.812	1.00E+00
42	TENM2	2.328	3.035	6.52E-17	NRG3	10.198	2.859	1.34E-10	SNX24	0.838	0.811	1.00E+00
43	LPCAT2	0.533	2.972	9.71E-17	ARHGAP18	1.004	2.845	1.86E-10	DIAPH3	1.429	0.810	1.00E+00
44	C2orf27A	1.366	2.856	1.78E-16	NCOA7	2.111	2.764	7.15E-10	ALOX5	0.019	0.808	1.00E+00
45	DCLK1	2.206	2.877	5.66E-16	KLHL4	2.707	2.719	1.09E-09	RPS19	0.952	0.807	1.00E+00
46	CCL2	0.674	2.890	9.22E-16	EFNA5	2.604	2.757	1.51E-09	AP000462.1	1.181	0.802	1.00E+00
47	APBB2	3.979	2.744	9.25E-16	PLXDC2	3.876	2.735	1.51E-09	NDUFA13	0.743	0.801	1.00E+00
48	CASC15	2.409	2.869	1.36E-15	AC090579.1	1.309	2.774	1.62E-09	PAM	5.619	0.800	1.00E+00
49	UBASH3B	0.554	2.949	1.38E-15	SULF1	4.817	2.830	1.67E-09	RGS3	0.610	0.787	1.00E+00
50	ADAM12	1.666	2.841	2.41E-15	PCED1B	1.155	2.748	1.93E-09	RFC3	0.343	0.774	1.00E+00
51	PRSS23	1.216	2.757	2.96E-15	MCC	5.252	2.637	3.06E-09	CIT	0.190	0.769	1.00E+00
52	PTGIS	1.056	2.924	3.36E-15	CPNE8	0.614	2.723	3.12E-09	ATP6V0D2	0.000	0.763	1.00E+00
53	LRP1B	0.910	3.062	3.71E-15	TENM4	1.377	2.669	6.77E-09	LCP1	0.000	0.746	1.00E+00
54	COTL1	0.334	2.934	4.28E-15	NPAS3	2.268	2.645	1.00E-08	NPPB	1.105	0.742	1.00E+00

Supplement — 147

55	EFNB2	0.647	2.826	4.52E-15	LPCAT2	0.526	2.727	1.01E-08	AP001825.1	1.276	0.742	1.00E+00
56	MECOM	2.076	2.858	5.83E-15	ELMO1	0.891	2.611	1.74E-08	ANLN	0.267	0.735	1.00E+00
57	SP100	0.844	2.697	5.95E-15	IL1R1	1.190	2.617	2.02E-08	RPL15	0.667	0.733	1.00E+00
58	AC093866.1	2.509	3.301	7.03E-15	PIEZO2	2.419	2.614	2.80E-08	COX6C	0.781	0.722	1.00E+00
59	NHS	1.729	2.772	7.79E-15	AP002989.1	2.722	2.615	4.02E-08	STAT4	0.914	0.720	1.00E+00
60	PRAG1	1.172	2.780	1.23E-14	MYH10	4.553	2.528	5.05E-08	ATP5F1B	0.590	0.712	1.00E+00
61	FBN1	2.062	2.693	1.69E-14	TFPI	1.179	2.549	5.23E-08	RPL34	0.686	0.712	1.00E+00
62	MYO10	1.633	2.749	1.94E-14	PLEKHG1	1.177	2.512	7.06E-08	PLAUR	0.076	0.711	1.00E+00
63	DEC1	3.876	2.898	5.86E-14	SYT1	1.037	2.691	7.46E-08	RPS15	0.533	0.705	1.00E+00
64	SULF1	4.141	2.752	6.01E-14	TENM3	3.301	2.537	8.32E-08	RPL5	0.857	0.696	1.00E+00
65	PAPPA	5.913	2.668	8.21E-14	PBX3	6.281	2.480	9.33E-08	TOP2A	0.419	0.693	1.00E+00
66	FEZ2	1.294	2.588	2.54E-13	ADAMTS9	2.037	2.497	1.20E-07	KRT18	0.629	0.688	1.00E+00
67	TENM3	3.118	2.610	2.73E-13	ADGRB3	1.101	2.568	2.25E-07	ENO1	0.952	0.676	1.00E+00
68	DOCK5	0.962	2.567	3.07E-13	ZNF804A	0.683	2.650	2.46E-07	RICTOR	1.162	0.672	1.00E+00
69	MYOF	1.550	2.584	3.41E-13	ARID5B	1.546	2.391	3.55E-07	LDHA	0.838	0.668	1.00E+00
70	FLNB	2.835	2.544	3.45E-13	ECE1	1.134	2.379	3.81E-07	RPS23	0.648	0.667	1.00E+00
71	CD44	0.975	2.591	4.09E-13	DYNC2H1	2.788	2.408	5.39E-07	LYN	0.171	0.667	1.00E+00
72	GRIA3	1.509	2.585	5.03E-13	BICC1	2.907	2.374	5.79E-07	CPEB4	1.924	0.666	1.00E+00
73	LIMA1	1.289	2.539	8.14E-13	NCKAP5	4.033	2.334	1.16E-06	MT-ATP6	0.400	0.661	1.00E+00
74	ARID5B	1.536	2.543	1.12E-12	DPYSL3	1.909	2.333	1.36E-06	RPL41	1.352	0.661	1.00E+00
75	MMP16	1.303	2.564	1.85E-12	ENTPD1	0.241	2.606	1.42E-06	LCORL	1.010	0.640	1.00E+00
76	AL137024.1	1.595	2.623	2.16E-12	LIMCH1	1.260	2.278	2.09E-06	TPX2	0.210	0.638	1.00E+00
77	MYH10	3.969	2.442	9.54E-12	VAV3	0.367	2.651	2.38E-06	FTH1	0.457	0.637	1.00E+00
78	PRKCA	1.351	2.472	9.69E-12	AHRR	0.283	2.411	3.77E-06	PLCB1	1.771	0.633	1.00E+00
79	NCOA7	1.622	2.456	1.16E-11	FBN1	1.800	2.278	4.80E-06	MEF2C	1.486	0.630	1.00E+00
80	TNC	2.745	2.636	1.99E-11	CHST15	0.165	2.606	5.62E-06	APBB1IP	0.000	0.629	1.00E+00
81	PDE3A	3.926	2.584	2.05E-11	CCDC80	2.522	2.301	5.98E-06	TNNI1	1.771	0.627	1.00E+00
82	BCAT1	0.922	2.416	2.83E-11	ETS1	1.072	2.167	8.89E-06	ATP5MG	0.648	0.624	1.00E+00
83	CCDC80	2.534	2.461	3.55E-11	SOX6	4.388	2.175	1.04E-05	C12orf40	0.400	0.623	1.00E+00
84	SACS	1.099	2.383	4.11E-11	CCL2	0.528	2.259	1.33E-05	CBL	0.610	0.619	1.00E+00
85	EMCN	0.625	3.069	6.36E-11	ITGA4	0.540	2.255	1.35E-05	SYK	0.000	0.613	1.00E+00
86	NRG1	1.673	2.591	7.86E-11	GMD5	1.532	2.113	1.39E-05	PRDX2	0.438	0.611	1.00E+00
87	CYTOR	1.929	2.352	9.25E-11	OXR1	2.239	2.159	1.40E-05	EPN2	1.181	0.607	1.00E+00
88	ANXA2	2.355	2.321	9.78E-11	SAT1	6.093	2.137	2.27E-05	STK10	0.267	0.606	1.00E+00
89	VIM	3.202	2.352	9.92E-11	SOX5	1.761	2.157	2.48E-05	CREM	0.971	0.605	1.00E+00
90	AC015522.1	1.977	2.650	1.32E-10	TCF4	2.792	2.101	2.57E-05	TNNC1	2.324	0.604	1.00E+00
91	PRKCA-AS1	0.359	2.450	1.72E-10	LAMB1	2.450	2.102	2.65E-05	ZFYVE16	0.971	0.603	1.00E+00
92	BNC2	1.511	2.397	1.73E-10	ATP11C	1.342	2.063	3.01E-05	CKM	0.610	0.602	1.00E+00
93	NPAS3	1.764	2.353	2.03E-10	AL138828.1	1.097	2.109	3.21E-05	RPL7A	0.705	0.602	1.00E+00
94	AC090579.1	0.964	2.387	2.20E-10	PVT1	1.732	2.068	3.33E-05	LINC01572	0.533	0.602	1.00E+00
95	SEPTIN11	2.159	2.295	3.38E-10	HECW2	3.709	2.087	3.77E-05	GNAS	1.790	0.599	1.00E+00
96	TAGLN	1.688	2.319	3.96E-10	POSTN	1.357	2.213	3.77E-05	MGST3	1.143	0.598	1.00E+00
97	ARHGAP18	0.693	2.337	4.01E-10	ROBO1	5.225	2.075	4.05E-05	RPS2	0.686	0.594	1.00E+00
98	EFNA5	1.872	2.323	5.69E-10	TGFB2	1.400	2.090	4.45E-05	CCNH	1.238	0.594	1.00E+00
99	MAP1B	3.311	2.240	6.08E-10	DPYD	1.047	2.060	4.64E-05	HOMER1	1.562	0.594	1.00E+00
100	SPOCK1	1.633	2.291	6.89E-10	SP100	0.645	2.061	4.71E-05	RPS27A	0.781	0.593	1.00E+00

Table S7: 100 most strongly expressed genes per subcluster (CM10, LK) identified by snRNA-seq. Genes are ranked according to their log₂ fold change vs average expression of entire dataset.

	CM10 Gene	CM10 Average	CM10 Log ₂ FC	CM10 P-Value	LK Gene	LK Average	LK Log ₂ FC	LK P-Value
1	ERVMER61-1	1.649	2.277	1.00E+00	VSIG4	1.038	10.743	1.27E-36
2	GALNT17	4.022	2.159	1.00E+00	CD86	1.015	10.710	7.15E-30
3	RGS6	1.874	2.009	1.00E+00	TRPM2	1.605	10.213	1.24E-35
4	LINC02069	1.416	1.878	1.00E+00	PIK3R5	2.855	10.040	5.17E-44
5	AL590814.1	1.247	1.784	1.00E+00	CLEC7A	1.416	9.897	2.44E-28
6	GABRB2	1.150	1.751	1.00E+00	SYK	1.793	9.788	4.80E-38
7	AL354771.1	2.075	1.700	1.00E+00	STAB1	1.180	9.773	3.61E-32
8	SYNPO2	1.504	1.685	1.00E+00	ATP8B4	4.083	9.467	6.04E-43
9	OPCML	1.577	1.608	1.00E+00	ITGAX	1.192	9.466	1.87E-29
10	SGCD	1.086	1.530	1.00E+00	HCK	1.180	9.395	3.66E-24
11	EPHA4	5.181	1.512	1.00E+00	AC131944.1	3.339	9.339	2.23E-31
12	AC107294.2	1.287	1.440	1.00E+00	MRC1	1.864	9.195	4.89E-35
13	BRINP3	4.127	1.419	1.00E+00	CYBB	2.077	8.796	2.85E-28
14	CCBE1	1.794	1.407	1.00E+00	FYB1	1.487	8.618	6.48E-27
15	MIR100HG	10.892	1.400	1.00E+00	MMP12	4.142	8.539	4.55E-25
16	CADPS	5.776	1.390	1.00E+00	SLC11A1	1.687	8.520	7.10E-28
17	AMZ1	1.199	1.360	1.00E+00	DOCK8	4.000	8.498	1.78E-37
18	Z85996.3	0.877	1.328	1.00E+00	SAMSN1	2.218	8.429	4.60E-31
19	LRRTM4	1.625	1.321	1.00E+00	APBB1IP	1.404	8.413	6.17E-25
20	FLT1	1.174	1.304	1.00E+00	HS3ST2	1.003	8.340	3.27E-09
21	PPP2R2B	3.354	1.285	1.00E+00	SPP1	11.351	8.334	4.75E-32
22	PIK3AP1	0.032	1.169	1.00E+00	ST18	1.086	8.195	8.74E-18
23	CRNDE	2.381	1.162	1.00E+00	LCP1	1.215	8.160	4.48E-27
24	GRAMD1B	5.711	1.154	1.00E+00	RBM47	5.687	8.148	4.80E-38
25	XYLT1	1.215	1.149	1.00E+00	PTPRC	2.808	8.109	6.95E-34
26	VWC2	1.368	1.132	1.00E+00	MGAM	1.038	8.105	3.45E-18
27	STARD13-AS	1.617	1.122	1.00E+00	KYNU	1.404	8.059	1.15E-22
28	GREB1L	1.022	1.116	1.00E+00	ATP6V0D2	1.145	7.986	1.23E-24
29	CPNE5	1.593	1.080	1.00E+00	DOCK10	4.720	7.515	7.28E-32
30	DPY19L2	1.311	1.063	1.00E+00	LNCAROD	7.186	7.354	1.44E-30
31	KCNJ3	0.571	1.041	1.00E+00	SLCO2B1	1.440	7.335	1.68E-22
32	STARD13	2.309	1.035	1.00E+00	PIK3AP1	1.487	7.286	1.27E-23
33	TMTC1	1.850	1.032	1.00E+00	ARHGAP15	1.239	7.132	2.37E-19
34	AC010967.1	1.134	1.030	1.00E+00	AL035446.2	2.029	7.110	2.11E-23
35	MAN1A1	2.196	1.017	1.00E+00	ALOX5	1.593	7.001	6.13E-24
36	AFF3	3.644	1.011	1.00E+00	ADGRE2	1.050	6.625	2.34E-18
37	STAB1	0.008	0.991	1.00E+00	KCNK13	2.407	6.597	1.75E-21
38	SPHKAP	1.826	0.990	1.00E+00	VAV3	4.236	6.528	9.32E-24
39	SEMA3A	1.681	0.983	1.00E+00	COL23A1	4.012	6.454	5.64E-22
40	EDA	5.221	0.982	1.00E+00	GNPMB	1.145	6.430	1.61E-16
41	SLC27A6	4.682	0.947	1.00E+00	CXCL8	1.180	5.871	8.23E-11
42	SLC24A3	0.475	0.940	1.00E+00	ADAP2	1.746	5.865	6.38E-17
43	AL450384.2	1.110	0.925	1.00E+00	TPRG1	5.605	5.831	1.08E-17
44	FOXO1	5.012	0.923	1.00E+00	MERTK	3.103	5.757	6.53E-17
45	SLIT2	11.190	0.885	1.00E+00	ST8SIA4	1.510	5.657	1.42E-12
46	AL591519.1	1.062	0.857	1.00E+00	MBP	1.664	5.633	4.90E-15
47	AC117834.1	1.335	0.848	1.00E+00	CHST15	1.180	5.525	6.81E-13
48	ADCY5	1.754	0.846	1.00E+00	TBXAS1	2.525	5.509	9.10E-15
49	LDLRAD4	5.961	0.842	1.00E+00	ENTPD1	1.699	5.503	7.27E-14
50	SCN5A	1.649	0.834	1.00E+00	CD163L1	2.926	5.431	1.42E-12
51	PLEKHA5	9.187	0.817	1.00E+00	IPCEF1	1.204	5.365	2.82E-12
52	OSBP2	1.343	0.817	1.00E+00	KCNMA1	2.431	5.312	1.43E-09
53	FRS2	1.794	0.816	1.00E+00	P2RY6	1.015	5.194	1.35E-11
54	BBOX1-AS1	0.796	0.807	1.00E+00	CD36	4.720	5.122	1.91E-12

Supplement — 149

55	AUTS2	19.926	0.773	1.00E+00	IQGAP2	1.664	5.087	3.40E-10
56	DGKI	2.534	0.761	1.00E+00	SKAP2	1.027	5.039	2.67E-10
57	MLIP-AS1	2.598	0.756	1.00E+00	PLAUR	1.581	5.022	6.19E-11
58	KIF26B-AS1	3.588	0.754	1.00E+00	SAMHD1	1.664	4.989	1.81E-11
59	SHROOM4	1.102	0.740	1.00E+00	NPL	1.274	4.908	1.52E-10
60	PDLIM5	21.929	0.740	1.00E+00	NABP1	2.018	4.889	2.74E-10
61	AC087286.2	1.625	0.738	1.00E+00	GPR34	1.463	4.887	2.60E-10
62	CERS6	2.470	0.735	1.00E+00	MCTP1	1.723	4.807	5.04E-10
63	DOCK9	1.158	0.734	1.00E+00	MYO1F	2.348	4.800	1.19E-10
64	PPARGC1A	1.392	0.734	1.00E+00	RCBTB2	1.086	4.750	3.31E-09
65	PBX1	9.573	0.731	1.00E+00	AHRR	1.416	4.714	3.81E-09
66	UGP2	2.357	0.727	1.00E+00	DOCK11	1.888	4.698	2.87E-09
67	AP001825.1	1.255	0.725	1.00E+00	UBASH3B	2.265	4.686	7.08E-09
68	AP001021.3	1.504	0.710	1.00E+00	PRKCB	1.180	4.654	3.07E-07
69	DISC1	6.395	0.704	1.00E+00	HPCAL1	1.156	4.624	1.42E-08
70	ESRRG	4.006	0.700	1.00E+00	RAB31	2.584	4.621	2.96E-09
71	ST18	0.008	0.696	1.00E+00	SNTB1	1.451	4.620	1.88E-07
72	P3H2	1.279	0.695	1.00E+00	LYN	2.549	4.604	2.88E-09
73	AC107068.2	3.572	0.684	1.00E+00	ZNF804A	2.737	4.576	9.53E-08
74	PIK3R1	1.158	0.683	1.00E+00	CTSB	4.330	4.562	2.63E-09
75	HOMER1	1.649	0.682	1.00E+00	DOCK2	3.363	4.524	2.80E-08
76	MLIP	8.334	0.675	1.00E+00	AC105916.1	1.180	4.226	7.52E-07
77	ICA1	1.464	0.672	1.00E+00	COTL1	1.027	4.219	3.31E-06
78	MKNK1	0.241	0.662	1.00E+00	PLXDC2	11.233	4.130	1.42E-06
79	GRK5	1.617	0.656	1.00E+00	SLC4A8	1.168	4.122	3.31E-06
80	CLSTN2	0.957	0.655	1.00E+00	FCGRT	1.168	4.111	2.09E-06
81	STRBP	1.311	0.654	1.00E+00	ELMO1	2.667	4.072	2.15E-06
82	MANBA	1.118	0.646	1.00E+00	CCDC200	1.003	4.040	6.65E-06
83	MID1	11.688	0.640	1.00E+00	LRMDA	10.348	3.954	2.69E-06
84	AC008496.2	2.140	0.635	1.00E+00	EEPD1	1.935	3.944	6.51E-06
85	AC124947.1	1.472	0.632	1.00E+00	PTPRJ	4.248	3.887	6.65E-06
86	INTS6L	1.199	0.631	1.00E+00	SLC9A9	2.100	3.887	1.50E-05
87	ATP1B1	2.019	0.622	1.00E+00	FMNL2	5.711	3.867	8.63E-06
88	ZFPM2-AS1	4.239	0.615	1.00E+00	PRKCA	4.047	3.808	2.03E-05
89	ARHGAP26	1.834	0.614	1.00E+00	LPCAT2	1.239	3.804	7.94E-05
90	WWC2	1.311	0.610	1.00E+00	AL136962.1	1.793	3.794	5.34E-05
91	TRPM2	0.008	0.610	1.00E+00	PRKCA-AS1	1.038	3.744	1.35E-04
92	LIMCH1	0.442	0.609	1.00E+00	PLIN2	1.286	3.729	7.98E-05
93	TRDN-AS1	6.564	0.604	1.00E+00	INSYN2B	1.192	3.716	2.74E-04
94	ADGRL3	1.392	0.602	1.00E+00	ABCA1	3.127	3.706	4.82E-05
95	COL18A1	1.054	0.599	1.00E+00	DAPK1	4.142	3.664	5.83E-05
96	TRDN	9.420	0.583	1.00E+00	DPYD	3.186	3.594	1.41E-04
97	NFXL1	1.368	0.577	1.00E+00	CPQ	3.316	3.576	1.28E-04
98	MTSS1	3.169	0.571	1.00E+00	GSAP	1.404	3.566	1.84E-04
99	AC109466.1	0.837	0.567	1.00E+00	MKNK1	1.758	3.564	1.62E-04
100	CAMK2D	6.982	0.567	1.00E+00	ARHGAP18	1.876	3.546	3.24E-04

9.2 List of abbreviations**A**

ACACB	Acetyl-CoA carboxylase beta
ACAD10	Acyl-CoA dehydrogenase family member 10
ACAD8	Isobutyryl-CoA dehydrogenase
ACAD9	Acyl-CoA dehydrogenase family member 9
ACADM	Medium-chain specific acyl-CoA dehydrogenase
ACADS	Short-chain specific acyl-CoA dehydrogenase
ACADSB	Short/branched chain specific acyl-CoA dehydrogenase
ACADVL	Very long-chain specific acyl-CoA dehydrogenase
ACADVL	Very long-chain specific acyl-CoA dehydrogenase
ACAT1	Acetyl-CoA acetyltransferase 1
ACAT2	Acetyl-CoA acetyltransferase 2
ACBD6	Acyl-CoA-binding domain-containing protein 6
ACN	Acetonitrile
ACO1	Cytoplasmic aconitate hydratase
ACSL	Acyl-CoA synthetase
ACSL4	Long-chain-fatty-acid-CoA ligase 4
ACTA2	Smooth muscle α -actin
ACTB	Beta-actin
ACTN1	Alpha-actinin 1
ACTN2	Alpha-actinin 2
ADH5	Alcohol dehydrogenase class 3
ADP	Adenosine diphosphate
ALDH7A1	Alpha-aminoacidic semialdehyde dehydrogenase
ALDH9A1	4-trimethylaminobutyraldehyde dehydrogenase
ALDOA	Fructose-bisphosphate aldolase A
ALDOC	Aldolase, fructose-bisphosphate C
AMPK	Adenosine monophosphate-activated protein kinase
ANP	Atrial natriuretic peptide
APD	Action potential duration
APOA1	Apolipoprotein A 1
APOE	Apolipoprotein E
Aqua dest.	Aqua destillata (distilled water)
ATP	Adenosine triphosphate
ATP2A2	Sarco/endoplasmic reticulum Ca ²⁺ -ATPase
ATP5H	ATP synthase subunit d
ATP5O	ATP synthase subunit O
ATP5S	ATP synthase subunit s

B

BAG3	BAG family molecular chaperone regulator 3
BBOX1	γ -butyrobetaine hydroxylase
BCA	Bicinchoninic acid
BDM	Butanedione monoxime
BMP4	Bone morphogenetic protein 4

BMP6	Bone morphogenetic protein 6
bp	Base pair
bpm	Beats per minute
BSA	Bovine serum albumin
BTS	N-benzyl-p-toluene sulphonamide

C

CACT	Carnitine-acylcarnitine translocase
CALD1	Caldesmon 1
CAS	CRISPR associated
Cas9	CRISPR associated protein 9
CCN2	Cellular communication network factor 2
CD36	Cluster of differentiation 36
CDM	Conditioned Medium
cDNA	Complementary DNA
CECAD	Exzellenzcluster cellular stress responses in aging-associated diseases
CERT	Ceramide transfer protein
CERT1	Cardiac event risk test 1
CKM	Creatine kinase M-type
CKMT2	Creatine kinase S-type
CM	Cardiomyocytes
c-MYC,	Cellular myelocytomatosis
CoA	Coenzyme A
COL1A1	Collagen type I alpha 1 chain
CON	Control
COX6C	Cytochrome c oxidase subunit 6C
COX7A1	Cytochrome c oxidase subunit 7A1
COX7A2	Cytochrome c oxidase subunit 7A2
COX7C	Cytochrome c oxidase subunit 7C
CPT1	Carnitine palmitoyltransferase 1
CPT2	Carnitine palmitoyltransferase 2
CRAT	Carnitine acetyltransferase
CRISPR	Clustered regularly interspaced short palindromic repeats
crRNA	CRISPR-RNA
CS	Citrate synthase
cTnT	Cardiac troponin T

D

DAG	Diacylglycerols
DAG1	Dystroglycan
DCM	Dilated cardiomyopathy
DCMA	Dilated cardiomyopathy with ataxia
DEC1	2,4-dienoyl-CoA reductase
DLAT	Dihydrolipoamide S-acetyltransferase
DMEM	Dulbecco's modified eagle medium
DMSO	Dimethyl sulfoxide

DNA Deoxyribonucleic acid
 DSB Double-strand break
 DTT Dithiothreitol

E

E2 Estradiol
 EB Embryoid bodies
 EC Endothelial cells
 ECH1 Delta(3,5)-Delta(2,4)-dienoyl-CoA isomerase
 ECHS1 Enoyl-CoA hydratase
 ECI1 Enoyl-CoA delta isomerase 1
 ECI2 Enoyl-CoA delta isomerase 2
 ECM Extracellular matrix
 ED Endocardium-like cells
 EDTA Ethylenediaminetetraacetic acid
 EHT Engineered heart tissue
 ENO2 Enolase 2
 ENO3 Enolase 3
 ER Endoplasmic reticulum
 ESR1 Estrogen receptor alpha
 ETFB Electron transfer flavoprotein subunit beta
 ETFB Electron transfer flavoprotein subunit beta

F

FABP3 Fatty acid-binding protein 3
 FABP5 Fatty acid-binding protein 5
 FACS Fluorescence-activated cell sorting
 FADH₂ Flavin adenine dinucleotide
 FAP Fibroblast activation protein alpha
 FATP Fatty acid transport protein
 FCS Fetal calf serum
 FHL2 Four and a half LIM domains protein 2
 FITM1 Fat storage-inducing transmembrane protein 1
 FN1 Fibronectin 1
 FOXO1 Forkhead box protein O 1
 FSC Forward scatter
 FTDA bFGF, TGFβ1, dorsomorphin and activin A-based hiPSC culture medium

G

g Relative centrifugal force
 G-6-P Glucose-6-phosphate
 GAA Alpha glucosidase
 GAPDH Glyceraldehyde-3-phosphate dehydrogenase
 GATA4 GATA binding protein 4
 gDNA Genomic DNA

GFP	Green fluorescent protein
GFPT1	Glutamine-fructose-6-phosphate transaminase 1
gnomAD	Genome Aggregation Database
GlcNAc	N-acetylglucosamine
GLUT	Glucose transporter
gRNA	Guide RNA
GUSB	Beta-glucuronidase
H	
HADHA	Trifunctional enzyme subunit alpha
HADHB	Hydroxyacyl-CoA dehydrogenase trifunctional multienzyme complex subunit beta
HAPLN1	Hyaluronan and proteoglycan link protein 1
HBP	Hexosamine biosynthetic pathway
HBSS	Hanks' balanced salt solution
HDR	Homology-directed repair
HDR	Homology-directed repair
HEK293	Human embryonic kidney 293
HEPES	4-(2-hydroxyethyl)-1-piperazineethanesulfonic acid
HIF1a	Hypoxia-inducible factor 1 alpha
HiPSC	Human induced pluripotent stem cells
HK1	Hexokinase 1
HK2	Hexokinase 2
HMOX2	Heme oxygenase 2
HSD17B12	Very-long-chain 3-oxoacyl-CoA reductase
Hz	Hertz
I	
IDH3A	Isocitrate dehydrogenase [NAD] subunit alpha
IDH3B	Isocitrate dehydrogenase [NAD] subunit beta
Indel	Insertion/ deletion
iPSC	Induced pluripotent stem cell
J	
JVS	Juvenile visceral steatosis
K	
KEGG	Kyoto encyclopedia of genes and genomes
KLF4	Kruppel-like factor 4
L	
L/G ratio	Δ Lactate/ Δ Glucose ratio
LAMA2	Laminin subunit alpha-2
LC	Liquid chromatography

LCAC	Long-chain acylcarnitine
LC-ESI-MS/MS	Liquid chromatography coupled to electrospray ionization tandem mass spectrometry
LCFA	LCFA
LC-MS	Liquid chromatography–mass spectrometry
LDHA	Lactate dehydrogenase A
LDHB	Lactate dehydrogenase B
LDL	Low-density lipoprotein
LDLR	Low-density lipoprotein receptor
LK	Leukocytes
LMNA	Lamin A/C
LPCAT3	Lysophospholipid acyltransferase 5
LRP1	Pro-low-density lipoprotein receptor-related protein 1

M

MB	Myoglobin
MCT	Monocarboxylate transporter
MDH1	Malate dehydrogenase 1
MDH2	Malate dehydrogenase 2
MKI67	Antigen Ki-67
mM	Millimolar
mN	Millinewton
mRNA	Messenger RNA
mtDNA	Mitochondrial DNA
mtND1	NADH dehydrogenase- 1
mtND2	NADH dehydrogenase- 2
MTTP	Microsomal triglyceride transfer protein large subunit
MYBPC3	Myosin-binding protein C
MYH6	Myosin heavy chain 6
MYH7	Myosin heavy chain 7
MYL2	Myosin light chain 2
MYL4	Myosin light chain 4
MYL6	Myosin light chain 3
MYL7	Myosin light chain 7
MYL9	Myosin light chain 9

N

NADH	Nicotinamide adenine dinucleotide phosphate
NCEH1	Neutral cholesterol ester hydrolase 1
NCEH1	Neutral cholesterol ester hydrolase 1
NCX	Na ⁺ /Ca ²⁺ -exchange protein 1
NDUFA10	NADH dehydrogenase [ubiquinone] 1 alpha subcomplex subunit 10
NDUFA11	NADH dehydrogenase [ubiquinone] 1 alpha subcomplex subunit 11
NDUFA4	NADH dehydrogenase [ubiquinone] 1 alpha subcomplex subunit 4
NDUFA8	NADH dehydrogenase [ubiquinone] 1 alpha subcomplex subunit 8
NHEJ	Non-homologous end-joining

O

OCT4	Octamer-binding transcription factor 4
OCTN	Organic cation transporters
OGDH	2-oxoglutarate dehydrogenase
OT	Off-target
Ox-Phos	Oxidative phosphorylation

P

PAM	Protospacer adjacent motif
PBS	Phosphate-buffered saline
PCA	Principal component analysis
PCD	Primary carnitine deficiency
PCR	Polymerase chain reaction
PDGFRB	Platelet-derived growth factor receptor beta
PDH	Pyruvate dehydrogenase
PDHA1	Pyruvate dehydrogenase E1 component subunit alpha
PDK1	Pyruvate dehydrogenase kinase 1
PDK3	Pyruvate dehydrogenase kinase 3
PDK4	Pyruvate dehydrogenase kinase 4
PFA	Paraformaldehyde
PFKM	ATP-dependent 6-phosphofructokinase
PGAM1	Phosphoglycerate mutase 1
PGAM2	Phosphoglycerate mutase 2
PGM1	Phosphoglucomutase 1
PKHD1L1	Polycystic kidney and hepatic disease 1-Like protein
PKM	Pyruvate kinase M1/2
PLN	Cardiac phospholamban (PLB)
POSTN	Periostin
POSTN	Periostin
PPP	Pentose phosphate pathway
PRKAG2	5'-AMP-activated protein kinase subunit gamma-2
PTFE	Polytetrafluoroethylene
PTPRC	Protein tyrosine phosphatase receptor type C
PVDF	Polyvinylidene fluoride

Q

qPCR	Quantitative real-time PCR
------	----------------------------

R

RNA	Ribonucleic acid
RNP	Ribonucleoprotein
RPMI	Roswell Park Memorial Institute
RT	Relaxation time
RYR2	Ryanodine receptor 2

S

SDHA	Succinate dehydrogenase
SDS	Sodium dodecyl sulfate
SEM	Standard error of the mean
SERCA2	Sarco/endoplasmic reticulum Ca ²⁺ -ATPase
SERPINE1	Serine proteinase inhibitor 1
SGCA	Alpha-sarcoglycan
SGCD	Delta-sarcoglycan
SLC22A5	Solute carrier family 22 member 5
SLC25A20	Mitochondrial carnitine/acylcarnitine carrier protein
SLC27A1	LCFA transport protein 1
SLC27A6	LCFA transport protein 6
SLC27A6	LCFA transport protein 6
snRNA-seq	Single-nucleus RNA sequencing
SOX2	Sex determining region Y-box 2
SR	Sarcoplasmic reticulum
SSC	Sideward scatter
SSEA3	Stage-specific embryonic antigen-3

T

T3	Triiodothyronine
TAC	Transverse aortic constriction
TAG	Triglyceride
TAGLN2	Transgelin 2
TALEN	Transcription activator-like effector nuclease
TAZ	Tafazzin
TBX5	T-Box transcription factor 5
TCA	Tricarboxylic acid
TCF21	Transcription factor 21
TEAB	Tetraethylammonium bromide
TFA	Trifluoroacetic acid
TGFβ	Transforming growth factor-beta
THP	N-trimethyl-hydrazine-3-propionate
Tm	Melting temperature
TMT	Tandem Mass Tag
TNC	Tenascin-C
TNNC1	Troponin C
TNNT2	Troponin T2
TPM2	Tropomyosin beta chain
TPM4	Tropomyosin alpha-4 chain
TPT1	Translational-controlled tumor protein
TRAM	Transgenic animal and genetic engineering models
tracrRNA	Trans-activating CRISPR RNA
TTN	Titin
TTP	Time to peak

U

U	Unit
UDP-GlcNAc	Uridine diphosphate N-acetylglucosamine
UKE	University Medical Center Hamburg Eppendorf

V

VLDL	Very-low-density lipoprotein
VLDL-CE	Very low-density lipoprotein-cholesteryl ester
VLDLR	Very low-density lipoprotein receptor
vs	versus
VTN	Vitronectin

W

Wnt	Wingless-type MMTV integration site family
-----	--

Z

ZFN	Zinc finger nuclease
-----	----------------------

9.3 Devices, materials and substances

9.3.1 Devices

4D-Nucleofector™ Core Unit and X Unit (Lonza)
 AbiPrism7900HT cycler (Applied Biosystems)
 ABL90 FLEX Analysator (Radiometer)
 Analytic Scale Genius (Sartorius AG)
 BD FACSAria™ IIIu (BD Biosciences)
 BD FACSCanto™ II (BD Biosciences)
 Benchmark XT (Ventana)
 Bioanalyzer 2100 (Agilent)
 C25 Incubator Shaker (New Brunswick Scientific)
 Cell culture incubator CB 220 (Binder)
 Cell culture incubators S2020 1.8, HERAcell 240 & 150i (Thermo Fischer Scientific)
 Cell culture incubators MCO-19M & MCO-20AIC (Sanyo)
 Centrifuges 5415 R & 5810 R (Eppendorf)
 Centrifuge J-6B (Beckmann)
 Centrifuges Rotanta/RP & Universal 30 RF (Hettich)
 ChemiDoc™ Touch Imaging System (Bio-Rad Laboratories)
 Cryopreservation system Asymptote EF600M (Grant Instruments)
 Electrophoretic Transfer Cell Mini Trans-Blot cell (Bio-Rad Laboratories)
 Gel electrophoresis cell Mini-PROTEAN 3 Cell (Bio-Rad Laboratories)
 Gel electrophoresis tank Sub-cell® GT (Bio-Rad Laboratories)
 Magnetic stirring and heating plate IKA Combimag RET (Janke & Kunkel GmbH & Co KG)
 Magnetic stirring plate Variomag / Cimarec Biosystem Direct (Thermo Scientific)
 Magnetic stirring plate Variomag / Cimarec Biosystem 4 Direct (Thermo Scientific)
 Microscope Axioskop 2 with AxioCam Color (Zeiss)
 Microscope Axiovert 25 (Zeiss) with ProgRes Speed XT core 5 camera (Jenoptik)
 Microscope BZ-X710 (Keyence)
 Microscope EVOS FL Cell Imaging System (Thermo Fischer Scientific)
 NanoDrop ND-1000 Spectrophotometer (Thermo Fischer Scientific)
 nCounter® SPRINT (NanoString)
 QIAcube HT System (Qiagen)
 Pipettes 10 / 100 / 1000 µL (Eppendorf)
 Pipette controller Accu-jet® pro (Brand)
 Power supply PowerPac Bacic (Bio-Rad Laboratories)
 Precision Advanced Scale (Ohaus)
 S88X dual output square pulse stimulator (Grass)
 Safety workbench HeraSafe (Heraeus)
 Safety workbench Safe 2020 (Thermo Fischer Scientific)
 Thermal cycler Hybaid PCR Sprint (Thermo Fischer Scientific)
 Thermal cycler vapo.protect (Eppendorf)
 Thermomixer comfort (Eppendorf)
 TissueLyser (Qiagen)
 Video-optical EHT analysis system (EHT Technologies GmbH)
 Water bath 25900 (Medax)
 Warming cabinet Kelvitron® t (Heraeus)

9.3.2 Software

AxioVision Rel. 4.8.2 (Zeiss)
 Bismark (Babraham Institute)
 CRISPOR 4.99 (Concordet JP, Haeussler M)

FACSDiva (BD Biosciences)
FASTQC (Babraham Bioinformatics)
Custom Alt-R[®] CRISPR-Cas9 guide RNA design tool (IDT[®])
Image Lab Version 5.2.1 (Bio-Rad Laboratories)
ImageJ 1.47v (Wayne Rasband)
Inkscape 1.1 (Inkscape)
Loupe Browser 5.0.1 (10x Genomics)
Perseus 1.6.15.0 (Mann and Cox Lab Group)
ProgRes[®] Capture Pro 2.8.8 (Jenoptik)
Prism 8.4.4 (GraphPad)
SDS 2.4.1 (Applied Biosystems)
SnapGene[®] 3.3.4 (GSL Biotech LLC)
TIDER 1.0.3 (Bas van Steensel lab)
Webgestalt 2019 (Zhang Lab Group)

9.3.3 Materials and equipment

250 mL Vacuum Filtration "rapid"-Filtermax (TPP, 99250)
500 mL Vacuum Filtration "rapid"-Filtermax (TPP, 99500)
Aspiration pipette 2 mL (Sarstedt, 86.1252.011)
Cell culture flask T175 (Sarstedt, 83.3911.002)
Cell culture flask T80 (Nunc, 178905)
Cell culture flask T75 and T175 for suspension culture (Sarstedt, 83.3911.502 / 83.3912.502)
Cell culture microplate 96 well μ Clear[®] black CELLSTAR[®] (Greiner Bio-One, 655090)
Cell culture plate 6 / 12 / 24-well (Nunc)
Cell scraper (Sarstedt, 83.1830)
Cell strainer 30 μ m (Sysmex, 04-004-2326)
Cryovial CryoPure 1.6 mL (Sarstedt, 72.380)
Flow cytometry tubes (Sarstedt, 55.1579)
Neubauer counting chamber (Karl-Hecht KG)
Pacing adapter/cables (EHT Technologies GmbH, P0002)
Pacing electrode carbon (EHT Technologies GmbH, P0001)
Pipette tips (Sarstedt)
Pipette tips with Biosphere filter (Sarstedt)
Reaction tube graduated 15 mL (Sarstedt, 62.554.502)
Reaction tubes conical 15 / 50 mL (Sarstedt)
Reaction tubes Safe Lock 0.2 – 2 mL (Eppendorf)
Round bottom tube 12 mL (Greiner Bio-One, 163160)
Serological pipettes 1 / 2 / 5 / 10 / 25 / 50 mL (Sarstedt)
Silicone rack (EHT Technologies GmbH, C0001)
Spinner flasks 500 / 1000 mL (Integra Biosciences, 182101 / 182051)
Syringe filtration unit Filtropur S 0.2 μ m (Sarstedt, 83.1826.001)
Teflon Spacer (EHT Technologies GmbH, C0002)
TissueLyser Steel Beads (QIAGEN, 69989)

9.3.4 Cell culture medium and serum

DMEM (Biochrom, F0415)
DMEM/F12 (Gibco, 21331-046)
DMEM, no glucose, no glutamine, no phenol red (Gibco, A1443001)
Fetal calf serum (Biochrom, S0615)
Horse serum (Life Technologies, 26050088)
RPMI 1640 (Gibco, 21875)

9.3.5 Reagents

1,4-Dithiothreitol (DTT, Roth, 6908.2)
 10x DMEM (Gibco, 52100-021)
 1-Thioglycerol (Sigma-Aldrich, M6145)
 2-Mercaptoethanol (Sigma-Aldrich, M6250)
 2-Propanol (Merck Millipore, 107022)
 6x DNA loading dye (Thermo Fisher Scientific, R0611)
 Accutase® Cell Dissociation Reagent (Sigma-Aldrich, A6964)
 Activin A (R&D Systems, 338-AC)
 Agarose (Invitrogen, 15510-027)
 Alt-R® S.p. Cas9 Nuclease 3NLS, (IDT®, 1081058)
 Alt-R® CRISPR-Cas9 tracrRNA, ATTO™ 550, (IDT®, 1075927)
 Alt-R® Cas9 Electroporation Enhancer, (IDT®, 1075916)
 Ammoniumpersulfate (APS, Bio-Rad Laboratories, 161-0700)
 Aprotinin (Sigma-Aldrich, A1153)
 Aqua ad iniectabilia (Baxter S.A., 001428)
 B27 Plus Insulin (Gibco, 17504-044)
 bFGF (basic FGF, R&D Systems, 233-FB)
 BMP4 (R&D Systems, 314-BP)
 BTS (N-Benzyl-p-Toluenesulfonamide, TCI, B3082-25G)
 Chloroform/trichloromethane (Roth, 4432.1)
 Collagenase II (Worthington, LS004176)
 D(+)-Glucose anhydrous (Roth, X997.2)
 DMSO (Sigma-Aldrich, D4540)
 DNase (Sigma-Aldrich, D8764)
 Dorsomorphin (Abcam, ab120843 or Tocris, 3093)
 EDTA (Roth, 8043.2)
 Ethanol, absolute (Chemsolute, 2246.1000)
 Fibrinogen (Sigma-Aldrich, F8630)
 Geltrex® (Gibco, A1413302)
 GeneRuler 1 kb DNA Ladder (Thermo Fisher Scientific, SM0313)
 GeneRuler 100 bp DNA Ladder (Thermo Fisher Scientific, SM0243)
 Glutaraldehyde (Science Services, E16222)
 HBSS (-) Ca²⁺/Mg²⁺ (Gibco, 14175-053)
 HEPES (Roth, 9105.4)
 Human serum albumin (Biological Industries, 05-720-1B)
 Hydrocortisone (Sigma-Aldrich, H4001)
 Insulin (Sigma-Aldrich, I9278)
 L-Carnitine–hydrochlorid (Sigma-Aldrich, C0283-5G)
 L-Glutamine (Gibco, 25030-081)
 Linoleic Acid-Oleic Acid-Albumin, 100x (Sigma-Aldrich, L9655-5ML)
 Lipidmix (Sigma-Aldrich, L5146)
 Matrigel® Basement Membrane Matrix (Corning, 354234)
 Matrigel® Growth Factor Reduced Basement Membrane Matrix (Corning, 354230)
 Methanol (J. Baker, 8045)
 Midori Green (Biozym, 617004)
 Na-Selenite (Sigma-Aldrich, T8158)
 Nitrogen, liquid (TMG)
 Non-essential amino acids (Gibco, 11140)
 Penicillin / Streptomycin (Gibco, 15140)
 Phosphoascorbate (2-Phospho-L-ascorbic acid trisodium salt, Sigma-Aldrich, 49752)
 Pluronic F-127 (Sigma-Aldrich, P2443)
 Polyvinyl alcohol (Sigma-Aldrich, P8136)
 PFA (Thermo Scientific, 28908)
 PVA (Sigma-Aldrich, P8136)

Roti®-Histofix 4% (Roth, P087.3)
 Saponin (Merck, 558255)
 Sodium azide (Sigma-Aldrich, 71290)
 Sodium chloride solution 0.9% (B. Braun, 3570210)
 TBS (Sigma-Aldrich, T6664)
 TGFβ1 (Peprotech, 100-21)
 Thrombin (Sigma-Aldrich, T7513)
 Transferrin (Sigma-Aldrich, S5261)
 Triiodothyronine (European Commission – Joint Research Center IRMM-469)
 Trizma® base (Sigma-Aldrich, T1503)
 TRIzol (Life Technologies, 15596026)
 Trypan Blue (Biochrom, L 6323)
 Trypsin-EDTA 0.5% (Gibco, 15400054)
 XAV-939 (Tocris, 3748)
 Y-27632 (Biaffin, PKI-Y27632-010)

9.3.6 Kits and enzymes

5x HOT FIREPol® EvaGreen® qPCR Mix Plus ROX (Solis BioDyne, 08-24-00008)
 Agencourt AMPure XP - PCR Purification (Beckman Coulter, A63880)
 Amaxa™ P3 Primary Cell 4D-Nucleofector X Kit L (Lonza, V4XP-3024)
 Amaxa™ P4 Primary Cell 4D-Nucleofector X Kit L (Lonza, V4XP-4024)
 DNeasy® Blood & Tissue Kit (QIAGEN, 69504)
 DreamTaq Green DNA Polymerase (Thermo Fischer Scientific, EP0711)
 HOT FIREPol® DNA Polymerase (Solis BioDyne, 01-02-00500)
 High-Capacity cDNA Reverse Transcription Kit (Applied Biosystems, 4368813)
 MinElute PCR Purification Kit (QIAGEN, 28004)
 MyTaq™ DNA Polymerase (Meridian Bioscience, BIO-21105)
 PfuTurbo Cx Hotstart DNA Polymerase (Agilent, 600410)
 QIAamp® 96 DNA QIAcube® HT kit (Qiagen, 51331)
 QIAquick® PCR Purification Kit (Qiagen, 28104)
 RNA 6000 Pico Kit (Agilent, 5067-1513)
 RNeasy Plus® Mini Kit (Qiagen, 74134)
 TRIzol Reagent (Life Technologies, 15596026)

9.3.7 Composition of reagents, buffers, and solutions

Table S8: Composition of used reagents, buffers, and solutions.

Reagent / buffer / solutions	Composition
Agarose for EHT casting	2% (w/v) Agarose 300 mL 1xPBS Sterilized by autoclaving before storage at 60 °C.
Aprotinin	33 mg/mL Aprotinin Aqua ad iniectabilia
BTS solution	30 mM BTS in DMSO
Dissociation buffer	HBSS (-) calcium/magnesium 200 U/mL Collagenase II 1 mM HEPES 10 µM Y-27632 30 µM BTS

DNase solution	100 mg DNase II, type V 50 mL PBS
EDTA	0.5 mM EDTA PBS
FACS buffer	PBS 5% (v/v) FCS 0.05% (v/v) Sodium azide 0.5% (w/v) Saponin (for intracellular staining)
Fibrinogen	200 mg/mL Fibrinogen 100 µg/mL Aprotinin 0.9%-NaCl solution
HEPES stock solution	1 M HEPES PBS Potassium hydroxide for adjustment of pH to 7.4
Phosphoascorbate, 250 mM	1 g Phosphoascorbate dissolved in 12.4 mL PBS
Pluronic F-127 solution	0.1% (v/v) Pluronic F-127 in PBS
Polyvinyl alcohol (50x)	20 g polyvinyl alcohol 100 mL Aqua dest.
Thrombin	100 U/mL Thrombin 60% (v/v) PBS 40% (v/v) Aqua ad iniectabilia
Transferrin–selenium	100 mg Transferrin 2 mL sodium selenite (382 µM)

9.3.8 Antibodies

Table S9: Primary antibodies used for flow cytometry/FACS.

Antibody	Dilution	Company and Cat#
Anti-cardiac troponin T-FITC	1:50	Miltenyi Biotec, 130-119-674
REA Control (I)-FITC	1:50	Miltenyi Biotec, 130-120-709
Rat Anti-Human SSEA-3 Antibody, PE Conjugated	1:50	BD Biosciences, 560237
Rat IgM, κ Isotype Control Antibody, PE Conjugated	1:50	BD Biosciences, 553943

9.3.9 Primer, ssODN and gRNA sequences

Table S10: Primer pairs for PCR and Sanger sequencing.

Target region	Sequence forward primer [5'→3']	Sequence reverse primer [5'→3']	Product [bp]
OCTN2 (N32S) OT#1	ATCCCAGTAAAAGGCATAAAAGC	TGCTCCATTTTCCCATCAATCT	924
OCTN2 (N32S) OT#2	CAGTTCCACATGCCCTTAGG	CCACCCACTCTTCCTCCTAG	939
OCTN2 (N32S) OT#3	TGTCTGGTGTGCTGGTTTTTC	TTGGTAAGGGTTGGGGAGTG	945
OCTN2 (N32S) OT#4	GCCATGCTGAACTGTGAGTC	TCCCCTCAGCAAAACAGATG	951
OCTN2 (N32S) OT#5	ACAGAGGAGGACAGTGAGTG	GCCAGGAAAGAGCATAGCAC	941
OCTN2 (N32S) OT#6	GTCTTGCATCACACCACCTG	CTTTGTAACCCAGGCTGGAA	1046
OCTN2 (N32S) OT#7	GAGGCACGCTACTCCCTGAG	CAGCAGTGTAGTGGGACGG	910
OCTN2 (N32S) OT#8	TGATTGGCTGCACATGTCAA	TGCTTAGACGGGCTAGAACC	910
OCTN2 (N32S) OT#9	ATGGAACCAGAGCACAGTCT	CCTTCCCAGCCATTAGAAC	908
OCTN2 (N32S) OT#10	GCGGTAATGCTCACTCATCC	ACCCCTTGTGTTATGTGAGGA	959
OCTN2 (-/-) gRNA1 OT#1	AAGTCAGGGGAATGCAGTG	GGGTTGACCAGGCTGCTG	1071
OCTN2 (-/-) gRNA1 OT#2	TCTCACTATGTTGCCAGGCT	ATTCTAGCAGTGCTGCGTGT	987
OCTN2 (-/-) gRNA1 OT#3	GCCACAGAGCTGGTAATGTATG	GTGGACGATCACGTCCCTTTG	916
OCTN2 (-/-) gRNA1 OT#4	TCTCAATGGTGGGATTCTTCTGTT	AGGGTTAGCCGTCCTCATTG	904
OCTN2 (-/-) gRNA1 OT#5	CCTTTCAAAGTGTTCAGCTACA	TCTTTGCAGCTGCTTTTATGGT	1028
OCTN2 (-/-) gRNA1 OT#6	GAGGAATTCGGATCCACCTGA	GTACTIONACTTTGATGGGC	921
OCTN2 (-/-) gRNA1 OT#7	CTTGTAGGTGAGCCCTTGAAT	TGTGGTCAGTGCCTCATTACTTA	980
OCTN2 (-/-) gRNA1 OT#8	CCACGCTGTCCACGATGAT	ATAAGGACCCTGGTCACGCT	938
OCTN2 (-/-) gRNA1 OT#9	ATCGTGCCAGGCCAACTTAT	GAGAGGCAGTGCATTCACCA	1000
OCTN2 (-/-) gRNA1 OT#10	ACCTTACTCAGCATAACACCAGA	TGTGTTCTTGACCTCATGC	960
OCTN2 (-/-) gRNA2 OT#1	TCCTCAAATTGCCGAGCAT	CACTCAGGCTTGGCTCCATT	932
OCTN2 (-/-) gRNA2 OT#2	ACTCCATGTGAGCAAGAACTATGT	GAAATGAGTGACAGAAACCAGAGC	900
OCTN2 (-/-) gRNA2 OT#3	CAGGCACCGAGTAGAAAGCA	TCATCATCACGCCACCTTCT	934
OCTN2 (-/-) gRNA2 OT#4	GTCCCATAGCCATGGTCAACAC	GGTGTGCCCTCCTTCTCTATTTT	933
OCTN2 (-/-) gRNA2 OT#5	GAAAGCTGCAGTGCCACATATT	CCTTCCATCTCTGGGAGCTATT	1099
OCTN2 (-/-) gRNA2 OT#6	AGCAGGGGACGAAGGTTTAC	GAGGGTCTCCGTTCCAGCAAG	931
OCTN2 (-/-) gRNA2 OT#7	GAATCAGTCCTTCTGAGGCAGTT	ATCACTTAGAAGTTGTGAGACCAT	907
OCTN2 (-/-) gRNA2 OT#8	CCTTTTGTTCCCACTGCTGTA	ACATGGTTGTGCCTTAGGCTAT	968
OCTN2 (-/-) gRNA2 OT#9	CACAGAAGGAAGAGGCAGCA	CTTCCAGGCCATGAGTCCAG	1009
OCTN2 (-/-) gRNA2 OT#10	CAGCAAGACCAAGAGACAAACC	ATCCATTGCTTTCCATCCCTATAA	827
OCTN2 (-/-) gRNA1	ACTTTCTCCTTACCTCCGCC	GCTATCAGGAACACGGAGGA	500
OCTN2 (-/-) gRNA2	TCTTGACCCATCTCCTCAG	GGTGAAAAGAGTGAGGCAGC	659
OCTN2 (-/-) Internal	ATGGGAAAGAAGCCTGCTCT	CTAGTCAACCGGGTCACAGA	530
OCTN2 (-/-) External	TGCCTTCCTAAGCCGAGC	GGTGAAAAGAGTGAGGCAGC	500
SLC22A5 (Exon 1)	GTCTTGGGTCGCCTGCTG	GTCTCCATCGCTAGGGTGT	652

Table S11: Primer pairs for qPCR.

Target	Sequence forward primer [5'->3']	Sequence reverse primer [5'->3']	Product [bp]
SLC22A5	TTTGGCTACATGGTGCTGCCA	GATGAACCACCAGAGTGCCAC	111
CD36	TCTTTCCTGCAGCCCAATG	AGCCTCTGTTCCAAGTATAGTGA	60
CPT1B	ACATCTCTGCCCAAGCTTCC	ACCATGACTTGAGCACCAGG	175
PDK4	AGAGGTGGAGCATTCTCGC	ATGTTGGCGAGTCTCACAGG	138
HK2	CAAAGTGACAGTGGGTGTGG	GCCAGGTCCTTCACTGTCTC	87
ENO1	GCCGTGAACGAGAAGTCCTG	ACGCCTGAAGAGACTCGGT	79
PKM	ATGTCGAAGCCCCATAGTGAA	TGGGTGGTGAATCAATGTCCA	118
GAPDH	TCGGAGTCAACGGATTTGGT	TCGCCCCACTTGATTTTGGGA	250
HIF1a	ACCCTAACTAGCCGAGGAAGA	GCACCAAGCAGGTCATAGGT	145
COL1A1	GGCCAGAAGAAGTGGTACA	CGCTGTTCTTGCAAGTGGTAG	199
GUSB	AAACGATTGCAGGGTTTCAC	CTCTCGTCGGTGACTGTTCA	171
β -ACTIN	CATGTACGTTGCTATCCAGGC	CTCCTTAATGTCACGCACGAT	250
mtND1	ATGGCCAACCTCCTACTCCTCATT	TTATGGCGTCAGCGAAGGGTTGTA	154
mtND2	CCATCTTTGCAGGCACACTCATCA	ATTATGGATGCGGTTGCTTGCCTG	172

Table S12: SsODN and gRNA sequences.

Component	Sequence [5'->3']
ssODN Template	CGAGTGGGGGCCCTTCCAGCGCCTC ATCTTCTTCTGCTCAGCGCCAGCAT CATTCCCAGTGGCTTACCGGCCTGT CCTCCGTGTTCTGATAGCGACCCCG GAGCACCGCTGCCGGGT
OCTN2 (N32S) gRNA	ACAGGCCGGTGAAGCCATTG
OCTN2 (-/-) gRNA 1	TTACATAGGGCGCACGACCA
OCTN2 (-/-) gRNA 2	GGCAGAGGTGATCATCCGCA

9.4 Financial support

This project was financially supported by the German Research Foundation (DFG) and the German Centre for Cardiovascular Research (DZHK).

9.5 Publications

Cuello F, Knaust AE, Saleem U, Loos M, Raabe J, Mosqueira D, Laufer S, Schweizer M, Van der Kraak P, Flenner F, Ulmer BM, Braren I, Yin X, Theofilatos K, Ruiz-Orera J, Patone G, Klampe B, Schulze T, Piasecki A, Pinto Y, Vink A, Hübner N, Sian Harding S, Mayr M, Denning C, Eschenhagen T, Hansen A. (2021) Impairment of the ER/mitochondria compartment in human cardiomyocytes with PLN p.Arg14del mutation. *EMBO Mol Med* 13:e13074.

Warnecke N, Ulmer BM, Laufer SD, Shibamiya A, Krämer E, Neuber C, Hanke S, Behrens C, Loos M, Münch J, Kühnisch J, Klaassen S, Eschenhagen T, Patten-Hamel M, Carrier L, Mearini G. (2021) Generation of bi-allelic MYBPC3 truncating mutant and isogenic control from an iPSC line of a patient with hypertrophic cardiomyopathy. *Stem Cell Res* 55:102489.

Shibamiya A, Schulze E, Krauß D, Reinsch M, Schulze ML, Steuck S, Mearini G, Mannhardt I, Schulze T, Klampe B, Werner T, Saleem U, Knaust A, Laufer SD, Neuber C, Lemme M, Behrens CS, Loos M, Weinberger F, Fuchs S, Eschenhagen T, Hansen A, Ulmer BM. (2020) Cell Banking of hiPSCs: A Practical Guide to Cryopreservation and Quality Control in Basic Research. *Curr Protoc Stem Cell Biol* 55:1–26.

Mannhardt I, Saleem U, Mosqueira D, Loos M, Ulmer BM, Lemoine MD, Larsson C, Améen C, De Korte T, Vlaming MLH, Harris K, Clements P, Denning C, Hansen A, Eschenhagen T. (2020) Comparison of 10 Control hPSC Lines for Drug Screening in an Engineered Heart Tissue Format. *Stem Cell Rep* 15:93–998.

10 Declaration of contributions

The results presented in this thesis are content of unpublished work and will be submitted in 2022. I hereby declare that the pre-analytical sample preparation, data analysis, visualization and interpretation of all results shown in this thesis were conducted by me.

Furthermore, I declare that all methods and procedures in this work were conducted by me except the ones indicated in the respective methodological description. Here, I summarize the contributions from the collaborators.

- Chapter 4.1.3 : The Southern blot probe design and procedure were kindly performed by Dr. Dr. Boris Skryabin (Transgenic animal and genetic engineering (TRAM), WWU, Münster, Germany).
- Chapter 4.1.4: The karyotyping analysis was kindly performed by Elisabeth Krämer and Giulia Mearini (IEPT, UKE, Hamburg, Germany).
- Chapter 4.7: The mass spectrometry procedure was kindly performed by Dr. Susanne Brodesser (CECAD Lipidomics/Metabolomics Facility, CECAD Research Center, University of Cologne, Cologne, Germany).
- Chapter 4.9: The mass spectrometry procedure was kindly performed by Dr. Xiaoke Yin (King's British Heart Foundation Centre of Research Excellence (Group leader: Prof. Dr. Manuel Mayr), King's College London, United Kingdom).
- Chapter 4.9: The electron microscopy was performed by Dr. Michaela Schweizer (Electron Microscopy Unit, Center for Molecular Neurobiology, UKE, Hamburg, Germany).
- Chapter 4.11: The single-nucleus RNA sequencing procedure was kindly performed by Sabine Schmidt and Dr. Giannino Patone (Cardiovascular and Metabolic Sciences (Group leader: Prof. Dr. Norbert Hübner), Max Delbrück Center for Molecular Medicine in the Helmholtz Association (MDC), Berlin)

11 Acknowledgements

In this final part I would like to acknowledge everyone who has contributed to this important chapter of my life and supported me to become a scientist.

First, I would like to express my appreciation to Prof. Dr. Thomas Eschenhagen for giving me the opportunity to work in his lab. The possibility to write my doctoral thesis at his institute allowed me to get familiar with high-end technologies and gain insight into fascinating biology. The scientific exchange I experienced here far exceeded my expectations. I would also like to thank Prof. Dr. Thomas Eschenhagen for contributing to this project with his scientific expertise.

For scientific inspiration, support and discussions, I would like to thank Prof. Dr. Friederike Cuello, Prof. Dr. Lucie Carrier, Dr. Marc Hirt and Dr. Florian Weinberger. I would like to emphasize the help of Dr. Dr. Justus Stenzig whose door was always open for discussions about carnitine and fibroblast biology.

I would also like to thank Prof. Dr. Julia Kehr for assessing my thesis and her interest in my research.

I would like to highlight my thanks to Dr. Giulia Mearini, Dr. Umber Saleem, Pan Bangfeng, Tim Stüdemann, Dr. Antonia Zech and Nele Warnecke, for always having a helping hand, for constructive scientific discussions and for conversations apart from science.

I am grateful to Charlotta Behrens with whom I shared all challenges of a PhD student. Our team effort at the beginning of our PhDs provided the basis for this project and I am happy that we could solve tough biological difficulties together.

Special thanks go to Birgit Klampe and Thomas Schulze for providing indispensable support in the cell culture. Without their help, it would not have been possible to perform all these experiments and differentiate the immense number of cardiomyocytes.

I also would like to thank my cousin Lukas Roth. I very much appreciate that he took his time to give valuable feedback to my work, although he was in the final phase of his own doctoral thesis himself.

I would like to acknowledge the great help and guidance of Dr. Bärbel Ulmer. She taught me all the important techniques and supported me mentally as well as physically. A great part of my scientific understanding is her merit.

I would like to heartily thank Prof. Dr. Arne Hansen for the supervision of this project and the unconditional support he gave to me. His scientific inspiration and guidance in planning experiments for my thesis were indispensable for accomplishing this project. His sacrificial

attitude and his unreserved trust in me and my ideas were the reason that I felt more than comfortable in this institute at any time.

Finally, I would like to thank my parents for their sacrifices, encouragement and trust ever since I can remember. They believed in me whatever I did and made this experience possible for me. I am happy to share this with them and with my grandmothers.

In the end, I am truly thankful to have a woman by my side who has motivated and supported me during any ups and downs over the last years. Merle Haufe has been there for me since the early beginning of my studies, during my doctoral thesis and I know that I can rely on her to pass whatever challenge will come after this chapter.

12 Thesis English language declaration

To whom it may concern,

I hereby declare that I am a native English speaker and have read the thesis “Modeling primary carnitine deficiency-mediated dilated cardiomyopathy in engineered heart tissue format”, written by Malte Florian Loos. I reviewed the thesis for grammatically correct English and the scientific language accuracy.

Please do not hesitate to contact me if you have any questions.

Lukas Roth

1 November 2021

Lukas Roth | PhD candidate
School of Medical Sciences | Faculty of Medicine and Health
The University of Sydney
Molecular Bioscience Building (G08)
Corner Maze Cres and Butlin Ave
Darlington NSW 2008
Sydney, Australia
Email: lukas.roth@sydney.edu.au
Tel: +61 431 813 814

13 Declaration of academic honesty - Eidesstattliche Erklärung

I hereby declare that the present dissertation entitled

“Modeling primary carnitine deficiency-mediated dilated cardiomyopathy in engineered heart tissue format“

was written independently by myself. No other sources or aids than those indicated were used. The submitted written form of the thesis complies with the electronic version. This thesis was not handed in in any other form for another examination procedure.

Hamburg, 11.11.2021

Malte Loos

Hiermit versichere ich an Eides statt, die vorliegende Dissertationsschrift mit dem Titel

“Modeling primary carnitine deficiency-mediated dilated cardiomyopathy in engineered heart tissue format“

selbst verfasst und keine anderen als die angegebenen Quellen und Hilfsmittel benutzt habe. Die eingereichte schriftliche Fassung entspricht der elektronischen Version. Ich versichere, dass diese Dissertation nicht in einem früheren Promotionsverfahren eingereicht wurde.

Hamburg, den 11.11.2021

Malte Loos